UNIVERSITY OF CALIFORNIA SAN DIEGO

Investigating the role of transport processes in intracellular organization and dynamics

A dissertation submitted in partial satisfaction of the
requirements for the degree
Doctor of Philosophy

in

Physics

by

Saurabh Sanjay Mogre

Committee in charge:

Professor Elena Koslover, Chair
Professor Alexander Groisman
Professor Wouter-Jan Rappel
Professor Samara L. Reck-Peterson
Professor Tatyana Sharpee

2021

The dissertation of Saurabh Sanjay Mogre is approved, and it is acceptable in quality and form for publication on microfilm and electronically.

University of California San Diego

2021

DEDICATION

To my parents,

who fostered my scientific curiosity, and without whose unyielding support and encouragement I would not have embarked upon this journey

EPIGRAPH

[...] all models are wrong, but some are useful.

—George Box

TABLE OF CONTENTS

LIST OF FIGURES

LIST OF TABLES

ACKNOWLEDGEMENTS

I would like to thank my advisor, Professor Elena Koslover, who has been a constant source of guidance and inspiration throughout this journey. Her unwavering support and mentorship has greatly enhanced my graduate experience. I hope to have imbibed her work ethic, attention to detail, and approach towards research for my future career.

I am also very thankful to my parents and my family for believing in me and encouraging me to pursue this Ph.D. Their support and motivation has been vital to my development and has led me to be the person I am today.

Special thanks to Frances Lu, who has been nothing but supportive and inspirational, and has helped me grow as a person and as a scientist.

I would like to extend my gratitude to all of my friends for their help in making graduate school an enriching experience. Anant Dhayal and Shubham Saini for their continued presence and support since the beginning of my Ph.D., and for making my days in San Diego greatly enjoyable; my friends from college: Arpit Agarwal, Niladri Chatterji, Parthe Pandit, Shantanu Thakar, Vighnesh Vatsal, and within my cohort at UCSD: Robin Heinonen, Jonathan Lam, Shruti Singh – for their camaraderie.

I am also thankful to have been able to work with wonderful colleagues in the Koslover group: Anamika Agrawal, Aidan Brown, Zuben Scott, who have elevated my research with their insightful discussions. Particular thanks to my collaborators at UCSD: Jenna Christensen, Cassandra Niman, Samara Reck-Peterson, and U.Penn.: Sydney Cason, Erika Holzbaur, without whom this dissertation would not have been possible.

Many thanks to the members of my dissertation committee for their valuable feedback and mentorship. It has been a great honor to have you be a part of my scientific development. Your support and guidance has been indispensable to me.

I am especially grateful for the amazing staff at the UCSD Physics department and the Physics Computing Facility: Sharmila Poddar, Catherine McConney, who have always been there

to help me navigate the logistics of graduate school.

I would like to acknowledge funding through the Visible Molecular Cell Consortium Fellowship. The financial support from this fellowship enabled my goal of pursuing interdisciplinary research bridging physics and cell biology.

There are countless people who have had a lasting impact on my Ph.D., apologies and many thanks to anyone that I have failed to mention explicitly. Last but not the least, I would like to acknowledge my cats Bijli and Shadow for bringing me much joy over the past years.

Chapter 2, in full, is a reprint of the material with minor edits, as it appears in: S. S. Mogre, E. F. Koslover, "Multimodal transport and dispersion of organelles in narrow tubular cells", *Physical Review E*, 97 (4), 042402, (2018). The dissertation author was the primary author of this paper.

Chapter 3, in full, is a reprint of the material with minor edits, as it appears in: S. S. Mogre, J. R. Christensen, C. S. Niman, S. L. Reck-Peterson, E. F. Koslover, "Hitching a ride: Mechanics of transport initiation through linker-mediated hitchhiking", *Biophysical journal*, 118 (6), 1357-1369, (2020). The dissertation author was the primary author of this paper.

Chapter 4, in full, has been submitted for publication of the material with minor edits, as it may appear in *Biophysical journal*, 2021. S. S. Mogre, J. R. Christensen, S. L. Reck-Peterson, and E. F. Koslover, "Optimizing microtubule arrangements for rapid cargo capture". The dissertation author was the primary author of this paper.

Chapter 5, in full, is currently being prepared for submission for publication of the material. S. S. Mogre, S. E. Cason, E. L. F. Holzbaur, and E. F. Koslover. The dissertation author was a primary author of this paper.

VITA

2015	B. Tech. and M. Tech. in Engineering Physics with specialization in Nanoscience, Indian Institute of Technology Bombay, India
2018–2020	Visible Molecular Cell Consortium Fellow, University of California San Diego
2019	Instructor of Record, University of California San Diego
2021	Ph. D. in Physics, University of California San Diego

PUBLICATIONS

Z. C. Scott, A. I. Brown, S. S. Mogre, L. M. Westrate, E. F. Koslover, "Diffusive search and trajectories on tubular networks: a propagator approach," *The European Physical Journal E*, 44 (6), 1-20, (2021).

S. S. Mogre, A. I. Brown, E. F. Koslover, "Getting around the cell: physical transport in the intracellular world," *Physical Biology*, 17 (6), 061003, (2021).

S. S. Mogre, J. R. Christensen, C. S. Niman, S. L. Reck-Peterson, E. F. Koslover, "Hitching a ride: Mechanics of transport initiation through linker-mediated hitchhiking," *Biophysical journal*, 118 (6), 1357-1369, (2020).

S. S. Mogre, E. F. Koslover, "Multimodal transport and dispersion of organelles in narrow tubular cells," *Physical Review E*, 97 (4), 042402, (2018).

K. Seki, S. S. Mogre, S. Komura, "Diffusion coefficients in leaflets of bilayer membranes," *Physical Review E*, 89 (2), 022713, (2014).

ABSTRACT OF THE DISSERTATION

Investigating the role of transport processes in intracellular organization and dynamics

by

Saurabh Sanjay Mogre

Doctor of Philosophy in Physics

University of California San Diego, 2021

Professor Elena Koslover, Chair

Transport of intracellular material is a fundamental process observed within the cells of organisms across all realms of life. While the biology may be vastly different across species, the physical mechanisms underlying motion remain largely consistent. Tubular cells such as neuronal axons and fungal hyphae are excellent systems to study transport owing to their simple geometry, robust transport machinery, and experimental tractability. We combine mathematical and computational approaches to explore how transport processes contribute to intracellular organization and affect biological function. Imaging data from neuronal and fungal cells are leveraged to develop functional models and verify their predictions.

In chapter 2, we set up a theoretical model of intracellular transport via a combination of diffusion and motor-protein-driven ballistic movement. We employ analytical techniques and numerical simulations to study the efficiency of different transport modes in achieving various cellular objectives. Our model describes length and time scales over which each transport mode dominates organelle motion, various metrics to quantify the exploration of intracellular space, and the role of regulatory mechanisms such as tethering.

Chapter 3 explores initiation of the hitchhiking transport process wherein a cargo colocalizes with a motor-driven carrier to engage in directed motion. A computational model is developed using data from imaging live cells of the fungus *Aspergillus nidulans*. The model predicts the dependence of hitchhiking initiation rates on the distribution of cytoskeletal tracks and carrier organelles, as well as the number, length and flexibility of the linker proteins that mediate contact between the carrier and the hitchhiking cargo.

The role of microtubule length and spatial organization in the capture of transported cargo is studied in chapter 4. General properties of optimal microtubule arrangements are derived using mathematical and computational modeling. Model predictions are supported by images of microtubules in *Aspergillus nidulans* hyphae.

Chapter 5 highlights the role of transport in interactions between autophagosomes and lysosomes in neuronal axons during autophagy. Leveraging data from hippocampal neurons, we identify parameter regimes that can result in fusion-independent switching of autophagosome motility.

This dissertation identifies common features underlying intracellular transport in tubular cells via modeling approaches rooted in physical principles.

Chapter 1

Introduction

The interior of a cell is a highly dynamic and crowded environment filled with a large variety of microscopic components. Many important biological functions rely on the physical movement of these components through the complex intracellular space. Nanometer-sized mRNA particles synthesized in the nucleus of a neuron are transported over hundreds of microns in an axon in order to be translated into proteins. In growing or injured cells, sub-micron scale raw materials need to be delivered accurately and in a timely fashion to specific locations. Management of waste within a cell requires engulfment of byproducts in an organelle followed by transport to the requisite machinery for recycling. Key functions such as metabolism and antioxidant activity require establishing physical contact between multiple transported entities. All of these processes require co-ordinated and efficient movement of the transported components through the intracellular milieu which can be achieved through a well managed cellular trafficking system. Eukaryotic cells in particular utilize a specialized machinery comprising cargo-carrying molecular motors that walk on cytoskeletal filaments such as microtubules.

Due to the significant involvement of intracellular transport in crucial cellular functions, defects in this process are implicated in many human pathologies (reviewed in [1] and [2]). Human neurons, in particular, are susceptible to transport anomalies owing to their extended

structure. Neurodegenerative disorders such as Multiple Sclerosis, Amyotrophic Lateral Sclerosis (ALS), Parkinson's disease, and Alzheimer's, among others, are attributed to disruption of axonal transport by mutations or other abnormalities [3–6]. Building a quantitative understanding of transport in neuron-like cells is therefore essential towards unraveling the mechanisms underlying these serious diseases.

Tubular cell projections such as neuronal axons and fungal hyphae, while being biologically important, are also particularly suitable model systems for intracellular transport. Microtubules in these cells are typically aligned with the tubular axis, and are often uniformly polarized towards the distal tip [7, 8]. These projections are also much longer than they are wide, with their width ranging between 1-2μm, while the length can extend from a few microns up to a meter [9–12]. Since cargo needs to be transported back and forth between the cell body and the distal tip, movement along the cell axis is more consequential than radial motion. As a result, transport in these cells can be modeled as a one-dimensional process along the axial direction, making it highly amenable to theoretical modeling approaches. In addition to their simplified geometry, the genetic tractability of these cells enables the use of various biological assays to explore the dynamics of intracellular transport. This dissertation is divided into four chapters focusing on various aspects of transport in tubular cell projections and their role in cellular organization and dynamics.

In chapter 2, we focus on two physical mechanisms utilized by Eukaryotic cells to achieve a wide variety of cellular objectives. Stochastic diffusive motion is typically observed over shorter (nanometer) length scales and plays a role in local mixing and interactions. For longer (μm-mm) distances, motor proteins carry the cargo along microtubules, resulting in processive motion. Each of these mechanisms has unique features and drawbacks, with interplay between the two modes being particularly important for cellular scale motion. We develop a theoretical "halting creeper" model to identify how each transport mode contributes to various cellular objectives. For organelles that search for a specific target, we obtain the average capture time

for given transport parameters and show that both diffusion and motor-driven motion contribute to target capture in the biologically relevant regime. Because many organelles have been found to tether to microtubules when not engaged in active motion, we study the competition between immobilization due to tethering and increased probability of active transport. We derive parameter-dependent conditions under which tethering enhances long range transport and improves the target capture time.

In addition to diffusion or direct engagement with motor-proteins, some cellular components are transported via hitchhiking by attaching to other motor-driven organelles. In chapter 3, we describe a quantitative model of intracellular cargo transport via hitchhiking. We focus specifically on the parameter regime relevant to the hitchhiking motion of peroxisome organelles in fungal hyphae. Geometric parameters for the model are obtained from fluorescence imaging in live cells of the fungus *Aspergillus nidulans*. Brownian dynamics simulations are combined with analytical modeling to simulate interactions between carrier and hitchhiker organelles. The model predicts the dependence of hitchhiking initiation on features of the cellular transport machinery, including the number and distribution of microtubules and carrier organelles, as well as the number, length and flexibility of the linker proteins that mediate contact between the carrier and the hitchhiking cargo. We also explore the effect of tethering organelles to microtubules, and show that it can result in substantial enhancement of hitchhiking initiation. This enhancement is related to organelle dispersion using the "halting creeper" model, which predicts improved dispersal efficiency and an increase in the overall transport rate. The predictions of the model are then compared with data obtained from tracking peroxisome motion in *A. nidulans*.

Various types or cargo are either continually synthesized throughout tubular cells, or are incorporated near the distal tip of cellular projections. These cargos need to engage rapidly with microtubules in order to be delivered to the cell body for processing. While some cargos can bind anywhere on a microtubule, preferential binding of cargo can occur near microtubule tips due to pools of motor-proteins. The arrangement of these capture regions along the cell

axis can significantly impact the time required by a cargo to find a microtubule. In chapter 4, we study the role of microtubule length and spatial organization in the cargo capture process using mathematical and computational modeling. We derive general features of microtubule arrangements that result in optimal cargo capture times for a variety of capture modalities. Using fluorescence microscopy, we obtain microtubule lengths in *A. nidulans*, and show that they satisfy optimality requirements set by the model.

Finally, we focus on interactions between transported organelles and its effect on biological function. Degradation of waste material in neurons is carried out via the autophagy pathway which involves engulfment of cytoplasmic components by autophagosomes followed by fusion with lysosomes, resulting in lowered pH and activation of degradative enzymes. Chapter 5 highlights the role of transport in interactions between autophagosomes and lysosomes in neuronal axons during autophagy. Many studies have shown that autophagosomes in neurons undergo bidirectional motion or remain stationary upon formation, and eventually switch to a robust retrograde motility[13, 14]. It is canonically believed that this motility switch results from fusion with lysosomes[15], and data from hippocampal and dorsal root ganglion (DRG) neurons do indeed show that most retrograde autophagosomes display markers of fusion. Using a minimal model, we hypothesize that the observed data may arise from fusion-independent motility switching for a range of feasible parameters. We reiterate these predictions using explicit agent-based simulations of organelle interactions. These results help distinguish between competing ideas within the field regarding whether fusion with lysosomes is necessary for autophagosomes to switch their motility.

The overall focus of this dissertation is to build a comprehensive picture of various physical aspects of transport to understand organization and dynamics within cells. Using cross-disciplinary techniques spanning between physics and cell biology, we have explored key features of intracellular transport. Our findings highlight tools to connect cellular dynamics with biological function, providing a stepping stone towards understanding human health and disease.

Chapter 2

Multimodal Transport and Dispersion of Organelles in Narrow Tubular Cells

2.1 Abstract

Intracellular components explore the cytoplasm via active motor-driven transport in conjunction with passive diffusion. We model the motion of organelles in narrow tubular cells using analytical techniques and numerical simulations to study the efficiency of different transport modes in achieving various cellular objectives. Our model describes length and time scales over which each transport mode dominates organelle motion, along with various metrics to quantify exploration of intracellular space. For organelles that search for a specific target, we obtain the average capture time for given transport parameters and show that diffusion and active motion contribute to target capture in the biologically relevant regime. Because many organelles have been found to tether to microtubules when not engaged in active motion, we study the interplay between immobilization due to tethering and increased probability of active transport. We derive parameter-dependent conditions under which tethering enhances long range transport and improves the target capture time. These results shed light on the optimization of intracellular

transport machinery and provide experimentally testable predictions for the effects of transport regulation mechanisms such as tethering.

2.2 Introduction

Transport of cargo within the intracellular environment is a highly essential and tightly regulated process. Most eukaryotic cells have an active transport machinery consisting of molecular motors moving on a network of cytoskeletal polymers such as microtubules or actin filaments. Organelles can couple directly to motor proteins via specialized adaptors [16], or hitch-hike on other motile organelles [17]. This mode of transport results in motion that is processive over variable length scales up to many microns. Many organelles execute bidirectional motion, switching direction between processive runs by either engaging alternate motor types or transferring to a cytoskeletal track with different orientation [18–22].

In addition to this motor-driven processive transport, effectively diffusive motion of organelles can arise due to thermal noise, active fluctuations of cytoskeletal networks [23], or hydrodynamic entrainment in flow set up by moving motors and cargo [24]. Evidence has shown that the short time-scale movement of organelles appears effectively diffusive even when the underlying cytoplasmic medium is primarily elastic [23, 25, 26]. For brevity, we will refer to this stochastic motion of organelles as passive diffusion, while acknowledging that the fluctuations underlying the motion can have a number of actively driven origins.

The interplay between active and passive transport modes gives rise to length-scale dependent effects. While processive transport is efficient at delivering cargo over long cellular distances, diffusion can more effectively spread organelles over smaller lengths. The balance between these transport modes has been quantified in previous work using the Péclet number, defined as $\mathrm{Pe} = vL/D$ where v is the processive velocity, L is the length-scale of interest, and D is the diffusivity in the passive state[27]. High Péclet numbers correspond to lengths where

active transport becomes dominant, assuming infinite processivity. In the case of finite processive run-lengths, effectively diffusive behavior arises at long times as the particle executes many runs in randomly chosen directions[28, 29].

While much previous work has relied on the mean squared displacement (MSD) as a measure of particle spreading[28–30], this metric cannot be directly translated into quantities of biological relevance such as the rate of arrival to intracellular targets or particle interaction rates. Theoretical studies of first passage times by particles engaged in multi-modal transport have demonstrated the existence of an optimum run-length both in the absence of diffusion[31, 32] and in the case where the particles can only interact with their target in the diffusive state[27, 33, 34]. These results suggest that the transport machinery in the cell may be optimized to allow substantial contributions from both processive and diffusive transport. In this work, we focus on the relative importance of both passive and active transport modes to biologically relevant transport objectives, assuming organelles are functional in both states of motion. Endosomes, peroxisomes, lipid droplets, and mitochondria are some example organelles known to employ multi-modal transport to move around within the cell while maintaining their function [35–38].

A variety of cellular processes rely on efficient transport to achieve distinct objectives necessary for biological function. One such objective is the establishment of a uniform distribution of particles throughout the cell, as is observed for peroxisomes, mitochondria and lipid droplets [11, 39, 40]. Establishing this distribution, starting from the point of genesis of particular organelles, requires rapid transport and broad dispersion across long cellular length-scales. Another objective is the delivery of organelles to specific subcellular regions. Examples include the motion of synaptic vesicles from the cell body to the pre-synaptic terminal of neuronal axons [41], and the transport of vesicles containing newly synthesized membrane-bound proteins from the Golgi apparatus to the cell boundary [42]. The role of different transport modes in this process depends on the length scale of separation between the site of organelle synthesis and their eventual target. A third cellular objective is the rapid encounter between an intracellular target and any one of

a uniformly distributed population of organelles. For instance, peroxisomes serve to neutralize oxidative metabolic byproducts, and the health of a cell is dependent on rapid removal of these toxic species as soon as they appear [43]. Similarly, early endosomes rely on contact with any of a population of lysosomes that aid in releasing the endosomal contents into the cytoplasm [44]. The efficiency of such target encounter depends both on the nature of transport processes for the organelles and on their density within the cell.

The organization of the cytoskeletal network has a potentially important role to play in the distribution of intracellular particles. While a number of past models for intracellular transport employed a continuum approximation for cytoskeletal density [27, 45, 46], it is becoming clear that the specific arrangement of distinct cytoskeletal tracks has a substantial impact on cargo transport [47]. Obstructions due to intersecting microtubules may cause particles to pause or switch tracks and change the direction of movement [21]. Localized traps arising from heterogeneous filament polarity have been found to hinder transport in cell-scale computational models [47]. In tubular cell projections such as neuronal axons and fungal hyphae tips, the arrangement of cytoskeletal filaments is highly simplified, with microtubules aligned along the tubular axis and in many cases uniformly polarized towards the distal tip [7, 8]. These projections range in length from tens to many hundreds of microns, and require cargo to be efficiently transported from the cell body to the distal tips and back again. In addition to being particularly amenable to theoretical models of transport phenomena, these cell types are of fundamental biological importance. Defects in axonal transport in neurons have been implicated in a number of human pathologies, ranging from multiple sclerosis to Alzheimer's to prion diseases [3] . Due to their simplified morphology and long length, these tubular cells form an ideal system for investigating the length-scale dependent effects of multimodal transport.

The discrete nature of cytoskeletal tracks within tubular cell projections limits active transport to narrow axially oriented bundles of microtubules [8]. It has been proposed in several cellular systems that transport efficiency is increased by directly tethering organelles to the

microtubules in order to prevent them from losing access to the tracks [22, 48, 49]. Tethering can occur by specialized adaptor proteins binding the organelle to cytoskeletal tracks, as in the case for axonal mitochondria that become preferentially anchored in cellular regions with high metabolic needs [50–52]. Alternately, the binding of multiple motor proteins to individual vesicles results in a tethering effect that is believed to contribute to observed motor cooperativity [22, 53]. Because tethering is expected to hinder short-range dispersion while enhancing the ability of organelles to engage in long-range processive walks, it can potentially serve as a regulatory mechanism for length-dependent transport.

In this chapter, we present a simplified model for transport in a tube through a combination of processive walks and diffusion. We analyze the relative contributions of the two transport modes, as well as the possibility of tethering to cytoskeletal tracks, in achieving the different transport objectives of the cell. Sec. 2.3 establishes our halting creeper model and its behavior in terms of the rate with which particles explore a one-dimensional environment. In Sec. 2.4, we use the developed model to study the effects of bidirectional transport on distributing particles uniformly within a domain. In Sec. 2.5, we explore the contribution of different transport modes to the delivery of individual particles, as well as target clearance by a dispersed particle population. Sec. 2.6 introduces an expanded model that accounts for particle tethering, delineating the effects of this mechanism on organelle dispersion and target capture times.

2.3 Halting creeper model

We define a simplified stochastic model for intracellular particles undergoing multi-modal transport, focusing on motion along a single dimension. Each “halting creeper" particle exists in either a passive diffusive state characterized by diffusion coefficient D or an actively moving state with constant speed v in either the positive or negative direction (Fig. 2.1). Switching between the states is a Markovian process with constant starting rate γ for transitioning from the

passive to the active state and constant stopping rate λ for transitioning from active to passive. Selection of the direction of motion is random at each initiation of an active run, and we assume complete symmetry between forward and backward motion. We note that this model is a more general form of previously defined creeping particle models [31], which have been analyzed in the limit $\gamma \to \infty, D \to 0$. Furthermore, a three-dimensional version of our halting creeper model has previously been explored in the context of mean squared displacement and local concentration fluctuations [27]. By contrast, in this work we focus explicitly on the efficiency with which such two-state transport distributes organelles throughout a cell and delivers them to intracellular targets.

Two important quantities which describe the behavior of a halting creeper particle are the active run-length ($\ell = v/\lambda$) and the equilibrium fraction of particles in the active state ($f = \frac{\gamma}{\lambda+\gamma}$). For much of the subsequent discussion, we non-dimensionalize all length units by the run-length ℓ and all time units by the run-time $1/\lambda$. We denote the remaining dimensionless parameters as $\hat{D} = \frac{D}{\ell^2\lambda}, \hat{\gamma} = \frac{\gamma}{\lambda}$, and dimensionless time as $\hat{t} = \lambda t$.

The Markovian nature of the transitions between active and passive states allows the calculation of a spatio-temporal propagator function $G(x,t)$ for the halting creeper, which gives the distribution of positions at time t given the particle started at the origin at time 0. This propagator is obtained by convolution in the space and time domain of the individual propagators for passive and active transport. After a Fourier transform in space ($\hat{x} \to k$, $G \to \widetilde{G}$) and a

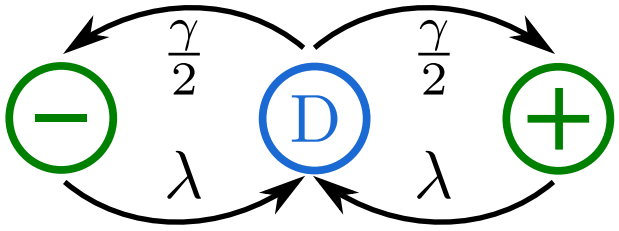

Figure 2.1: Schematic for the transition between particle states. 'D' denotes diffusive particles, '+' denotes particles moving in the rightward direction, whereas '-' denotes particles moving in the leftward direction. The arrows are labeled with transition rates between states.

Table 2.1: Estimated values of transport parameters for some biological systems. Run length can be obtained as $\ell = v/\lambda$. Parameters can be converted to dimensionless units according to: $\hat{D} = D\lambda/v^2$, $\hat{\gamma} = \gamma/\lambda$, $\hat{\rho} = \rho v/\lambda$.

Transport System	Rate of switching to active transport $\gamma\,(s^{-1})$	Rate of switching to passive transport $\lambda\ (s^{-1})$	Velocity of active transport $v\,(\mu\mathrm{m}/s)$	Diffusivity $D\,(\mu\mathrm{m}^2/s)$	Density of population $\rho\ (\mu\mathrm{m}^{-1})$	Approx. size of cellular region $L\,(\mu\mathrm{m})$
Peroxisomes in fungal hyphae [11]	0.015[i]	0.29	1.9	0.014	1.5	50
Lysosomes in kidney cells [21, 54]	0.17	0.15	0.52	0.071	–	20
Mouse neuron transport vesicles in vitro [55]	0.33[i]	2.7	0.8	0.03	0.14	–
Mitochondria in *Drosophila* axons [56]	0.17	0.15	0.35	–	1.3	1000
Dense core vesicles in *Aplysia* neurons [57, 58]	0.22[i]	2.2[ii]	0.36[iii]	0.002[iii]	1.7	100
$\mathrm{PrP}^{\mathrm{C}}$ vesicles in mouse axons [55, 59]	0.36	0.15	0.85	–	0.4	100

[i] Estimated from equilibrium fraction in active state.

[ii] Estimated from single particle trajectory.

[iii] Estimated from MSD plot

Laplace transform in time ($\hat{t} \to s$, $\widetilde{G} \to \widehat{\widetilde{G}}$), the multi-modal propagator for particles initially in an

equilibrium distribution between passive and active states is given by

$$\widehat{\widetilde{G}}(k,s) = \frac{(\lambda+s)(\gamma+\lambda)(\gamma+\lambda+s) + \left(D\gamma(\lambda+s) + v^2\lambda\right)\ k^2}{(\gamma+\lambda)\left[s(\lambda+s)(\gamma+\lambda+s) + \left(D(\lambda+s)^2 + v^2(\gamma+s)\right)\ k^2 + v^2 D\ k^4\right]}, \tag{2.1}$$

as derived in Appendix A.1. This propagator serves as the basis for our subsequent calculations on the efficiency of particle spreading and target site search.

2.3.1 Particle spreading: mean squared displacement

The mean squared displacement (MSD) is a commonly used measure of spreading speed for diffusing particles. For the halting creeper model, it can be calculated directly from the propagator as

$$\begin{aligned} \left\langle \hat{x}(\hat{t})^2 \right\rangle &= \mathscr{L}^{-1}\left[-\frac{\partial^2 \widehat{\widetilde{G}}}{\partial k^2}\bigg|_{k=0} \right] \\ &= 2(1-f)\hat{D}\hat{t} + 2f\left[\hat{t} + (e^{-\hat{t}} - 1)\right], \end{aligned} \tag{2.2}$$

where the Laplace inversion $\mathscr{L}^{-1}$ is carried out analytically via the residue theorem.

This expression for the MSD is composed of a linear superposition of fraction $1-f$ of diffusing particles and fraction f of particles undergoing active walks that are persistent over a dimensionless time-scale of 1. The latter component corresponds to an MSD that scales ballistically as $f\hat{t}^2$ for $\hat{t} \ll 1$ and diffusively as $2f\hat{t}$ for $\hat{t} \gg 1$. In the case of small diffusivity, there is an additional transition time when the ballistic motion begins to dominate over the passive diffusion. This occurs at $\hat{t}^* = \frac{2\hat{D}}{\hat{\gamma}}$. When $\hat{t}^* \ll 1$, the MSD transitions from diffusive to ballistic and back to diffusive scaling (Fig. 2.2a), as has previously been demonstrated with lattice models of mixed diffusive and processive transport[28]. The long-time behavior of the particle is defined

by an effective diffusion coefficient

$$\hat{D}_{\text{eff}} = (1-f)\hat{D} + f, \tag{2.3}$$

which in the limit of $\hat{t}^* \ll 1$ is dominated by the term corresponding to bidirectional active walks ($\hat{D}_{\text{eff}} \to f$).

The relative importance of processive versus diffusive transport over a length-scale x can be characterized by the Péclet number [27]: $\text{Pe}(x) = vx/D$, which is a dimensionless quantity often used to compare the contributions from advection and diffusion for particles in a flowing fluid [60]. A large Péclet number $\text{Pe} \gg 1$ corresponds to transport that is dominated by the processive motion. In the case where active motion remains processive only up to distances comparable to the run length ℓ, the relevant Péclet number for long-range transport is $Pe(\ell) = 1/\hat{D}$. Our dimensionless diffusion constant thus describes the relative contribution of diffusion above processive motion over a length scale comparable to the average run-length. For the remainder of the discussion, we focus on the case where the transition time $\hat{t}^* = \frac{2\hat{D}}{\hat{\gamma}} < 1$, so that a distinct regime of processive motion appears between the regimes dominated by passive diffusion and effectively diffusive bidirectional walks. This is the case for the organelle transport examples listed in Table 2.1. We note in passing that the presence of a discernible processive motion is key to identifying active runs in experimental particle-tracking data[11, 57, 61], so that systems not in this regime are unlikely to be selected for studies of active transport.

2.3.2 Particle spreading: range

An alternate metric for the efficiency of particle spreading is the overall range — the average size of the domain that has been explored by a halting creeper particle after an interval of time. For a one-dimensional model, the range of each particle is given by its maximum position minus its minimum position over the course of its trajectory. As will be discussed further in

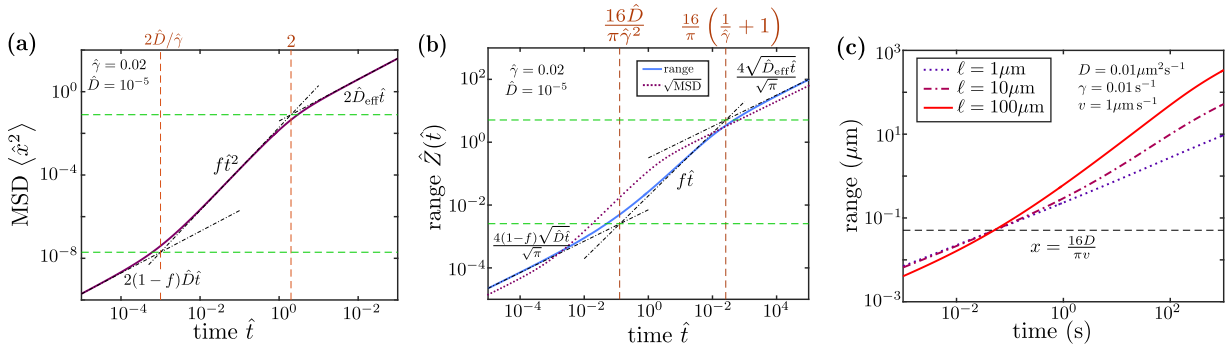

Figure 2.2: Contribution of passive and active motion to spreading of particles at different length and time scales. (a) Mean squared displacement for halting creepers. Black dash-dotted lines show scaling regimes. Vertical dashed lines indicate transition times between the regimes. Horizontal dashed lines indicate transition length scales. (b) Dimensionless range versus time for a halting creeper particle, with scaling regimes, transition times, and transition length scales indicated. Dotted curve shows the root mean squared displacement for comparison. (c) Range versus time for typical parameter values for intracellular organelles, showing the increase in long-range transport with increasing run length, above a length scale indicated by the horizontal dashed line.

Section 2.5, the range is directly related to rate at which a dispersed population of particles first encounters a target.

Our model permits calculation of the range over time for a halting creeper using the renewal equation method [31, 62]. Namely, we define the distribution of first passage times to a target at position $x > 0$ (for a particle starting in a diffusive state at the origin) as $F_D(t;x) = F_{D+}(t;x) + F_{DD}(t;x)$, where F_{D+} gives the distribution of first passage times for the fraction of particles that arrive at the target while walking in the positive direction and F_{DD} gives the distribution of times for particles arriving in the passive diffusive state. Similarly, we consider the components of the propagator function defined in Appendix A.1, where $G_{DW}(x;t)$ gives the spatial distribution at time t of particles that began in a diffusive state at the origin at time 0, and are found in the actively walking state at time t. The other components G_{DD}, G_{WD}, G_{WW} are defined analogously, with additional expressions for G_{+D}, G_{+W} giving the propagator for particles that are initially walking in the positive direction, and end up in either the diffusive or

the actively walking state. One of the renewal equations for this system is then given by,

$$G_{DD}(x;t) = \int_0^t dt' \left[F_{DD}(t';x) G_{DD}(0;t-t') + F_{D+}(t';x) G_{+D}(0;t-t') \right], \tag{2.4}$$

A similar expression for purely processive bidirectional motion appears in [31]. In Eq. 2.4, the distribution of particles which start in the diffusive state and remain in the diffusive state ($G_{DD}(x;t)$) comprises two terms – the first of which is a convolution between the probability that the particle first hits the target x at time t' in the diffusive state ($F_{DD}(t';x)$) and the probability of it returning to position x within the remaining time $t-t'$, also in the diffusive state ($G_{DD}(0;t-t')$). The second term includes a convolution between the probabilty that the particle first hits the target while walking forward ($F_{D+}(t';x)$) and the probability that it returns to position x in the diffusive state ($G_{+D}(0;t-t')$). Analogous renewal equations are derived for G_{DW}, G_{WD}, G_{WW}.

After a Laplace transform in time, this convolution structure can be expressed as a product, which yields a system of equations,

$$\begin{bmatrix} \widehat{G}_{DD}(0) & \widehat{G}_{+D}(0) \\ \widehat{G}_{DW}(0) & \widehat{G}_{+W}(0^+) \end{bmatrix} \begin{bmatrix} \widehat{F}_{DD} \\ \widehat{F}_{D+} \end{bmatrix} = \begin{bmatrix} \widehat{G}_{DD}(x) \\ \widehat{G}_{DW}(x) \end{bmatrix}, \tag{2.5}$$

where $\widehat{F}$ and $\widehat{G}$ denote the respective Laplace-transformed functions. Here, $G_{+W}(0^+;t-t') = \lim_{\varepsilon \to 0^+} G_{+W}(\varepsilon;t-t')$ corresponds to the probability density for a particle that starts at time t' just before the origin walking in the positive direction, to be at the origin and in a walking state at time t.

This system can be solved to calculate the first passage time $\widehat{F}_D = \widehat{F}_{DD} + \widehat{F}_{D+}$ for particles that began in the diffusive state. Corresponding renewal equations for $G_{WD}(x;t)$ and $G_{WW}(x;t)$

yield the first passage time for particles that began in the active state:

$$\begin{bmatrix} \widehat{G}_{DD}(0) & \widehat{G}_{+D}(0) \\ \widehat{G}_{DW}(0) & \widehat{G}_{+W}(0^+) \end{bmatrix} \begin{bmatrix} \widehat{F}_{WD} \\ \widehat{F}_{W+} \end{bmatrix} = \begin{bmatrix} \widehat{G}_{WD}(x) \\ \widehat{G}_{WW}(x) \end{bmatrix}. \tag{2.6}$$

The range of the halting creeper particles over time ($Z(t)$) can be related to the Laplace transform of the overall first passage time $\widehat{F}(s;x)$ according to [31],

$$Z(t) = \mathscr{L}^{-1}\left[\frac{1}{s}\int_{-\infty}^{\infty}\widehat{F}(s;x)dx\right], \tag{2.7}$$

where $\widehat{F}$ is a linear combination of $\widehat{F}_D$ and $\widehat{F}_W$, weighted by the equilibrium probability that the particle starts in an active or a passive state. To calculate the range function, we analytically perform the Fourier inversion of the propagators $\widehat{G}_{DD}(0), \widehat{G}_{+D}(0), \widehat{G}_{DW}(0), \widehat{G}_{+W}(0^+)$ by integrating over k. The spatial integral over x results in the right hand side of the renewal equations being expressed as $\widehat{\widetilde{G}}_{DD}(k=0)$, etc. While short-time and long-time limits of the range can be obtained directly from the large s and small s limits of the renewal equations, the relevant time-scales for biological processes can span across many orders of magnitude, thus making it desireable to calculate the particle spreading efficiency over all time scales. To this end, we invert the Laplace transform numerically using Talbot's algorithm [63].

As shown in Fig. 2.2, the range exhibits similar transitions in scaling as the MSD. However the transitions between the different regimes are shifted to longer times. At short times, the average range of particles with an equilibrium initial distribution between active and passive states can be calculated by solving the renewal equations in the limit $s \to \infty$ and performing the Fourier and Laplace inversions analytically for the lowest order terms in $1/s$. The expression for the short time average range is given (in dimensionless units) by

$$Z(\hat{t}) \to 4(1-f)\sqrt{\frac{\hat{D}}{\pi}}\sqrt{\hat{t}} + f\hat{t}. \tag{2.8}$$

Thus, the ballistic motion dominates over the diffusive motion above a critical transition time

$$\hat{t}^*_{\text{range}} = \frac{16\hat{D}}{\pi\hat{\gamma}^2}. \tag{2.9}$$

In the case where particles spend very little time in active motion ($\hat{\gamma} \ll 1$), this time-scale is substantially longer than the transition time $\hat{t}^*$ for the MSD. The corresponding length scale for the transition from primarily diffusive to primarily ballistic motion is

$$\hat{x}^*_{\text{range}} = \frac{16\hat{D}}{\pi\hat{\gamma}(1+\hat{\gamma})}. \tag{2.10}$$

At longer times, there is a subsequent transition from the ballistic scaling of the range to the effectively diffusive long-time scaling,

$$Z(\hat{t}) \to 4\sqrt{\frac{\hat{D}_{\text{eff}}}{\pi}}\sqrt{\hat{t}}, \quad \hat{t} \gg \hat{t}^{**}_{\text{range}}, \tag{2.11}$$

which occurs at a secondary transition time t^{**}_{range} and corresponding length scale x^{**}_{range} given by,

$$\begin{aligned} \hat{t}^{**}_{\text{range}} &= \frac{16\hat{D}_{\text{eff}}}{\pi f^2}, \\ \hat{x}^{**}_{\text{range}} &= \frac{16}{\pi}\left(1+\frac{\hat{D}}{\hat{\gamma}}\right). \end{aligned} \tag{2.12}$$

In the case of a small fraction of time spent walking, this transition time is again shifted substantially above what would be expected from the MSD behavior, where the corresponding transition occurs at $\hat{t}^{**} = 2$. In the limit $\hat{D}/\hat{\gamma} \ll 1$, the transition time for the range can also be expressed as $\hat{t}^{**}_{\text{range}} = \frac{16}{\pi}(1+1/\hat{\gamma})$, comparable to the cycle time required for a single particle to transition between an active and a passive state and back again.

This result highlights the fundamental insufficiency of the MSD in describing the efficiency with which the particles explore their domain. Specifically, for a very small equilibrium walking

fraction f, the time required for the active walks to contribute substantially to the average range can be well above the time-scale $1/\gamma$ for an individual particle to start walking. Similarly, in this regime the range will only exhibit diffusive scaling at time-scales long enough for individual particles to execute multiple starting and stopping transitions. Examples of particle motion where the pause time substantially exceeds the processive run time include organelles (such as peroxisomes) whose active transport is mediated by hitch-hiking on other organelles [17], and particles whose motion is driven by hydrodynamic entrainment due to cytoplasmic flow associated with nearby passing particles [24]. In such cases, the MSD does not accurately represent the rate at which these particles explore their domain.

We note that in the case where $\hat{D} < 1$, which corresponds to most biologically relevant examples, increasing the run length (*e.g.:* by decreasing the stopping rate λ) raises the particle range for all length scales above $x > \frac{16D}{\pi v}$ (Fig. 2.2), corresponding to the length at which the Peclet number $\mathrm{Pe}(x)$ becomes substantial. The implication is that longer processive runs improve the ability of particles to explore their domain at all length scales where active walks move faster than diffusion.

2.4 Particle dispersion through bidirectional transport

Having established the speed of particle spreading via multi-modal bidirectional transport, we now turn to consider explicitly the efficiency with which such transport can achieve a particular cellular goal. Certain metabolic and regulatory needs of the cell require a well-dispersed distribution of organelles throughout the cell interior. For instance, mitochondria are found throughout neuronal axons, providing a locally available energy source through glucose metabolism [51]. In fungal hyphae, peroxisome organelles are maintained at near uniform distribution[11], allowing for rapid neutralization of toxic metabolic byproducts [43].

Establishing a well-mixed distribution relies not only on the ability of particles to move

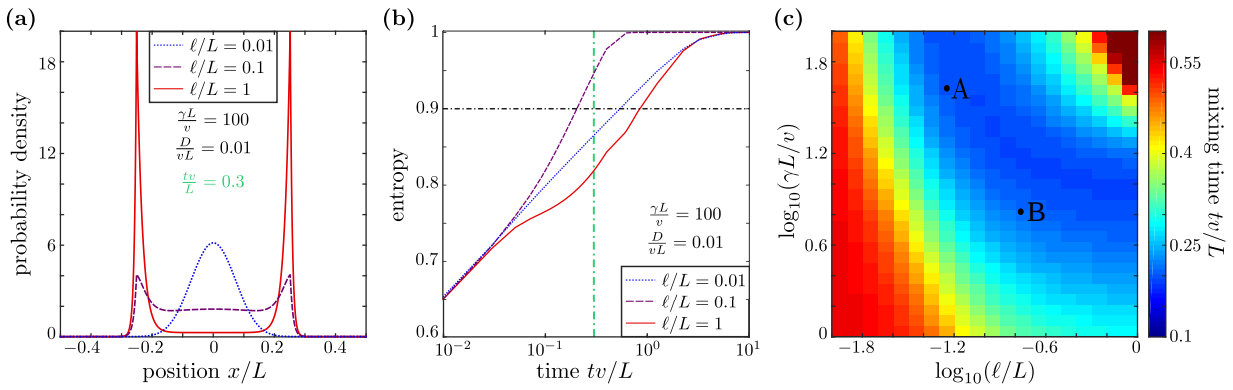

Figure 2.3: Dispersion of particles towards a uniform distribution via bidirectional transport. All length units are non-dimensionalized by domain length L and all time units by L/v. (a) Particle distribution density for different run lengths, at dimensionless time 0.3. (b) Entropy vs time for different run lengths. The horizontal dash-dot line denotes the threshold entropy for the system to be considered well-mixed. The vertical (green) dash-dot line is at dimensionless time 0.3 (c) Time to reach a well-mixed state as a function of run length (ℓ) and rate of transition to an active state (γ). Points A and B are drawn at corresponding transport parameters for lysosomes in monkey kidney cells and PrP^C vesicles in mouse axons, respectively (Table 2.1).

rapidly through the cell, but also on the ability of a transport mechanism to disperse and flatten regions of highly concentrated particles. We focus specifically on the rate with which a bolus of particles is spread over a cellular region. Such a process becomes necessary, for instance, in the case of rapid organelle production in response to an external signal, where the organelles must then be spread through long cellular projections such as axons or hyphae.

We use the halting creeper model to explore how different transport parameters affect the efficiency of such dispersion. Because we are interested in the initial establishment of an equilibrium spatial distribution, we consider particles that originate at $x = 0$ in the passive state, whose distribution is given by $G_D(x,t) = G_{DD}(x,t) + G_{DW}(x,t)$. This function can be evaluated by numerical Fourier-Laplace inversion of the transformed distribution, as described in Appendix A.1. The time evolution of the distribution is plotted in Fig. 2.3a. Note that long walk lengths result in little dispersion of particles, with the distribution splitting into two narrow, processively moving peaks. Short walk lengths lead to an effectively diffusive motion, with the particle distribution assuming the form of a slowly spreading Gaussian. An intermediate walk

length combines both the rapid spreading of the distribution with the flattening of localized peaks to enable more efficient dispersion. The limits for large and small walk lengths suggest that there exists an optimal run length ℓ for which the particles are most efficiently mixed.

A number of different metrics have been developed for quantifying the rate of mixing driven by stochastic processes [64–66], including several that track the approach of a bolus of particles towards uniform spread [67, 68]. A commonality of these measures is their dependence on a particular length scale of interest [66] over which particles are to be mixed. For our one-dimensional system, we introduce a length L corresponding to the size of the domain on which uniform distribution is desired. This length represents the approximate extent of the tubular cell region across which particles are being dispersed. It can range over many orders of magnitude, with mammalian axons reaching up to a meter in length. Example values for some cellular systems are listed in Table 2.1. We calculate the spatial distribution of halting creeper particles originating in the center of a domain of length L with reflecting boundary conditions, implemented using the standard image method [69]. The mixing of the particles is quantified via the Shannon entropy of the distribution [68, 70], defined as

$$S = -\sum_{i=1}^{N} \frac{p_i \log(p_i)}{\log(N)}, \tag{2.13}$$

where the domain is broken up into N bins, and p_i is the probability of a particle being located in bin i. Optimal mixing is achieved when the organelles are uniformly distributed, in which case $p_i = \frac{1}{N}$ and $S = 1$. Conversely, a distribution with all particles in a single section is the least mixed state, with $S = 0$. The entropy has an inherent dependence on the number of bins used for discretizing the probability distribution, and we employ $N = 5000$ throughout our calculations.

The time evolution of the entropy is dependent on the dimensionless run-length ℓ/L (Fig. 2.3b), with long runs corresponding to an initially slow rise in entropy as the bolus of particles evolves into two coherent spatial peaks until sufficient reversals are achieved to disperse the particles throughout the domain. Short run lengths limit the rate of entropy increase over

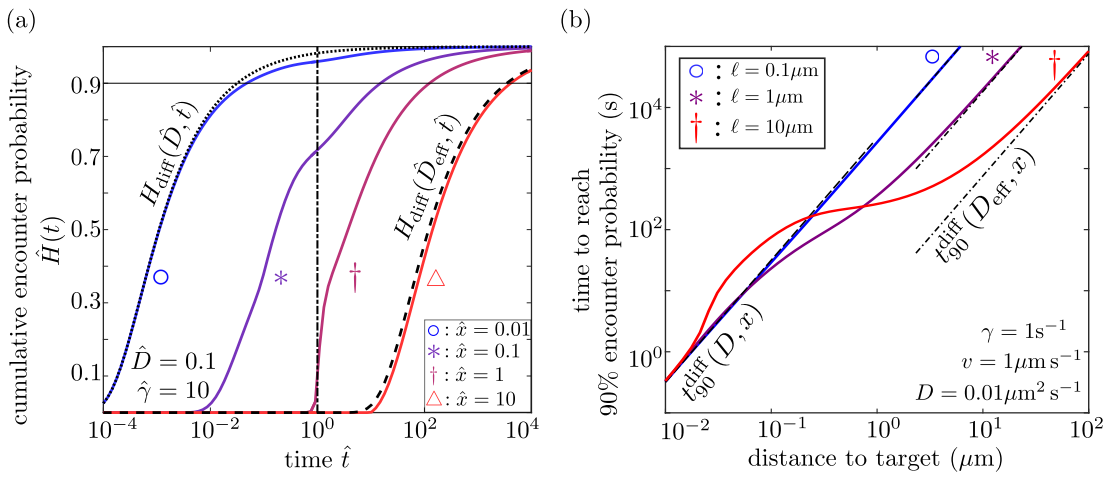

Figure 2.4: Target capture times for a single particle. (a) Cumulative encounter probability for different initial distances to the target ($\hat{x}$). The dotted and dashed lines denote the encounter probability for diffusive particles with a diffusion coefficient $\hat{D}$ and $\hat{D}_{\text{eff}}$ respectively. The dash-dot line denotes the average time required for a particle in the active state to cover a distance of $\hat{x}=1$. All length units are non-dimensionalized by ℓ and all time units by ℓ/v. (b) Time to reach 90% capture probability for different run lengths, assuming rapid starting rate $\gamma=1\text{s}^{-1}$ and distances appropriate for intracellular organelle transport. The dotted and dashed lines denote $t_{90\%}$ for diffusive particles with diffusion coefficient $\hat{D}$ and $\hat{D}_{\text{eff}}$, respectively.

long times, because the particle distribution spreads slowly as an effectively Gaussian peak. We consider the system to be well-mixed when the entropy crosses a threshold value $S_t=0.9$ and define the time taken to reach this state as the mixing time t_{mix}. This mixing time depends in a non-monotonic fashion on both the starting rate (γ) and run length (ℓ) of processive walks (Fig. 2.3c). High values of γ, corresponding to particles that spend most of their time in the active state, give rise to an optimum run length to achieve the most rapid mixing. This effect arises from the need to reverse the direction of active walks in order to efficiently disperse particles within the domain. However, each such reversal necessitates a waiting time of $1/\gamma$ during which the particles are in a passive state and spreading very slowly. Consequently, at low values of γ mixing is most efficiently achieved by particles that carry out very long walks. The results shown in Fig. 2.3 assume a small value of passive diffusivity ($\frac{D}{Lv}=0.01$). Increasing this diffusivity would lead to a monotonic rise in the entropy, as diffusion enhances the particle mixing.

2.5 Target Search by Multimodal Transport

2.5.1 Search by a single particle

In addition to achieving uniform dispersion of particles, another goal of intracellular transport is to deliver organelles to specific cellular regions. This transport objective arises, for instance, when synaptic vesicles must reach the presynaptic bouton of a neuron [41]. Using our one-dimensional halting creeper model, we consider the first passage time of a single particle towards a stationary target located at distance x. For simplicity, we consider the case where x is much smaller than the overall extent of the domain, so that the distance to the target x and the processive run length ℓ are the only relevant length scales in the problem. As in the case of our dispersion calculations (Sec. 2.4), we consider particles that are initially in the passive state, as applicable to the distribution of newly synthesized organelles.

The distribution of first passage times can be obtained from the renewal equation Eq. 2.5, by carrying out analytic Fourier inversion followed by numerical Laplace inversion of the propagators (see Appendix A.1). The cumulative distribution of encounter times to the target is plotted in Fig. 2.4a, showing the transition from a passively diffusive process at small distances ($\hat{x} < x^*_{\text{range}}$) to an effectively diffusive process (with diffusivity $\hat{D}_{\text{eff}}$) at distances much longer than the run length ($\hat{x} > 1$). For comparison, the cumulative distribution for a purely diffusive process is given by

$$H_{\text{diff}}(\hat{x},\hat{t};\hat{D}) = 1 - \text{erf}\left[\frac{\hat{x}}{\sqrt{4\hat{D}\hat{t}}}\right]. \tag{2.14}$$

By contrast, intermediate distances show a sharp increase in the cumulative probability of target encounter at time $\hat{t} = \hat{x}$, corresponding to the arrival of the first processively walking particles.

Because the average first passage time of a random walk in a semi-infinite domain diverges [69], we focus on the time required for particles to hit the target with sufficiently high

probability. Analogous to our calculations of particle dispersion in Section 2.4, we define the hitting time $t_{90\%}$ as the time by which there is a 90% chance that the particle has hit the target. We note that $t_{90\%}$ is well-defined even on a semi-infinite domain due to the recurrent nature of random walks in one dimension, ensuring a finite hitting time for all particles [69]. For short distances, the time for probable encounter of the particle scales as expected for purely diffusive motion with diffusivity $\hat{D}$ (Fig. 2.4b),

$$t_{90}^{\text{diff}}(\hat{x};\hat{D}) = \frac{\hat{x}^2}{4\hat{D}\left[\text{erf}^{-1}(0.1)\right]^2} \tag{2.15}$$

where erf is the error function. At long times, a similar scaling is observed with effective diffusivity $\hat{D}_{\text{eff}}$.

As is the case when the transport objective is to achieve a uniform distribution of particles, increasing the length of processive runs does not necessarily result in more efficient transport. This is true despite the fact that, unlike previous models of multimodal transport [27, 33, 34], we consider our particles capable of accessing their target in both the passive and active states. A run length that is much longer than the distance to the target can hinder particle delivery, because particles have a 50% chance of initiating their motion in the wrong direction. They then require a long time to stop, turn, and return towards the target. At the same time, very short processive runs decrease the overall rate of spread for the particle distribution and thus slow down the target encounter. These two effects give rise to an optimum in the efficiency of target delivery, with minimal values of target hit time $t_{90\%}$ occuring at intermediate run lengths ℓ (Fig. 2.4b). This effect is a direct analogue to the optimum walk-length for achieving uniform distribution. The existence of this optimum walk length has also previously been noted for creeper models without any paused or passive state [31, 32].

We additionally provide a calculation of first passage times in the alternate case where the particle is capable of accessing its target in the passive state only (see Appendix A.5). In such a

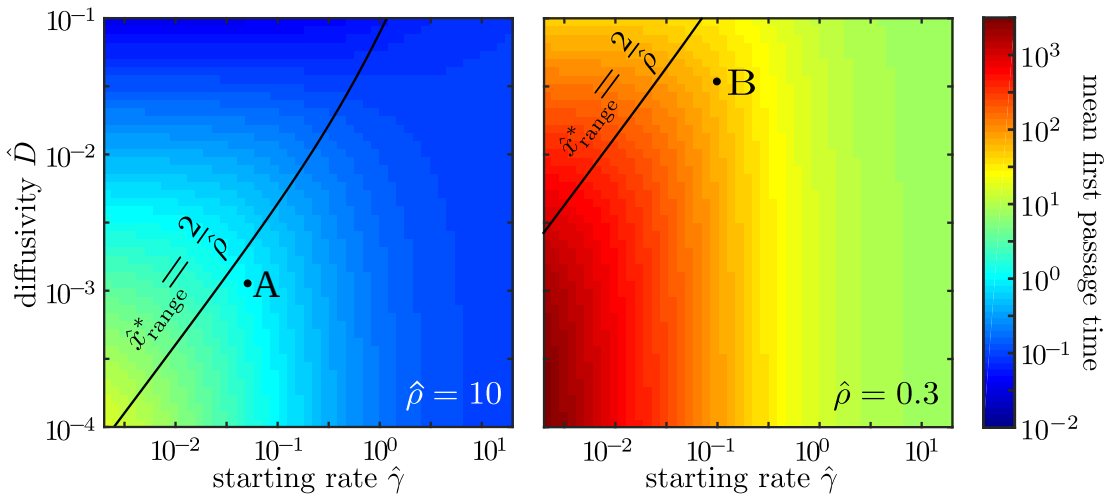

Figure 2.5: Average time for target capture by a population of uniformly distributed particles, with two different densities (left: $\hat{\rho} = 8$ and right: $\hat{\rho} = 0.3$). All units are non-dimensionalized by run length ℓ and run time ℓ/v. Marked points show estimated parameters for two cellular systems (A: peroxisome transport in fungal hyphae [17], and B: vesicle transport in *Aplysia* axons [57]; see Table 2.1). Black lines mark the transition between diffusion-dominated and transport-dominated motion on the length scale of inter-particle distance (Eq. 2.19).

system, the optimal walk length decreases substantially compared to the model where both states are functional, as the rapid processive transport must be counterbalanced by sufficient time spent in the passive regime in order to capture the target. This effect is distinct from the disadvantage of long walks which can lead the particle away from its target, underlying the non-monotonic dependence on ℓ in Fig. 2.4.

2.5.2 Search by a population of particles

A closely related objective of intracellular transport is the capture of a target by any one of many moving particles. In this case we assume particles that are initially uniformly distributed with some density ρ, and consider the mean first passage time (MFPT) for the first of them to hit the target. Some biological examples include the clearance of toxic cytoplasmic metabolites by any one of a uniformly scattered field of peroxisome organelles [43], the influx of peroxisomes to plug septal holes in damaged fungal hyphae [71], or the arrival of lysosomes to fuse with a

phagosome and digest its engulfed contents [44]. For simplicity, we assume the target is itself immobile and must wait for the particles to come to it via some combination of active and passive transport. In this situation, the relevant length scale is defined by the typical initial spacing between the particles ($1/\rho$). In the limit of a uniform distribution over a very long domain, the MFPT can be related directly to the range of the moving particles [31]. Specifically, the mean first passage time is given by

$$\text{MFPT} = \int_0^\infty e^{-\rho Z(t)} dt \tag{2.16}$$

where $Z(t)$ is the average range of particles over time t. The behavior of the MFPT is dictated by the dimensionless length scale for the separation between particles [$1/\hat{\rho} = 1/(\rho\ell)$]. When this length scale is short enough that active walks remain processive ($1/\hat{\rho} \ll \hat{x}^{**}_{\text{range}}$), we can approximate the particle range as a linear combination of a diffusive and a ballistic process. The MFPT can then be calculated analytically by plugging Eq. 2.8 into Eq. 2.16 and integrating the resulting exponential.

$$\text{MFPT} \approx \frac{1}{f\hat{\rho}} - \sqrt{\frac{4\hat{D}}{\hat{\gamma}^2\hat{\rho}f}} \exp\left[\frac{\hat{x}^{*}_{\text{range}}\hat{\rho}}{4}\right] \text{erfc}\left[\frac{\hat{x}^{*}_{\text{range}}\hat{\rho}}{4}\right], \tag{2.17}$$

where erfc is the complementary error function. The limits for high and low particle concentration are given by

$$\begin{aligned} &\text{MFPT} \to \frac{\pi(1+\hat{\gamma})^2}{8\hat{D}\hat{\rho}^2}, \quad \frac{1}{\hat{x}^{*}_{\text{range}}} \ll \hat{\rho} \ll \frac{1}{\hat{x}^{**}_{\text{range}}}, \\ &\text{MFPT} \to \frac{1}{f\hat{\rho}}, \quad \hat{\rho} \ll \frac{1}{\hat{x}^{*}_{\text{range}}}, \end{aligned} \tag{2.18}$$

where the high density limit corresponds to diffusive scaling of MFPT with the distance between particles while the low density limit corresponds to ballistic scaling. Setting these two limits equal to each other indicates that a transition in the encounter times occurs at a critical length

scale

$$\frac{1}{\hat{\rho}_{\text{crit}}} = \frac{\hat{x}^*_{\text{range}}}{2}, \tag{2.19}$$

which can be equivalently expressed as

$$f\text{Pe}\left(\frac{1}{\hat{\rho}}\right) = \frac{8}{\pi(1+\hat{\gamma})^2}. \tag{2.20}$$

This transition corresponds to a particle density where processive walks begin to dominate the ability to rapidly encounter targets, which occurs when the Péclet number for the distance between particles, multiplied by the fraction of time spent walking, is of order unity.

A calculation of the mean first passage time accurate at all length scales can be carried out by numerical inversion of the Laplace-transformed range function (Sec. 2.3.2), and the results are plotted in Fig. 2.5 for two values of particle density. The black line indicates the transition between behavior dominated by diffusive versus by processive particle motion (Eq. 2.19). Below this line, active transport dominates the motion of the particles and the time to reach the target is insensitive to the passive diffusivity. Above this line, passive diffusion dominates and the target search is insensitive to the fraction of time that the particles spend in processive motion. The parameters relevant to two example biological systems (peroxisome transport in fungal hyphae and vesicle transport in *Aplysia* neurons) are marked with dots.

The parameters for peroxisome transport fall near the transition region, where both passive diffusion and active processive walks contribute to the ability of these organelles to reach any target position within the cell. While previous modeling studies have indicated that both transport mechanisms are important to the maintenance of a uniform distribution of peroxisomes in hyphae [11], we demonstrate here that the particle density falls in an intermediate regime such that diffusion and active walks both contribute to efficient target search by the population of

peroxisomes. In the case of vesicle transport in *Aplysia* neurons, the lower density of organelles suggests a greater contribution from the active mode as seen in Fig. 2.5.

We note that for our model with capture occuring in both the active and passive state, the range over the relevant length scale increases monotonically with the fraction of time spent walking. Hence, the rate of capture is always increased by raising the frequency of starting an active walk ($\hat{\gamma}$). This is not the case for particles that can only capture their target in the passive state (see Appendix A.5), which could include encapsulated proteins that must first exit a vesicle to carry out their function. For such particles, frequent runs decrease the fraction of time spent in a functional state and thus hinder target capture (Fig. A.3), an effect that has previously been noted in studies of multi-modal search processes[27, 34].

2.6 Transport in a Tube and the Benefits of Tethering

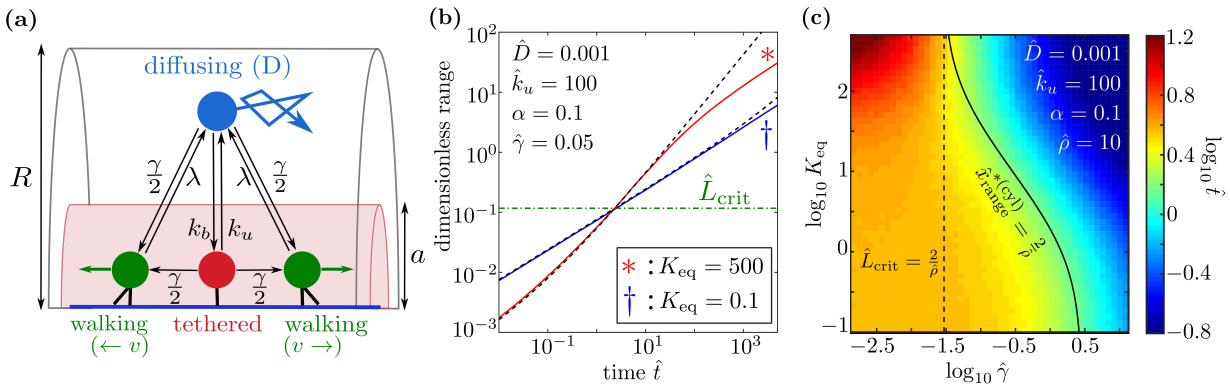

Figure 2.6: Effects of tethering on transport. a) Schematic for the tethering model. The smaller cylinder denotes the region within which particles can tether to the microtubule or initiate active transport. The transition rates between states are indicated with the arrows. b) Range vs time for weak ($K_{\text{eq}} = 0.1$) and strong ($K_{\text{eq}} = 500$) tethering. Dashed black lines show analytical approximations in the limits of no tethering and infinitely strong tethering, accurate for short to intermediate times (Eq. 2.24). Horizontal dash-dotted line indicates the transition length-scale $\hat{L}_{\text{crit}}$ where tethering becomes advantageous. c) Average time for target capture by a population as a function of the starting rate $\hat{\gamma}$ and binding strength K_{eq}. The solid line indicates the transition from diffusive to active transport as the dominant transport mode at different values of tethering strength. The dashed line shows the transition where strong tethering becomes advantageous for target encounter.

Active transport in a cell occurs via motor proteins attached to microtubule tracks. Even very narrow cellular projections are typically substantially wider than the diameter of a single microtubule. Consequently, organelles must navigate transversely through the cytoplasmic environment in order to encounter a microtubule and engage in active processive motion. A mechanism to keep organelles located close to the microtubule can improve transport efficiency by reducing this search time. In many cases, organelles are believed to be tethered to the microtubule tracks, preventing them from dissociating and diffusing even when they pause after a processive walk. This tethering can be accomplished by additional inactive motors attached to the organelle [48, 72] or by specific molecular adaptors linking the organelle directly to the microtubule [50, 73].

It has been speculated that tethering can enhance transport by forcing the organelle to remain in proximity to the microtubule tracks, thereby effectively increasing the rate at which processive walks are initiated [22]. At the same time, tethering can severely limit the intracellular space that can be explored by an organelle in the passive state, either by reducing the axial diffusivity in the case where inactive motors slide diffusively along microtubules [48, 49], or by halting it entirely in the case of organelle docking [50]. The benefits of tethering thus depend on the relative balance between active and passive transport, as well as the radial size of the domain around the microtubule, which determines the delay associated with encountering the track. The former aspect is dependent on the length scale over which transport must be achieved, as discussed in the previous sections.

We extend our halting creeper model to a three-dimensional cylindrical domain of radius R, wherein active runs can be initiated only within a radius of size $a < R$, corresponding to a small region surrounding a central track. While cellular projections such as hyphae and axons generally have multiple microtubule bundles [11, 74], this model serves as an approximation where the size of the cylindrical domain sets the cross-sectional density of the microtubule bundles. In a typical fungal hypha, there are on average two microtubule bundles along the axis [11, 75, 76].

Assuming the microtubule bundles to be points distributed uniformly on the transverse section of the cylinder, the average distance between two bundles can be calculated as $128r/45\pi$, where r is the radius of the cross section [77]. The domain radius in our model can be considered to be half of this distance, which gives an estimate of $R \approx 0.45\mu$m for a typical hyphal diameter of 2μm. This is substantially larger than the peroxisome radius ($\approx$ 100nm) [11], so that organelles can only interact with the microtubules over a small fraction of the available cross-sectional area.

In addition to bidirectional walking and passive diffusion states, the particles in this extended model can also enter a tethered state with rate k_b while within the encounter radius a. For simplicity, we assume particles in the tethered state are entirely immobilized. The model could be extended in a straight-forward manner to limited but non-zero diffusivity while in the tethered state. Exit from the tethered state occurs at rate k_u, with the particle unbinding to a uniform radial distribution within the capture radius a. A dimensionless binding strength for tethering is defined by $K_{\text{eq}} = k_b/k_u$.

We note that this model assumes that tethering does not in any way hinder the initiation of an active run, so that particles transition to the active state with the same rate regardless of whether they are bound or freely diffusing within the capture radius. While it is possible for tethering to either speed up or slow down the association of an organelle with a motor or a carrier particle, depending on the length, flexibility, and configuration of the tether, we neglect this effect here. Our model for tranport in a cylindrical tube around a microtubule track is summarized schematically in Fig. 2.6a.

In the limit of rapid transverse diffusivity or small domain size ($D/R^2 \gg \gamma, k_b$), diffusive particles remain equilibrated throughout the cross section of the domain, and the effective rates of starting a walk or binding become $\alpha^2\gamma$ and $\alpha^2 k_b$, respectively, where $\alpha = a/R$. In this limit, the delays associated with transverse diffusive transport are eliminated, and the equilibrium fraction of particles in each state can be easily calculated (Appendix A.2). For particles starting

at equilibrium, the long-time diffusivity is then given by

$$\begin{aligned}
\hat{D}_{\text{eff}} &= \hat{D} f_{\text{diff}} + f_{\text{walk}}, \\
f_{\text{walk}} &= \frac{\hat{\gamma}\alpha^2}{\hat{\gamma}\alpha^2 + \left(\frac{\alpha^2 K_{\text{eq}} + \hat{\gamma}/\hat{k}_u + 1}{K_{\text{eq}} + \hat{\gamma}/\hat{k}_u + 1}\right)}, \\
f_{\text{diff}} &= \frac{\left(\frac{\hat{\gamma}/\hat{k}_u + 1}{K_{\text{eq}} + \hat{\gamma}/\hat{k}_u + 1}\right)}{\hat{\gamma}\alpha^2 + \left(\frac{\alpha^2 K_{\text{eq}} + \hat{\gamma}/\hat{k}_u + 1}{K_{\text{eq}} + \hat{\gamma}/\hat{k}_u + 1}\right)}
\end{aligned} \tag{2.21}$$

where f_{walk} and f_{diff} are the fraction of particles in the active and diffusive state, respectively. We again non-dimensionalize all length units by the run-length ℓ and all time units by the run-time ℓ/v, for consistency with previous calculations.

In the more general case where the delay due to transverse diffusion is included, it can be shown (see Appendix A.3) that for a particle which begins uniformly distributed in the diffusive state within radius a, the mean waiting time to enter a walking state is identical to the fast-diffusion limit and is given by,

$$\langle \hat{t}_w \rangle = \frac{1}{\hat{\gamma}} \left[\frac{\alpha^2 K_{\text{eq}} + 1 + \hat{\gamma}/\hat{k}_u}{\alpha^2 (K_{\text{eq}} + 1 + \hat{\gamma}/\hat{k}_u)} \right]. \tag{2.22}$$

This average time ranges from $1/(\alpha^2\gamma)$ in the limit of low binding strength to $1/\gamma$ in the limit of strong binding, and is independent of the diffusivity D. In the case of very slow diffusion, those particles that escape the binding radius a take a long time to return, but such escape before initiating a walk becomes concomitantly less likely, with these two effects canceling each other out in the calculation of the average time to start walking. Because particles are assumed to distribute uniformly across radius a when leaving the tethered state, this equivalence of the average time to initiate a subsequent walk means that the long-time behavior of particles matches the fast-diffusivity limit, regardless of the actual value of D.

By contrast, we note that the standard deviation in the time required to start a walk, for a

particle that starts diffusive and uniformly distributed within a, is dependent on the diffusivity (see Appendix A.3). Slow diffusion and strong binding can greatly increase the variance in the time required for a particle to start a walk, leading to large variability in the amount of time individual particles remain in a passive or tethered state over a particular time interval of observation. This extreme case may contribute to the identification of apparently immobile populations of particles observed in some *in vivo* organelle tracking studies [39].

The effectiveness of tethering in improving transport over a long time can be inferred from the derivative of the effective diffusivity $\hat{D}_{\text{eff}}$ with respect to the binding strength K_{eq}. A positive derivative signifies that long-range transport is accelerated by tethering, whereas a negative value indicates that tethering hinders transport. Tethering is advantageous in the long-time limit when the following criterion is satisfied:

$$(1-\alpha^2)\left(\frac{\hat{\gamma}}{\hat{\gamma}+1}\right)\text{Pe}(\ell) > 1. \tag{2.23}$$

This expression summarizes the idea that tethering is helpful for long-range transport in situations where the domain is wide ($\alpha^2 \ll 1$), where the rate of walking is substantial compared to the pausing rate ($\hat{\gamma} \gg 1$), and where active runs move the particles faster than diffusion over the longest processive length scale ($\text{Pe}(\ell) \gg 1$).

Below the long-time diffusive limit, the extent to which tethering aids transport depends on the length scale of interest. In particular, at times much shorter than the cycle time to initiate and stop an active walk, the dimensionless particle range can be approximated by

$$Z(\hat{t}) \approx 4 f_{\text{diff}} \sqrt{\frac{\hat{D}\hat{t}}{\pi}} + f_{\text{walk}}\hat{t}, \tag{2.24}$$

in a manner analogous to Eq. 2.8. This expression can be inverted to calculate the time at which a particular range is reached. Comparing the low K_{eq} and high K_{eq} limits indicates that the ability

of particles to tether to the track allows them to explore more rapidly over length scales above

$$\hat{L}_{\text{crit}} = x^*_{\text{range}} \frac{(1+\hat{\gamma})^2}{(1-\alpha^2)^2}. \tag{2.25}$$

For large domains ($\alpha \ll 1$) and low propensity for active walking ($\hat{\gamma} \ll 1$), tethering is helpful over all length scales where processive active motion is the dominant form of transport, as defined by the critical length $\hat{x}^*_{\text{range}}$ (Eq. 2.10).

We use kinetic Monte Carlo methods to simulate the spreading of particles within our cylindrical model. The simulations are accelerated with the use of analytically calculated Green's functions to propagate the particles within homogeneous cylindrical domains (see Appendix A.4), allowing for efficient sampling of particle behavior over a broad set of parameters.

The average axial range for a population of particles can be obtained as a function of time from the simulations. Fig. 2.6b shows the time evolution of the range for weak and strong tethering. The transport parameters used are relevant for peroxisomes in fungal hyphae (Table 2.1), with the domain width assumed to be $R = 1\mu$m and a central region of width $a = 0.1\mu$m. For consistency with previous calculations, results are reported in dimensionless units, using the run length ($\ell \approx 7\mu$m) and processive walking time ($1/\lambda \approx 3$ s) as the length and time units. The critical length scale for this system is $\hat{L}_{\text{crit}} \approx 0.12$, below which the average range for strongly tethered particles is lower than the weakly tethered ones. For length scales above $\hat{L}_{\text{crit}}$, strongly tethered particles explore over a greater range. The full extent of a hyphal growth tip ($\hat{L} \approx 8$) is several times longer than this critical length scale, highlighting the potential benefit of tethering for distributing peroxisome particles over the entire growth tip.

Having established the length scales over which tethering is advantageous, we now calculate explicitly the effect of tethering on the average search time by a population of particles with dimensionless density $\hat{\rho}$. The capture time is defined as the first passage time to an arbitrary cross-section of the cylinder, by a population of particles equilibrated between states and uniformly

distributed along the axis of the cylinder. We note that in the case of a target that is located off the central axis where active motion and tethering take place, this target could only be reached if the particle passes through the appropriate axial location in the passively diffusing state. The capture time should then be calculated using the distribution of first passive passage times, as discussed in Appendix A.5. In the limit of very rapid transverse diffusivity, capture times for an off-axis target could be derived directly from the first passive passage to a cross-section. For slow transverse diffusivity, multiple passages through the cross-section in the passive state would be required to hit a target that is much smaller than the cross-sectional area. Because the relationship between particle range and first passage times (Eq. 2.16) breaks down in the case where only passive passage is considered, extracting target capture times in our full three-dimensional model would require direct simulation of first passage by individual particles. While this case would make a promising extension for future work, for the sake of simplicity we focus here on targets localized at the central axis.

A surface plot of the average capture times versus binding strength K_{eq} and walking rate $\hat{\gamma}$ is shown in Fig. 2.6c. The effect of tethering on the average time to target capture varies depending on $\hat{\gamma}$. For particles with a very small probability of engaging in active runs, tethering hinders target search by limiting mobility in the passive state. For particles with a high propensity for active motion, tethering can aid their ability to encounter targets by increasing the amount of time spent in the region where active runs can be initiated. We approximate the parameter regime where this transition occurs by analytically calculating the integral for the MFPT (Eq. 2.16), using the short time approximation of the particle range (Eq. 2.24). Comparing the low K_{eq} and high K_{eq} limits yields a transition at a critical particle density

$$\hat{\rho}_{\mathrm{tether}} = \left(\frac{2}{\hat{L}_{\mathrm{crit}}}\right)\left(\frac{1+\alpha^2\hat{\gamma}}{1-\alpha^2}\right)^2. \tag{2.26}$$

For small values of $\alpha, \hat{\gamma}$, this transition is equivalent in form to the critical length scale where

processive walks first begin to play an important role, as calculated in Eq. 2.19. For parameters relevant to the motion of peroxisomes in fungal hyphae, we compare the critical particle density ($\hat{\rho}_{\text{tether}} \approx 17$) with the observed density of peroxisomes ($\hat{\rho} \approx 10$). Because the observed density is comparable to the critical density, we expect that tethering would not substantially hinder the ability of the peroxisomes to patrol the cytoplasm and encounter targets within the cell.

For a given finite binding strength K_{eq}, the MFPT to the target will be dominated by either diffusive or processive motion, depending on the fraction of particles in each state. The transition to the regime where encounter times are sensitive to the initiation of active walks occurs when the spacing between particles hits a critical length scale where such walks between to dominate. This length can be obtained analogously to the expression for $\hat{x}^*_{\text{range}}$ (Eq. 2.10) by replacing the starting rate $\hat{\gamma}$ with an effective starting rate based on the average time to initiate a walk: $\hat{\gamma}_{\text{eff}} = 1/\langle t_w \rangle$. In the case of rapid binding/unbinding ($\hat{k}_u \gg \hat{\gamma}$), this rate is approximated as

$$\hat{\gamma}_{\text{eff}} \approx \hat{\gamma}\left[\frac{\alpha^2(K_{\text{eq}}+1)}{\alpha^2 K_{\text{eq}}+1}\right] \tag{2.27}$$

The critical particle density is then given by

$$\hat{\rho}^{(\text{cyl})}_{\text{crit}} = \frac{2}{\hat{x}^{*(\text{cyl})}_{\text{range}}} = \frac{\pi\hat{\gamma}_{\text{eff}}}{8\hat{D}}, \tag{2.28}$$

where $\hat{x}^{*(\text{cyl})}_{\text{range}}$ is the length scale for transition between diffusive and processive motion in the model of a halting creeper within a cylindrical domain. This transition is shown with a solid black line in Fig. 2.6c.

2.7 Summary

We have employed a simplified “halting creeper" model, consisting of stochastic interchange between passive diffusion and active processive walks, to investigate the efficiency of

transport within an extended cylindrical domain. Specifically, this model is applicable to the transport of organelles within long narrow cellular processes such as neural axons and fungal hyphae. We explore the space of relevant parameters, including the rates of transition between passive and active states and the relative speed of diffusion versus active transport, as characterized by the Péclet number over different length scales. Our results highlight the importance of the relevant length scale in determining the contributions of the different transport modes and we identify simple expressions for the time [$t^*_{\text{range}} = \frac{16D\lambda^2}{\pi v^2\gamma^2}$] and length [$x^*_{\text{range}} = \frac{16D\lambda^2}{\pi v\gamma(\lambda+\gamma)}$] at which processive motion dominates particle spreading. We emphasize the use of the average range as a metric for the ability of particles to explore their domain via multimodal transport, demonstrating passive diffusion can play an important role over longer length scales than expected based on the classic analysis of the mean squared displacement.

We focus specifically on the contributions of active and passive transport to several key objectives relevant to the cell. First, we consider the establishment of a uniform distribution from a bolus of particles, demonstrating that efficient dispersion is achieved at intermediate run-lengths that can be substantially smaller than the domain size. This result indicates the importance of bidirectional active transport with frequent reversals in the movement of particles that must be spread broadly throughout a large domain, as is the case with metabolic organelles such as peroxisomes and mitochondria. Second, we quantify the rate at which a single particle first encounters a stationary target, showing again an advantage to intermediate run lengths that minimize the time wasted pursuing a long processive walk in the wrong direction. Third, we consider the rate of encounter to a target by the first of a population of halting creeper particles, identifying the parameter regime where active transport or diffusion dominate the motion, and showing that examples of biological interest fall in the intermediate regime where both modes of transport contribute substantially to target encounter.

Finally, we investigate an extension of the one-dimensional model to a cylindrical domain, where active transport can only occur in a narrow region along the axis and where particles can

enter a halted tethered state that both enhances the effective rate of initiating an active run and limits their ability to explore the domain while in the passive state. The advantages of tethering to microtubule tracks have been a topic of much speculation in the literature on intracellular transport [22, 48, 49]. We delineate the parameter regime in which tethering is expected to aid the long-time dispersion of particles (Eq. 2.23) and identify a critical length scale L_{crit} (Eq. 2.25) below which tethering hinders the ability of the particles to explore their domain. For several example intracellular transport systems (Table 2.1), this critical length is on the order of a few hundred nanometers, confirming the advantages of tethering for transport over micron length scales.

The results derived in this work highlight the complementary role of diffusion and processive transport in fulfilling cellular goals for delivering and distributing cytoplasmic organelles. The derived expressions can be employed for analyzing data on measured transport parameters to determine the length scales and transport objectives where active motor-driven motion is expected to dominate, where bidirectional transport with limited processivity is advantageous, and where tethering to cytoskeletal tracks can aid overall organelle dispersion.

2.8 Acknowledgements

Chapter 2, in full, is a reprint of the material with minor edits, as it appears in: S. S. Mogre, E. F. Koslover, "Multimodal transport and dispersion of organelles in narrow tubular cells", *Physical Review E*, 97 (4), 042402, (2018). The dissertation author was the primary author of this paper.

Chapter 3

Mechanics of Transport Initiation through Linker-Mediated Hitchhiking

3.1 Abstract

In contrast to the canonical picture of transport by direct attachment to motor proteins, recent evidence shows that a number of intracellular 'cargos' navigate the cytoplasm by hitchhiking on motor-driven 'carrier' organelles. We describe a quantitative model of intracellular cargo transport via hitchhiking, examining the efficiency of hitchhiking initiation as a function of geometric and mechanical parameters. We focus specifically on the parameter regime relevant to the hitchhiking motion of peroxisome organelles in fungal hyphae. Our work predicts the dependence of transport initiation rates on the distribution of cytoskeletal tracks and carrier organelles, as well as the number, length and flexibility of the linker proteins that mediate contact between the carrier and the hitchhiking cargo. Furthermore, we demonstrate that attaching organelles to microtubules can result in a substantial enhancement of the hitchhiking initiation rate in tubular geometries such as those found in fungal hyphae. This enhancement is expected to increase the overall transport rate of hitchhiking organelles, and lead to greater efficiency in organelle

dispersion. Our results leverage a quantitative physical model to highlight the importance of organelle encounter dynamics in non-canonical intracellular transport.

3.2 Introduction

Regulated movement of proteins, vesicles, and organelles plays an important role in the growth, metabolism and maintenance of cellular health. These particles move within a crowded and dynamic intracellular environment, aided by a dedicated transport machinery that typically comprises molecular motor proteins walking upon a network of cytoskeletal filaments. Precise control of transport ranging over length scales from a few microns to tens of centimeters is achieved by regulating the interactions between moving and stationary cargo, motors, and other cytoskeletal structures. Defects in the regulation of organelle movement can lead to pathologies, particularly in long cells such as neurons, where axonal transport deficiencies have been implicated in neurodegenerative disorders including Alzheimer's, amyotrophic lateral sclerosis (ALS), and multiple sclerosis [3–5].

The traditional picture of intracellular transport involves the direct attachment of cargo to adaptor proteins that recruit cytoskeletal motors, which carry the cargo processively along microtubule tracks [16, 78, 79]. However, recent experimental evidence suggests that a variety of cargos such as peroxisomes, lipid droplets, messenger ribonucleoprotein (mRNP) complexes, RNA granules and the endoplasmic reticulum can attach to other motile organelles, and navigate the cytoplasm through a mode of transport known as "hitchhiking" [6, 11, 17, 80–85]. Hitchhiking is characterized by the presence of a motor-driven "carrier" organelle which is required for processive transport of a cargo (the hitchhiker). Specifically, organelle hitchhiking has been defined as conforming to three criteria: 1) long-range co-migration of cargo and carrier organelles, 2) lack of membrane fusion between distinct cargo and carrier particles, and 3) cargo transport is dependent on carrier movement, while carriers can move independently of cargo [86]. The

ubiquity of hitchhiking cargos across systems suggests that this is a broadly applicable transport mechanism, whose efficiency may dictate the distribution and delivery of particles that are critical for optimal cellular function.

Previous theoretical models of canonical microtubule-based transport have focused on the distribution of cytoskeletal tracks [47], interplay between diffusive and processive transport [27, 87], characteristics of motor processivity and turning [53], and cargo behavior at microtubule intersections [19, 88]. The non-canonical hitchhiking mechanism, however, is governed by fundamentally different interactions at the molecular and organelle level, as compared to classic motor-driven transport. The physical principles that underlie hitchhiking efficiency have not yet been quantitatively explored.

Although the molecular components of hitchhiking have yet to be fully identified for many cargos, linker proteins which link the hitchhiking cargo to the carrier organelle have been identified in some cases [6, 86]. For example, in the filamentous fungus *Ustilago maydis*, mRNAs and their associated polysomes attach to early endosomes via an interaction between RNA-binding protein Rrm4 and early endosome-associated protein Upa1 [80–83]. In both *Ustilago maydis* and *Aspergillus nidulans*, another filamentous fungus, peroxisomes hitchhike on early endosomes [17, 85]. In *Aspergillus*, the protein PxdA is required for peroxisome hitchhiking [17], and is a putative linker between early endosomes and peroxisomes. In rat neurons, RNA granules hitchhike on motile lysosomes using the ALS-associated protein Annexin A11 as a linker [6]. While such linker proteins have been shown to be required for hitchhiking in these circumstances, it remains unknown how their mechanical and structural properties modulate hitchhiking efficiency.

In some cell types, organelles such as peroxisomes and mitochondria have been observed to attach to microtubules when not being actively transported [50, 89, 90]. Such tethering allows for regulated placement of organelles within the cell [50, 51, 91, 92]. Tethering may also enhance the ability of cargo to interact with the transport machinery, increasing the rate of initiating active runs while restricting short-range diffusion [87]. Peroxisomes in particular have been found to

exhibit both diffusive motion and microtubule tethering depending on cell type and context [11, 89], indicating that both modes of motion may play a role in organelle motility. Here, we explore how tethering to microtubule tracks can enhance the rate of transport initiation for hitchhiking cargos, by placing them within easy reach of passing carrier organelles.

Given the complexity of intracellular transport processes, many studies of transport have focused on the simplified geometries found in long cylindrical cellular projections [11, 17]. Such projections feature polarized arrays of parallel microtubules, with few intersections and essentially one-dimensional movement of cargo. Neuronal axons and the hyphae of filamentous fungi exhibit a similar cylindrical geometry. Filamentous fungi such as *Aspergillus nidulans* are particularly amenable to genetic manipulation and imaging, providing convenient experimental systems for studies of intracellular transport [8].

Linearly extended cellular systems such as axons and hyphae generally require efficient transport machinery to maintain a well-dispersed distribution of organelles. This distribution is determined both by the site of organelle biogenesis and by the transport machinery available to spread organelles away from these sites. In the filamentous fungus *Penicillium chrysogenum* peroxisome generation occurs preferentially at the hyphal tip [93]. In *Ustilago maydis*, an actin-dependent slow polar drift has been demonstrated to result in an accumulation of peroxisomes at the hyphal tip in the absence of hitchhiking transport [11]. In both cases, the hyphae are sufficiently long (on the order of 40μm from the last nucleus to the hyphal tip) that organelles with a typical diffusivity ($D \approx 0.02\mu\text{m}^2/\text{s}$ [11]) would require many hours to spread through the hypha by diffusion alone. Processive transport mechanisms such as hitchhiking are thus crucial to maintaining these organelles broadly distributed throughout the cell.

In this chapter we investigate the effects of cellular and cytoskeletal geometry, as well as mechanical properties of the transport machinery, on the initiation of hitchhiking runs by a cargo that encounters and attaches to a carrier organelle. We develop an analytical and computational model of hitchhiking transport initiation within tubular geometries, quantifying the rate of cargo-

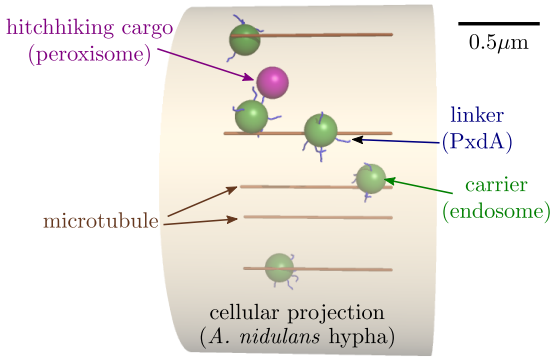

Figure 3.1: Schematic of the model for hitch-hiking initiation. A simulation snapshot is shown with all model components labeled. Specific components for peroxisome hitchhiking in *Aspergillus nidulans* are indicated in parentheses. Scale bar: 0.5μm.

carrier contact for a wide range of biologically feasible parameters. In particular, we focus on peroxisome hitchhiking in fungal hyphae, leveraging experimental observations to identify the relevant parameter regime. We analyze the role of linker proteins in mediating the contact between carrier and cargo organelle, and establish optimum mechanical and structural parameters for linkers that can maximize the hitchhiking initiation rate. For organelles that can tether to microtubule tracks, we quantify the potential enhancement of the hitchhiking rate due to tethering, and identify its effect on overall organelle dispersion in the cell.

3.3 Methods

Overdamped Brownian dynamics simulations are employed to explore the dynamics of carrier and cargo organelles as they first encounter each other for hitchhiking initiation. Our focus is on the parameter regime where the following conditions are applicable: 1) a cylindrical domain with parallel microtubule tracks, 2) carrier and cargo organelles that are substantially smaller than the domain width, 3) cargo organelles that are sufficiently sparse to preclude cargo-cargo interactions, 4) linker proteins of length smaller than the domain width. In particular, these conditions are relevant to the dynamics of hitchhiking peroxisomes, carried by early endosomes

in fungal hyphae.

The carriers (*e.g.*: endosomes) are modeled as spheres of radius $r_e = 100$nm, moving in a domain of length $L = 1\mu$m and radius $R = 1\mu$m with periodic boundaries in the axial direction. The radius of the domain is set to match the typical radius of fungal hyphae (see Appendix B) for measurements in *A. nidulans*) [11]. The domain represents a section of cell around a single cargo capable of hitchhiking. In *A. nidulans* hyphae, peroxisomes are observed at an average linear density of approximately 1 organelle within a 1μm long region of the hypha (see Appendix B), which sets the length of our simulated domain. This length allows us to assume only one peroxisome within the domain of interest, neglecting second-order effects. It should be noted that the fraction of peroxisomes actually engaged in hitchhiking at any given time is quite small (approximately 5% in *U. maydis* hyphae [11]). Given a density of linker-bearing endosomes of approximately 3 per μm (see Appendix B), we would expect less than 2% of carrier organelles to be already encumbered by a hitchhiker. We therefore assume all carriers that enter the domain are not carrying a hitchhiker. For simplicity, our model also ignores any carrier organelles not capable of initiating hitchhiking (*eg:* due to lack of linkers) and any other organelles in the cell that do not serve as carriers. These additional components could provide buffeting effects through sterics or hydrodynamic entrainment [24] which are not included in our model.

Microtubules are modeled as N straight lines distributed uniformly within the domain cross section. Microtubule dynamics are not included in the current model, although they provide an interesting avenue for future study. We ignore transverse fluctuations of microtubules, given that their persistence length *in vivo* ($l_p \approx 30\mu$m [94]) is much longer than the domain length. The linear density of carrier organelles (ρ) gives the number of carriers per unit length of hypha. Our simulation includes ρL carriers within the simulated domain. Each carrier is attached to a microtubule track by a single zero-length stiff spring representing a molecular motor complex. The attachment point of the spring to the microtubule moves processively in either direction at a constant velocity of 2μm/s, comparable to the measured velocities of fungal peroxisomes and

early endosomes [17]. Upon leaving the domain, the carrier organelle reappears at the other side, on a newly selected microtubule, thereby maintaining a constant carrier density while representing organelles whose typical run-length is much longer than the domain length L.

Cargo organelles (*e.g.:* peroxisomes) are represented by spheres of radius $r_p = 100$nm, which either diffuse freely through the domain, or have a point on their surface attached to a fixed microtubule at the axial center of the domain. Both carriers and cargo experience Brownian forces and torques corresponding to translational diffusivity $D_t = k_b T/(6\pi\eta r)$ and rotational diffusivity $D_r = k_b T/(8\pi\eta r^3)$, where η is the viscosity of the domain. The viscosity is chosen such that $D_t \approx 0.014\mu\text{m}^2/\text{s}$ for the cargo organelle, in keeping with measured diffusivities of peroxisomes in *Ustilago maydis* hyphae [11]. Steric interactions between organelles and with the cylindrical boundary of the domain are implemented using a stiff harmonic potential.

The simulations are evolved forward using a fourth-order Runge-Kutta algorithm [95] with time-steps of 10^{-4}s. Each simulation trial is run for a total of 5s, allowing each carrier to pass 10 times through the domain. 2500 trials are carried out for each combination of carrier density ρ and microtubule number N.

Linker proteins that mediate contact between carrier and cargo are modeled as continuous semiflexible worm-like chain (WLC) polymers [96] with varying length. Positions of the base of the linker protein are chosen uniformly on the carrier surface, and the initial linker tangent is assumed perpendicular to the surface. Using analytically calculated distributions for the end point of a WLC [97], we tabulate the spatial distribution of the probability that a cargo organelle overlaps with the tip of a linker for a given configuration of the carrier and cargo (see Appendix B). Using this tabulated probability, at each time step we check whether linker-mediated contact between the carrier and cargo has occurred. This approach avoids resolving the dynamics of the linker protein configurations, working instead in the fast-equilibration limit where the position of each linker tip is sampled from its equilibrium distribution at each timestep.

For each simulation trial, we record the time until the single cargo organelle first contacts

either the carrier surface or the tip of a linker protein. We note that these encounter times provide a lower limit on the waiting time until hitchhiking initiation. Namely, in Fig. 2-5 we assume that each encounter successfully and immediately results in a hitchhiking event. The role of unsuccessful encounters is explored in a subsequent section (Fig. 7) by introducing a finite reaction rate k_{rxn} for initiating a successful hitchhiking interaction while the linker and cargo are in contact.

The empirical cumulative distribution function for contact events is used to extract an effective rate of contact. Over the simulation timescale, the cumulative distribution functions observed fit well to a double exponential form $Q(t) = 1 - f_1 e^{-t/\tau_1} - f_2 e^{-t/\tau_2}$ (see Appendix B). This functional form is chosen *ad hoc* to enable smooth interpolation of the data within the simulation time-frame, and extrapolation to longer times, in order to calculate the average waiting time until contact. No specific physical meaning is assigned to the resulting two time scales. The average rate of hitchhiking initiation is defined by $k_{\text{hit}} = (f_1\tau_1 + f_2\tau_2)^{-1}$. Variation in this initiation rate is approximated by bootstrapping [98] over all simulation trials for a given set of parameters. All error bars shown give the standard error in k_{hit} over 100 bootstrapping runs.

Brownian dynamics simulation code (in Fortran90) and scripts for implementing linker distributions and obtaining encounter rates from simulation results are provided in a GitHub repository: `https://github.com/lenafabr/hitchhiking_initiation`.

3.4 Results and Discussion

3.4.1 Rate of encounter with carrier organelles

The efficiency of hitchhiking transport initiation is governed in part by geometric parameters, such as the density of microtubules and carrier organelles, as well as the length and distribution of linkers on the carrier surface. In order to be picked up for a hitchhiking run, the cargo must be sufficiently close to a passing carrier to be able to engage with a linker protein.

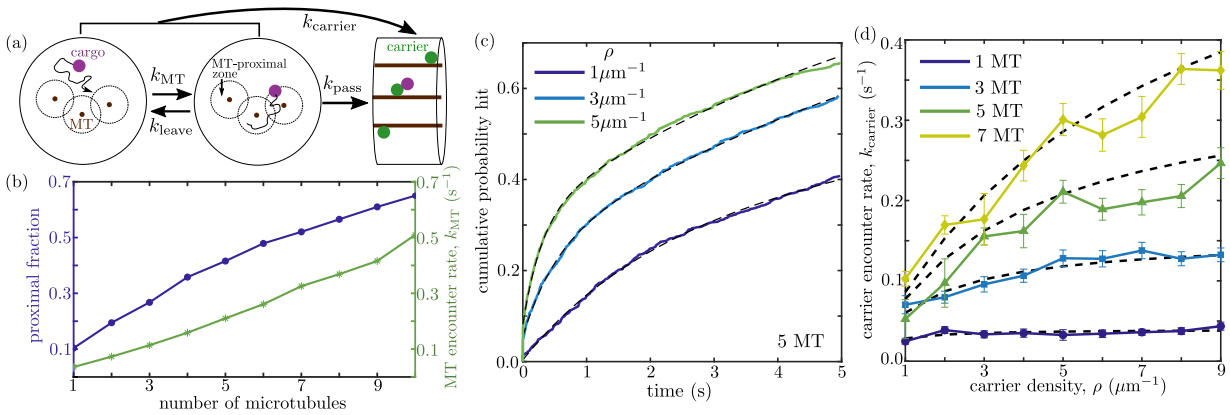

Figure 3.2: Dynamics of cargo encounter with carrier organelles. (a) Schematic model for carrier encounter, illustrating the two-step process of first entering a MT-proximal zone, then waiting for a carrier passage event. (b) Average fraction of domain cross-sectional area within distance $2r_e + r_p$ from a microtubule (left) and rate k_{MT} to encounter a microtubule if starting outside the proximal zone (right). (c) Cumulative distribution of carrier encounter times, plotted for simulations with three different carrier densities. Dashed lines give fit to a double-exponential function used to extract an effective encounter rate. (d) Average carrier encounter rate, for different numbers of microtubules and carrier density. Symbols indicate simulation results; dashed black lines show predictions from approximate kinetic model (Eq. 3.2).

We begin first by considering the rate of encounters between a diffusing cargo organelle and a processively moving carrier. This rate corresponds to hitchhiking initiation in the limit of very short, densely packed linkers, where the entire carrier surface is capable of binding the cargo.

A Brownian dynamics simulation framework is employed to explore how the density of microtubules and carriers modulates organelle encounter in a tubular region of radius $R = 1\mu\mathrm{m}$ with parameters relevant to peroxisome transport in hyphae (Fig. 3.1). The radius of the tubular region corresponds to the average radius of *A. nidulans* hyphae, as obtained from experimental measurements (see Appendix B). A variable number (N) of parallel microtubules are uniformly scattered throughout the tubular region. A single cargo of radius $r_p = 100\mathrm{nm}$ and translational diffusivity $D_t = 0.014\mu\mathrm{m}^2/\mathrm{s}$ represents the peroxisome and a variable linear density ρ of carrier organelles of radius $r_e = 100\mathrm{nm}$ move with processive velocity $v = 2\mu\mathrm{m/s}$ along the microtubule tracks. Brownian forces on the carrier organelles drive fluctuations around their attachment point to the microtubules. Periodic axial boundary conditions allow for maintenance of a constant

density of processively moving carriers in the local vicinity of the cargo.

In order to come in contact with a carrier, the cargo must first approach sufficiently close to a microtubule track (within a distance of $r_p + 2r_e = 0.3\mu$m), and then be hit by a passing carrier before moving away from the track again (Fig. 3.2a). For a single, centrally located microtubule, the region of proximity covers a fraction $f_1 = (r_p + 2r_e)^2/(R - r_p)^2 \approx 0.1$ of the available cross-sectional domain area. As multiple parallel microtubules are placed within the domain, their proximity regions cover an increasing fraction of the cross-sectional area. We vary the number of microtubules N in our simulation, randomizing the placement of each microtubule and the initial radial position of the peroxisome within the domain. Fig. 3.2b shows the fraction of iterations where the peroxisome starts within reach of a microtubule (equivalent to the MT-proximal area fraction f_N), as well as k_{MT}, an effective rate for peroxisomes initiated outside of the MT-proximal area to first reach this area (see Methods for details of rate calculations).

The time for a cargo to encounter a passing carrier is governed both by the dynamics of entering and leaving the MT-proximal region (rates k_{MT}, k_{leave}) and the rate k_{pass} of carrier passage in the vicinity of a cargo that is within reach of a microtubule. Because the velocity of processive motion is rapid compared to the cargo diffusivity, we treat the carrier arrival as a constant rate process while the peroxisome is within the MT-proximal region. The rate of this arrival is given by

$$k_{\mathrm{pass}} = v\rho \frac{(r_e + r_p)^2}{f_N (R - r_p)^2}, \tag{3.1}$$

where $v\rho$ is the rate at which carriers pass the axial position of the cargo and the second term corresponds to the equilibrium probability that the radial position of the passing carrier is within reach of the cargo, assuming the cargo is uniformly distributed within the MT-proximal area. The effective rate of leaving the MT-proximal area must be such that the cargo spends fraction f_N of its time within this area at equilibrium. Namely, $k_{\mathrm{leave}} = k_{\mathrm{MT}}[1 - f_N]/f_N$. These three rates allow for

an approximate calculation of the waiting time for a cargo organelle distributed uniformly within the domain to first encounter a carrier, using the simplified kinetic scheme shown in Fig. 3.2a. The inverse of this time gives the effective carrier encounter rate (see Appendix B for derivation):

$$k_{\text{carrier}} = \frac{k_{\text{pass}} k_{\text{MT}} (k_{\text{leave}} + k_{\text{MT}})}{k_{\text{pass}} k_{\text{leave}} + (k_{\text{MT}} + k_{\text{leave}})^2}. \tag{3.2}$$

When carrier passage is very frequent ($k_{\text{pass}} \to \infty$), the average time to carrier encounter reduces to $1/k_{\text{carrier}} \to (1 - f_N)(1/k_{\text{MT}})$, equivalent to the probability the cargo starts outside of the microtubule region multiplied by the time to reach that region.

The typical time-scale for cargo-carrier encounter in simulated trajectories is obtained by fitting the computed cumulative distribution function to a double exponential process (Fig. 3.2c; details in Appendix B). As shown in Fig. 3.2d, effective encounter rates obtained from the simulations are well represented by the simplified kinetic model of Eq. 3.2.

At low carrier density, increasing the microtubule number beyond a couple of microtubules has little effect on the rate with which the cargo first encounters a carrier. In this regime, the diffusing cargo has time to enter and leave the MT-proximal region while waiting for a carrier to pass by. Each carrier passage event becomes essentially independent from the previous one, in terms of the probability that it will hit the cargo. Splitting up a fixed carrier density across more microtubules does not change the overall frequency of these independent passage events and thus has little effect on the encounter rate. By contrast, at higher carrier densities increasing the number of parallel microtubules can greatly speed up the encounter process. In this limit, carriers arrive very rapidly and the encounter is limited by the cargo approaching sufficiently close to a microtubule to enable contact. Hence, increasing k_{MT} by raising the number of microtubules will increase the overall encounter rate.

Similarly, when there are very few microtubules in the domain, the encounter rate is nearly independent of the carrier density. A greater frequency of carrier passage events along a single

microtubule will not speed up encounter times that are dominated by the cargo coming in radial proximity of that microtubule. At higher microtubule numbers, the cargo spends most of its time within the MT-proximal region and increasing carrier density enhances the rate at which some carrier passes the cargo on a nearby microtubule.

We quantified the number of microtubule plus-ends in *Aspergillus nidulans* hyphae, and found approximately $N \approx 5$ parallel microtubules at the hyphal tips (see Appendix B). For this number of microtubules, the rate of cargo encounter with a carrier increases with the carrier linear density up to $\rho \approx 5\mu\text{m}^{-1}$, after which it is insensitive to the presence of additional carrier organelles. We also quantified the linear density of fluorescently-tagged early endosomes in *A. nidulans* hyphae and found approximately 5 endosomes per μm length of hypha (see Appendix B). As approximately 55% of endosomes carry the PxdA linker protein responsible for peroxisome hitchhiking [17], we would expect the rate of peroxisome encounter with a PxdA-bearing endosome ($\rho \approx 2.8\mu\text{m}^{-1}$) to be approximately 0.2s^{-1}.

3.4.2 Rate of encounter with linker proteins

Organelle hitchhiking is generally believed to involve the cargo (hitchhiker) attaching to a carrier organelle surface via one or more linker proteins [86]. For the case of peroxisome transport in *A. nidulans*, the putative linker protein (PxdA) is present on a subpopulation of early endosomes and is required for peroxisome hitchhiking [17]. This protein contains a long predicted coiled-coil region, which is approximately 90nm in length if fully extended [17]. Given that the linker protein may be comparable in size to the organelles themselves, its length, distribution, and mechanical properties have the potential to substantially impact the efficiency of hitchhiking initiation. We thus incorporate extended linker proteins on the carrier surface into our dynamic model and proceed to explore how linker protein parameters modulate the rate at which the cargo organelle can get picked up for a hitchhiking run.

We use a multi-scale approach to integrate the linkers into our Brownian dynamics

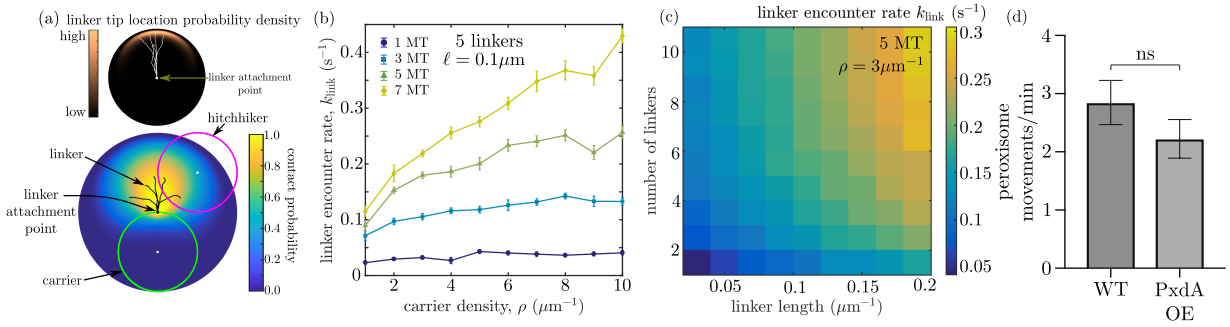

Figure 3.3: Rates of encounter with hitchhiking linkers. (a) Model of linker protein chains attached to carrier surface. Top: end distribution of a WLC of length $\ell = \ell_p$, with initial end orientation fixed. Representative configurations of the linker are indicated in white. The color represents the probability density of the linker tip location. Bottom: probability of contact between the tip of a linker (black lines) on a carrier (green) and the hitchhiking cargo (magenta). The color represents the contact probability for each position of the hitchiker center relative to the linker attachment point. (b) Rate at which the cargo encounters the first linker tip, as a function of the carrier density and the number of microtubules. (c) Effect of linker length and linker number per carrier on the encounter rate. (d) Bar graph of the peroxisome flux in wild-type (WT) hyphae and hyphae overexpressing PxdA(Δ1-500)-TagGFP (PxdA OE). Peroxisome flux is quantified as the number of peroxisome movements across a line drawn 10μm from the hyphal tip in a 1 minute movie. Wild-type hyphae had 2.84 ± 0.38 (SEM) peroxisome movements per minute, while hyphae with overexpressed PxdA(Δ1-500)-TagGFP had 2.22 ± 0.33 (SEM) peroxisome movements per minute. $p = 0.2569$, Mann-Whitney test. Error bars=SEM. $n = 46$ WT hyphae and 49 PxdA OE hyphae. See Appendix B for details of peroxisome flux quantification.

simulations. The linkers are treated as semiflexible “worm-like" chains (WLC) [96] of length ℓ, with one end fixed at a given position on the endosome and the initial tangent fixed to be perpendicular to the endosome surface. It is not known whether linker proteins are capable of diffusing over the carrier surface. In the extreme case of very rapidly diffusing linkers, any close approach of the hitchhiking cargo to the moving carrier would result in an encounter with a linker, given that the proteins could explore the entire carrier surface very fast compared to the relative motion of the organelles. This limiting case approaches the situation where the entire carrier surface is capable of interacting with the cargo, as discussed in the previous section, albeit with an expanded effective carrier radius resulting from the added extension of the linker beyond the carrier surface. We focus here on the opposite limit, where a given number of linker proteins is attached to fixed points on the carrier surface with no diffusion permitted for the attachment points.

Assuming that the conformation of an individual linker protein equilibrates much faster than the large organelle movements, we employ a separation of timescales in our simulation. Specifically, we assume that each linker samples its configuration from an equilibrium distribution independently on each Brownian dynamics step. We make use of the analytically known distribution function for a WLC with fixed end orientation [97] to compute the probability that a free linker end will intersect with the hitchhiking cargo for a given position of the cargo relative to the anchoring point of the linker (Fig. 3.3a). These probability distributions are used to sample whether the cargo has come into contact with a linker tip during each simulation step. The hitchhiking initiation time is then taken to be the total simulation time until the first such contact with a linker tip occurs. We note that this model assumes all contacts between a linker tip and a cargo organelle lead to rapid formation of a long-lasting interaction that results in a hitchhiking run. In particular, the entire surface of the hitchhiking cargo is assumed capable of interacting with the linker protein. The hitchhiking rates discussed here are thus an upper estimate on actual initiation rates.

The rate of encounter with a linker tip shows a similar dependence on microtubule and carrier density (Fig. 3.3b) as the rate of coming into contact with the carrier organelle itself (Fig. 3.2b), discussed in the previous section. Specifically, increasing the carrier density has little effect for low microtubule numbers. Interestingly, the rates of linker contact are quite similar to the rate of carrier contact, even for a fairly small number of linkers on the carrier surface. Fig. 3.3c shows how the rate of linker encounter with cargo depends on the number and length of the linkers. Due to the flexibility and length of the linker proteins, only a small number of linkers (~ 5, for linkers of size comparable to the putative PxdA coiled-coil region) is sufficient to obtain near maximum initiation rates. This prediction from the physical model is consistent with experimental measurements, which show that overexpressing PxdA linker proteins in *A. nidulans* does not increase the rate of hitchhiking initiation (Fig. 3.3d).

Using the standard expansion for a nearly straight wormlike chain, the linker tip will project a typical distance $\Delta z \approx \ell[1-\ell/(6\ell_p)]$ from the carrier surface [99]. For proteins of length $\ell = 100$nm and persistence length $\ell_p = 100$nm, a single instantaneous encounter between cargo and carrier surface is expected to yield a roughly 6% chance of any given linker on that carrier intersecting with the cargo. For 5 independent linkers, this means that approximately 30% of carrier encounters will result in immediate linker contact. This fraction is increased further because the diffusion of cargo and carrier during a passage event allows them to sample a greater fraction of each other's surface, as has been quantified for the case of molecular diffusion towards receptor patches on a sphere [100].

In addition, by projecting beyond the surface of the carrier, the linker proteins serve as antennae, allowing contact while the cargo is further away from the carrier. This type of interaction effectively replaces r_e with $r_e + \Delta z$ and results in more rapid encounters. Consequently, for long and numerous linkers, the rate of initiation can be even faster than the rate of contact with the carrier. This effect arises from the extra range afforded by long linker proteins, allowing contact with the linker to occur while the cargo is still at a substantial distance from the carrier

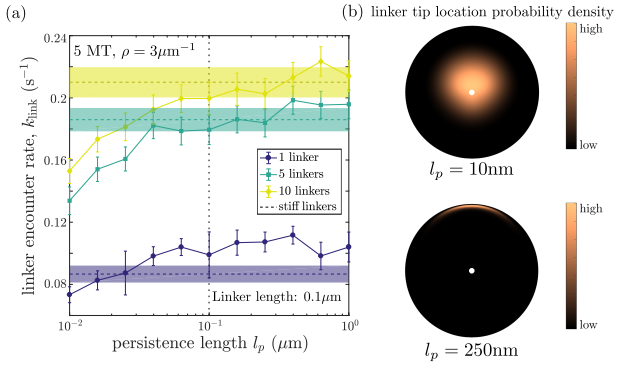

Figure 3.4: Dependence of encounter rate on linker flexibility. (a) Rate at which cargo encounters a linker tip, as a function of linker persistence length for different linker numbers. Dashed lines with shaded areas denote contact rate for infinitely stiff linkers along with standard error. Dotted vertical line denotes $l_p = 0.1\mu$m, used in all other simulations. (b) End distribution of a WLC of length $\ell = 100nm$ with initial orientation fixed, highlighting the increased extension Δz yet smaller area coverage of stiffer linkers. Top: $l_p = 10$nm, bottom: $l_p = 250$nm

surface.

The rate at which linker contact occurs depends not only on the geometry and density of the linker proteins, but also on their flexibility (Fig. 3.4). In order to project beyond the surface of the carrier organelle, the linker proteins must be relatively stiff ($\ell_p \gtrsim \ell$). For linkers with a substantially shorter persistence length, the smaller value of Δz implies that the cargo organelle would need to approach closer to the carrier surface in order to have a high likelihood of encountering the linker tip (Fig. 3.4b). Interestingly, when there is only one linker on each carrier, a slight optimum in linker flexibility is observed. This effect arises from the fact that the tip of a stiffer linker thermally explores a smaller area in the plane parallel to the surface of the carrier. Thus, when linker density is low, semiflexible linkers with ℓ_p comparable to ℓ increase the probability of an encounter with the linker tip each time the cargo approaches a carrier, above what it would be for infinitely stiff linkers. We note that the effective persistence length of coiled-coil protein structures is reported to be in the range of $30-170$nm [101–104]. While the detailed structure and mechanical properties of the PxdA linker are unknown, this protein appears to fall in the expected range for an efficient hitchhiking linker – namely, it has a predicted coiled-coil domain with comparable persistence length and end-to-end length. The

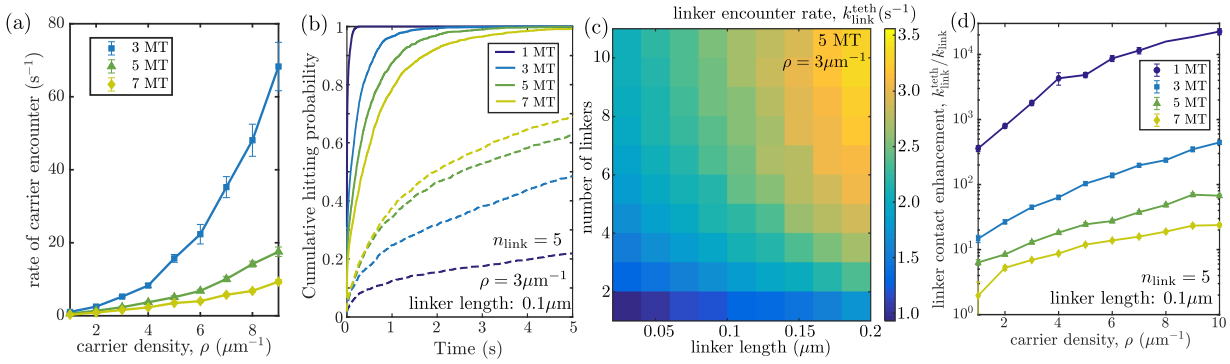

Figure 3.5: Effect of cargo tethering to microtubule on encounter rates with carrier organelles and their linker proteins. (a) Rate of encounter with a carrier organelle, for different numbers of microtubules in the domain. (b) Cumulative hitting probability with the tip of a linker protein, for tethered (solid lines) and untethered cargo (dashed lines), showing more rapid encounters in the tethered case. (c) Enhancement of overall contact rate with a linker protein tip, due to tethering of cargo. (d) Encounter rate between a tethered cargo and linker protein tip, as a function of linker length and number. (e) Ratio of encounter rates with linker protein tips, for a tethered versus diffusive cargo.

coiled-coil domain of PxdA is thus expected to have sufficient stiffness that would allow the protein to project beyond the endosome surface, while remaining sufficiently flexible so that the linker tip could explore a substantial area around its attachment point.

3.4.3 Tethering to microtubules enhances the rate of hitchhiking initiation

A number of organelles, including mitochondria, melanophores, and peroxisomes are known to become tethered to microtubule tracks by regulatory proteins that are crucial for maintaining their cellular distribution [50, 89, 92, 105, 106]. Such tethering not only helps localize organelles along extended cell regions (as in neurons) [51, 105] but is also thought to facilitate interactions between multiple organelles by restricting their three-dimensional diffusion through the cytoplasm [92]. In the case of hitchhiking cargos such as peroxisomes in *Aspergillus* and *Ustilago*, tethering to a microtubule has the potential to enhance the rate of hitchhiking initiation by eliminating the time spent out of reach of the microtubule-bound carrier organelles. We explore the effect of cargo tethering in the context of our hitchhiking initiation model by

attaching the cargo surface to a randomly selected microtubule and quantifying the rate at which the cargo first encounters the carrier surface or a carrier-borne linker protein.

Tethering of the cargo to a microtubule substantially increases the rate of encounter with a carrier organelle, particularly in the case of low microtubule density (Fig. 3.5a). This enhancement arises from two related effects. First, the lower volume available to the cargo makes it much more likely in equilibrium (and hence at the start of the simulation) that the cargo starts in close contact with a carrier organelle. This is particularly the case for high carrier densities and low microtubule numbers, where the carriers cover nearly the entire volume available to tethered cargo. A related effect is that, even for cargos that start far from any carrier, the need to first reach a microtubule track is eliminated ($k_{\mathrm{MT}} \to \infty$), so that the rate of carrier encounter becomes comparable with the rate of carriers passing a hyphal cross-section along the same (or nearby) microtubule.

When the hitchhiking cargo is tethered to a microtubule, increasing the number of microtubules along the hypha greatly slows the rate of encounter with a passing carrier. Because we assume a constant linear density of carrier organelles per length of hypha, additional microtubules provide more options for where the carriers are located in the hyphal cross-section, diverting some of them away from the one microtubule to which the cargo organelle is attached. Hence, fewer microtubules makes it more likely that each carrier will come in contact with the cargo as it passes the relevant cross-section of the hypha.

When hitchhiking initiation requires encounter with the tip of a linker protein, tethering of the cargo can also greatly increase the rate at which such encounters occur (Fig. 3.5b-d). Unsurprisingly, tethering has the greatest effect on encounter rates at low microtubule numbers and short linker lengths, where facilitating the rate at which the cargo comes near the carrier surface has a large effect on the hitchhiking initiation. For high microtubule numbers and long linkers, the effect of tethering is less pronounced because even freely diffusing cargos spend most of their time within the maximum distance ($r_p + 2r_e + \Delta z$) of the microtubule tracks that allows for hitchhiking initiation during carrier passage events. As seen in Fig. 3.5d, tethering plays a

greater role when the carrier density is high, since it is in this regime where contact with diffusive cargo is rate-limited by the cargo coming in proximity of a microtubule track. At lower carrier densities, the encounter time is dominated by waiting for a carrier passage event and tethering to a microtubule has less effect.

For the typical microtubule and PxdA bearing early endosome density observed in *A. nidulans* hyphae ($N \approx 5$, $\rho \approx 3\mu\text{m}^{-1}$; see Appendix B), and for the predicted PxdA coiled-coil linker length ($\ell \approx 90$nm), tethering of peroxisomes is expected to increase the rate of hitchhiking initiation by more than 12-fold (Fig. 3.5d). Peroxisome hitchhiking in hyphae can thus be greatly enhanced by attaching the peroxisomes to microtubules. The enhancement remains substantial even if the peroxisomes are assumed to be much larger (8-fold enhancement for $r_p = 300$nm; see Appendix B). Published kymographs of labeled peroxisomes in Δ*pxdA* hyphae [17] hint that peroxisomes exhibit little axial motion over time periods of up to 10 sec. While time-sampling limitations of this data preclude a definitive demonstration of tethering, the observed motion is not inconsistent with these organelles being attached to stationary cellular structures. Furthermore, in human cells, the peroxisomal membrane protein PEX14 has been shown to bind to tubulin and to be critical for peroxisome motility along microtubules [89]. There is thus reason to propose that fungal peroxisomes may also be attached to microtubules and, as shown here, that this tethering may contribute to their ability to hitchhike throughout the hypha.

3.4.4 Success rate for hitchhiking initiation

Our mechanical model indicates that, for parameters relevant to *A. nidulans* hyphae, the rate at which a peroxisome encounters a PxdA linker on a passing endosome is approximately 0.2s^{-1} if the peroxisome is untethered and approximately 2s^{-1} if it is tethered to a microtubule. These timescales set an upper limit to the rate of hitchhiking initiation, since not all encounters with the linker will result in a successful hitchhiking run.

We can measure the initiation rate for peroxisome hitchhiking directly by tracking individ-

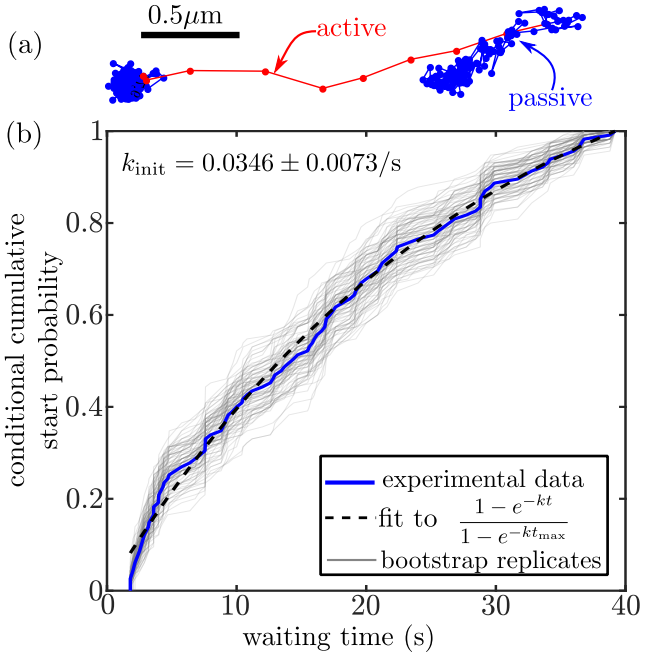

Figure 3.6: Experimentally measured hitchhiking initiation rate for peroxisomes in *A. nidulans* hyphae. (a) Example trajectory of individual peroxisomes, with passive segments marked in blue and active segments in red. (b) Cumulative distribution of start times for active motion, conditional on an active run occuring during the measured time window ($t_{\max}$). Grey curves show variation from bootstrapping. Dashed line gives fit to conditional cumulative distribution of Poisson process.

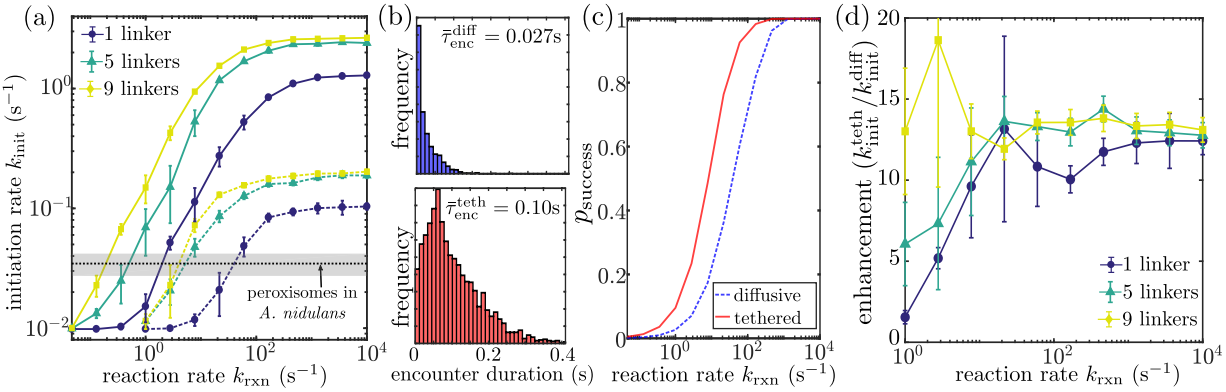

Figure 3.7: Hitchhiking initiation depends on rate of successful reaction between linker and cargo during an encounter event. (a) Overall rate of hitchhiking initiation, as a function of the reaction rate k_{rxn} for each linker. Dashed curves give results for diffusive cargo and solid curves for tethered cargo. Horizontal line represents experimentally measured initiation rate, with shaded region indicating standard error. (b) Distribution of encounter durations with an individual linker for diffusive (top) and tethered (bottom) cargo. (c) Probability of an encounter successfully resolving in hitchhiking for diffusive (dashed line) and tethered (solid line) cargo. (d) Enhancement in initiation rate due to tethering, for different values of k_{rxn}.

ual peroxisome trajectories obtained from time-lapse Lattice light sheet imaging of *A. nidulans* hyphae. A wavelet-based adaptive thresholding algorithm [61] is leveraged to classify sections of the particle trajectories as processive runs versus passive motion (Fig. 3.6a; see Appendix B). For all trajectories with an active run of duration at least 1sec, we look at the distributions of times from the start of the trajectory until the active run is initiated (Fig. 3.6b). The empirical cumulative distribution function is fitted to the conditional cumulative distribution for a Poisson process with a constant rate k_{init}, given that an event occurs before the end of the tracking period ($t_{\max}$). The resulting estimate for the hitchhiking initiation rate is $k_{\text{init}} = 0.035 \pm 0.007\text{s}^{-1}$. This rate of hitchhiking initiation is nearly an order of magnitude lower than our predicted rate of linker protein encounter, even for untethered peroxisomes.

This discrepancy implies that only a small fraction of encounter events with the PxdA linkers result in the successful initiation of a hitchhiking run. We therefore incorporate unsuccessful encounters directly into our model by introducing another rate constant k_{rxn}, giving the rate at which a successful binding reaction occurs between the linker protein and the peroxisome surface, while the two are within contact distance of each other. This is a microscopic rate constant effectively incorporating the molecular-scale sampling of the peroxisome surface by the linker, after it has already come within binding range. The higher the value of k_{rxn}, the more likely a linker encounter of a certain duration will result in the successful initiation of hitchhiking. The base model described in previous sections corresponds to the limit with $k_{\text{rxn}} \to \infty$, when all encounters result in a hitchhiking run. As k_{rxn} decreases, many encounters are unsuccessful and the expected rate of hitchhiking initiation diminishes dramatically (Fig. 3.7a).

In addition to finding the time until first encounter, the simulations can also be used to quantify the distribution of durations for each linker encounter event ($P_{\text{enc}}(t)$; see Appendix B). The average duration for a diffusive peroxisome encounter with a linker protein is found to be $\overline{\tau}_{\text{enc}}^{\text{diff}} \approx 0.03\text{s}$, whereas the average duration for a tethered peroxisome encounter is $\overline{\tau}_{\text{enc}}^{\text{teth}} = 0.1\text{s}$ (Fig. 3.7b). Tethered peroxisomes tend to experience longer encounters with a linker, as the carrier

organelle passes by and maneuvers around the cargo on the microtubule. Using the distribution of encounter durations, we can find the average probability that a linker encounter event will be successful for a given k_{rxn}. This relationship is given by

$$p_{\text{success}} = 1 - \int_0^\infty P_{\text{enc}}(t) e^{-k_{\text{rxn}} t} dt. \tag{3.3}$$

Due to the longer duration of encounter events, the overall probability that an encounter will result in successful initiation is always higher for a tethered than a diffusive cargo (Fig. 3.7c). Interestingly, the ratio of hitchhiking initiation rates for tethered versus diffusive peroxisomes is largely insensitive to k_{rxn}, for values above $k_{\text{rxn}} \gtrsim 5\text{s}^{-1}$ (Fig. 3.7d), even though tethered encounters are up to 3-fold more likely to be successful. This observation indicates that individual encounters for diffusive peroxisomes are not independent of each other, so that even a short encounter with a linker protein means the peroxisome is in a position where subsequent encounters will happen frequently.

Comparison with the experimentally measured hitchhiking initiation rate (horizontal line in Fig. 3.7a) indicates that for untethered peroxisomes and a saturating number of linkers, the reaction rate is expected to be roughly $k_{\text{rxn}} \approx 4\text{s}^{-1}$, with corresponding success probability $p_{\text{success}} \approx 0.1$. If the peroxisomes are tethered, the probability of each encounter successfully initiating a hitchhiking run would need to be $p_{\text{success}} \approx 0.02$ to yield the observed initiation rate.

Such a low success rate may arise from a variety of biological or mechanical reasons. First, it is possible that an individual peroxisome and PxdA-bearing endosome are incabable of forming a hitchhiking interaction during a given encounter. In particular, it is unclear if PxdA is the actual linker between peroxisomes and early endosomes, or if it is only one component of a hitchhiking apparatus. It is also unclear if the coiled-coil region of PxdA is consistently in a fully extended form or if it takes on multiple conformations that may make it less capable of readily interacting with hitchhiking cargo. Other proteins may also regulate PxdA activity or be involved

in linking peroxisomes to early endosomes in other ways. For example, only a certain percentage of peroxisomes may display a binding receptor for PxdA, creating a smaller pool of peroxisomes competent to hitchhike.

Furthermore, even if the peroxisome and the PxdA linker are capable of binding, this binding reaction may be comparatively slow, so that many contacts do not result in successful hitchhiking initiation. For instance, binding receptors on the peroxisome may not cover the entire surface, forcing the linker protein tip to explore a portion of the peroxisome surface before actually binding. The linker may also need to sample many conformations before making a successful contact with a receptor. As the proteins comprising the hitchhiking apparatus are unknown, the strengths of contacts between the peroxisome and early endosome are unclear and may be weak, resulting in broken contacts before hitchhiking is initiated. Finally, if peroxisomes are indeed tethered to microtubules, there may be a high energy requirement to break those tethers and initiate a hitchhiking event, resulting in an effectively slow reaction rate and a high fraction of unsuccessful encounters.

Given all of these potential effects beyond the encounter of a hitchhiking cargo with a linker protein, it is perhaps not surprising that such encounters should be much more frequent than actual hitchhiking initiation events. The geometric and mechanical parameters described here thus determine the frequency of opportunities for hitchhiking to occur. This sets an upper limit on the rate of hitchhiking initiation, for the case of easily broken tethers, a fully reactive peroxisome surface, and very rapid binding of the linker to the peroxisome surface.

3.4.5 Effect of initiation rate on overall cargo dispersion

Our exploration of the dynamics of cargo and carrier encounters indicates that tethering of cargo to microtubules can greatly enhance the rate of hitchhiking initiation. However, tethering of the cargo also inhibits its ability to move diffusively throughout the domain. Therefore, we sought to determine how these two competing factors (hindered diffusion but increased hitchhiking

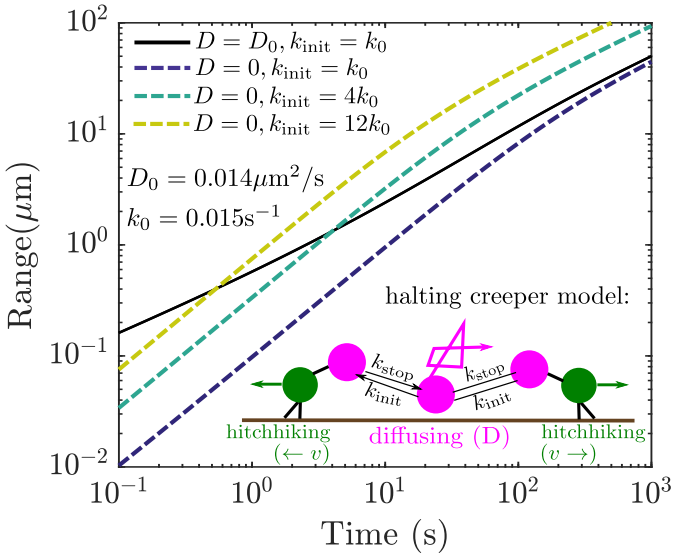

Figure 3.8: Range of a halting creeper particle engaged in bidirectional runs alternating with diffusive or tethered periods. Solid black line gives range for a particle that diffuses freely with diffusivity D_0, between processive runs initiated with a rate k_0. Dashed lines give range for particles that are tethered when not engaged in an active run, but with increasing initiation rates.

rate due to tethering of a cargo) would balance each other to affect the long-range dispersal of hitchhiking cargo organelles throughout a cylindrical region.

To address this, we switch to a simplified, analytically tractable model which focuses on the motion of hitchhiking cargo organelles along the hyphal axis. Specifically, we leverage the one-dimensional "halting creeper" model [87] where cargo organelles are treated as point particles subject to multimodal transport. The particles exhibit memoryless stochastic switching between bidirectional processive motions (with velocity v, starting rate k_{init}, and stopping rate k_{stop}), interspersed with diffusive periods of diffusivity D (Fig. 3.8 inset). The more detailed mechanical model for hitchhiking initiation described in previous sections allows us to calculate the effective starting rate k_{init} with and without tethering of the cargo organelles to microtubules.

In prior work [87], we developed an analytical expression for the range of an exploring “halting creeper" particle. Particle range constitutes a metric of interest for intracellular transport processes because it enables direct calculation of the average time for any target in the cell to be found by the first of a uniformly distributed set of particles. It also provides an estimate for

the distance from its site of biogenesis which an organelle explores over a finite time period. The range thus determines the extent to which organelles accumulate at their site of formation versus dispersing throughout the cell. It can be shown [87] that the range of a halting creeper transitions between a ballistic regime [range $Z(t) = fvt$] and an effectively diffusive regime [$Z(t) = \sqrt{4D_{\text{eff}}t/\pi}$], where $D_{\text{eff}} = (1-f)D + fv^2/k_{\text{stop}}$ is an effective long-time diffusivity, and $f = k_{\text{init}}/(k_{\text{init}} + k_{\text{stop}})$ is the equilibrium fraction of time in processive motion. The transition to the long-range diffusive regime occurs at a time $t^{**} = 16D_{\text{eff}}/(\pi f^2 v^2)$. Increasing the starting rate for processive motion (k_{init}) enhances the overall particle range at long times (above t^{**}), while decreasing the transition time where the effectively diffusive motion sets in. By contrast, in the absence of tethering, short-time motion is enhanced, creating a separate regime dominated by diffusion only with range $Z(t) = \sqrt{4Dt/\pi}$.

In Fig. 3.8 we show the expected range of particles with different combinations of diffusivity and processive starting rate. The solid line represents approximate parameters relevant to the motion of peroxisomes as measured in *Ustilago maydis* fungal hyphae, where the peroxisomes appear to exhibit diffusive, untethered motion between processive runs [11]. Namely, we set diffusivity $D_0 = 0.014\mu\text{m}^2/\text{s}$, hitch-hiking velocity $v = 1.9\mu\text{m/s}$, and run-length $vk_{\text{stop}} = 6.5\mu\text{m}$. The initiation rate for processive runs is estimated at $k_0 = 0.015\text{s}^{-1}$, such that approximately 5% of peroxisomes are expected to be hitchhiking at any given time [11]. Tethering of such particles to a microtubule will reduce the diffusivity to zero, but can enhance the starting rate by a factor of roughly 12-fold, for the case of 5 parallel microtubules (see Fig. 3.5d). We thus plot how such increased processive starting rate due to tethering can enhance the range of spreading particles over time. We note that even a 4-fold increase in the starting rate raises the range of the particles above a time-scale of a couple of seconds. The 12-fold increase estimated from our hitch-hiking simulations is expected to raise overall long-time particle range by a factor of about 3-fold.

The halting creeper model thus provides insight into the relation between organelle dispersion, the rate of hitchhiking initiation, and its enhancement due to tethering. It also

highlights the possible consequences of a breakdown of the tethering mechanism leading to inefficient dispersion of organelles.

3.5 Conclusions

In this work, we describe a computational framework for elucidating the key physical parameters that govern the efficiency of hitchhiking initiation. Using an analytical approach, we delineate the effects of geometry and transport machinery on the rate of encounter between a carrier and a hitchhiking organelle. In particular, we focus on the effects of the number of cytoskeletal tracks upon which the carrier organelles move and the linear density of the carriers. We show that encounter rates are nearly independent of the carrier density for low microtubule numbers, where the process is dominated by the ability of the diffusing cargo to come within proximity of a microtubule track. Splitting up the same carrier density across larger number of microtubules can improve the encounter rate through increasing the cross-sectional coverage by the moving carriers.

In some cells, linker proteins are known to mediate the contact between a carrier and a hitchhiking organelle. We calculate the rate of encounter between a carrier and a hitchhiking organelle as a function of the length and the number of linkers on the carrier. Our results show that very few linkers of moderate length are sufficient to saturate the contact rate. This result helps explain experimental measurements showing that overexpression of PxdA linker protein does not increase the hitchhiking frequency of peroxisomes in *A. nidulans* fungal hyphae. Further exploring the effects of linker flexibility, we show that moderately stiff linkers provide optimal contact rates between the carrier and hitchhiking cargo, by allowing the linker tips to explore large volumes of space while extending substantially above the surface of the carrier.

Leveraging our simulation framework, we study the effect of tethering organelles to microtubules on the initiation of hitchhiking. The increased proximity to moving carriers results

in a large enhancement of the contact rate, an effect that is particularly pronounced for small microtubule numbers and high carrier densities. Comparison of computed rates for cargo-linker encounter and and measured hitchhiking initiation rates for peroxisomes in *A. nidulans* hyphae indicates that only a small fraction of encounter events appear to result in successful hitchhiking. Nevertheless, by increasing the frequency of opportunities for such contact events to occur, tethering of the peroxisomes to microtubules is expected to enhance the rate of hitchhiking initiation by about an order of magnitude.

Based on this enhancement in the initiation rate, we compute the increased range covered by organelles exploring the cell through rare, sporadic hitchhiking runs. Our results show that tethering can substantially increase the amount of intracellular space explored over time-scales of seconds or higher, despite restricting diffusive transport.

Our computational framework is generally applicable to any transport process that relies on attaching to a carrier organelle, either directly or through stiff or flexible linker proteins. While we focus on the simple geometry of a cylindrical domain, the parameters employed here (carrier density, density of parallel microtubules) are local in nature. Hence, the initiation rates found can be applied to any system where microtubules are arranged in a parallel fashion around the current position of the cargo organelle. This includes cellular projections such as fungal hyphae and neuronal axons and dendrites, as well as micron-sized regions of the cell soma with no microtubule intersections. Hitchhiking initiation rates in the vicinity of intersecting microtubules are left as an extension of interest for further study.

Another topic of further interest is characterizing the biophysical processes that determine the duration and processivity of a hitchhiking run. In past studies where motor-driven organelles are observed to halt or change direction, such terminations of processive motion were attributed to microtubule intersections [21, 88, 107], tug-of-war between multiple motors [53], changes in motor activation state [22], or obstacles encountered by the organelle [107, 108] or the motors themselves [109]. The effect of a hitchhiking cargo on all of these processes governing the run-

length of a motor-driven carrier is currently unclear. Furthermore, additional mechanisms may be responsible for terminating or regulating hitchhiking runs specifically, including dissociation of the hitchhiker from the carrier and tug-of-war or cooperative events that may arise from a single cargo attaching to two different carriers. Establishing the underlying physical mechanisms that determine hitchhiking run-length is a fruitful topic for future study, necessary to developing a complete quantitative understanding of this non-canonical mode of intracellular transport.

3.6 Acknowledgments

We thank Hiroyuki Hakozaki for assistance with lattice light sheet imaging and processing as well as the Nikon Imaging Center at UC San Diego for help with imaging and data analysis.

Chapter 3, in full, is a reprint of the material with minor edits, as it appears in: S. S. Mogre, J. R. Christensen, C. S. Niman, S. L. Reck-Peterson, E. F. Koslover, "Hitching a ride: Mechanics of transport initiation through linker-mediated hitchhiking", *Biophysical journal*, 118 (6), 1357-1369, (2020). The dissertation author was the primary author of this paper.

Chapter 4

Optimizing Microtubule Arrangements for Rapid Cargo Capture

4.1 Abstract

Cellular functions such as autophagy, cell signaling and vesicular trafficking involve the retrograde transport of motor-driven cargo along microtubules. Typically, newly formed cargo engages in slow undirected movement from its point of origin before attaching to a microtubule. In some cell types, cargo destined for delivery to the perinuclear region relies on capture at dynein-enriched loading zones located near microtubule plus-ends. Such systems include extended cell regions of neurites and fungal hyphae, where the efficiency of the initial diffusive loading process depends on the axial distribution of microtubule plus-ends relative to the initial cargo position. We use analytic mean first passage time calculations and numerical simulations to model diffusive capture processes in tubular cells, exploring how the spatial arrangement of microtubule plus-ends affects the efficiency of retrograde cargo transport. Our model delineates the key features of optimal microtubule arrangements that minimize mean cargo capture times. Namely, we show that configurations with a single microtubule plus-end abutting the distal tip and

broadly distributed other plus-ends allow for efficient capture in a variety of different scenarios for retrograde transport. Live-cell imaging of microtubule plus-ends in *Aspergillus nidulans* hyphae indicates that their distributions exhibit these optimal qualitative features. Our results highlight important coupling effects between the distribution of microtubule tips and retrograde cargo transport, providing guiding principles for the spatial arrangement of microtubules within tubular cell regions.

4.2 Introduction

Microtubules form an essential component of the intracellular transport system, allowing for long-distance distribution and delivery of components driven by kinesin and dynein motors. In eukaryotic cells, microtubules are organized in a wide variety of arrangements depending on cellular geometry and specific biological transport objectives [110, 111]. These architectures range from centrally anchored radial arrays, to swirling or planar-polarized structures nucleated at the cell periphery, to parallel structures in the narrow cylindrical domains of neuronal projections and fungal hyphae [112]. The stark variation in cytoskeletal organization across different cell types raises a fundamental question regarding how the arrangement of microtubules affects cargo transport functionality. Furthermore, pharmacalogical modulation of cytoskeletal architecture by stabilization of dynamic microtubules has been proposed as a potential intervention to reduce transport deficits associated with neurological injury and disease [113].

Many studies have sought to relate the efficiency of cargo transport with cytoskeletal filament arrangements in various contexts. For disordered networks, the dependence of cargo delivery time on filament polarity, bundling, length, orientation, and local density has been established via continuum models and simulations of explicit network architectures [47, 114–118]. Cellular-scale cargo distribution in these models generally relies on multi-modal transport, incorporating processive runs whose direction is determined by the microtubule arrangement,

interspersed with pauses or diffusive phases that allow transition between microtubules [87, 119]. The microtubule architecture thus modulates transport efficiency both by directing processive motion and by determining the rate of capture for cargo in the passive state.

One biologically important objective for intracellular transport is the capture of newly formed cargo and its delivery towards the perinuclear region. Such cargo includes signaling endosomes [120, 121] or autophagosomes [13] formed at distal regions, or COPII-coated vesicles that bud from the endoplasmic reticulum throughout the cell [122]. Because directed motor-driven transport is much faster than diffusion of vesicular organelles, the initial step of cargo capture can play an important role in determining the overall timescale of delivery towards the nucleus.

Cells with long tubular projections, such as neurons and fungal hyphae, provide a particularly convenient model system for retrograde cargo transport. In neuronal axons, microtubules are highly polarized, with their plus-ends pointing towards the distal tip [123]. Similar plus-end-out polarization is observed in the distal segment of multinucleated hyphae for fungi such as *Aspergillus nidulans* and *Ustilago maydis* [8]. Here, we consider the efficiency of cargo capture for transport towards the cell body in these tubular model systems.

Because these geometries are much longer than they are wide, the axial distribution of cargo capture positions becomes particularly important. Given the typical diffusivity of vesicular organelles on the order of $D \approx 0.01 \mu\text{m}^2/\text{s}$, it should take on the order of 1 minute for cargo to explore the radial cross-section of an axon or hypha with radius approximately 1μm. By contrast, the time to reach the cell body via pure diffusive transport would range from hours (for a 10μm hyphal tip) to years (in a millimeter-long axon). Cells rely on processive retrograde transport to replace these unreasonably long time-scales with a much more rapid directed velocity on the order of 1μm/s.

In animal and fungal cells, processive retrograde transport is carried out primarily by cytoplasmic dynein-1 motors that carry cargo towards anchored microtubule minus-ends. In some cell types, dynein accumulates near the tips of growing microtubules (plus-ends) and forms

enriched pools referred to as 'comets' that can act as localized capture regions for cargo [124–128]. The placement of comets can be controlled by varying microtubule length (or nucleation sites in axons), and their positioning in relation to where cargo is formed can determine the diffusive search time before initiation of active transport.

We consider the process of cargo binding to a dynein comet and look for possible arrangements of microtubule plus-ends along the axial direction that facilitate this process for various positions of cargo entry. Our focus is on the initial cargo capture process, with the processive retrograde motion assumed to be relatively fast regardless of the microtubule arrangement.

We begin by examining simplified microtubule arrangements that capture cargo entering at the distal tip of a cell. Using an analytic one-dimensional model to represent the tubular geometry, we calculate the capture time, defined as the mean first passage time (MFPT) to encounter the capture zone at a microtubule plus-end. We derive the conditions for which the MFPT is minimized, and validate the one-dimensional approximation using three-dimensional (3D) Brownian dynamics simulations. The analysis is then extended to include broadly-distributed randomized microtubule configurations evaluated for efficiency of cargo capture with different initial distributions. General features are established for microtubule arrangements that allow efficient capture for both distally and uniformly derived cargos. A minimal model of microtubule dynamics highlights how such optimal arrangements may be obtained by tuning microtubule catastrophe rates. Supplemental results are provided in Appendix C to establish that the optimal configuration remains efficient even when cargo can be captured throughout the microtubules and even when the retrograde transport time itself is explicitly taken into account. Finally, we quantify live-cell images of *A. nidulans* fungal hyphae to demonstrate that observed microtubule distributions in hyphal tips exhibit the general features identified for optimal arrangements.

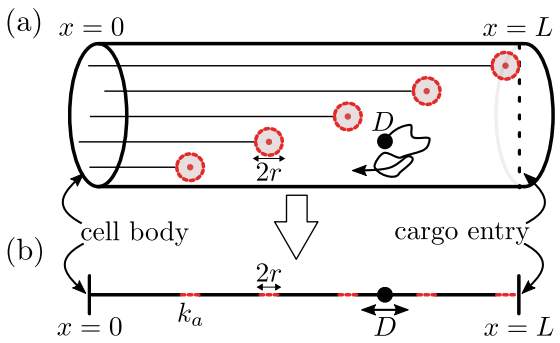

Figure 4.1: **Schematic for cargo capture at microtubule plus-ends in tubular cells. (a)** A depiction of a simplified microtubule arrangement in a tubular cell. Cargo enters at $x = L$ and diffuses with diffusion coefficient D. Cargo is captured at microtubule plus-ends depicted as red circles. **(b)** Schematic of the equivalent 1D model. A capture rate k_a is introduced to account for the time spent by the cargo diffusing radially at the microtubule plus-end axial location.

4.3 Methods

Experimental methods for imaging microtubules in *Aspergillus nidulans* hyphae are provided in Appendix C. The development and implementation of the mathematical model and computational simulations are described below.

4.3.1 Model development assumptions

We briefly summarize the fundamental underlying assumptions that motivated the construction of our mathematical models.

1. The cargo motion prior to capture by a microtubule is assumed to be diffusive in nature. In particular, we assume cargos detach from the plasma membrane before capture at the microtubule tips. Apparently diffusive trajectories in the cytoplasm have been observed for fungal peroxisomes [11], as well as virus-laden endosomal particles and lysosomes in mammalian cells [54, 129], and endocytic particles in yeast [130]. In some cases vesicular particles undergo subdiffusive rather than diffusive motion [131, 132]. In many others, the apparent random walk behavior arises not from thermal Brownian motion but rather from spatially dispersed active forces from actomyosin contraction [23, 133] or hydrodynamic

entrainment by passing motor-driven organelles [11]. Newly formed organelles such as endosomes may exhibit short-range motion along the cortical actin cytoskeleton shortly after release from the membrane [130]. For simplicity, we subsume all these behaviors in an effectively diffusive model. To plug in a concrete diffusivity we use the value of $D \approx 0.01 \mu\text{m}^2/\text{s}$ measured for fungal peroxisomes [11], but other effective diffusivities could easily be utilized in the context of this model.

2. The cellular domain is assumed to be a cylinder that is much longer than it is wide. This assumption is relevant for (*e.g.*) fungal hyphae tips (1μm wide and 5-40μm long [11, 12]) and neuronal axons (a few μm across [9], with lengths ranging from hundreds of micrometers to over a meter [10]).

3. We assume cargo capture occurs primarily at microtubule plus-ends, which serve as a site for accumulation of dynein motors. This assumption is in concert with prior models of search-and-capture of cellular targets by proteins bound at the microtubule plus ends [134–136]. In particular, the accumulation of dynein motors in comet-like regions at the microtubule tips is thought to lead to enhanced capture at the plus-end for endosomes and other organelles [125, 126, 128]. We also briefly explore the opposite extreme of capture along the full microtubule when establishing the optimal microtubule architectures for rapid capture. In Appendix C we examine this assumption explicitly by considering capture regions of different length.

4. We focus on the initial capture process of cargo onto microtubules, assuming that retrograde transport itself proceeds in a rapid, directed fashion after capture. Thus, the capture times here provide a lower limit to which should be added an additional time for retrograde transit to the cell body. From any given position along the domain, retrograde transport tends to be much faster than diffusive transport, implying that optimal microtubule structures should be determined primarily by the initial capture process. This assumption is examined further in Appendix C, where the additional processive transit time is explicitly incorporated.

5. For clarity of visualization and discussion, we assume microtubules are nucleated near the cell body, so that the position of plus-end tips is equivalent to microtubule length. This assumption is valid for fungal hyphal tips, in the region past the last nucleus[137]. In neuronal axons, shorter microtubules are nucleated in a staggered fashion throughout the domain. However retrograde-moving cargo tend to step past the microtubule minus-ends onto the next microtubule segment with only short (few second) pauses that imply the cargo is unlikely to dissociate fully into a diffusive state [138]. Even with these tiled microtubule arrangements the retrograde cargo can exhibit effectively processive motion. Thus we focus on the positions of microtubule plus-ends, regardless of their actual length, for modeling cargo capture.

6. In order to highlight the role of steady-state cytoskeletal architecture, we focus primarily on a model with stationary microtubules. This assumption is then relaxed to incorporate a basic model of microtubule dynamics, reminiscent of prior work on search-and-capture by microtubule plus-ends [134, 136].

4.3.2 Simplified model system for cargo capture

To explore the role of microtubule configurations on cargo capture in a narrow cellular domain, we leverage both an analytically tractable one-dimensional model and three-dimensional Brownian dynamics simulations for cargo motion in a tube.

We consider a tubular domain of length L and radius R, with $x = 0$ denoting the cell body and $x = L$ corresponding to the distal end of the cell (Fig. 4.1a). We set $R = 1\mu$m, as appropriate for both neuronal axons [9] and fungal hyphae [11, 12]. The cargo is modeled as a diffusive particle that either enters the cell at the distal tip, or starts uniformly distributed throughout the tube. Cargo diffusivity is set to $D = 0.01\mu\text{m}^2/\text{s}$, in accordance with prior measurements for vesicular cargo in fungal hyphae [11]. Microtubules are treated as straight axial filaments,

assumed to be scattered uniformly throughout the radial cross-section of the domain. The filaments are assumed to be polarized with their minus-ends at the cell body ($x = 0$) and their plus-ends distributed at different axial positions.

Cargo is assumed to load onto a microtubule plus-end (representing a dynein-enriched comet region) instantaneously upon entering within the capture range ($r = 0.2\mu$m) of the microtubule tip. The range r is taken to represent a typical contact range from an organelle to a point-like microtubule plus-end. The effect of longer comet lengths is explored further in Appendix C. Throughout the text, we refer to the engagement of cargo to a microtubule via dynein comets as the "cargo capture" process. If the cargo reaches the proximal end of the domain without interacting with a plus-end, it is assumed to have been absorbed at the cell body.

4.3.3 Analytic one-dimensional model

For very narrow domains ($R \ll L$), the simple model described above can be mapped to an effectively one-dimensional system, as illustrated in Fig. 4.1b. The axial positions of cargo and microtubules are projected onto the axis of the cell, represented by a linear segment of length $0 \leq x \leq L$. Cargo can be captured while diffusing within absorbing intervals in the domain, with the rate of absorption determined by the particular arrangement of microtubules.

Plus-ends are denoted as discrete intervals of width $2r = 0.4\mu$m, placed at specific axial positions. In an interval corresponding to one microtubule end, the capture rate is set to k_a, representing the rate of encountering the microtubule by diffusion across the radial cross-section. The value of k_a is estimated by computing the mean first passage time in a reflecting cylinder of radius R to a central absorbing cylinder of radius r [69], according to

$$k_a = \frac{8DR^2}{4r^2R^2 - r^4 - 3R^4 - 4R^4 \ln(r/R)} \approx 0.02\text{s}^{-1},$$

for the estimated parameters $R \approx 1\mu$m, $r \approx 0.2\mu$m, and $D \approx 0.01\mu\text{m}^2/\text{s}$. For microtubule

configurations with multiple nearby plus-ends, the absorption rate is assumed to scale linearly with the number of plus-ends whose capture range overlaps in a given interval. Under this set of assumptions, a particular arrangement of microtubules can be represented by a series of linear intervals with varying absorption rates that are integer multiples of k_a. Cargo capture is then represented by a one-dimensional diffusive process in a domain with a reflective boundary at $x = L$ (cell tip), absorptive boundary at $x = 0$ (cell body), and discrete partially absorbing intervals distributed throughout its length. The MFPT to capture for this process can be obtained analytically by considering all possible paths of the cargo between the different absorbing intervals. Ref. [139] describes a propagator-based approach for computing the mean first passage time to capture a diffusing particle on a network with heterogeneous absorption rates on individual edges. The linear model described here serves as a specialized case of such a network. Details of the derivation for the linear model are provided in the Appendix C.

4.3.4 3D simulations for capture dynamics

To validate the approximate one-dimensional model, we also carry out 3D Brownian dynamics simulations of cargo capture by microtubule tips, directly reproducing the cylindrical system illustrated in Fig. 4.1a. The simulations assume a domain of length $L = 10\mu$m, and radius $R = 1\mu$m, reflecting the relevant regime for hyphal tips (region past the last nucleus) in *Aspergillus nidulans* fungal hyphae. Microtubules are modeled as parallel straight lines nucleating at the proximal end of the domain, and are distributed randomly over the cross-section. Diffusing cargos are assumed to be instantaneously captured when approaching within a distance of 0.2μm from the microtubule plus-ends. For a given axial configuration of microtubule ends, the MFPT is computed by averaging over 1000 independent simulations, each sampling a different radial distribution of microtubule positions.

When incorporating microtubule dynamics (in Fig. 4.6), we turn to a minimal model involving microtubule growth and catastrophe. Microtubules are allowed to grow at a speed

$v_g = 0.18\mu$m/s, corresponding to typical speeds measured in the hyphae of the fungus *Ustilago maydis* [140], which displays similar geometry and transport dynamics to *A. nidulans*. A growing microtubule that reaches the distal tip of the cell is assumed to remain paused at that location. Both growing and paused microtubules can enter the shrinking state with a catastrophe rate k_{cat}. We assume that the cargo-capture ability of microtubule plus-ends (*e.g.:* presence of dynein comets) is lost upon catastrophe, so that there is no capture while in the shrinking state. The number of microtubules in the model (n_{MT}) refers specifically to capture-capable microtubules. Consequently, microtubules that undergo catastrophe instantaneously disappear, and a new zero-length microtubule in the growing state appears in its place to maintain a constant number of capture-capable regions in the cell.

Based on this model, the steady state density of growing microtubule plus-ends [$P(x)$] and the number of paused microtubules at the distal tip (N_{end}) are given by

$$\begin{aligned} P(x) &= n_{\text{MT}} \left(\frac{k_{\text{cat}}}{v_g} \right) e^{-k_{\text{cat}} x / v_g}, \\ N_{\text{end}} &= n_{\text{MT}} e^{-k_{\text{cat}} L / v_g}. \end{aligned} \tag{4.1}$$

The derivation for these expressions is provided in Appendix C.

Initial microtubule lengths are drawn from this steady state distribution, and microtubules are allowed to grow and shrink according to the described dynamics. Cargo capture at microtubule tips is simulated using the same process as described for static microtubules. For a given catastrophe rate, we carry out 1000 independent simulation runs, each starting with a different initial configuration of microtubule ends (uniformly sampled in the radial dimension, and sampled from Eq. C.7 in the axial dimension). All simulations are carried using custom-built code in Fortran 90, parallelized on the Open Science Grid [141, 142]. Code for both simulations and analytical calculations with the 1D model is provided at `https://github.com/lenafabr/transportSimCyl`.

A table of the main model parameters is provided in Appendix C.

4.3.5 Minimal-distance metric to quantify clustering of capture regions

In order to quantify the axial dispersion or clustering of capture regions (*i.e.:* microtubule plus-ends), we define a "minimal-distance" metric for a configuration of n_{MT} points on an interval. Namely, this metric measures the average distance between a uniformly distributed probe and its nearest point in the configuration.

The configuration is described by points $x_i \in [0,L]$, with $1 \leq i \leq n_{\mathrm{MT}}$. An additional point $x_0 = 0$ is included to represent absorption at the cell body. The closest capture region for a random number u distributed uniformly between 0 and L is located at x_i if $u \in (y_i, y_{i+1})$, where y_i are the mid-points between consecutive absorbing points ($y_i = (x_{i-1} + x_i)/2$, $1 \leq i \leq n_{\mathrm{MT}}$). End-points of the domain are denoted by $y_0 = 0$ and $y_{n_{\mathrm{MT}}+1} = L$, respectively. The average distance between the uniformly distributed probe u and its nearest absorbing region is then given by,

$$\begin{aligned} \bar{x} &= \frac{1}{L} \sum_{i=0}^{n_{\mathrm{MT}}} \left(\int_{y_i}^{y_{i+1}} |u - x_i| \, du \right) \\ &= \frac{3x_{n_{\mathrm{MT}}}^2}{4L} - x_{n_{\mathrm{MT}}} + \frac{L}{2} - \frac{1}{2L} \sum_{i=1}^{n_{\mathrm{MT}}-1} x_i \left(x_{i+1} - x_i \right). \end{aligned} \tag{4.2}$$

We use $d = \bar{x}/L$ as the clustering metric throughout the text. Smaller values of d correspond to well-dispersed microtubule plus-ends, with a minimal value of $1/(4n_{\mathrm{MT}} + 2)$ for the configuration where consecutive points are equally spaced. Larger values indicate clustering of microtubule plus-ends along the axis, with a maximal value of $d = 0.25$ for the configuration with all plus-ends at the distal tip.

4.4 Results and Discussion

4.4.1 Separation of microtubule ends for distal capture

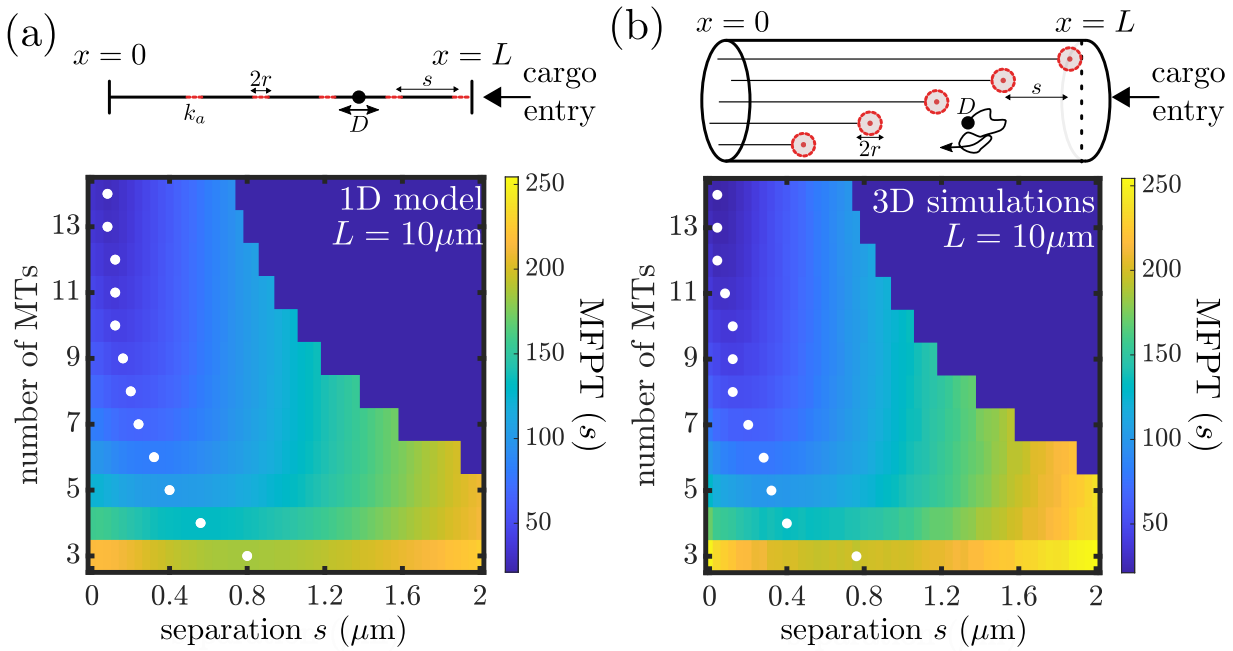

Figure 4.2: **Cargo capture times for axially separated microtubules. (a)** Mean first passage time (MFPT) as a function of number of microtubules and separation (s) between consecutive microtubules for the effective 1D model. The longest microtubule extends from the cell body at $x = 0$ to the cell tip at $x = L$, which serves as the point of cargo entry. Subsequent microtubules are axially separated by a distance s. White dots mark the separation distance s that gives the minimum MFPT for a given number of microtubules. **(b)** Analogous plot for the 3D model of a tubular domain.

We first consider the problem of optimizing the axial distribution of a limited number of capture regions (*e.g.:* dynein comets at microtubule plus-ends) for rapid capture of diffusive cargo entering at the distal tip of a tubular cell. To begin with, we consider two extreme arrangements of microtubule plus-ends. On the one hand, clustering plus-ends near the distal tip will enable distally-produced cargos to quickly encounter and bind to the microtubule. On the other hand, any cargo that diffuses past the clustered plus-ends may then embark on very long trajectories down the tube, resulting in a long-tailed distribution of capture times. In general, a diffusive particle that starts at distance x_0 from one absorbing end of a domain of length L will have a mean

first passage time of $\tau = x_0(L-x_0)/(2D)$ to reach the ends, a quantity that approaches infinity as the domain becomes infinitely long. By contrast, scattering capture regions broadly throughout the domain ensures a uniform availability of capture regions and precludes very long trajectories prior to capture. However, if the number of microtubule tips is fixed, such a broad distribution results in a lower density near the distal origin of the particles and forces each one to diffuse further along the axis before encountering a tip. To quantify this trade-off, we compute the mean first passage time (MFPT) to capture distally-produced diffusing cargo for different spacings of microtubule ends away from the distal tip of the cell.

Specifically, we focus on regularly spaced configurations to explore two key parameters that play a role in cargo capture. First, the number of microtubules (n_{MT}) determines the number of capture regions that a cargo can attach to, with a higher quantity generally corresponding to faster capture. Second, the axial separation (s) of consecutive microtubule ends tunes the breadth of their distribution away from the point of cargo entry. Unevenly scattered microtubule end positions are discussed in subsequent sections.

The geometric parameters of the model reflect a typical hyphal tip (beyond the last nucleus) of the fungus *Aspergillus nidulans*, which serves as a convenient model system owing to its neuron-like geometry and genetic tractability. Model construction details are provided in the Methods section. An important advantage of a narrow tubular geometry is that it can be modeled analytically as an approximately one-dimensional system. Since the length of our domain is typically much larger than the radius, a simplified model that represents the tube as a line with localized binding regions can encompass the overall behavior of the capture process. The one-dimensional approximation (Fig. 4.2a, top panel) represents the microtubule tips as short intervals with a finite capture rate within each interval that encompasses the rate of radially encountering the microtubule while within that slice of the domain. The average time to capture includes trajectories that pass through multiple capture regions until successfully undergoing capture within one of them. The MFPT of this process can be computed using a previously

developed method for reaction rates on heterogeneous tubular networks [139], as described in Appendix C. Fig. 4.2a shows a plot of the MFPT versus the number of microtubules and the separation between consecutive microtubule ends.

To verify the validity of the approximate one-dimensional model, we compare our results to 3D Brownian dynamics simulations that encompass the full model system with a tubular domain and spherical capture regions of radius r representing the microtubule ends. Details of the 3D model are provided in the Methods section. As shown in Fig. 4.2, the 1D analytic calculations and 3D simulations give nearly identical results for the MFPT. The mean relative error in the MFPT between the 1D and 3D approaches is $\sim$6.6%. This close correspondence establishes the robustness of the approximate 1D model for representing the narrow tubular geometry. We proceed to employ the 1D model for the remainder of the calculations discussed below.

Interestingly, the MFPT to capture shows non-monotonic behavior as separation s is increased from 0, reaching a minimum at an intermediate separation distance between microtubule ends. The existence of the minimum is a consequence of the competition between capturing cargos quickly near the entry point, and extending the overall capture region for cargos that might evade the initial cluster. As the number of microtubules, viz. the overall capture capacity, is increased, the optimal separation decreases. This follows from the fact that fewer cargos can escape the initial capture near the tip when a large number of microtubules are present. The optimal separation ranges between $\sim 0.01\mu$m for 14 microtubules to $\sim 0.8\mu$m for 3 microtubules. Converting the optimal separation to the overall distance over which plus-ends are scattered, the results indicate that it is optimal to distribute plus-ends over a distance of $\sim 1.4-2\mu$m from the cell tip for a 10μm cell.

The existence of an optimum separation distance for a given number of microtubules highlights the benefit of scattering capture sites for cargo generated at the cell tip. Intuitively, scattered configurations of microtubule ends are more effective in that they are able to capture cargo that diffuses past the distal region, precluding very long trajectories that explore a large fraction of

the domain prior to returning for capture. Because the MFPT between two absorbing boundaries scales in proportion to the domain length, we would thus expect the optimal microtubule end separation to be larger for longer domains. We therefore proceed to explore the effect of domain length on the optimal microtubule distribution.

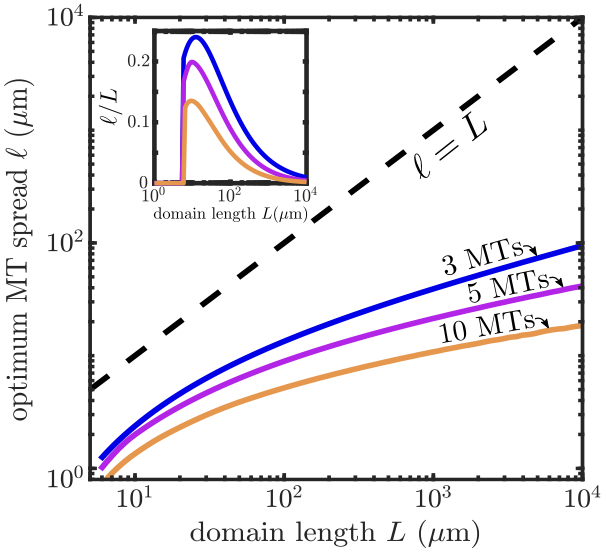

Figure 4.3: **Effect of cell length on microtubule arrangement.** The optimal total spread of microtubule plus-ends ($\ell = sn_{\mathrm{MT}}$) is plotted versus the length of the cellular domain (L), for cargos entering at the distal tip and captured by microtubule plus-ends. Inset shows the fraction of the entire domain length over which the plus-ends should be spread.

While many tubular cell projections exhibit a similar width of $1-2\mu$m, the length from the distal tip to the nearest nuclear region can vary widely. In fungal hyphae, the distance from the hyphal tip to the first nucleus can range from a few to tens of microns in length [11, 12]. Neuronal axon lengths can vary from hundreds of micrometers up to a meter long [10]. In Fig. 4.3a, we compute the optimal separation between microtubule ends for cylindrical domains of different length, where the domain length represents the axial distance from the tip to the nearest nucleus.

As expected, the optimum separation increases for longer domain lengths. However, the rate of increase is distinctly sublinear with L. This effect arises because as the region containing the microtubule ends becomes longer, it is increasingly likely that the cargo is captured before leaving to explore the rest of the domain. Because this initial capture process is independent of

the domain length, the dependence on L becomes increasingly shallower as the microtubule ends are more spread out. Consequently, for long tip-to-nucleus distances, an optimum arrangement of microtubule ends concentrates them over a small fraction of this distance. Cell projections of length $10-20\mu$m require the widest relative separation of capture regions (Fig. 4.3a, inset), scattering the microtubule ends over $\sim 15-25\%$ of the domain.

The scattering of microtubule ends engenders a trade-off between rapidly capturing cargo at its point of entry, and minimizing search time for cargo that wanders within the cell. The optimum distribution therefore depends on the location within the cell where cargo first becomes capable of interacting with the microtubule plus-ends. In Appendix C, we show how the optimal plus-end separation varies for cargo that must first undergo a maturation process before becoming available for capture. Examples of organelle maturation include neuronal autophagosomes which may require fusion with other organelles prior to engaging in retrograde transport [14, 15, 143]. Maturation times above a few minutes allow the cargo to diffuse a substantial distance away from the distal tip, so that optimal microtubule plus-ends separations become larger.

Varying the maturation rate effectively tunes the initial distribution of capture-ready cargo. The increased optimal separation of capture zones underscores the importance of initial cargo distribution in determining the most efficient arrangement of microtubules. While there is still a trade-off between clustered and dispersed microtubule plus-ends, matching the location of capture regions to the starting distribution of the cargo leads to more efficient capture. Indeed, a more general treatment would account for various initial cargo distributions. These can be incorporated in the model as initial conditions ranging between two extremes: cargo entering at the cell tip or cargo being distributed uniformly within the cell.

4.4.2 Optimal microtubule configurations for multiple capture conditions

In the previous section, we focused on cargo produced at the distal tip, and loaded onto microtubules only within a 200nm contact radius of the plus-end. However, both of these

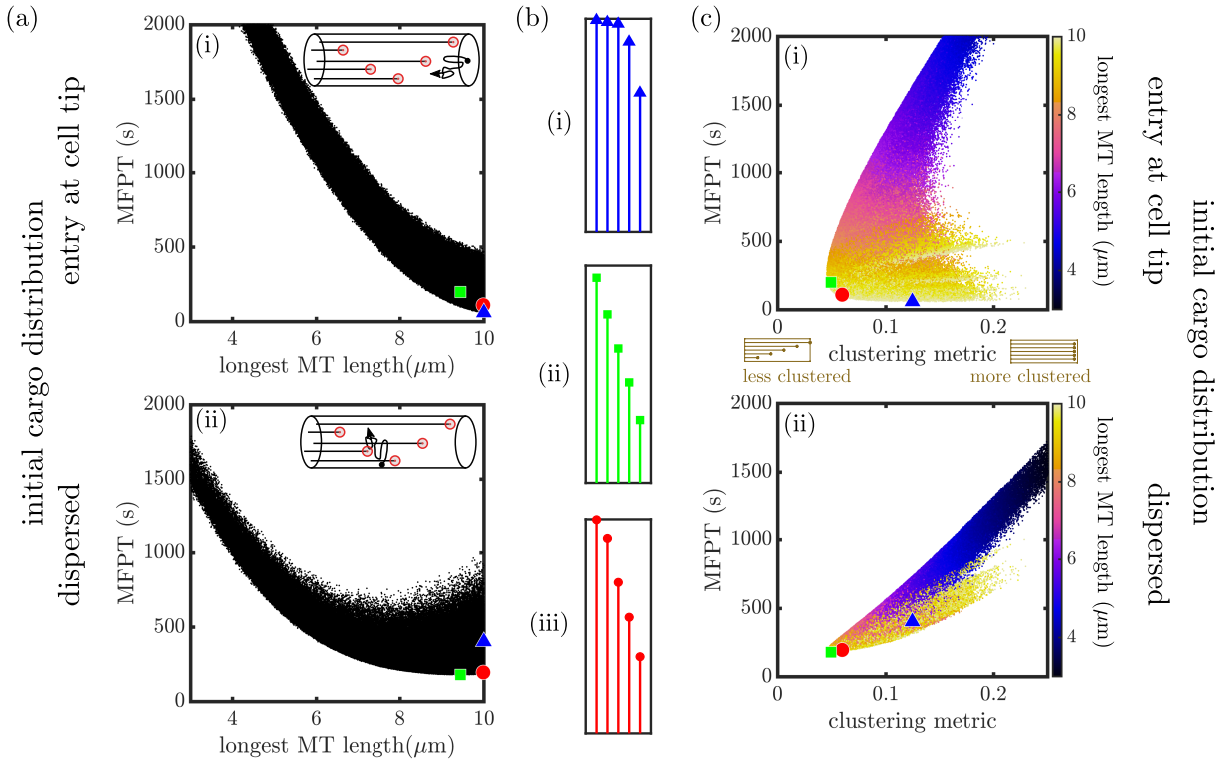

Figure 4.4: **MFPT for random microtubule configurations**. **(a)** Scatter plots showing the MFPT to capture at microtubule plus-ends vs the length of the longest microtubule for 10^6 randomly sampled configurations with 5 microtubules each in a domain of length 10μm. (i) Cargos start at the cell tip. (ii) Cargos start uniformly. Blue triangle indicates the overall fastest configuration for (i). Green square indicates the overall fastest configuration for (ii). Red circle denotes a configuration that falls within the lowest 3% of MFPTs for all capture conditions studied, including results shown in this figure and in Fig. 4.5. **(b)** Microtubule configurations corresponding to the (i) blue triangle, (ii) green square, and (iii) red circle in panel (a). **(c)** Scatter plots showing the MFPT plotted against a clustering metric for the randomly sampled configurations, with color indicating longest microtubule length for each configuration. (i) cargos start at cell tip. (ii) cargos start uniformly. Blue triangle, green square, and red circle denote configurations illustrated in panel (b).

assumptions do not necessarily hold for all retrograde transport systems. For example, while the distal tips of hyphae are the most endocytically active [144], some endosomes may be produced elsewhere along the membrane. Other organelles, such as peroxisomes, may bud from the endoplasmic reticulum all along the hyphal length. We therefore consider for comparison the extreme case of cargo produced uniformly throughout the extended cell region. Furthermore,

dynein comets exhibit a gradual decrease in density over a micrometer length scale [125], so that capture may not be limited to such a short range of the microtubule plus-end. In this section, we explore the overall features of optimal microtubule configurations for retrograde transport initiation in a variety of cargo production and capture conditions.

We generate 10^6 random configurations of 5 microtubules, with plus-end positions selected uniformly at random across the domain. The number of microtubules was chosen to be relevant for the tip region of *A. nidulans* hyphae [12]. For each configuration, we compute the MFPT for capture at the microtubule plus-ends both for distally-initiated and uniformly-initiated cargo (Fig. 4.4).

One of the key features of the microtubule configuration is the extent to which it covers the entire cellular domain. This is particularly important for the case of cargo entry at the distal tip, where the presence of a microtubule end near the entry point can greatly speed up capture. We use the length of the longest microtubule in each configuration to describe this feature, demonstrating that the capture time generally decreases as the longest microtubule length is increased (Fig. 4.4a.i). The optimal configuration in this case involves microtubule plus-ends scattered over approximately 40% of the length of the cellular region, with several microtubules approaching near-maximal length. It should be noted that for the case of very long capture regions, the dependence on the longest microtubule length becomes an even stronger predictor of the capture time, with little variability among different configurations that have the same longest length (see Appendix C).

When cargo is produced uniformly throughout the domain, the capture efficiency is not so well-correlated with the length of the longest microtubule (Fig. 4.4a.ii). In this scenario, the optimal microtubule architecture exhibits a broad dispersion of the plus ends throughout the domain (Fig. 4.4b.ii), in keeping with the broad initial distribution of the cargo. We therefore sought to establish another metric that quantifies the extent to which plus-ends are dispersed or clustered throughout the domain.

For cargo produced at the distal tip of the cell, the length of the longest microtubule determines the position of the nearest capture region relative to the point of cargo entry. For cargo initiated uniformly across all axial positions, we can define an analogous quantity which we term the minimal-distance clustering metric (d). Namely, for a given set of microtubule end positions, we compute the expected value of the distance between a point selected uniformly at random and the nearest microtubule end to that point (see details in Methods). Because particles are also captured at the cell body, a capture region at $x = 0$ is appended to all microtubule configurations. The minimal distance metric measures the clustering of capture regions: high values correspond to highly clustered microtubule plus-ends (with a maximal value of $d_{\max} = 0.25$); low values correspond to plus-ends spread evenly out over the entire domain (minimal value $d_{\min} = 1/(4n_{\mathrm{MT}} + 2)$).

The MFPT to capture at microtubule ends is plotted versus this clustering metric for each of the sampled microtubule configurations in Fig. 4.4c. When particles start at the distal end of the domain, the capture times are largely insensitive to the clustering metric (Fig. 4.4c.i). The most optimal (lowest MFPT) configuration for cargo produced at the distal tip (blue triangle) has a moderately high clustering metric ($d = 0.12$), corresponding to slightly separated ends near the distal tip (see Fig. 4.4b.i), similar to the optimum found in Fig. 4.2.

By contrast, when cargo starts uniformly throughout the domain, lower clustering ensures that there is always a capture region close to the starting position of the particle, allowing for faster capture times (Fig. 4.4c.ii). The optimal configuration sampled for this scenario (green square, illustrated in Fig. 4.4b.ii) has a relatively low clustering metric of $d = 0.049$, close to the minimal possible value of this metric ($d_{\min} = 0.046$ for $n_{\mathrm{MT}} = 5$). This effect arises because clustered configurations near the cell tip require the dispersed cargo to diffuse over long distances through the cell before it can either reach the cell body or the plus-ends located near the cell tip. On the other hand, evenly dispersed plus-ends provide capture regions throughout the cell, so that all cargos have a capture region nearby regardless of where they initiate.

For both distally initiated and uniformly dispersed cargo, the overall features of optimal microtubule configurations are unaltered if we include an explicit retrograde transit time to get the overall MFPT to reach the cell body (see Appendix C). This is unsurprising because from any given position along the tubule diffusive transport to the cell body is much slower than active retrograde transport, so that the optimal microtubule architecture is dominated primarily by the initial capture time.

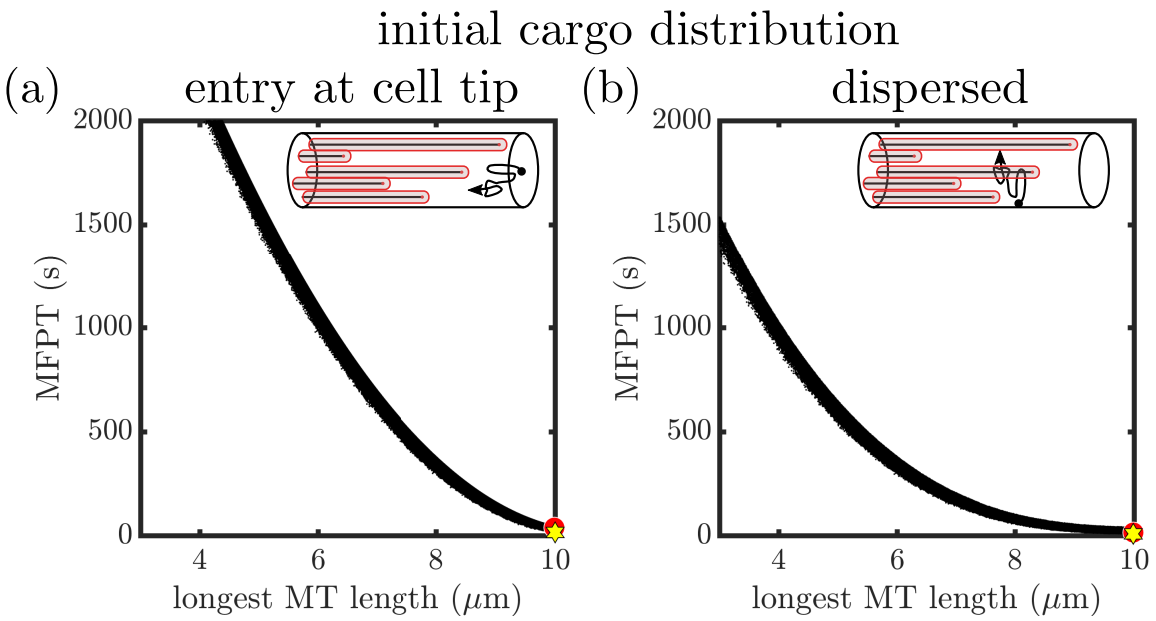

Figure 4.5: **Cargo capture along full length of microtubule.** Scatter plots of the MFPT for cargo capture along the full length of the microtubule, shown for 10^6 randomly sampled configurations with 5 microtubules each in a domain of length 10μm. **(a)** Cargo is initiated at the distal tip. **(b)** Cargo is initiated uniformly throughout the domain. Yellow star denotes the configuration with the fastest capture for each initial cargo distribution. Red circle shows the globally optimized configuration corresponding to Fig. 4.4b.iii.

Notably, the results so far have focused on cargo that is captured by point-like dynein comets located at microtubule plus ends. However, dynein comets generally exhibit a gradual decrease in density over a micrometer length-scale. In Appendix C we provide equivalent results for the MFPT to capture by regions of increasing length. The extreme case corresponds to capture regions that are equal in length to the entire microtubule. Such a model is applicable to cargo

that can be captured equally well along the full microtubule rather than just near the plus-end. In Fig. 4.5, we see that in this situation the MFPT to capture is determined primarily by the length of the longest microtubule, regardless of whether the cargo is initiated distally or throughout the domain. This is a direct consequence of our assumption that the microtubules are nucleated near the cell body, so that plus-ends placed closer to the distal end correspond to a greater total length of microtubule available for capture.

Our analysis shows that the length of the longest microtubule is a strong predictor of the MFPT when cargos are captured by long regions of the microtubule (Fig. 4.5), and a moderate predictor when distally produced cargos are captured at the microtubule ends (Fig. 4.4a.i). In the case of uniformly dispersed cargo, the minimal-distance clustering metric is a complementary predictor of capture efficiency (Fig. 4.4c.ii). Microtubule configurations that fulfill both of these criteria (high longest length and low clustering) are expected to yield a fast capture time for all of the scenarios considered. We identify a set of 6 microtubule configurations that fall in the lowest 3% of MFPT for both distally produced and uniformly produced cargos, and for the two extremes of plus-end capture and capture along the whole microtubule. Of these, the configuration with the lowest MFPT for distal initiation and plus-end capture is shown with red circles in Fig. 4.4 and 4.5. The configuration has one microtubule reaching nearly to the end of the domain and the other microtubules distributed roughly evenly over more than half of the domain length (Fig. 4.4b.iii).

Overall, these findings highlight the features of ideal microtubule configurations for efficiently capturing cargo for retrograde transport. Namely, configurations with one long microtubule and other microtubules of broadly distributed lengths result in near-optimal capture times regardless of whether cargos are produced distally or throughout the domain, and of whether they are captured by point-like dynein comets at microtubule ends or more broadly along the whole microtubule.

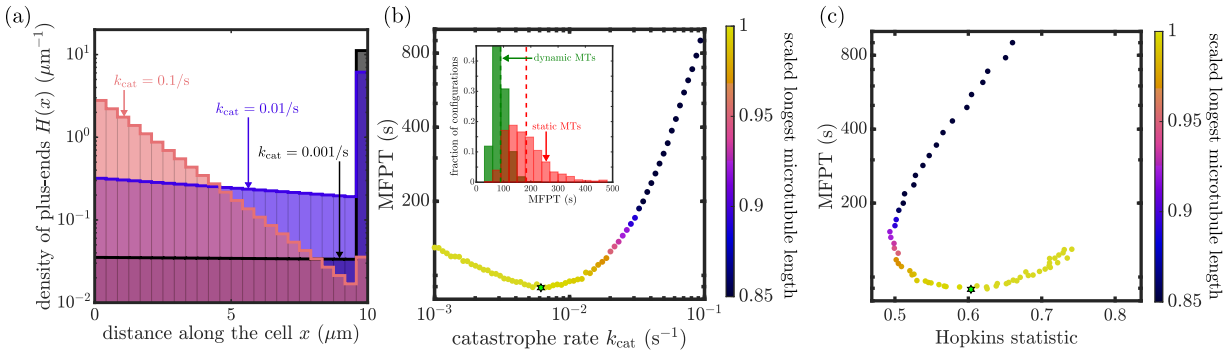

Figure 4.6: **Cargo capture by dynamic microtubules (a)** Steady-state distributions of microtubule plus-ends along the cell axis, for different values of the catastrophe rate (k_{cat}). **(b)** MFPT to capture cargo versus k_{cat} for dynamic microtubules. Inset compares the distribution of capture times to simulations with stationary microtubules sampled from the steady-state length distribution corresponding to the optimal value of k_{cat} (marked with green star). Dashed lines indicate the mean value for the corresponding distributions. **(c)** MFPT to capture vs average clustering (minimal-distance metric) for dynamic microtubules. The green star indicates the configuration with minimum MFPT. The inset denotes a representative microtubule configuration corresponding to the optimal catastrophe rate. Color in (b) and (c) indicates the average length of the longest microtubule, scaled by the domain length. All plots are shown for a domain of length $L = 10\mu$m, radius $r = 1\mu$m, and 5 dynamic microtubules with growth rate $v_g = 0.18\mu$m/s. MFPTs are obtained using 3D simulations, with cargo starting at the distal tip.

4.4.3 Establishing optimal configurations through microtubule dynamics

The results above demonstrate the overarching features of microtubule configurations that result in optimal cargo capture. Our model is agnostic as to the dynamic processes by which a cell might establish such an optimum configuration. Furthermore, a key simplifying assumption of the model is that individual microtubule architectures remain fixed throughout the capture process, so that the distribution of microtubule lengths serves as a source of quenched disorder for the position of the capture regions. Realistically, microtubules in fungal hyphae grow and shrink on roughly 30sec timescales [140]. Microtubules in growing neuronal projections are similarly dynamic, although those in mature axons tend to remain relatively stable over time [145, 146]. A variety of prior studies have highlighted the importance of microtubule dynamics in dictating the time-scales of capture for relatively stationary cellular targets (including mitotic kinetochores and cortical regions) [147–150]. In this section, we briefly explore the role of plus-end dynamics in

the capture of diffusive cargo.

We incorporate microtubule dynamics in the 3D simulations by including basic growth and catastrophe processes, as described in Materials and Methods, while fixing a total number of $n_{\mathrm{MT}} = 5$ capture-capable microtubule tips. Our minimal dynamic microtubule model fixes the growth velocity ($v_g = 0.18\mu$m/s) according to published data in fungal hyphae [140]. The catastrophe rate k_{cat} sets a time-scale on which a growing microtubule halts and begins to shrink, and is used as a free control parameter to tune microtubule distributions. Microtubules that reach the end of the domain are assumed to be capped and to remain fixed until a catastrophe event occurs.

The catastrophe rate modulates the steady-state distribution of microtubule lengths (Fig. 4.6a). In this simple model, the length of the longest microtubule in the domain and the clustering of microtubule ends are coupled together. Low values of k_{cat} result in most of the microtubule plus-ends accumulating at the distal tip of the domain, corresponding to a high value for the longest MT length and for the clustering metric. Intermediate values of k_{cat} allow the microtubule ends to spread more broadly through the domain, while high values result in substantial shortening of all microtubules.

We carry out simulations with dynamic microtubules, focusing on the mean time to capture by microtubule plus-ends for particles starting at the distal tip of the cell. Due to the coupling between the longest microtubule length and the end clustering, an optimum value of $k_{\mathrm{cat}} \approx 0.007\mathrm{s}^{-1}$ emerges for minimizing capture time (Fig. 4.6b). For this value, the longest microtubules are still able to reach the distal tip of the cell, but other microtubule ends remain relatively well scattered over a broad span of the distal region, as indicated by an average clustering metric of $d \approx 0.14$ (Fig. 4.6c). This optimal catastrophe rate is within the range of the measured values ($0.006 - 0.04\mathrm{s}^{-1}$) in a variety of cellular systems [140]. The existence of an optimal catastrophe rate of this order of magnitude has previously been established in quantitative models of 'search-and-capture' of mitotic kinetochores by the plus-ends of dynamically growing

and shrinking microtubules [134, 136].

We note that the absolute values for the capture times are substantially lower when microtubule dynamics are included in the simulation (Fig.4.6b, inset). This difference arises from a combination of two effects. First, growing microtubule ends sweep through the domain, tending to pick up any particles that have meandered away from the distal region. Second, the ability of dynamic microtubules to sample several configurations over the hundred-second timescale of particle capture makes it more likely that some microtubule end will encounter the particle, precluding the occasional very long trajectories associated with particles having to return to the distal end for capture. These results emphasize the importance of microtubule dynamics for efficient capture not only of stationary targets [136, 147] but also of vesicular organelles destined for retrograde transport [135].

Despite the overall faster capture times, the dynamic model reproduces the overall features of optimal microtubule end configurations for particle capture. The existence of an optimal catastrophe rate further highlights the balance between allowing a few microtubules to stretch to the distal end of the cell while retaining a broad distribution of microtubule ends throughout the domain.

4.4.4 Microtubule arrangements in *Aspergillus nidulans*

The theoretical work described here provides guiding principles for the performance of different microtubule architectures in capturing cargo. A logical avenue for further study would be to quantify microtubule configurations in actual cellular domains, and to compare the distributions observed with the features identified for optimal capture. To this end, we image hyphae of the fungus *Aspergillus nidulans* and visualize microtubule plus-ends along the hyphal axis.

A. nidulans is a filamentous fungus that forms multinuclear tubular projections (hyphae). Owing to its genetic tractability and simplified geometry, *A. nidulans* has been used as a model organism for studies of microtubule-based transport [8, 12, 86]. In the hyphal region beyond the

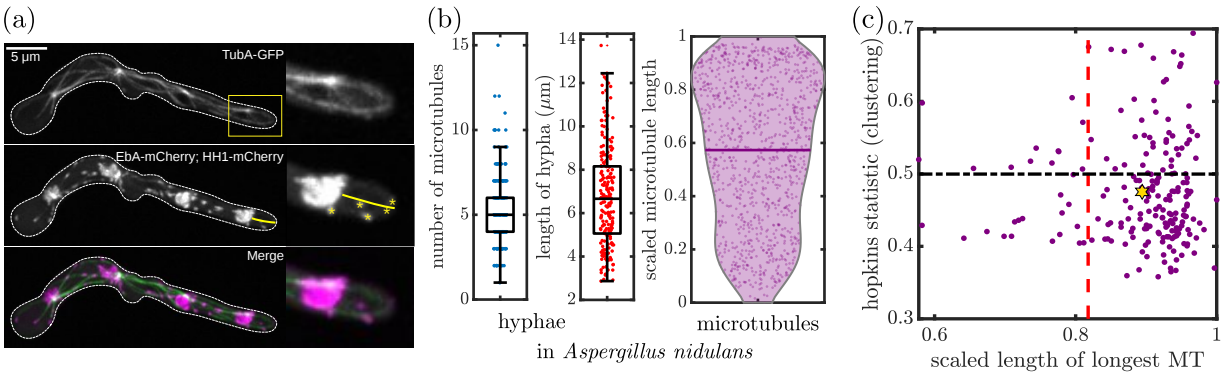

Figure 4.7: **Microtubule configurations in *Aspergillus nidulans* hyphae (a)** Micrographs of *A. nidulans* germlings expressing fluorescently tagged tubulin (TubA-GFP, top), plus-end binding protein EbA/EB1 (EbA-mCherry), and nuclei (HH1-mCherry, middle panel). White dotted line shows the outline of the hypha. Yellow box denotes the cropped region shown on the right. Yellow line denotes measured length between hyphal tip and closest nucleus. Yellow asterisks denote EB1 plus-ends. **(b)** Number of microtubules (left), hypha length (center), and scaled microtubule length (right) for $n = 210$ hyphal tip regions. Microtubule lengths are scaled by the length of the corresponding region from the last nucleus to the cell tip. **(c)** Scatter plot showing the scaled length of the longest microtubule, and the clustering metric for hyphal microtubule configurations. The mean value for these metrics is indicated by the green point (scaled longest MT 0.89 ± 0.005; clustering metric $d = 0.073 \pm 0.002$). The vertical red line (0.82 ± 0.0002) and the horizontal black line (0.09 ± 0.00004) denote the average value of each corresponding metric for 10^6 uniformly sampled configurations. All intervals and error bars correspond to mean $\pm$ standard error.

most distal nucleus, microtubules form parallel, polarized arrangements, with plus-ends growing towards the distal tip [8]. The distal hyphal segment is on the order of 10μm in length and 1μm in radius [17, 151], allowing it to be approximated as a narrow, effectively one-dimensional tubular region. Endosomes carrying signaling particles are thought to initiate primarily at the distal tip [152, 153], while other organelles, such as peroxisomes, may form by fission or budding from the endoplasmic reticulum throughout the hyphal axis [154].

A. nidulans germlings (spores that have recently germinated to form hyphae) expressing GFP-tagged microtubules (tubulin TubA-GFP), mCherry-tagged microtubule plus-ends (microtubule plus-end associated protein EB1 [EbA]-mCherry), and mCherry-tagged nuclei (histone H1 [HH1]-mCherry) were imaged using spinning disk confocal microscopy (details in Appendix C). Sections of the hypha extending from the last nucleus to the cell tip were chosen for analysis.

Hyphal length from nucleus to tip was determined by tracing a line along the axis from the end of the last nucleus to the cell tip (Fig. 4.7a, left). Microtubule plus-ends were enumerated by counting EbA-mCherry puncta within the region beyond the last nucleus (Fig. 4.7a, right). Finally, lengths of microtubules were estimated by projecting the locations of the EbA-mCherry puncta along the traced hyphal axis (yellow line in Fig. 4.7a).

Based on data from $n = 210$ hyphae, the average length of the region from the last nucleus to the tip was $6.76 \pm 0.16 \mu$m (s.e.m.). Each post-nuclear hypha region contained 5.13 ± 0.15 (s.e.m.) microtubules with an average length of $4.15 \pm 0.08 \mu$m (s.e.m.). Fig. 4.7b shows the distributions of the observed hypha and microtubule lengths. Due to the large variability in cell size, we scale microtubule lengths with respect to the length of the individual hypha. For all hyphae, scaled length of the longest microtubule and the minimal-distance clustering metric for microtubule plus-end positions is calculated and plotted in Fig. 4.7c.

We compare microtubule arrangements in *A. nidulans* to the null hypothesis of microtubule ends scattered uniformly throughout the domain. This comparison helps identify non-uniform features of the microtubule distribution which can then be compared to our computational predictions for optimal arrangements. To this end, we generate 10^6 randomly sampled microtubule configurations. Each configuration has a number of microtubules drawn from the distribution observed in *A. nidulans* hyphae (Fig. 4.7b, left), with each scaled microtubule length selected uniformly at random (between 0 and 1). The longest microtubule length and the clustering metric is computed for each random configuration, and the average values are plotted as dashed lines on Fig. 4.7c.

The quantification of observed hyphal microtubule configurations demonstrated substantial differences from the null hypothesis of uniformly distributed random configurations. Namely, the mean scaled length of the longest microtubule was significantly longer than the value that would be expected for uniform architectures ($p < 0.001$ from one-sided t-test). Furthermore, the mean clustering metric for *A. nidulans* microtubules (0.073 ± 0.002) is significantly lower

than the 0.09 ± 0.00004 value for random configurations ($p < 0.001$ from one-sided t-test). It should be noted, by contrast, that configurations selected specifically for long microtubules would be expected to have a clustering metric substantially above the uniformly distributed value, due to accumulation of multiple plus-ends at the distal tip. These comparisons indicate that microtubule arrangements in *A. nidulans* hyphae tend to have one long microtubule, with the remaining plus-ends broadly distributed throughout the domain. These features match the optimal configuration predicted from the computational model for particle capture at plus-ends. The hyphal measurements highlight the fact that microtubules exhibit a distinctly non-uniform, yet non-clustered, length distribution that should lead to efficient capture of both particles entering at the cell tip and those produced throughout the entire hypha.

4.5 Conclusions

We have employed analytical modeling and computational simulations to highlight the role of microtubule arrangements in capturing cargo within tubular cells. For cargo entering at the distal end of the cell and captured at microtubule plus-ends, we show that spreading capture regions away from the entry point results in faster engagement with microtubules. The effect of cell size on such optimal arrangements is explored, revealing that for cell lengths on the order of 10μm, it is optimal to distribute microtubule ends over up to 25% of the axial length. In longer cells, it becomes advantageous to cluster the plus-ends over a relatively smaller fraction of the domain.

By analyzing random microtubule configurations, we establish general principles for rapid cargo capture across various scenarios for initial cargo distribution and capture modality. We show that configurations with a single long microtubule reaching the cell tip, accompanied by broad dispersal of the remaining microtubule ends, are ideal for rapidly capturing a variety of cargo. Such distributions can be established by tuning microtubule catastrophe rates as highlighted by

simulations of cargo capture in a minimal model of dynamic microtubules. Notably, our results emphasize that an intermediate catastrophe rate is optimal for capture not just because it allows for more rapid microtubule dynamics [134, 136] but also because it enables a broader steady-state distribution of microtubule plus-ends.

Finally, we image microtubules in *A. nidulans* hyphae and show that their length distributions follow the general principles for optimality laid down by our model. These results highlight novel aspects of cytoskeletal organization and its impact on cargo capture, providing possible mechanisms to establish optimal arrangements and validating predictions using *in vivo* data.

A central challenge for microtubule organization in a cell is the necessity for a single cytoskeletal architecture to serve as a transport highway for a variety of different cargos with different transport objectives. In this study, we focused specifically on the retrograde delivery of cargo to the nuclear region. However, other cargos require delivery from the nucleus to the periphery or broad distribution throughout the cellular domain. These alternate objectives impose different utility functions on the possible microtubule configurations. For directed delivery, long microtubules enable cargo to be deposited close to the distal tip, but axial separation of microtubule end positions has been shown to promote retention at the tip by reducing the recirculation of entrained cytoplasmic fluid [155]. For broad distribution of bidirectionally moving cargo, short microtubules may reduce the processive run-time of directed transport [138], resulting in increased frequency of reversals and more rapid distribution of cargo [87]. Architectures with short microtubules of mixed polarity can also enable dispersion of cargos whose motion is dominated by a single motor type, as observed in the proximal regions of mammalian dendrites [156]. The analytically tractable 1D modeling approach and 3D simulations developed here can be extended in future work to consider the impact of microtubule length distributions on this broad variety of intracellular transport systems.

By delineating the role of microtubule arrangements in individual transport processes, we can begin to gain a comprehensive picture of the evolutionary pressures guiding the observed

microtubule architectures in live cells. Furthermore, establishing the impact of cytoskeletal morphology on the efficiency of key transport objectives is critical to developing a predictive understanding of how pharmacological or genetic perturbations in cytoskeletal filament length modulate cellular functions.

4.6 Acknowledgements

We thank Eric Griffis and the UCSD Nikon Imaging Center for assistance with imaging.

Chapter 4, in full, is submitted for publication of the material. S. S. Mogre, J. R. Christensen, S. L. Reck-Peterson, and E. F. Koslover. The dissertation author was the primary author of this paper.

Chapter 5

Modeling Organelle Interaction and Maturation Processes in Autophagy

5.1 Abstract

Macroautophagy is a key process involved in neuronal homeostasis and degradation of cellular waste. Neuronal autophagosomes form constitutively in the distal tip of the axon and must transport to the soma to recycle their cargo. Cargo turnover requires autophagosomes to fuse with lysosomes to acquire degradative enzymes and lower their pH. However, the timing and number of these fusion events in the axon have proven difficult to detect using microscopy alone. Here we generate a theoretical model that reproduces data from live and fixed imaging of primary hippocampal neurons, and find that lysosome-autophagosome fusion likely occurs independently of autophagosomal motility in the axon. Endogenous staining for lysosomal enzymes and the v-ATPase indicates endolysosomes in the distal axon are relatively mature and our computational model suggests autophagosome maturation requires only a single fusion event in the axon, making breakdown of the inner autophagosomal membrane the rate-limiting step. These results clarify the timing and importance of lysosomal fusion for autophagosome maturation in axons.

5.2 Introduction

Neurons are terminally differentiated cells that last throughout the lifetime of the organism. One important pathway for maintaining cellular health and homeostasis over this long time period is macroautophagy (hereafter: autophagy), the formation of “self-eating" double-membraned organelles that engulf and degrade cellular waste [157]. Neuronal autophagy defects are implicated in most neurodegenerative disorders including Parkinson’s disease, Alzheimer’s disease, and Amyotrophic Lateral Sclerosis (ALS) [158] and genetically blocking autophagosome formation causes neurodegeneration in mice [159, 160]. It is thus important to understand the specifics of this process and how it pertains to neuronal health.

Neuronal autophagosomes form primarily in the distal tip of the axon, where they clear dysfunctional proteins, aggregates, and organelles from the presynaptic region [14]. However, the vast majority of protein and organelle production occurs in the soma [161–163]. Thus, autophagosomes must traverse the length of the axon, up to 1m in humans, to turnover and recycle their cargo [164, 165]. Initially autophagosomes undergo diffusive or bidirectional transport in the tip while engulfing cargo and closing their membranes, then they acquire microtubule motors and motor-regulating proteins and switch to robust retrograde motility towards the soma [166, 167]. During this transport, axonal autophagosomes mature by fusing with late endosomes and lysosomes, which are formed in the soma and actively delivered to the axon [14, 162, 167]. Fusion is necessary for the autophagosome to acquire degradative enzymes and establish the low pH at which they function. The maturation of autophagosomes during transport from the axonal tip to the soma is a well-studied phenomenon; however, there is a lack of studies exploring the quantitative aspects of autophagosome maturation in relation to transport or interactions with lysosomes.

In this work, we focus on the interplay between axonal transport of autophagosomes and autophagosomal maturation, two primary components of neuronal autophagy (Fig. 5.1 a).

Using a combination of analytical and computational approaches, we construct a comprehensive model of organelle transport, interactions, and maturation during the axonal autophagy. Our model reproduces features of organelle distribution and maturation as observed in primary hippocampal neurons, highlighting the role of dynamic parameters in regulating these quantities. Staining for endogenous lysosomal and autophagosomal markers indicates roughly half of axonal autophagosomes fuse with a lysosomal structure prior to exit from the distal tip, and further that the majority of lysosomes in the distal tip actually contain both degradative enzymes and at least one vacuolar ATPase to establish and maintain the acidic pH necessary for degradation. However, autophagosomes in the axon mature very slowly, with only about a quarter in the proximal axon demonstrating a fully acidified lumen. We show that the observations from experimental data may arise from a fusion-independent motility switching process, coupled with slow degradation of autophagosomal contents. Our results shed light on possible mechanisms that can regulate organelle dynamics, and contribute to a quantitative understanding of cellular organization in neuronal autophagy.

5.3 Results

5.3.1 Autophagosome Maturation in Axons as a Two-Step Process

Studies in primary dorsal root ganglion (DRG) and hippocampal neurons and *in vivo* have established that autophagic vacuoles (AVs) initiate near the distal axonal tip and mature via endolysosomal fusion during transport towards the soma [14, 167, 168]. However, the reported extent and spatiotemporal distribution of the maturation process vary widely between different cell types and measurement modalities (Fig. 5.1b).

Characterizing AV maturation is complicated in part by the multiple different possibilities for defining a mature state. Markers of maturity include the acquisition of specific membrane proteins, the acidification of the AV interior, and the presence and activity of degradative enzymes

Figure 5.1: **Double-membraned autophagosomes mature during transport from the distal tip of the axon to the soma.** **(a)** Autophagic vesicles (AVs) form *de novo* near the axonal tip, remaining stationary or engaging in transient diffusive or bidirectional motion. A switch to retrograde motion occurs at a rate k_s, resulting in persistent motion towards the soma at a velocity v_p. Lysosomes formed near the soma and moving with a velocity v_y can fuse with the AV, resulting in increased acidification and activation of degradative enzymes. **(b)** Multiple studies have investigated the maturation of AVs along the axon, using a variety of techniques. Depending on technique and cell type, the results vary widely. **(c)** When AVs fuse with endolysosomes, the endolysosome's contents enter the intermembrane space and its membrane proteins remain in the outer membrane. Following breakdown of the inner autophagosomal membrane (IAM), the autophagic cargo is exposed to the lysosomal proteases and subject to degradation. **(d)** Some methods of determining autophagosomal maturity detect more immature AVs than others. Colocalization with endolysosomal membrane proteins, LysoTracker dye colabelling, and fluorescence of enzymatic activity reporters all effectively show whether or not fusion with an endolysosome has occured, but do not clearly say anything about whether the IAM has been degraded and/or whether the autophagosomal cargo are undergoing degratation. However, because it is initially protected by the IAM, the quenched EGFP moiety of the mCherry(mCh)-EGFP-LC3 reporter labels specifically fully matured and acidified AVs wherein cargo is undergoing degradation. **(e)** Left, example kymograph showing LC3 in the AV lumen and lysotracker in the interlumenal space. Right, plotting LysoTracker colabelling and mCh-GFP quenching together illustrates the large difference in rates of fusion and IAM breakdown in hippocampal neurons.

(a)

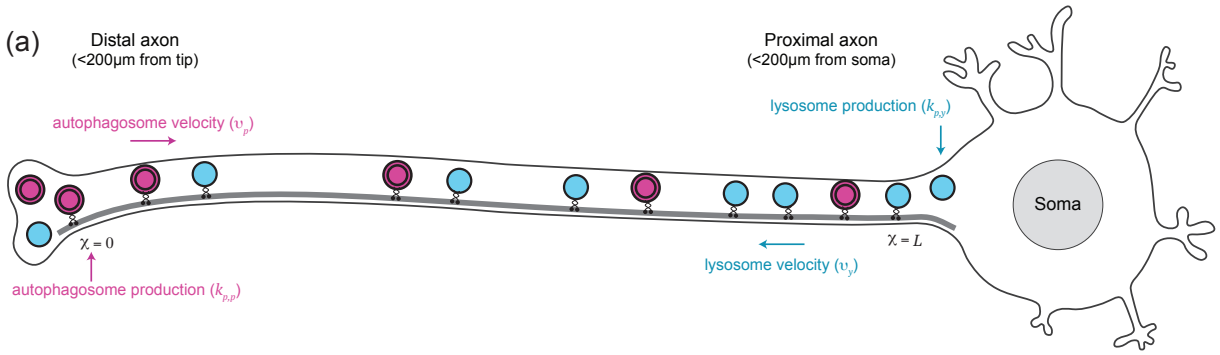

(b)

Cell type	Maturity measurement method	Distal maturity	Proximal maturity	Study/Group
Dorsal root ganglia (primary)	Rab7 colocalization	~95%	~95% (along the axon shaft)	Cheng…Sheng, 2015, JCB
Dorsal root ganglia (primary)	LAMP1 colocalization	~10%	~97% (along the axon shaft)	Maday…Holzbaur, 2012, JCB
Dorsal root ganglia (primary)	LysoTracker colabelling	~35%	~96% (along the axon shaft)	Maday…Holzbaur, 2012, JCB
Dorsal root ganglia (primary)	active glucocerebrosidase (MDW941)	~80%	not reported	Farfel-Becker…Sheng, 2019, Cell Reports
Cortical (primary)	active Cathepsin L or D (Magic Red)	~100%	not reported	Farfel-Becker…Sheng, 2019, Cell Reports
Hippocampal (primary)	Rab7 colocalization	~90%	~90%	Cason…Holzbaur, 2021, JCB
Hippocampal (primary)	LAMP1 colocalization	~85%	~100%	Cason…Holzbaur, 2021, JCB
Hippocampal (primary)	LysoTracker colabelling	~60%	~90%	Cason…Holzbaur, 2021, JCB
Dorsal root ganglia (primary)	mCh-EGFP-LC3 (% GFP quenched)	~50%	~70%	Maday…Holzbaur, 2012, JCB
Cortical (iPSC-derived)	mCh-EGFP-LC3 (% GFP quenched)	~10%	~40%	Boecker…Holzbaur, 2021, Curr. Biol.
Hippocampal (primary)	mCh-EGFP-LC3 (% GFP quenched)	~5%	~25%	Cason…Holzbaur, 2021, JCB

(c)

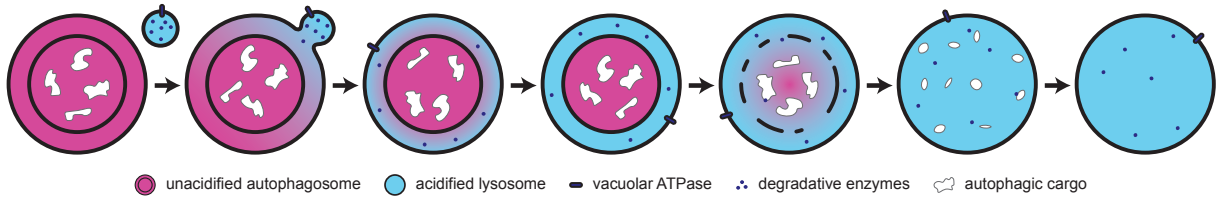

(d)

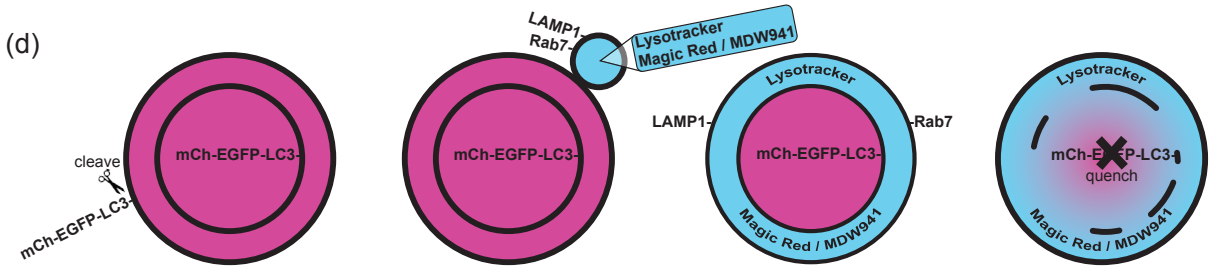

(e)

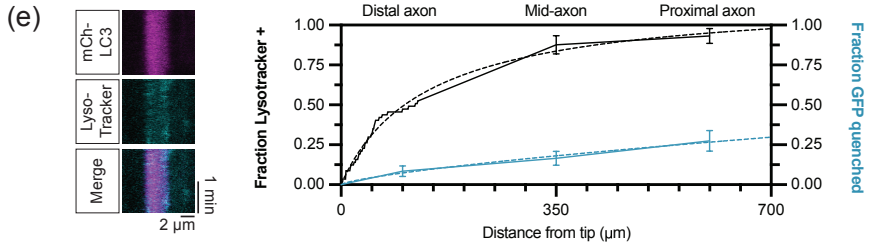

within the AVs. These different markers are not necessarily acquired simultaneously, and may well appear at different rates or in different cellular locations, depending on cell type.

Initial work in DRGs suggested that AV maturation occurs quickly in the distal tip, demonstrated by the colocalization between autophagosomal marker LC3 (microtubule associated protein 1 light chain 3) and late endosomal marker Rab7 (Ras-like protein in brain 7) or lysosomal marker LAMP1 (lysosome-associated membrane protein 1) [14]. Additionally, about 50% of the LC3+ AVs detected in the distal tips of DRGs colabeled for the dye LysoTracker, which specifically labels acidic membrane-bound organelles. Similarly about half of distal AVs appeared acidified based on fluorescence of the dual-color LC3 reporter mCherry (mCh)-EGFP-LC3. This reporter fluoresces in the red and green wavelengths in nonacidified environments, but only red in acidic environments due to the quenching of the EGFP moiety below pH 5.8 [169, 170]. In the proximal axonal regions, roughly 75% of AVs show quenching of the EGFP. These results in DRG neurons imply rapid fusion with lysosomal vesicles and concomitant acidification shortly after AV production in the distal region, followed by a small amount of further maturation during the journey towards the proximal axon.

Measurements in primary cortical neurons also showed the presence of degradative enzyme activity in distal AVs, based on the fluorogenic activity sensors Magic Red and MDW941 [162]. Live-imaging in primary hippocampal neurons confirmed the finding that LC3+ puncta colocalize robustly with Rab7 and LAMP1 in the distal axon and colabel with LysoTracker [167]. However, use of the mCh-EGFP-LC3 reporter in primary hippocampal neurons revealed much slower acidification, with almost no AVs in the distal axon and only $\sim 25\%$ of those in the proximal axons showing acidity-triggered EGFP quenching [167]. Slow acidification is also seen in iPSC-derived cortical i^3 neurons, where only about 40% of AVs were GFP negative in the proximal axon [171]. Overall, measurements in these cell types indicate a discrepancy between different markers of maturation in different cellular locations. AVs appear to acquire some features of maturity while still in the distal axon, while others are observed primarily in the

proximal region.

The double-membraned nature of AVs is key to reconciling these seemingly disparate observations (Fig. 5.1c). When an AV and endolysosome fuse, the endolysosomal membrane becomes part of the outer membrane and the contents of the endolysosomal lumen become part of the intermembrane space. Thus any degradative enzymes and H^+ ions in the endolysosome reside in the space between the outer and inner membranes until the inner autophagosomal membrane (IAM) is broken down, exposing the central lumen to enzymatic degradation. While LC3 colocalization with LysoTracker or fluorogenic enzyme activity sensors gives the impression of a fully mature autolysosome with active cargo degradation occuring, in fact these structures may well still have their inner membrane intact, confining any acidity or enzymatic activity to the intermembrane space. In non-neuronal cells including mouse fibroblasts, Lysotracker can actually be visualized specifically localizing to the intermembrane space and then collapsing inward when the IAM is degraded [172]. Unfortunately, axonal AVs are condensed due to the narrow diameter of the axon and rarely appear as rings after leaving the tip, making this intermembrane space and inner membrane collapse difficult to resolve. Nevertheless, we can occasionally resolve LysoTracker localizating to the intermembrane space in axons (Fig. 5.1e).

Unlike LysoTracker, MagicRed, and MDW941, the tandem mCh-EGFP-LC3 marker localizes specifically to the inner lumen of the AV (Fig. 5.1 d). Initially LC3 localizes to both the inner and outer membranes, conjugated to the lipid phosphatidylethanolamine so the protein extends into the lumen on the inner membrane and into the cytosol on the outer membrane. The protein extending into the cytosol is rapidly cleaved by the autophagy protease ATG4 leaving only the lumenal protein, and fluorophores, intact. Once the AV is closed, GFP-LC3 never recovers following photobleaching, confirming the lumenal state of the LC3 signal [14]. Therefore quenching of the EGFP moiety can be used as a more specific readout of autophagosomal maturity, indicating the point at which the inner membrane breaks down and the lumenal LC3 and other cargo are exposed to the lysosomal pH and enzymes (Fig. 5.1e).

Overall, AV maturation can thus be thought of as a two-step process. The first step involves fusion with one or more endolysosomes to acquire degradative enzymes and trigger acidification of the intermembrane space. Given that LysoTracker marking occurs at similar levels to the presence of endolysosomal membrane markers, the acidification of the intermembrane space can be assumed to occur rapidly upon fusion. The second, slower, step involves breakdown of the inner autophagosomal membrane to enable the enzymes and acidic environment to reach the lumen.

The two-step maturation process can largely account for the disparate data observed in prior studies. Based on live-cell experiments, AVs in cortical neurons (either primary or iPSC-derived) and hippocampal neurons fuse with endolysosomes in the distal tip, as indicated by Rab7, LAMP1, LysoTracker, MagicRed, and MDW941 colocalization [162, 171]. However, only 8-10% have broken down their inner membrane and therefore fully matured within the first 200μm of the axon, indicated by mCh-EGFP-LC3 fluorescence [167, 171]. However, AVs in DRG neurons not only fuse in the distal axon with endolysosomes, as indicated by Rab7, LAMP1, and LysoTracker colocalization, but also rapidly break down their inner membrane while still in the distal region, as determined by quenching of the EGFP moeity of mCh-EGFP-LC3 [14, 15]. We may thus hypothesize that AVs in the central nervous system (CNS) breakdown their inner membrane more slowly than AVs in the peripheral nervous system (PNS).

Using the mCh-EGFP-LC3 marker as a readout of IAM breakdown, we can also reconcile the differences observed between GFP quenching and LysoTracker labeling, two techniques that both measure acidification. The levels of LysoTracker colabeling ($\approx$ 40% in the distal axon and $\approx$ 95% in the proximal axon) and GFP quenching ($\approx$ 50% in the distal axon and $\approx$ 70% in the proximal axon) more or less agree in DRG neurons, suggesting a short time between fusion and IAM degradation, perhaps comparable to the 6.6 minutes observed in mouse fibroblasts. However, in hippocampal neurons, LysoTracker colabeling ($\approx$ 60% in the distal axon and $\approx$ 90% in the proximal axon) and GFP quenching ($\approx$ 5% in the distal axon and $\approx$ 25% in the proximal axon)

are drastically different, suggesting a long time between fusion and IAM degradation.

Using additional live-cell measurements alongside mathematical modeling, we proceed to explore quantitatively the kinetics and relative spatial distribution of the two steps (fusion and inner membrane break-down) of the phagosome maturation process.

5.3.2 Spatial Distribution of Autophagosome Maturation in Hippocampal Neurons

Most of the studies above thus describe a system in which nearly all neuronal AVs *in vitro* fuse with endolysosomes in the distal tip of the axon, then mature as they transit along the axon, with those in PNS axons degrading their IAM rapidly and those in the CNS degrading their IAM 3-4x more slowly. However, work from Maday and colleages [14] demonstrates a delay in the initial fusion event. It is worth noting in all the other studies, LC3 and/or Rab7/LAMP1 were overexpresssed; however, Maday et al. used cells from GFP-LC3 knock-in mice where LC3 was being expressed at endogenous levels. It is therefore possible that the high amount of early fusion seen in the other studies is an overexpression artifact.

We therefore carried out rigorous immunofluorescence measurements to determine spatial distribution of fusion throughout the axon under entirely endogenous expression conditions. We chose to conduct this experiment in primary hippocampal neurons because the CNS is more impacted by neurodegenerative diseases and hippocampal preparations yield a more homogenous population of cells than do cortical preparations. In brief, primary rat hippocampals dissected at embryonic day 18 were fixed in Bouin's solution at 7 days *in vitro*, permeabilized in methanol, then probed with primary and secondary antibodies to detect AVs and lysosomes. This experiment, while unable to detect IAM degradation, provides a readout of initial AV-lysosome fusion unperturbed by overexpression.

We initially quantified the total number of LC3+ and LAMP1+ puncta per 30μm of axon in either the distal (within $\approx 200\mu$m of the axon tip) and proximal (within $\approx 200\mu$m of the

Figure 5.2: **Autophagosomes fuse with lysosomes in the distal axon absent overexpression.** (a) Number of LC3+ puncta per 30μm in the distal and proximal axon. (b) Histogram showing the spatial distribution of LC3+ puncta in the distal axon. (c) Number of LAMP1+ puncta per 30μm in the distal and proximal axon. (b) Histogram showing the spatial distribution of LAMP1+ puncta in the distal axon. (e) & (h) Micrographs showing LC3+ and LAMP1+ puncta in the distal and proximal axon respectively. The merged micrograph shows LC3+ puncta colocalized with LAMP1+ puncta. (f) Cumulative fraction of LC3+ puncta colocalized with LAMP1. (g) Fraction of LC3+ puncta colocalized with LAMP1 in distal and proximal axons. (i) & (l) Micrographs showing LC3+ and AEP+ puncta in the distal and proximal axon respectively. The merged micrograph shows LC3+ puncta colocalized with AEP+ puncta. (j) Cumulative fraction of LC3+ puncta colocalized with AEP. (k) Fraction of LC3+ puncta colocalized with AEP in distal and proximal axons. (m) & (p) Micrographs showing LC3+ and CathepsinL+ puncta in the distal and proximal axon respectively. The merged micrograph shows LC3+ puncta colocalized with CathepsinL+ puncta. (n) Cumulative fraction of LC3+ puncta colocalized with AEP. (o) Fraction of LC3+ puncta colocalized with CathepsinL in distal and proximal axons. (q) & (t) Micrographs showing LC3+ and ATP6V1F+ puncta in the distal and proximal axon respectively. The merged micrograph shows LC3+ puncta colocalized with ATP6V1F+ puncta. (r) Cumulative fraction of LC3+ puncta colocalized with ATP6V1F. (s) Fraction of LC3+ puncta colocalized with ATP6V1F in distal and proximal axons.

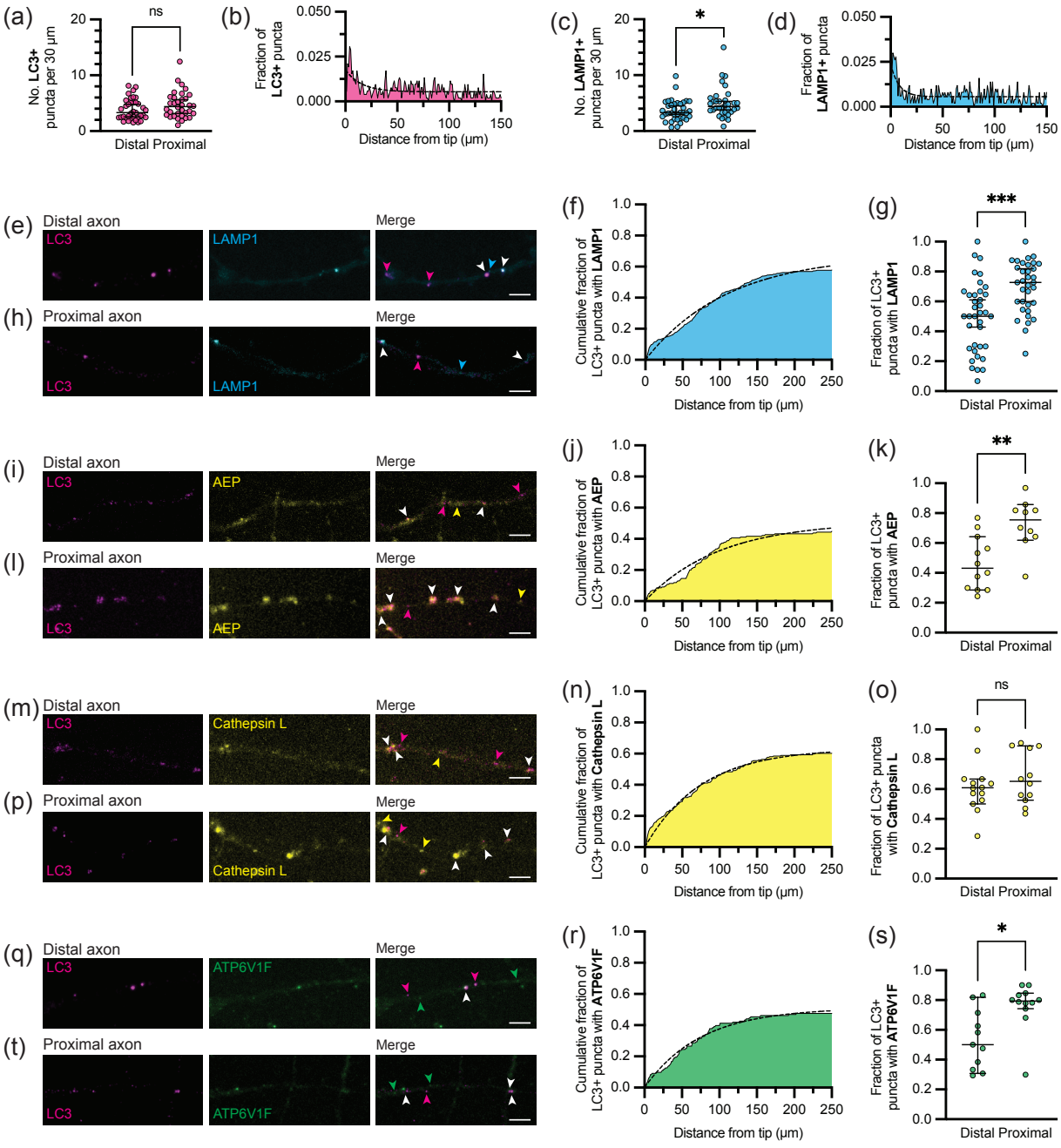
(a)
ns
No. LC3+ puncta per 30 µm
Distal Proximal
(b)
Fraction of LC3+ puncta
Distance from tip (µm)
(c)
*
No. LAMP1+ puncta per 30 µm
Distal Proximal
(d)
Fraction of LAMP1+ puncta
Distance from tip (µm)
(e)
Distal axon
LC3
LAMP1
Merge
(h)
Proximal axon
LC3
LAMP1
Merge
(f)
Cumulative fraction of LC3+ puncta with LAMP1
Distance from tip (µm)
(g)
***
Fraction of LC3+ puncta with LAMP1
Distal Proximal
(i)
Distal axon
LC3
AEP
Merge
(l)
Proximal axon
LC3
AEP
Merge
(j)
Cumulative fraction of LC3+ puncta with AEP
Distance from tip (µm)
(k)
**
Fraction of LC3+ puncta with AEP
Distal Proximal
(m)
Distal axon
LC3
Cathepsin L
Merge
(p)
Proximal axon
LC3
Cathepsin L
Merge
(n)
Cumulative fraction of LC3+ puncta with Cathepsin L
Distance from tip (µm)
(o)
ns
Fraction of LC3+ puncta with Cathepsin L
Distal Proximal
(q)
Distal axon
LC3
ATP6V1F
Merge
(t)
Proximal axon
LC3
ATP6V1F
Merge
(r)
Cumulative fraction of LC3+ puncta with ATP6V1F
Distance from tip (µm)
(s)
*
Fraction of LC3+ puncta with ATP6V1F
Distal Proximal

soma) region (Fig. 5.1a) and found similar distributions for both (Fig. 5.2, a-d). The density of lysosomes in the proximal region is slightly higher than in the distal region (Fig. 5.2 c), while AV density does not change significantly between the two regions (Fig. 5.2 a). In the distal region both organelles accumulated in the tip/growth cone, where the LC3+ puncta are likely represent biogenesis events and nascent AVs that have not yet begun retrograde transport (Fig. 5.2, b and d).

Next we quantified colocalization between the markers and found that roughly half of the AVs in the distal axon colocalized with LAMP1 which, given our resolution (200nm), likely represent fused or fusing vesicles (Fig. 5.2, e-f). Likewise, about half of the lysosomes in the distal axon colocalized with LC3.A higher number of AVs were positive for LAMP1 in the proximal axon. Thus, an additional $\approx 25\%$ of AVs fused with a lysosome in the axon shaft after exiting the distal end (Fig. 5.2 g).

In addition to LAMP1, LC3 colocalized with lysosomal enzymes Asparagine endopeptidase (AEP) and Cathepsin L in the distal axon (Fig. 5.2, i-p). Like LAMP1 colocalization, AEP colocalization increased in the proximal axon (Fig. 5.2 k). Both enzymes and LAMP1 were acquired by AVs within the first 150μm, as demonstrated by the plateau in the cumulative fractions (Fig. 5.2, j and n), suggesting the majority of the fusion events occur within that region.

Finally, lysosomal proteases require low pH to function, so we tested for the presence of an activated vacuolar ATPase (vATPase) by measuring colocalization with a V1 subunit. The V1 subunit of the vATPase is cytoplasmic and forms an activated vATPase, which pumps protons across a membrane to decrease pH, when interacting with a transmembrane V0 subunit. Therefore colocalization between the V1 subunit (ATP6V1F) and membrane-bound LC3 suggests the formation of an active vATPase. Again, roughly half of the LC3 puncta in the distal axon colocalized with ATP6V1F, the V1 subunit seemed to be acquired within the first 150μm of axon, and an additional $\approx 30\%$ of AVs appeared to fuse with V1+ vesicles along the axon shaft (Fig. 5.2, q-t).

Importantly, LAMP1 acquisition was strongly associated with both degradative enzyme

acquisition and vATPase acquisition, suggesting the lysosomes with which the AVs fused were degradatively competent. While some studies agree that competent lysosomes are present in the distal axon, others have found that lysosomes far from the nucleus are more immature and not degradtively active. We therefore measured the degradative capacity of the lysosomes by measuring the colocalization between LAMP1 and AEP, Cathepsin L, or ATP6V1F. Three-quarters of the LAMP1 puncta colocalized with the other markers in the distal axon, indicating the population of lysosomes is primarily mature. Further, LAMP1 colocalization with either lysosomal enzymes or the vATPase did not increase in the proximal axon, in contrast with other studies that find lysosomes closer to the soma are more degradative. Thus, at endogenous expression levels, we find the majority of lysosomes throughout the axon are degradatively competent. Further, it is worth noting that we saw very few instances where an LC3 punctum colocalized with LAMP1 but not AEP, Cathepsin L, or ATP6V1F, suggesting the AVs are specifically fusing with the competent lysosomes ($\approx 75\%$ of the population) and not with the immature lysosomes. We therefore conclude that $\approx 50\%$ of AVs fuse with degradatively competent lysosomes in the first 150μm of axon, $\approx 25\%$ fuse as they move along the axon shaft prior to the proximal axon, and $\approx 25\%$ enter the soma without having ever fused with a lysosome.

5.3.3 Autophagosome-lysosome fusion can be described by a minimal mathematical model

We next proceed to develop a minimalist mathematical model for the first step of the AV maturation process: the fusion of autophagosomes and endolysosomes. The model is parameterized against experimental data and aims to elucidate how organelle transport and interaction parameters dictate the spatial distribution of autophagosome maturation. The second step of inner-membrane degradation is introduced into the model framework in a subsequent section.

Because axons are much longer than they are wide, we focus primarily on dynamics in

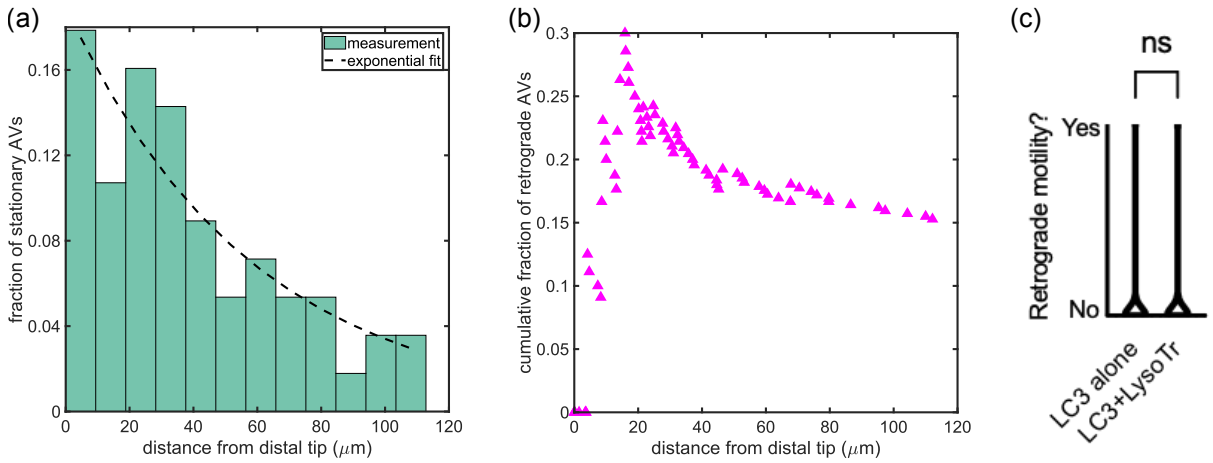

Figure 5.3: (a) distribution of stationary AV (for fitting lambda – initial biogenesis position). (b) fraction retrograde in the distal axon (either cumulative fraction vs x or just dots for individual cells). (c) distal fraction retrograde with and without LysoTracker label, indicating motility independent of fusion.

the axial direction. This allows us to simplify the model system to a one-dimensional domain of length $L = 700\mu$m, representing the typical length of primary hippocampal axons at 7-8 days *in vitro*, a common time-point used in transport studies [173]. Our model includes the biogenesis of AVs and lysosomes in the distal axonal region and in the soma respectively, along with their motion and interactions. Details and model assumptions are provided within the methods section.

In our model, lysosomes are produced at the proximal end near the soma with rate k_{py}. Upon biogenesis, lysosomes immediately move in the anterograde direction towards the axonal tip at a constant velocity $v_y = 2\mu$m/s [173]. AVs are formed at rate k_{pp} in the distal axon. The spatial distribution of AV formation is taken to be exponential ($H(x) \sim e^{-x/\lambda}$), where x is the distance from the distal tip. The characteristic length scale for AV biogenesis positions is taken to be $\lambda = 100\mu$m, based on the observed distribution of stationary autophagosomes.

After formation, AVs remain stationary until switching to retrograde motility with a fixed switching rate k_s. The retrograde motion of AVs occurs with a fixed velocity $v_p = 0.75\mu$m/s [173]. While past descriptions of axonal autophagosome dynamics implied that fusion with an endolysosome was a prerequisite for switching to retrograde motility, our measurements imply that a

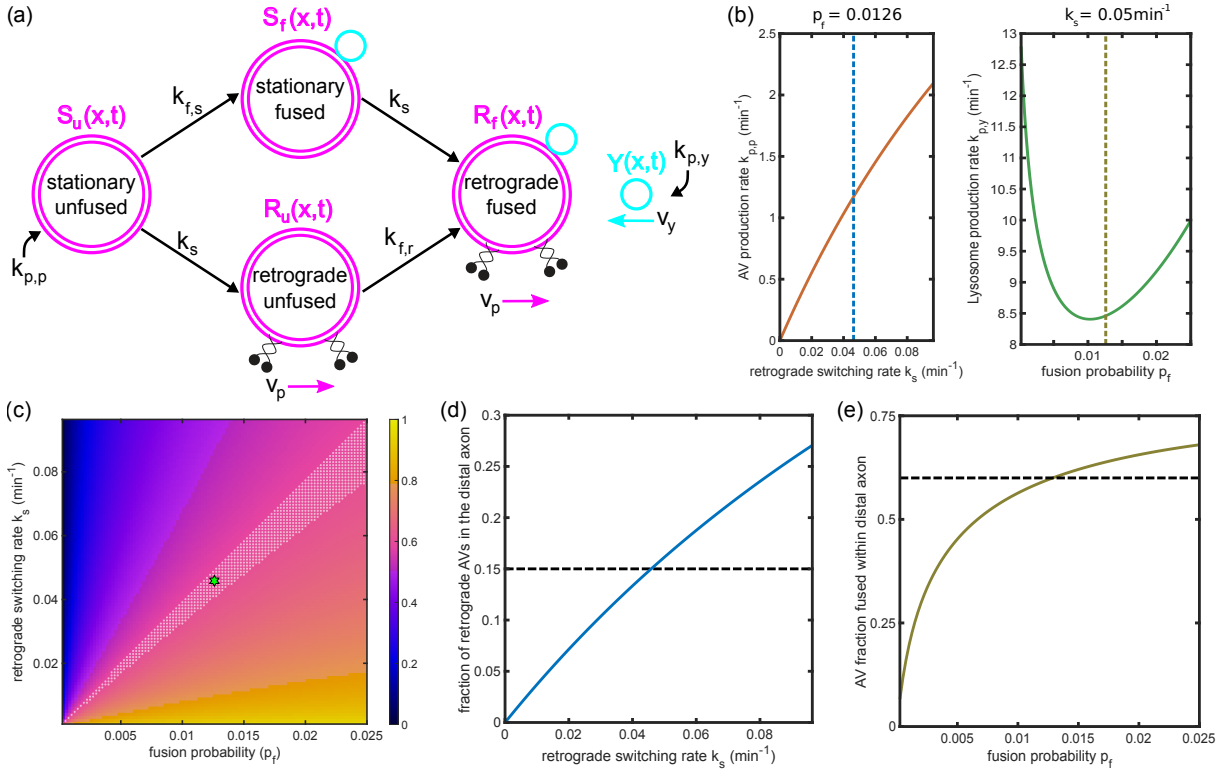

Figure 5.4: **Minimal model for autophagosome-lysosome interaction dynamics.** **(a)** Schematic of the model. **(b)** (left) AV production rate $k_{p,p}$ required to match the average linear density of LC3+ puncta observed within the distal axon of hippocampal neurons, plotted against the switching rate k_s. The dashed line denotes the switching rate matched in (d).(right) Lysosome production rate $k_{p,y}$ required to match the average linear density of LAMP1+ puncta observed within the distal axon of hippocampal neurons, plotted against the fusion probability p_f. The dashed line denotes the fusion probability matched in (e). **(c)** Overall fraction of AVs fused within the distal axon f_F, plotted against the fusion probability p_f, and the retrograde switching rate k_s. The gray region denotes values of f_F within 2.5% of the observed measurement. The green star denotes a parameter combination matching the fraction of retrograde AVs. **(d)** Overall fraction of AVs exhibiting retrograde motility within the distal axon, plotted against the switching rate k_s. The observed fraction within the distal axon of hippocampal neurons is denoted by the dashed black line. **(e)** Overall fraction of AVs fused within the distal axon, plotted against the fusion probability p_f. The dashed line denotes the experimentally measured value determined from LC3+ puncta colocalized with LAMP1+ puncta in hippocampal neurons.

substantial fraction ($\sim 20\%$) of autophagosomes reach the proximal axon without having acquired lysosomal markers (Fig. 5.2g). While we cannot rule out some dependence of the motility switch upon the AV maturation state, we initially assume a single constant switching rate to maintain model simplicity.

Each time a lysosome passes an AV, a fusion event can occur with a probability p_f. Again for simplicity, we assume this fusion probability is constant, independent of organelle position along the axon and of AV motility state. Upon fusion, the endolysosome disappears, and the autophagosome is marked as one where fusion has occurred. In this model formulation, prior fusions are assumed to have no effect on the ability of the AV to fuse with subsequent endolysosomes.

The dynamics of this system can be probed by stochastic agent-based simulations that track the movement and fusion of individual organelles. More efficiently, we can describe the system behavior via a set of mean-field dynamic equations for the spatial distribution of organelles with different states of fusion and motility (Fig. 5.4a). Namely, $Y(x,t)$ describes the distribution of endolysosomes; S_u and S_f give the distribution of un-fused and fused stationary AVs, respectively; R_u and R_f give the analogous distributions for retrograde AVs. At spatial position x, the rate at which fusion events occur is proportional to the density of lysosomes and AVs, as well as a rate constant k_f. The probability that fusion occurs during passage depends both on this rate constant and the time it takes for the two organelles to pass each other. Thus for fusion with a stationary AV we set $p_f = 1 - e^{-k_{f,s}\tau_s}$ where $\tau_s = \ell/v_y$ is the passage time and $\ell = 1\mu$m gives the range within which the two organelles can overlap, equivalent to the sum of their diameters. An analogous expression gives the fusion rate $k_{f,r}$ for a retrograde autophagosome, based on $\tau_r = \ell/(v_y + v_p)$.

The dynamic mean-field equations are then given by:

$$\frac{\partial}{\partial t}S_u(x,t) = k_{p,p}H(x,t) - k_s S_u(x,t) - \ell k_{f,s} Y(x,t) S_u(x,t), \tag{5.1a}$$

$$\frac{\partial}{\partial t}S_f(x,t) = \ell k_{f,s} Y(x,t) S_u(x,t) - k_s S_f(x,t), \tag{5.1b}$$

$$\frac{\partial}{\partial t}R_u(x,t) = k_s S_u(x,t) - \ell k_{f,r} Y(x,t) R_u(x,t) - v_p \frac{\partial}{\partial x}R_u(x,t), \tag{5.1c}$$

$$\frac{\partial}{\partial t}R_f(x,t) = k_s S_f(x,t) + \ell k_{f,r} Y(x,t) R_u(x,t) - v_p \frac{\partial}{\partial x}R_f(x,t), \tag{5.1d}$$

$$\frac{\partial}{\partial t}Y(x,t) = v_y \frac{\partial}{\partial x}Y(x,t) - \ell \left[k_{f,r}(R_u + R_f) + k_{f,s}(S_u + S_f)\right] Y(x,t). \tag{5.1e}$$

The boundary conditions for this system are

$$\begin{aligned} v_y Y(L,t) &= k_{p,y}, \\ R_{u/f}(0,t) &= 0. \end{aligned} \tag{5.2}$$

Equations 5.1 and 5.2 are solved to obtain organelle distributions at steady state, as described in the Methods. Parameters used for the model are noted in Table 5.1. For equivalent parameter values, the mean-field model accurately reproduces stochastic simulations with discrete interacting organelles.

Our minimal model of organelle dynamics involves four free parameters, namely, the AV production rate $k_{p,p}$, the lysosome production rate $k_{p,y}$, the probability of fusion p_f, and the rate of switching to retrograde motility k_s. We establish the relevant values of these parameters by comparing to robust experimentally accessible metrics. Specifically, we set the production rates $k_{p,p/y}$ in order to match the measured linear density of AVs and endolysosomes in the distal axon (defined as the the region within 250μm from the distal tip). The distal density of AVs is found to be $\rho_P = 0.13 \pm 0.01 \mu\text{m}^{-1}$ and the distal density of puncta with endolysosomal markers is $\rho_Y = 0.14 \pm 0.02 \mu\text{m}^{-1}$ (Fig. 5.2a & 5.2b respectively). The density ρ_Y includes all unfused endolysosomes, as well as all AVs that are in the fused state.

The production rates that fit the experimentally measured densities vary dependending on the parameters p_f and k_s (Fig. 5.4b). Notably, higher switching rates (k_s) require an increase in the AV production rate to give the same experimentally observed average distal density. This is because faster switching to the retrograde state decreases the total time AVs spend in the domain, so that more of them must be produced to maintain a particular steady-state density. For the lysosomal production rate, higher fusion probabilities require more lysosomes to be produced to maintain the observed density ρ_Y. At low fusion probabilities, most lysosomes pass out of the domain without fusing, so that again a higher production rate is necessary to maintain the same density.

An additional metric of interest is the fraction of distal AVs that are in the fused state. In Fig. 5.4b we plot this fraction as a function of the remaining free parameters (k_s and p_f). Unsurprisingly, the fused fraction increases with the fusion probability p_f. Furthermore, it increases at lower values of the switching rate k_s. Low switching rates imply lower AV production, and the higher ratio of lysosome to AV production results in a greater overall fraction of fused AVs in the distal zone. The grey region in Fig. 5.4b indicates the experimentally measured value of the distal fused fraction $f_F = 0.53 \pm 0.04$, defined here as the fraction of LC3+ puncta colocalizing with the LAMP1 marker (Fig. 5.2f). This experimental measurement substantially narrows the region of feasible parameter values.

The fourth experimentally accessible metric used to parameterize the model is the fraction of distal AVs in the retrograde motility state. This quantity is measured by manual classification of mCh-EGFP-LC3 puncta in live hippocampal cells, giving $f_R = 0.15 \pm 0.05$ (Fig. 5.3). This metric is dependent primarily on the switching rate k_s according to

$$f_R = \frac{e^{x_d/\lambda}(\lambda - x_d) - \lambda}{e^{x_d/\lambda}(\lambda - x_d - v_p/k_s) - (\lambda - v_p/k_s)},$$

where $x_d = 250\mu$m is the boundary of the distal region. The extracted value for parameters

specified in Table 5.1 is $k_s = 0.05\text{min}^{-1}$. This corresponds to each AV persisting in the stationary state for an average of 20min after its biogenesis, including all initial steps of formation after the point when the LC3 marker is present.

For this fixed value of switching rate, a narrow range of fusion probabilities corresponds to the observed fraction of fused AVs in the distal region (Fig. 5.4c). Namely, we find $p_f \approx 0.013 \pm 0.04$, indicating that a very small fraction of passage events between an endolysosome and an autophagosome is expected to lead to successful fusion.

The four experimentally measured metrics (ρ_P, ρ_Y, f_R, f_S) thus allow us to set the four free parameters in our model: $k_s \approx 0.05\text{min}^{-1}, p_f \approx 0.013, k_{p,p} = 1.16\text{min}^{-1}$ and $k_{p,y} = 8.47\text{min}^{-1}$. Furthermore, the minimalist nature of the model allows for a quantitative understanding for how variation of each of these parameters will alter the expected fusion and motility state of the AVs. In the subsequent section we highlight the model predictions regarding the distribution of organelles and fusion events.

5.3.4 Dynamic model predicts quantitative features of organelle distributions

We use the parameterized mean-field model described in the previous section to predict specific features of the spatial distribution for organelles and fusion events. Furthermore, stochastic simulations with the same set of parameters are used to both validate the mean-field approximation and to facilitate visualization of the organelle distributions.

Firstly, we plot the expected density of puncta with autophagosome and endolysosome markers in the distal axon (Fig. 5.5a). Notably, the “LAMP1+ puncta" in our model correspond to both unfused lysosomes and phagosomes that have undergone at least one fusion event. The predicted densities decrease away from the distal axonal tip, as observed in measurements on hippocampal neurons (Fig. 5.2b,d).

We next consider the fraction of AVs that have undergone a fusion event, at different

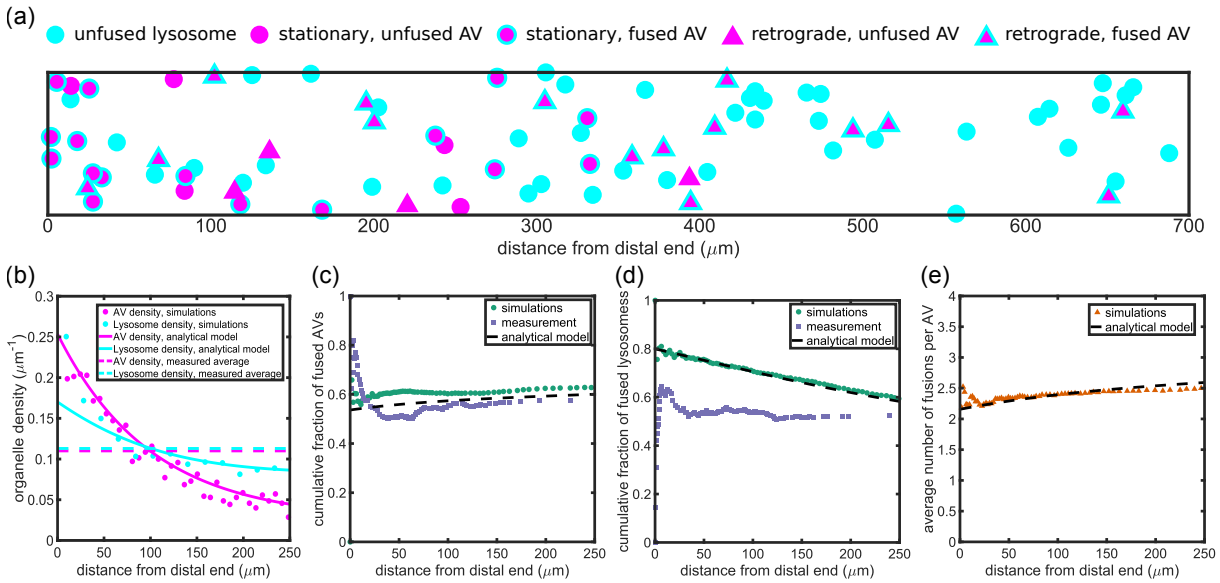

Figure 5.5: **Minimal model predicts quantitative features of organelle interactions.(a)** A snapshot of the simulation of organelle dynamics at steady state. Distances along the horizontal direction are to scale. The vertical direction and organelle sizes are not to scale. **(b)** Linear density of organelles plotted against the distance from the distal tip. Predictions from simulations and analytical modeling are denoted by dots and solid lines respectively. Average organelle densities measured in the distal hippocampal axon are denoted by dashed lines. **(c)** Cumulative fraction of fused AVs plotted against the distance from the distal tip. The green circles denote predictions from explicit simulations, the purple squares denote measurements from colocalization of LC3+ puncta with LAMP1+ puncta in the the distal hippocampal axon. The dashed line denotes predictions from the analytic model. **(d)** Cumulative fraction of fused lysosomes plotted against the distance from the distal tip. The green circles denote predictions from explicit simulations, the purple squares denote measurements from colocalization of LAMP1+ puncta with LC3+ puncta in the the distal hippocampal axon. The dashed line denotes predictions from the analytic model. **(e)** The average number of fusions among AVs that have fused at least once plotted against the distance from the distal tip. The orange triangles denote the prediction from simulations, the dashed line denotes the prediction from the analytic model.

positions along the distal region (Fig. 5.5b). The mathematical model and simulations predict that the fraction of AVs which have fused is largely constant whether one looks at the first few dozen micrometers of the distal tip or the entire 250μm distal region. This result implies that most AVs undergo their first fusion in the far distal tip at their biogenesis location rather than acquiring the endolysosomal markers as they move along their retrograde journey. In fact, simulations with these model parameters indicate that 81% of autophagosomes undergo fusion before switching to a retrograde state. We note that this effect does not require that retrograde motion be specifically

triggered by a fusion event as was assumed in past work [15], but rather is a consequence of the long time spent by each phagosome in a stationary state, making fusion likely to occur before motility switching.

An alternate model would allow the switch to retrograde motion to occur only for AVs that have fused with at least one endolysosome. Such a model can be parameterized against the same experimental measurements and gives very similar predictions for distribution of organelles and the fraction of AVs fused. This is unsurprising, since the base model already has most of the autophagosomes carry on fusion before initiating retrograde motion. Notably, however, the two models give different predictions for the fraction of autophagosomes that are fused within the proximal region. In the base model, approximately 84% of AVs found within 250μm of the soma are expected to carry lysosomal markers, similar to experimental measurements (Fig. 5.2g). In the model where retrograde motility is triggered by fusion, this number jumps up to nearly 100%, since the only way for an autophagosome to reach the soma is to have first fused and become mobile. Hence, the presence of unfused AVs in the proximal axon is consistent with the base model where retrograde motility is independent of fusion.

5.3.5 Few fusion events are sufficient to achieve observed autophagosome maturation

One of the advantages of mathematical modeling is that it can enable us to assess features of the system which are difficult to measure experimentally. While colocalization of various markers allows the determination of whether an AV has fused with at least one endolysosome, such data gives no indication of how many endolysosomes fuse into a single AV. Past descriptions of AV maturation have generally assumed multiple fusion events with endolysosomes as the autophagosome moves down the axon. However, recent data indicates that markers for the transmembrane SNARE protein Stx17 no longer colocalize with LC3+ AV puncta once the inner membrane has broken down (as assessed by EGFP quenching) [174]. Such measurements

imply that maturation of the AV may correspond to an inability to fuse with subsequent passing endolysosomes.

We consider two extreme models for the ability of AVs to undergo multiple fusions. The model described thus far allows for unlimited fusions, with the fusion probability p_f taken to be independent of the AV maturity. In principle, this model allows for a “snow-ball" effect, where a single AV can pick up many endolysosomes during its journey down an axon, leaving a paucity of lysosomal organelles that are able to reach the distal tip. We can compute a spatial density of fusion events at steady state according to:

$$\begin{aligned} Z_s(x) &= \ell \left(\frac{k_{f,s}}{k_{s,u}} \right) Y(x) \left[S_u(x) + S_f(x) \right] \\ \frac{d}{dx} Z_r(x) &= \left(\frac{k_s}{v_p} \right) Z_s(x) + \ell \left(\frac{k_{f,r}}{v_p} \right) Y(x) \left[R_u(x) + R_f(x) \right], \end{aligned} \tag{5.3}$$

where $Z_s(x)$ and $Z_r(x)$ are the distributions of number of fusion events among stationary and retrograde AVs respectively. Normalizing by the AV density gives the average number of fusion events per particle among AVs that are present at each position along the axon [$N_f(x) = (Z_s + Z_r)/(S_u + S_f + R_u + R_f)$]. This quantity is plotted in Fig. 5.5e. Given the low fusion probability in the parameterized model ($p_f \approx 0.013$), we expect an average of only ~ 2.5 fusion events per AV throughout the distal region. Thus each individual autophagosome is expected to fuse with only a small number of endolysosomes, despite the lack of any built-in mechanism for limiting the number of fusions in this model.

An alternate extreme scenario is one where each AV is allowed to fuse with only a single endolysosome and further fusions are prohibited. The dynamics of such a "one-and-done" model are described by the same set of equations given in Eq. 5.1, with the exception of the endolysosome consumption depending only on unfused AVs. The resulting parameters that match experimental measurements are very similar to the original model with unlimited fusions. The only substantial difference is in the production rate for endolysosomes, which is found to be

30% lower in the one-and-done model to yield the same distal density of puncta with lysosomal markers. This shift is expected since there are fewer fusion events that decrease the number of such puncta in the "one-and-done" model. The model predictions for this case, in terms of the spatial distribution of fused and unfused puncta, are virtually unchanged from the case with unlimited fusions.

Overall, our measurements of the distributions for AV and endolysosomal puncta do not permit us to differentiate whether each AV can fuse with only one lysosome or with an unlimited quantity of them. However, the mathematical model indicates that the actual number of fusions for each AV is expected to be quite small, even without an explicit mechanism to limit subsequent fusion.

5.3.6 Spatial profile of autophagosome membrane breakdown is consistent with slow degradation

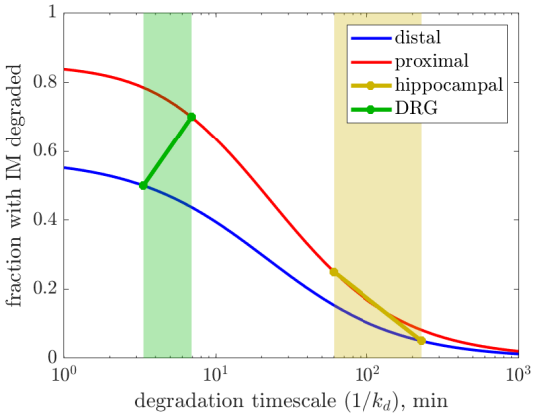

Figure 5.6: **Modeling IAM degradation** Modeled fraction of f_d of autophagosome with degraded inner membrane, plotted as a function of the degradation time ($\tau_d = 1/k_d$). Densities are averages over the most distal (blue) and most proximal (red) 250μm regions of a modeled axon of length 700μm. Parameters used in the model are the same ones extracted from Fig. 5.4. The range of degradation times corresponding to measured values of f_d are shown in yellow for hippocampal neurons and green for DRG neurons.

Having established and parameterized a spatial model for the first step of autophagosome

maturation (fusion with endolysosomes), we next proceed to consider the second step in the maturation process. This step involves break-down of the AV inner membrane, which occurs after the acquisition of degradative enzymes via a fusion event, corresponding to the experimentally measured quenching of the EGFP fluorophore in the AV lumen (Fig. 5.1d). For simplicity, we assume that IAM membrane degradation is a constant rate process, occurring with rate constant k_d for all AVs that are in the fused state. We define additional dynamic equations to account for the degradation step:

$$\frac{dR_f^{(i)}}{dt} = k_s S_f^{(i)} + \ell k_{f,r} Y R_u^{(i)} - v_p \frac{\partial}{\partial x} R_f^{(i)} - k_d R_f^{(w)} \tag{5.4a}$$

$$\frac{dR_f^{(d)}}{dt} = k_s S_f^{(d)} + \ell k_{f,r} Y R_u^{(d)} - v_p \frac{\partial}{\partial x} R_f^{(d)} + k_d R_f^{(w)} \tag{5.4b}$$

$$\frac{dS_f^{(i)}}{dt} = -k_s S_f^{(i)} + \ell k_{f,s} Y S_u^{(i)} - k_d S_f^{(i)} \tag{5.4c}$$

$$\frac{dS_f^{(d)}}{dt} = -k_s S_f^{(d)} + \ell k_{f,s} Y S_u^{(d)} + k_d S_f^{(i)}. \tag{5.4d}$$

Here, the superscript (i) refers to an AV with an intact inner membrane and the superscript (d) refers to one where the inner membrane has been degraded. The total densities $R_f = R_f^{(i)} + R_f^{(d)}$ and $S_f = S_f^{(i)} + S_f^{(d)}$ still obey the basic model equations (Eq. 5.1).

For any given value of the decay rate k_d, we can compute the local fraction of AV puncta expected to exhibit a degraded IAM according to $f_d = (R_f^{(d)} + S_f^{(d)})/(R_f + S_f + R_u + S_u)$. The distal value of f_d is obtained by averaging all densities in the numerator and denominator over the first 250μm from the distal tip. Similarly, the proximal fraction is found by averaging over the last 250μm near the soma.

The distal and proximal degraded fractions are plotted in Fig. 5.6 as a function the average degradation time $\tau_d = 1/k_d$. These calculations allow us to extract an estimate for the degradation time-scale in hippocampal neurons, which have a distal value of $f_d^{(\text{dist})} \approx 0.05$ and a proximal value $f_d^{(\text{prox})} \approx 0.25$. This corresponds to a range of $\tau_d \approx 1-4$ hr. For DRG neurons, the measured

fractions with degraded IAM are $f_d^{(\mathrm{dist})} \approx 0.5$ and $f_d^{(\mathrm{dist})} \approx 0.7$ corresponding to a degradation time of $\tau_d \approx 4-6$ min.

Overall, these results highlight a potential difference between the AV maturation process in different neuronal cell types. In both cell types, the initial fusion events, acquisition of lysosomal markers, and acidification of the intermembrane space occur primarily at the distal tip. However, measurements in hippocampal neurons are consistent with a much slower degradation of the IAM, so that the majority of AVs reach the soma with an intact inner membrane.

5.4 Discussion

We have developed a model of organelle dynamics in autophagy to shed light on aspects of organelle interaction, maturation, and motility. Our model reproduces organelle densities in the axon, which were determined empirically here using staining for endogenous autophagosomal and lysosomal proteins. We also quantified the amount of fusion and degradative state of lysosomes and autophagosomes in primary hippocampal neurons in the absence of overexpression, which increased the fidelity of our model.

Additionally we performed a meta-analysis of previous studies that measured autophagosomal maturation in axons and highlighted important differences in the measurement techniques: while acquisition of endolysosomal membrane markers (Rab7, LAMP1), enzymatic activity reporters (Magic Red, MDW941), and LysoTracker convey important information about fusion, they are unable to determine whether or not the IAM has broken down and therefore whether or not the AV's cargo is undergoing degradation. Conversely, the use of markers that specifically localize to the inner lumen of the AV (mCh-EGFP-LC3) shed light on later stages of autophagosomal maturation, including IAM breakdown and lumen acidification.

In addition to predicting fusion likelihood and AV maturation in the axon, our model also provides insight on the coordination between fusion and motility switching by AVs. Using

kinetic modeling and simulations, we show that populations of retrograde AVs that have fused with lysosomes can arise from fusion-independent switching events for certain parameter ranges. Thus, while fusion is correlated with a switch to unidirectional transport towards the soma, the two events are independent.

Both autophagy and axonal transport are affected in neurodegeneration, making the study of this process invaluable for human disease. Our model can be leveraged to inform future experiments perturbing axonal transport and autophagosomal maturation in the context of neurodegeneration-causing mutations or protein aggregates, in addition to basic studies of the autophagy pathway in neurons. Using endogenous measurements of autophagosome maturation and computational modelling, we have reconciled multiple conflicting studies of autophagosome motility and maturation and quantitatively connected organellar transport and fusion.

5.5 Materials and Methods

5.5.1 Primary hippocampal culture

Sprague Dawley rat hippocampal neurons at embryonic day 18 were obtained from the Neurons R Us Culture Service Center at the University of Pennsylvania. Cells (proximity ligation assay, 40,000 cells on 7mm glass; live imaging, 200,000 cells on 20 mm glass) were plated in glass-bottom 35 mm dishes (MatTek) that were precoated with 0.5 mg/ml poly-L-lysine (Sigma Aldrich). Cells were initially plated in Attachment Media (MEM supplemented with 10% horse serum, 33 mM D-glucose, and 1 mM sodium pyruvate) which was replaced with Maintenance Media (Neurobasal [Gibco] supplemented with 33 mM D-glucose, 2 mM GlutaMAX (Invitrogen), 100 units/ml penicillin, 100 mg/ml streptomycin, and 2% B-27 [ThermoFisher]) after 5-20 h. Neurons were maintained at 37 C in a 5% CO2 incubator; cytosine arabinoside (Ara-C; final conc. 1 μM) was added the day after plating to prevent glia cell proliferation. Neurons (4-6 DIV) were transfected with 0.35–1.5 μg of total plasmid DNA using Lipofectamine 2000 Transfection

Reagent (ThermoFisher, 11668030) and incubated for 18-24 h.

5.5.2 Live-cell neuron imaging and analysis

One hour prior to imaging, HaloTag® ligands and/or most SNAP-tag® ligands were applied for 15 min at a final concentration of 100 nM, followed by a 30-45 min washout; SNAP-tag® ligand Blue 430 was applied for 30 min at a final concentration of 2 μM, followed by a 30 min washout. In applicable experiments, neurons were incubated with LysoTracker (25 nM) for 15-30 min, which was then removed for imaging. In applicable experiments, BafilomycinA1 (100 nM) or DMSO was added 2h prior to imaging, and then neurons were imaged in the third hour of continued treatment. Neurons were imaged in Imaging Media (HibernateE [Brain Bits] supplemented with 2% B27 and 33 mM D-glucose). Autophagosome behavior was monitored in the proximal (<100 μm from the soma), distal (<100 μm from the distal tip), or mid-axon of 6–8 DIV neurons imaged at a rate of 1 timepoints/sec for 2-3 min. Neurons were imaged in an environmental chamber at 37°C on a Perkin Elmer UltraView Vox spinning disk confocal on a Nikon Eclipse Ti Microscope with an Apochromat 100 x 1.49 numerical aperture (NA) oil-immersion objective and a Hamamatsu EMCCD C9100-50 camera driven by Volocity (PerkinElmer). Only cells expressing moderate levels of fluorescent proteins were imaged to avoid overexpression artifacts or aggregation. It should be noted that the quality of the primary neuron dissections affected autophagosomal motility, but compared conditions were always collected from the same dissections and imaging sessions.

Kymographs were generated in ImageJ (https://imagej.net/ImageJ2) using the MultiKymograph plugin (line width, 5) and analyzed either in ImageJ or using the MatLab program KymoSuite (J. Nirschl, University of Pennsylvania). Puncta were classified as either anterograde (moving $\geq$10μm towards the axon tip), retrograde (moving $\geq$10μm towards the soma), or stationary/bidirectional (net movement $\leq$10μm during the video). Because fluorescent LC3 is cytosolic (as well as punctate) and neurites occasionally crossed in culture, raw videos were referenced

throughout kymograph analysis to ensure only real puncta ($\geq$ 1.5 SD from the axon mean) were included in analyses. All comigration analyses were performed using kymographs. Line scans were generated for presentation purposes from raw video stills and normalized either within that line (for positive channels) or to the local region (for negative channels; surrounding 10μm area).

5.5.3 Immunofluorescence experiments and analysis

Neurons were fixed at 7 days *in vitro* for 30 minutes at room temperature using Bouin's solution supplemented with 8% sucrose and diluted 50% in maintenance media. Bouin's solution was then removed and the cells were washed in PBS before being stored for up to 6 months in PBS at 4°C. Cells were then permeabilized for 8 minutes at -20°C in methanol and washed in PBS, then blocked for 1 hour at room temperature in blocking solution (recipe). Primary and secondary antibodies (see Table 5.2 for maunfacturers and dilutions) were diluted in blocking solution and each left on cells for 1 hour at room temperature, with 3 x 5 min washes in PBS after each incubation. Cells were mounted in Prolong Gold (company) and imaged within 48 hours at 100x on the spinning disk confocal described above.

5.5.4 Statistics for cell-based experiments

All statistical analyses were performed in Prism (GraphPad, San Diego, CA). All error bars represent S.E.M. and n indicates the number of events or cells pooled across at least 3 trials per experiment. Parametric or nonparametric tests were used where appropriate, but formal testing was not performed. Statistical measures are described in the legends.

5.6 Acknowledgements

We thank Andrea Stavoe for insights and discussions.

Chapter 5, in full, is currently being prepared for submission for publication of the material. S. E. Cason, S. S. Mogre, E. L. F. Holzbaur, and E. F. Koslover. The dissertation author was a primary author of this paper.

Table 5.1: Parameters for modeling the dynamics of organelles in autophagy

Parameter	Type	Description	Value	Ref.
L	Fixed	Length of the domain	700μm	[173]
v_p	Fixed	Autophagosome velocity	0.75μm/s	[173]
v_y	Fixed	Lysosome velocity	2μm/s	[173]
r_p	Fixed	Autophagosome radius	400nm	[14]
r_y	Fixed	Lysosome radius	100nm	[14]
λ	Measurement	Autophagosome spawn length	100μm	This study
ρ_Y	Measurement	Average distal lysosome density	$0.11\mu\text{m}^{-1}$	This study
ρ_P	Measurement	Average distal AV density	$0.11\mu\text{m}^{-1}$	This study
f_R	Measurement	Distal fraction of retrograde AVs	0.15	This study
f_F	Measurement	Distal fraction of fused AVs	0.6	This study
$k_{p,p}$	Output	Autophagosome production rate	1.16min^{-1}	This study
$k_{p,y}$	Output	Lysosome production rate	8.47min^{-1}	This study
k_s	Output	Rate of switching to retrograde motility	0.05min^{-1}	This study
p_f	Output	Fusion probability	0.013	This study

Table 5.2: Manufacturers and dilutions for materials used in Chapter 5

Antibody	Host	Dilution	Manufacturer
anti-LC3	Mouse	1:250	Abcam ab48394

Appendix A

Propagators and first passage times for one-dimensional multimodal transport

A.1 Propagator for a one-dimensional halting creeper

We calculate the position distribution of a particle switching between diffusive transport with diffusivity D and processive motion with speed v. Switching between states is a Poisson process with rate γ for entering an active state and rate λ for leaving an active state (see Fig. 2.1). The overall spatial distribution can be obtained by a convolution of propagators for individual states, summed over all possible state transitions.

Starting at an intial position $x = 0$, the spatial distribution of a diffusive particle at a time t is

$$R_D(x,t) = \frac{1}{\sqrt{4\pi Dt}} e^{-\frac{x^2}{4Dt}}. \tag{A.1}$$

We define the joint distribution that the particle first switches to an active state at time t while at position x by,

$$H_D(x,t) = \gamma e^{-\gamma t} R_D(x,t). \tag{A.2}$$

A Fourier transform in space ($x \to k$), followed by a Laplace transform in time ($t \to s$) gives,

$$\widehat{\widetilde{H}}_D(k,s) = \frac{\gamma}{(\gamma + Dk^2 + s)}. \tag{A.3}$$

The position distribution of particles starting at $x = 0$ in the active state, moving with a velocity v at time t is given by

$$R_{\pm}(x,t) = \delta(x \mp vt). \tag{A.4}$$

The corresponding joint distribution for the time and location of switching from the active to the passive state is

$$H_{\pm}(x,t) = \lambda e^{-\lambda t}\delta(x \mp vt). \tag{A.5}$$

The Fourier and Laplace transformed distribution is given by

$$\widehat{\widetilde{H}}_{\pm}(k,s) = \frac{\lambda}{(\lambda + s \mp \mathrm{i}kv)}. \tag{A.6}$$

We define a “step" in the particle’s trajectory as a switch from the passive to the active state and back to the passive state again. If the particle starts in the passive state at zero time, the position and time distribution at the end of one such step can be expressed as

$$\begin{aligned} M(x,t) = \int_{-\infty}^{\infty} dx' \int_0^t dt'\, H_D(x',t') \\ \times \left[\frac{H_+(x-x',t-t') + H_-(x-x',t-t')}{2}\right], \end{aligned} \tag{A.7}$$

where the first term denotes a particle reaching x' at time t' via diffusion and the second term denotes the particle covering a distance $x - x'$ in the remaining time $t - t'$ by walking, integrated over all values of x' and t'. The Fourier and Laplace transformed function for the

propagation of the particle after a full step of active and passive motion is given by,

$$\widehat{\widetilde{M}}(k,s) = \widehat{\widetilde{H}}_D(k,s)\left(\frac{\widehat{\widetilde{H}}_+(k,s)+\widehat{\widetilde{H}}_-(k,s)}{2}\right). \tag{A.8}$$

To get the spatial propagator of a halting creeper particle that both starts and ends in a passive state, we sum over all possible paths between the active and passive states, convolved with the probability that the particle does not leave the passive state in the final time interval (given by $H_D(x,t)/\gamma$). The resulting expression for the propagator can then be expressed as:

$$\begin{aligned} G_{DD}(x,t) = \frac{H_D}{\gamma} &+ M *_{x,t}\left(\frac{H_D}{\gamma}\right) \\ &+ M *_{x,t} M *_{x,t}\left(\frac{H_D}{\gamma}\right) + ..., \end{aligned} \tag{A.9}$$

where $*_{x,t}$ denotes convolution with respect to x and t. The first term in the summation corresponds to a particle that never left the passive state, the second term to a particle that performs a single active step before returning to the passive state, the third term includes two active steps, and so forth. Applying a Fourier transform in space and a Laplace transform in time transforms the convolutions into a geometric series, leading to

$$\begin{aligned} \widehat{\widetilde{G}}_{DD}(k,s) &= \frac{\left(\frac{\widehat{\widetilde{H}}_D(k,s)}{\gamma}\right)}{1-\widehat{\widetilde{M}}(k,s)} \\ &= \frac{(s+\lambda)^2+k^2v^2}{(s+\gamma+Dk^2)\left((s+\lambda)^2+k^2v^2\right)-\gamma\lambda(s+\lambda)}, \end{aligned} \tag{A.10}$$

where the second line follows by substituting expressions from Eqs. A.3, A.8.

The distributions for the other quantities appearing in Eqs. 2.5, 2.6 of the main text can be derived similarly. The transformed distributions are:

$$
\begin{aligned}
\widehat{\widetilde{G}}_{DW} &= \frac{\gamma(s+\lambda)}{(s+\gamma+Dk^2)\left((s+\lambda)^2+k^2v^2\right)-\gamma\lambda(s+\lambda)} \\
\widehat{\widetilde{G}}_{WW} &= \frac{(s+\gamma+Dk^2)(s+\lambda)}{(s+\gamma+Dk^2)\left((s+\lambda)^2+k^2v^2\right)-\gamma\lambda(s+\lambda)} \\
\widehat{\widetilde{G}}_{WD} &= \frac{\lambda(s+\lambda)}{(s+\gamma+Dk^2)\left((s+\lambda)^2+k^2v^2\right)-\gamma\lambda(s+\lambda)} \\
\widehat{\widetilde{G}}_{\pm D} &= \frac{\lambda(s+\lambda\pm ikv)}{(s+\gamma+Dk^2)\left((s+\lambda)^2+k^2v^2\right)-\gamma\lambda(s+\lambda)} \\
\widehat{\widetilde{G}}_{\pm W} &= \frac{(s+\gamma+Dk^2)(s+\lambda\pm ikv)}{(s+\gamma+Dk^2)\left((s+\lambda)^2+k^2v^2\right)-\gamma\lambda(s+\lambda)}.
\end{aligned}
\tag{A.11}
$$

A linear combination of these distributions, weighted by the equilibrium fraction of particles in each state is used to derive the overall propagator in Eq. 2.1:

$$
\widehat{\widetilde{G}} = \frac{\gamma}{\gamma+\lambda}\left(\widehat{\widetilde{G}}_{WD}+\widehat{\widetilde{G}}_{WW}\right)+\frac{\lambda}{\gamma+\lambda}\left(\widehat{\widetilde{G}}_{DD}+\widehat{\widetilde{G}}_{DW}\right). \tag{A.12}
$$

The expressions obtained can be transformed back to real space and real time by a combination of analytical and numerical methods. To calculate the Laplace-transformed expressions in Eq. 2.5, 2.6, and 2.7 we invert the Fourier transform analytically as $\widehat{G}(x,s) = \frac{1}{2\pi}\int_{-\infty}^{\infty} e^{ikx}\widehat{\widetilde{G}}(k,s)\,dk$. The Laplace transform of the range and first passage time distribution can then be inverted numerically using Talbot's algorithm [63].

A.2 Equilibrium fraction of particles

For narrow tubular cells or a rapid transverse diffusivity ($D/R^2 \gg \gamma, k_b$), binding and walking events take much longer than the time required for particles to equilibrate throughout the cross section. In this limit, the effective rates of starting a walk or binding to a tether become $\alpha^2\gamma$ and $\alpha^2 k_b$, respectively, where $\alpha = a/R$. The governing equations for the fraction of particles in

each state are then given by,

$$\begin{aligned}
\frac{df_{\text{walk}}}{dt} &= \gamma f_{\text{bound}} + \alpha^2 \gamma f_{\text{diff}} - \lambda f_{\text{walk}}, \\
\frac{df_{\text{bound}}}{dt} &= \alpha^2 k_b f_{\text{diff}} - (k_u + \gamma) f_{\text{bound}}, \\
\frac{df_{\text{diff}}}{dt} &= k_u f_{\text{bound}} + \lambda f_{\text{walk}} - \alpha^2 (k_b + \gamma) f_{\text{diff}}, \\
f_{\text{diff}} + f_{\text{walk}} + f_{\text{bound}} &= 1.
\end{aligned} \tag{A.13}$$

The time derivatives vanish in the steady state, reducing Eq. A.13 to a system of linear equations which can be solved to obtain,

$$\begin{aligned}
f_{\text{walk}} &= \frac{\gamma\alpha^2}{\gamma\alpha^2 + \lambda\left(\frac{\alpha^2 k_b + \gamma + k_u}{k_b + \gamma + k_u}\right)} \\
f_{\text{diff}} &= \frac{\lambda\left(\frac{\gamma + k_u}{k_b + \gamma + k_u}\right)}{\gamma\alpha^2 + \lambda\left(\frac{\alpha^2 k_b + \gamma + k_u}{k_b + \gamma + k_u}\right)} \\
f_{\text{bound}} &= \frac{\lambda\left(\frac{\alpha^2 k_b}{k_b + \gamma + k_u}\right)}{\gamma\alpha^2 + \lambda\left(\frac{\alpha^2 k_b + \gamma + k_u}{k_b + \gamma + k_u}\right)}.
\end{aligned} \tag{A.14}$$

A.3 Analytical model for multimodal transport in a cylinder, with tethering

In this section we develop the full analytical model for axial transport in a cylinder of radius $R = 1$ for particles capable of passive diffusion with diffusivity D, of initiating active processive walks with a rate γ while within a region of radius α of the central axis, and of entering a stationary tethered state with binding rate k_b while in the same region. The rate constant for unbinding from a tethered state is k_u and for transitioning between an active walk and passive diffusion is λ (see Fig. 2.6(a) for illustration of the model). For ease of the derivation, all length units in this section as well as Appendix A.4 are non-dimensionalized by the cylinder radius R

and all time units are nondimensionalized by R/v where v is the processive velocity of actively walking particles. We give our final results in fully dimensional units to facilitate comparison with other sections of the manuscript.

Our model is developed in an analogous manner to the approach previously used for modeling facilitated diffusion by DNA-binding proteins that occurs via a combination of 3D diffusion and 1D sliding along a filament [175]. We describe the particle motion by a system of individual states with Markovian transitions between them. The rates of transition between the states are time-varying, depending specifically on the time interval since the particle first entered the state. These states (Fig. A.1) consist of: a tethered state (h), a walking state (w), a state (n) wherein the particle started at radius $\alpha-\varepsilon$ and has remained within a radius α, a state (n_u) where the particle started uniformly distributed within radius α and has remained within that inner region, a state (f) where the particle started at radius $\alpha+\varepsilon$ and has remained outside the inner region at a radius greater than α and a state f_u where the particle started uniformly distributed in the outer region and has remained in the outer region. When computing statistics for the overall motion of the particle, we take the limit $\varepsilon \to 0$. The axial propagation of a particle in states n, n_u, f, f_u is given by the propagator function for diffusive motion $R_D(x,t)$ (Eq. A.1). The axial propagation in state w is given by $\frac{1}{2}[R_+(x,t)+R_-(x,t)]$ (Eq. A.4).

We construct a transition matrix of propagators $\mathbf{H}$, where $H_{a,b}(x,t)$ is the joint probability density for the time and position of a particle initially at the origin in state a making its first transition out of that state, into state b. A Fourier transform in space $x \to k$ and a Laplace transform in time $t \to s$ is carried out to yield the transformed propagator $\hat{\tilde{\mathbf{H}}}(k,s)$. The components of this propagator matrix are derived from the Laplace-transformed solutions for first passage times to an inner or outer absorbing boundary for a particle diffusing in a cylindrical domain [176]. For

instance, the transition propagator from the n state to the f state is given by,

$$\begin{aligned} H_{nf}(x,t) &= e^{-(k_b+\gamma)t} J_{nf}(t) R_D(x,t) \\ \widetilde{H}_{nf}(k,t) &= e^{-(k_b+\gamma-Dk^2)t} J_{nf}(t) \\ \widehat{\widetilde{H}}_{nf}(k,s) &= \hat{J}_{nf}(s+k_b+\gamma+Dk^2), \end{aligned} \tag{A.15}$$

where $J(t)$ is the distribution of times for a diffusive particle starting at radius $\alpha-\varepsilon$ to exit to an absorbing cylindrical boundary at radius α. The full matrix of components is listed below:

$$\begin{aligned} \widehat{\widetilde{H}}_{f_u,n} &= \frac{2\alpha}{(1-\alpha^2)\sigma_D} \frac{I_1(\sigma_D)K_1(\alpha\sigma_D) - I_1(\alpha\sigma_D)K_1(\sigma_D)}{I_0(\alpha\sigma_D)K_1(\sigma_D) + K_0(\alpha\sigma_D)I_1(\sigma_D)}, \\ \widehat{\widetilde{H}}_{f,n} &= \frac{I_0((\alpha+\varepsilon)\sigma_D)K_1(\sigma_D) + K_0((\alpha+\varepsilon)\sigma_D)I_1(\sigma_D)}{I_0(\alpha\sigma_D)K_1(\sigma_D) + K_0(\alpha\sigma_D)I_1(\sigma_D)}, \\ \widehat{\widetilde{H}}_{n_u,f} &= \frac{2}{\alpha\sigma_b} \frac{I_1(\alpha\sigma_b)}{I_0(\alpha\sigma_b)}, \quad \widehat{\widetilde{H}}_{n,f} = \frac{I_0((\alpha-\varepsilon)\sigma_b)}{I_0(\alpha\sigma_b)} \\ \widehat{\widetilde{H}}_{n_u,w} &= \frac{\gamma}{D\sigma_b^2}\left(1-\widehat{\widetilde{H}}_{n_u,f}\right), \quad \widehat{\widetilde{H}}_{n,w} = \frac{\gamma}{D\sigma_b^2}\left(1-\widehat{\widetilde{H}}_{n,f}\right) \\ \widehat{\widetilde{H}}_{n_u,h} &= \frac{k_b}{D\sigma_b^2}\left(1-\widehat{\widetilde{H}}_{n_u,f}\right), \quad \widehat{\widetilde{H}}_{n,h} = \frac{k_b}{D\sigma_b^2}\left(1-\widehat{\widetilde{H}}_{n,f}\right) \\ \widehat{\widetilde{H}}_{h,w} &= \frac{\gamma}{s+\gamma+k_u}, \quad \widehat{\widetilde{H}}_{h,n_u} = \frac{k_u}{s+\gamma+k_u} \\ \widehat{\widetilde{H}}_{w,n_u} &= \frac{\lambda(s+\lambda)}{(s+\lambda)^2+k^2}, \end{aligned} \tag{A.16}$$

where $\sigma_D = \sqrt{(s+Dk^2)/D}$, $\sigma_b = \sqrt{(s+\gamma+k_b+Dk^2)/D}$ and I_ν, K_ν are the modified Bessel functions of order ν of the first and second kind, respectively. All other components of $\widehat{\widetilde{\mathbf{H}}}$ not listed in Eq. A.16 correspond to transitions not allowed in the model and are equal to 0. To calculate the overall distribution of particles, we additionally define a vector of propagators $\widehat{\widetilde{\mathbf{F}}}$. Each component $\widehat{\widetilde{F}}_a$ corresponds to the Fourier-Laplace transformed spatial distribution of particles that first reached state a at time 0 and have moved a displacement x at time t, without having left that state. These components can be expressed in terms of the transition propagators $H_{a,b}$ by calculating the overall probability that the particle has not left its current state. For

instance,

$$
\begin{aligned}
F_n(x,t) &= \left[1 - \int_0^t J_{nf}(t')dt'\right] e^{-(k_b+\gamma)t} R_D(x,t) \\
\widehat{\widetilde{F}}_n(k,s) &= \frac{1}{s+Dk^2+k_b+\gamma}\left[1 - \widehat{\widetilde{J}}_{nf}(k, s+Dk^2+k_b+\gamma)\right] \\
&= \frac{1}{s+Dk^2+k_b+\gamma}\left(1 - \widehat{\widetilde{H}}_{nf}\right).
\end{aligned}
\tag{A.17}
$$

The other components can be derived analogously, to give:

$$
\begin{aligned}
\widehat{\widetilde{F}}_{f_u} &= \frac{1}{D\sigma_D^2}\left(1 - \widehat{\widetilde{H}}_{f_u,n}\right), \quad \widehat{\widetilde{F}}_f = \frac{1}{D\sigma_D^2}\left(1 - \widehat{\widetilde{H}}_{f,n}\right) \\
\widehat{\widetilde{F}}_{n_u} &= \frac{1}{D\sigma_b^2}\left(1 - \widehat{\widetilde{H}}_{n_u,f}\right), \quad \widehat{\widetilde{F}}_n = \frac{1}{D\sigma_b^2}\left(1 - \widehat{\widetilde{H}}_{n,f}\right) \\
\widehat{\widetilde{F}}_w &= \frac{s+\lambda}{(s+\lambda)^2+k^2}, \quad \widehat{\widetilde{F}}_h = \frac{1}{s+\gamma+k_u}.
\end{aligned}
\tag{A.18}
$$

The overall propagator for a particle moving through this system of states can be found by a convolution over all possible transition paths, analogous to the discrete path sampling technique used for calculating kinetics on potential energy surfaces [177]. Specifically, the spatial density of a particle that started at the origin in state i at time 0 and is in state j at time t is given by

$$
\begin{aligned}
&G_{i,j}(x,t) = \\
&= \delta_{i,j} F_i + \sum_{n=1}^{\infty} \sum_{k_1,k_2,\ldots k_n} H_{i,k_1} * \ldots * H_{k_{n-1},k_n} * H_{k_n,j} * F_j
\end{aligned}
\tag{A.19}
$$

where n is the number of intermediate states over which the particle transitions and k_l is the identity of the l-th intermediate state.

Replacing the convolutions with multiplication of the Fourier-Laplace transformed propagators we find the overall spatial distribution for a particle that started in a linear combination of

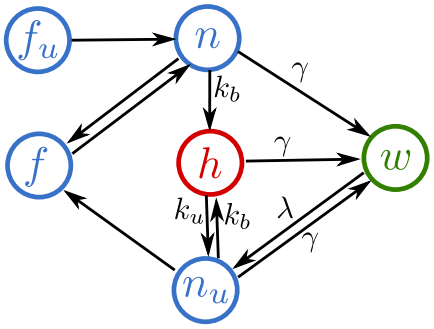

Figure A.1: Schematic state diagram illustrating the particle states used to develop the analytical model for multi-modal transport in a cylinder. Allowed transitions are labeled with arrows and the rates for the constant-rate transition processes (to and from tethered or actively walking state) are indicated. The transitions between diffusive states occur with a time-varying rate that can be derived by evaluating the matrix components in Eq. A.16 at $k = 0$.

initial states described by the vector **P**.

$$\begin{aligned}\widehat{\widetilde{G}}(k,s;\mathbf{P}) &= \lim_{\varepsilon\to 0}\mathbf{P}\cdot\left(\sum_{n=0}^{\infty}\widehat{\widetilde{\mathbf{H}}}^{n}\right)\cdot\widehat{\widetilde{\mathbf{F}}} \\ &= \lim_{\varepsilon\to 0}\mathbf{P}\cdot\left(\mathbf{I}-\widehat{\widetilde{\mathbf{H}}}\right)^{-1}\cdot\widehat{\widetilde{\mathbf{F}}}\end{aligned} \tag{A.20}$$

where **I** is the identity matrix.

The Laplace-transformed mean squared displacement can be found directly from the propagator by taking derivatives with respect to k. Its long time limit is found by expanding to lowest order in s and taking the coefficient of the $1/s^2$ term:

$$\lim_{t\to 0}\mathrm{MSD} = \left[-\lim_{s\to 0}s^2\left(\frac{\partial^2}{\partial k^2}\widehat{\widetilde{G}}(k,s)\bigg|_{k=0}\right)\right]t = 2D_{\mathrm{eff}}t, \tag{A.21}$$

where the effective long time diffusivity D_{eff} is given in Eq. 2.21.

The average time for a particle with initial distribution **P** among the different states to first

initiate a walk can be found as the time integral of the probability that no walk has yet occurred:

$$\langle t_w(\mathbf{P})\rangle = \int_0^\infty dt \int_0^\infty dx\, G^*(x,t;\mathbf{P}) \tag{A.22}$$

where G^* is obtained from Eq.A.20 with alternate transition matrices $\widehat{\widetilde{\mathbf{H}}}^*, \widehat{\widetilde{\mathbf{F}}}^*$ defined by removing the rows and columns of $\widehat{\widetilde{\mathbf{H}}}, \widehat{\widetilde{\mathbf{F}}}$ corresponding to the walking state (w). The average time to start walking for a particle initially uniformly distributed within the inner radius α can be evaluated as

$$\langle t_w\rangle = \left[\left(\mathbf{I} - \widehat{\widetilde{\mathbf{H}}}^*\right)^{-1}\right]_{n_u,\cdot} \cdot \widehat{\widetilde{\mathbf{F}}}^* \Bigg|_{k=0,s=0} \tag{A.23}$$

where the subscript $(n_u,.)$ indicates the corresponding row of the inverse matrix. The resulting expression is given in Eq. 2.22.

We similarly calculate the mean squared time to initiate a walk, using

$$\left\langle t_w^2\right\rangle = -2\frac{\partial}{\partial s}\left[\left(\mathbf{I} - \widehat{\widetilde{\mathbf{H}}}^*\right)^{-1}\right]_{n_u,\cdot} \cdot \widehat{\widetilde{\mathbf{F}}}^* \Bigg|_{k=0,s=0}. \tag{A.24}$$

The variance in the time to start walking is given by $\sigma^2 = \left\langle t_w^2\right\rangle - \langle t_w\rangle^2$. While the full closed-form expression is too cumbersome to include here, in the limit of rapid unbinding from the tethered state ($k_u \gg \gamma, k_u \gg D/a^2$), the variance in the walking time is

$$\lim_{k_u\to\infty} \sigma^2 = \frac{4D(1+\alpha^2 K_{\mathrm{eq}})^2 - \alpha^2\gamma(3-4\alpha^2+\alpha^4+4\log\alpha)(1+K_{\mathrm{eq}})}{4\alpha^4 D\gamma^2(1+K_{\mathrm{eq}})^2} \tag{A.25}$$

Fig. A.2 shows the Fano factor, a measure of the variability in a stochastic process defined as the standard deviation in the time to start walking, relative to the average time. Large variability in how long it takes a passively diffusing particle to start walking is seen in the case of slow

diffusion and strong binding.

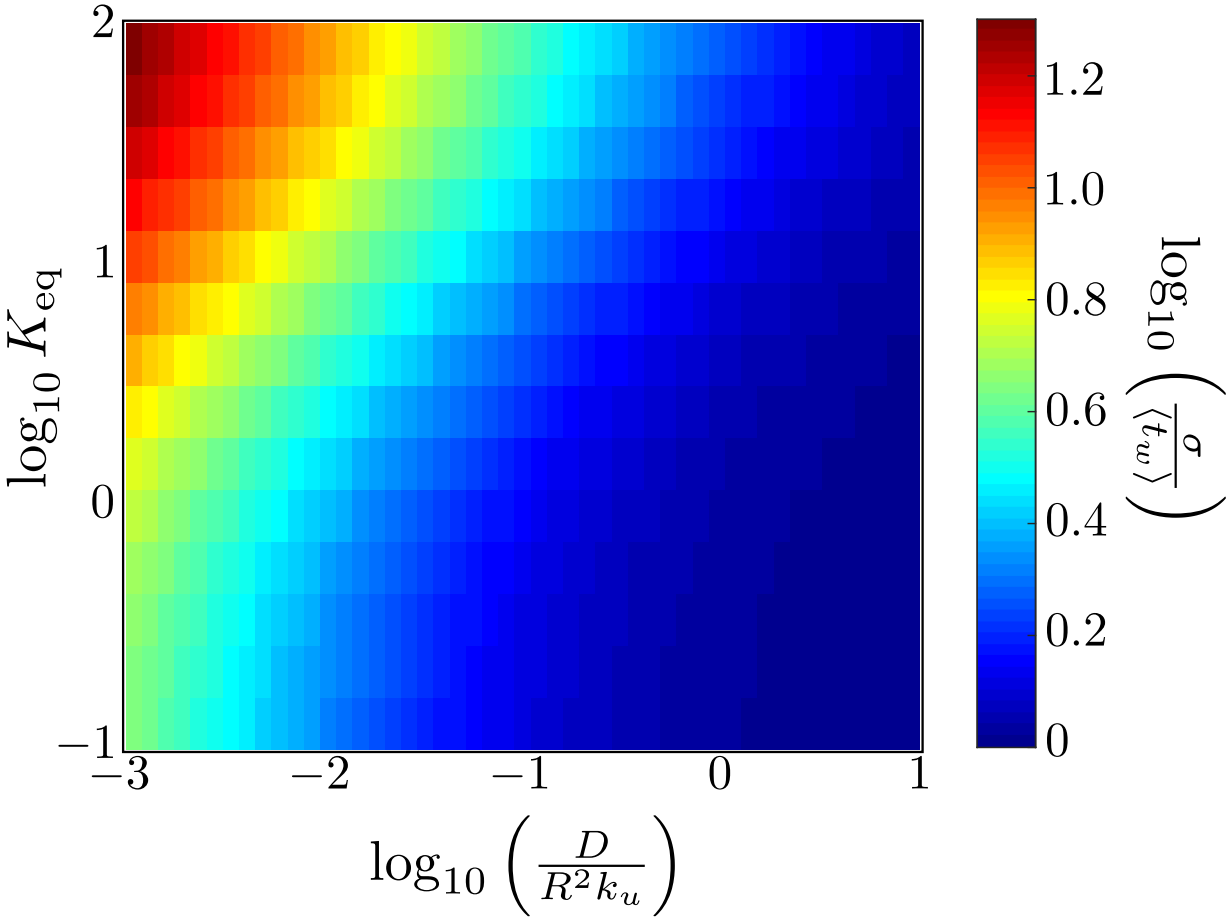

Figure A.2: Fano factor $\sigma/\langle t_w \rangle$ quantifying the variability in the time required for a particle to first begin a processive walk. The particle is assumed to start uniformly distributed within the inner radius α. Results shown are for parameters $\alpha = 0.1, k_u = 100, \gamma = 10^{-2}$

A.4 Simulation details

We simulate moving particles within a cylindrical domain of unit radius and unbounded length. The axial position of each particle is tracked to determine the range and the mean squared displacement. We also track the radial position to determine the probability of state transitions for the particles.

Each particle is assigned to a walking, diffusive or tethered state at initialization. The

fraction of particles in each state is determined by the equilibrium distribution given in Eq. A.14. Unbound particles in the diffusive state start uniformly distributed radially throughout the cross section.

We divide the cylindrical domain in two concentric sections (Fig. 2.6a). The inner domain of radius α denotes the region within which particles can transition from the diffusive state to the walking or tethered state. Particles execute explicit Brownian dynamics with a time-step Δt when their radial position is smaller than $3\alpha/2$. This includes the inner domain along with a buffer region of radius $\alpha/2$. The time step is chosen to be smaller than all relevant time-scales in the model: $\Delta t \ll \min(1/k_b, 1/\gamma, \alpha^2/2D)$. Note that this choice of time-step prevents multiple events occuring within a single step.

Particles outside the capture domain can spend a long time diffusing before reaching the region of interest. To accelerate the simulation, we make use of the first passage time distribution for diffusive particles between two cylindrical boundaries. The cumulative encounter probability to an absorbing inner boundary of radius α with a reflective outer boundary of unit radius is given by,

$$\Phi(t) = 1 - \frac{\pi^2}{2}\sum_{n=1}^{\infty}\left[\frac{J_0^2(\beta_n\alpha)\beta_n\alpha}{J_0^2(\beta_n\alpha) - J_1^2(\beta_n)}\right] \times [J_0(\beta_n r)Y_1(\beta_n) - Y_0(\beta_n r)J_1(\beta_n)] \times [Y_1(\beta_n\alpha)J_1(\beta_n) - J_1(\beta_n\alpha)Y_1(\beta_n)]\, e^{-\beta_n^2 Dt} \quad \text{(A.26)}$$

where J_ν and Y_ν are the bessel functions of the first and second kind respectively, with order ν [176]. The β_n are eigenvalues of the equation $J_1(\beta_n)Y_0(\beta_n\alpha) - J_0(\beta_n\alpha)Y_1(\beta_n) = 0$. The time required to reach the inner domain starting from an initial radial position r is drawn from the above distribution and the particles are propagated along the axis according to the diffusive propagator R_D (Eq. A.1) over this time interval.

The simulation is run using a hybrid Brownian Dynamics – kinetic Monte Carlo algorithm

where the probability of a state transition depends on the radial position of the particle. Particles in the diffusive state within the inner domain ($r < \alpha$) can transition to the tethered or walking states at a combined rate $k_b + \gamma$. A transition is attempted at every diffusion time-step based on the relative probabilities for tethering and walking. Transitions leading away from the tethered state occur with a rate k_u to the diffusive state, and with a rate γ to the walking state. Particles in the walking state transition to the diffusive state a rate λ. Each time particles re-enter the diffusive state, they are uniformly distributed in the radial dimension within the inner region (of radius α), ensuring symmetry between the binding and unbinding position. A schematic of these transitions is shown in Fig. 2.6(a). For each transition out of a tethered or walking state, the waiting time is drawn from an exponential distribution with the mean equal to the corresponding transition rate. The particles are propagated in space according to the distribution for the given state over the duration of the waiting time. The simulation continues until all particles have covered a predetermined time interval.

A.5 First passive passage time

For certain intracellular particles such as mRNAs [178] and proteins encapsulated within transport vesicles, we would expect that the particles are unable to perform their target-capture functions while in the processively moving state. Under this restriction, it is desirable to know how much time is required for an organelle to reach its target in the correct state while undergoing multi-modal transport. An important quantity in this context is the passive first passage time distribution ($F_P(x,t)$), which is the overall probability density for the time t at which the particle first passes position x in a diffusive state. While the renewal equations (Eq. 2.5 and Eq. 2.6) can be used to obtain the probability of first passage occuring in the diffusive state, in order to obtain the required distribution we must also consider particles that achieve first passage in the processive state and after subsequent state transitions eventually return to the target in the diffusive state.

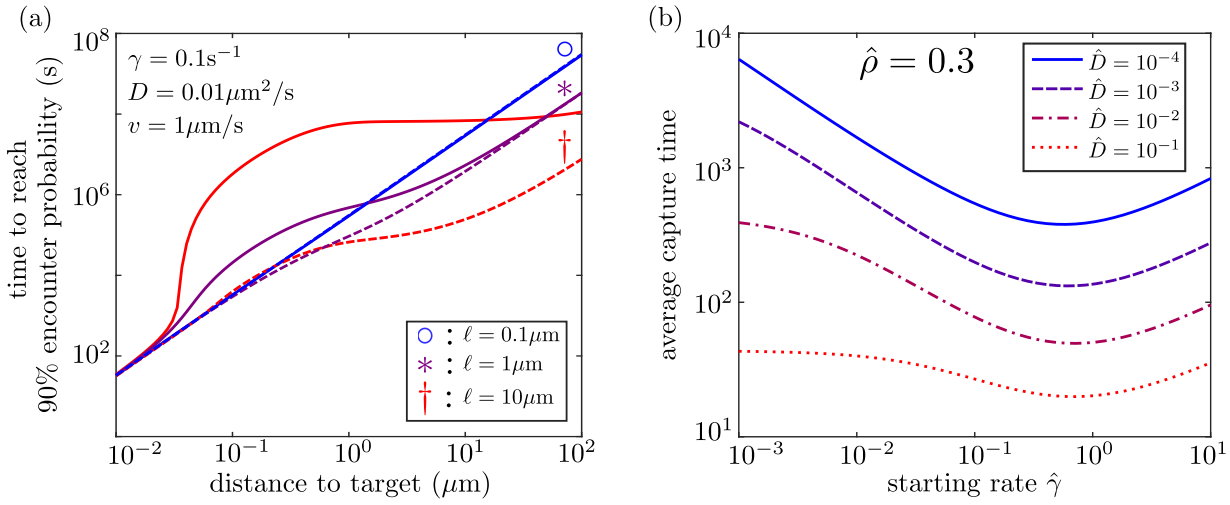

Figure A.3: Effects of state dependent activity: a) Time to reach 90% capture probability $t_{90\%}$ for different run lengths and biologically relevant transport parameter values. Solid lines denote $t_{90\%}$ for particles that can capture their target only in the passive state. Dashed lines denote $t_{90\%}$ for particles that capture their target in either state. $\circ, *, \dagger$ denote run lengths of 0.1μm,1μm, and 10μm respectively. Plots for $\ell = 0.1\mu$m overlap. b) Average time for target capture by a uniformly distributed population as a function of the starting rate $\hat{\gamma}$ for different values of diffusivity $\hat{D}$. The particle density $\hat{\rho} = 0.3$ and other parameter ranges include the observed parameters for peroxisome transport in fungal hyphae.

The halting creeper model allows for the calculation of $F_P(x,t)$ by summing over all trajectories that first pass the target in the diffusive state at the specified time. For particles that pass in the processive state, the turning events required to return to the target can be expressed as a series of convolutions over time. A Laplace transform $\left(F_P(x,t) \to \widehat{F}_P(x,s)\right)$ converts these convolutions to multiplication, leading to an expression for the first passive passage time distribution as follows,

$$\widehat{F}_P(x,s) = \widehat{F}_{*D}(x,s) + \widehat{F}_{*+}(x,s)\left[\widehat{F}_{+D}(0^-,s) + \widehat{F}_{+-}(0^-,s)\widehat{F}_{-D}(0^+,s)\right]\sum_{m=0}^{\infty}\left[\widehat{F}_{+-}(0^-,s)\widehat{F}_{-+}(0^+,s)\right]^m, \tag{A.27}$$

where $\widehat{F}_{ij}(x,s)$ denotes the Laplace transformed first passage time distribution of a particle

starting in the state i and reaching the target position x in the state j. The possible states are the passive state (D), walking in the forward or backward direction $(\pm)$, and walking in any direction (W). An asterisk $(*)$ denotes a sum over all possible starting states, weighted by the respective steady state probabilities for each state. The first term in the expression denotes the particles that reach the target in the diffusive state for the first time. Subsquent terms in the infinite sum include particles which need to change states and return to the target position, with each term denoting an additional return to the target in a non-functional state.

Under the assumption of symmetric starting rates, we can write $\widehat{F}_{+-}(0^-,s) = \widehat{F}_{-+}(0^+,s)$, and $\widehat{F}_{+D}(0^-,s) = \widehat{F}_{-D}(0^+,s)$, which reduces Eq. A.27 to

$$\widehat{F}_P(x,s) = \widehat{F}_{*D}(x,s) + \frac{\widehat{F}_{*+}(x,s)\widehat{F}_{-D}(0^+,s)}{1-\widehat{F}_{-+}(0^+,s)} \tag{A.28}$$

Eqs. 2.5,2.6 allow us to calculate the probability density of a particle that starts at equilibrium executing first passage at a particular time while in the passive state $\left(\widehat{F}_{*D}(x,s)\right)$ or while actively walking forward $\left(\widehat{F}_{*+}(x,s)\right)$. Other quantities appearing in Eq. A.28 can be calculated from the renewal equations for particles starting in the active state walking backward,

$$\begin{aligned} G_{-D}(x;t) &= \int_0^t dt' \left[F_{-D}(t';x)G_{DD}(0;t-t') \right. \\ &\qquad \left. + F_{-+}(t';x)G_{+D}(0;t-t')\right], \\ G_{-W}(x;t) &= \int_0^t dt' \left[F_{-D}(t';x)G_{DW}(0;t-t') \right. \\ &\qquad \left. + F_{-+}(t';x)G_{+W}(0^+;t-t')\right]. \end{aligned} \tag{A.29}$$

After a Laplace tranform, Eq. A.29 reduces to a system of linear equations,

$$\begin{bmatrix} \widehat{G}_{DD}(0) & \widehat{G}_{+D}(0) \\ \widehat{G}_{DW}(0) & \widehat{G}_{+W}(0^+) \end{bmatrix} \begin{bmatrix} \widehat{F}_{-D}(x) \\ \widehat{F}_{-+}(x) \end{bmatrix} = \begin{bmatrix} \widehat{G}_{-D}(x) \\ \widehat{G}_{-W}(x) \end{bmatrix}, \tag{A.30}$$

where the argument $(t \to s)$ is implied. The right-hand side can be evaluated at $x = 0^+$ by carrying out the Fourier inversion of $\widehat{\widetilde{G}}_{-D}$, $\widehat{\widetilde{G}}_{-W}$ through direct integration of the expressions in Eq. A.11 over k. The Laplace transformed first passive passage time distributions $\widehat{F}_{-D}, \widehat{F}_{-+}$ are then inverted numerically using Talbot's algorithm [63].

We study the implications of this search process, where particles are functional only in the passive state, by first calculating the time required for a single particle to reach its target with 90% probability (Fig. A.3a). As in the case where both active and passive states allow capture, we see that an intermediate run-length can optimize the capture time. However, when only passive capture is allowed, this optimal run-length is shifted to much shorter values, as would be expected since long run lengths result in the particle spending less time in a functional state.

Additionally, we calculate the average time required by any particle within a uniformly distributed population (of density $\hat{\rho} = 0.3$) to reach a stationary target (Fig. A.3b). As compared to a particle that is functional in both states (Fig. 2.5), the diffusivity has a much bigger role to play for a particle that can only capture while passive. Because increasing diffusivity allows a particle to search a wider region during each sojourn in a functional state, the diffusion coefficient substantially modulates the capture time even at very large values of $\hat{\gamma}$. Furthermore, in the case of passive capture, increasing the fraction of processively moving particles does not necessarily speed up capture. An optimum starting rate $\hat{\gamma}$ arises from two competing effects. On the one hand, the faster transport in the processive state allows particles to reach the region near the target more rapidly. On the other hand, a large value of the starting rate proves detrimental, as particles reaching the target are less likely to be in the functional state. This optimization in terms of the fraction of time spent moving processively has previously been noted by several studies on two-dimensional multi-modal search processes[27, 34, 179].

A search process where the particle is functional only in the passive state is applicable to components, such as neurotransmitters, that are encapsulated within vesicles but must be released in order to carry out their function. Additionally, in the case of a tubular cell region (see Section

2.6), a target that is located away from the microtubule track could only be reached when the organelle is in the diffusive state.

Appendix B

Methods for *Aspergillus nidulans* strain development, image processing, and Brownian dynamics simulations for hitchhiking initiation

B.1 *Aspergillus nidulans* growth conditions

A. nidulans strains were grown on yeast extract and glucose media agar gum plates for maintenance [180]. *A. nidulans* spores were then transferred prior to imaging to 1% glucose minimal media [181] supplemented with 1mg/ml uracil, 2.4mg/ml uridine, 2.5μg/ml riboflavin, 1μg/ml para-aminobenzoic acid, and/or 0.5μg/ml pyridoxine if required.

For TIRF microscopy of mature hyphae overexpressing PxdA(Δ1–500)-TagGFP from the AlcA promoter, spores were inoculated onto minimal media agar gum plates with 100mM threonine (without glucose) for 22-25 hours at 37°C. Colonies were excised from agar plates and inverted onto an eight-chambered Nunc Lab-Tek II coverglass (Thermo Fisher Scientific) for

imaging. PxdA(Δ1–500)-TagGFP expression was confirmed by observation of motile puncta in the 488-channel (imaged as described in Section B.3.3)).

For lattice light sheet and spinning disk microscopy of *A. nidulans* germlings, *A. nidulans* spores were resuspended in 1 mL of 0.01% Tween-80. The spore/Tween-80 solution was then added 1:1000 to 1% glucose minimal media supplemented with 1μg/ml para-aminobenzoic acid on 1.5 thickness 5mm circular coverglass, and incubated for 20-24 hours at 30°C.

B.2 *Aspergillus nidulans* Strain construction

Table B.1: *A. nidulans* strains used in Chapter 3

Strain	Genotype	Source
RPA288	*yA*::[*gpdA*(p)-mCherry-FLAG-PTS1::*Afpyro*]; *pyroA4*; *pyrG89*; Δ*nkuA*::*bar*	[17]
RPA402	*wA*, [*ebA*-mCherry-*Afribo*], [*tubA*-GFP-*Afpyro*]; *pyroA4*; *pyrG89*; *pabaA1*; Δ*nkuA*::*argB*	This study
RPA495	*yA*::[*gpdA*(p)-mCherry-FLAG-PTS1::*Afpyro*]; [TagGFP2::*rabA*::*AfpyrG*]; *pyroA4*; *pyrG89*; *pabaA1*; Δ*nkuA*::*argB*+	[17]
RPA1205	*yA*::[*gpdA*(p)-mCherry-FLAG-PTS1::*Afpyro*]; *pyroA4*; *wA*::[*alcA*(p)-*pxdA*(Δ1–500)-tagGFP::*pyrG*]; *pyrG89*; Δ*nkuA*::*bar*	This study

Aspergillus nidulans strains used in this study are listed in Table B.1. Strain RPA402 expressing EbA-mCherry and TubA-GFP was created through genetic crossing, as previously described [182]. Strain RPA1205 overexpressing PxdA(Δ1–500)-TagGFP was created by homologous recombination of a single copy at the *wA* (white) locus using *AfpyrG* (*Aspergillus fumigatus pyrG*) selection into a strain lacking the *A. nidulans* homolog of human KU70, *nkuA* [181]. A PxdA construct without the first 500 amino acids was chosen and created following difficulties with cloning a GFP-tagged PxdA full-length construct, and because PxdA without the

first 500 amino acids rescues a *pxdA*Δ strain similarly to full-length PxdA (unpublished). The PxdA(Δ1–500)-TagGFP DNA construct contains an AlcA promoter sequence [183] followed by the PxdA gene without the region encoding the first 500 amino acids [17], TagGFP codon optimized for *A. nidulans*, *pxdA*'s native 3′ UTR, and the *AfpyrG* selectable marker, all flanked by 1 kb *wA* locus arms of homology. These fragments were all inserted into the Blue Heron Biotechnology pUC vector at 5′ EcoRI and 3′ HindIII restriction sites using isothermal assembly [184]. The plasmid was confirmed by sequencing, and linear DNA to be transformed into *A. nidulans* was created by PCR using primers at the 5′ and 3′ ends of the *wA* arms of homology.

B.3 Imaging Methods

B.3.1 Lattice light sheet microscopy

A. nidulans germlings are grown on 1.5 thickness 5mm circular coverglass as described in Section C.8, then mounted and imaged on a home-built lattice light sheet microscope to obtain timelapse z-stacks of endosomes and peroxisomes. Our home-built lattice light sheet microscope was constructed following the design described by Chen et al. [185] and detailed design information provided by the Betzig group at the Howard Hughes Medical Institute Janelia Research Campus. The optical layout was modified yet retained the relative optical component locations and optical performance of the original layout. A square lattice pattern, corresponding to 73 Bessel beams, was displayed on a SLM (Forth Dimension Displays, SXGA3DM). A 488nm laser (Coherent Genesis MX) with 0.2mW total output was shaped with two cylindrical lens pairs to illuminate the pattern. The Fourier transform of the resulting beams was projected by a 500mm lens onto an annular mask, conjugate to the back focal plane (BFP) of the excitation objective lens. The annular mask used, corresponding to numerical aperture 0.55(outer diameter) and 0.44(inner diameter) of the excitation objective lens, spatially filtered the pattern to remove unwanted diffraction orders. This annular mask provided for a 10μm beam waist (FWHM)

and sheet thickness at the center of 0.92μm, measured by scanning and imaging 0.2μm beads (Thermo Fisher Scientific F8811). The BFP was projected onto galvo mirrors and used to dither the lattice pattern in the x direction continuously over a 30μm range in 0.15μm step for even sheet illumination. The fluorescence signal was imaged with a sCMOS Camera (Hamamatsu Photonics Orca Flass4.0 v3) through a bandpass filter ET525/50m (Chroma Technology) with a 20msec exposure time. All imaging was performed at room temperature. To acquire 3D images the sample was moved in 0.98μm steps over a 19.6μm range by the piezo stage it was mounted on. This corresponds to 0.51μm steps and a 10.2μm range in the detection optical axis because of a 31.5° angle between the stage axis and the light-sheet plane. Following data acquisition, the image volumes underwent rotation and deconvolution based on a measure PSF with a custom cudaDeconv software (`https://github.com/dmilkie/cudaDecon`) using the Richardson-Lucy deconvolution algorithm distributed by the Betzig group and LLSpy software developed by Dr. Tally Lambert at Harvard University (`https://github.com/tlambert03/LLSpy`) to automate the process. Maximum intensity projections of the deconvolved and rotated data were created using FIJI/ImageJ [186, 187].

B.3.2 Spinning disk microscopy

A. nidulans germlings were imaged using a Yokogawa W1 SoRa confocal scanhead mounted to a Nikon Ti2-E microscope, set to 1x intermediate magnification, with an Apo TIRF 100x 1.49 NA objective. The scope was run with NIS Elements using the 488nm and 561nm lines of a six-line (405nm, 445nm, 488nm, 515nm, 561nm, and 640nm) LUNF-XL laser engine and a Prime95B camera (Photometrics). Image channels were acquired sequentially using bandpass filters for each channel (525/50 and 595/50). *Z*-stacks were acquired using a piezo Z stage (Mad City Labs). The *z*-range used to image a field of germlings was set manually depending on germling extension from the coverglass surface.

B.3.3 TIRF microscopy

For TIRF imaging, time-lapse images were collected using a TIRF 100x /1.49 oil immersion objective on an inverted epifluorescence Ti-E microscope with Perfect Focus System (Nikon) and controlled by NIS-Elements software (Nikon). Stage position is controlled by a ProScan linear motor stage controller (Prior). GFP or mCherry fluorescence was excited by a 488-nm (50mW) or 561-nm (50mW) laser line, respectively, from an LUNV laser engine (Nikon). Excitation and emission paths were filtered with the appropriate single bandpass filter cubes (Chroma) and emitted signal was detected using an EM-CCD camera (Andor, iXon Ultra 888).

B.4 Estimating parameters for *A. nidulans* hyphae

B.4.1 Estimating linear density of peroxisomes and endosomes

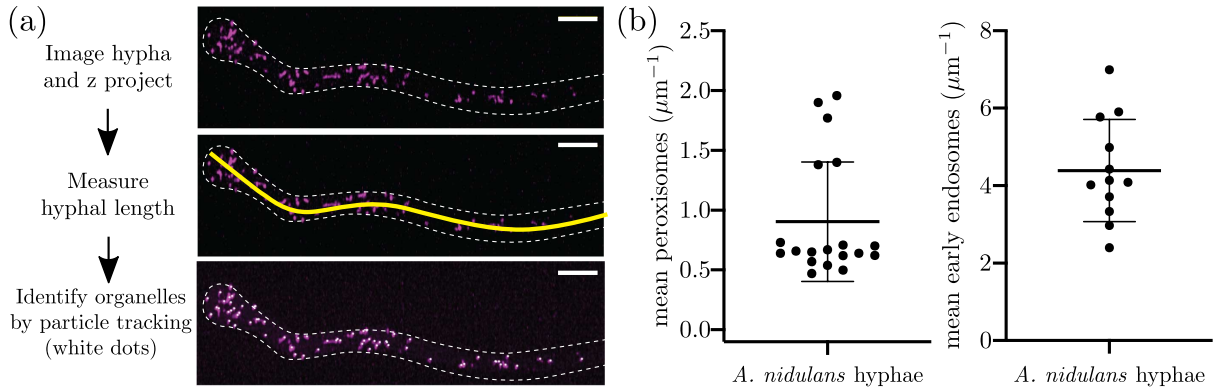

Figure B.1: (a) Schematic of organelle density quantification. (Top) Maximum intensity z-projection of an *A. nidulans* germling expressing mCherry-Pts1 (peroxisome marker). White dotted line shows outline of the hypha. (Middle) Yellow line shows example hyphal length measurement. (Bottom) White dots represent each peroxisome identified . Scale bar, 5μm, (b) Scatter plots of organelle density per μm hyphal length. Each circle represents the organelle density of one hypha quantified in the 10th frame of a timelapse movie. Mean peroxisome density was 0.90 ± 0.11 (SEM) per μm hyphal length. Mean early endosome density was 4.57 ± 0.41 (SEM) per μm hyphal length. Error bars=SD. $n = 19$ hyphae for peroxisome density measurements and 12 hyphae for early endosome density measurements.

To calculate endosome or peroxisome density, lattice light sheet images of an *A. nidulans*

strain expressing TagGFP-RabA (endosomes) and mCherry-Pts1 (peroxisomes) were deconvolved and z-aligned as described in Section B.3.1. Maximum intensity projections were then created using FIJI/ImageJ[186]. As our simulations take into account organelle (early endosome or peroxisome) density per unit hyphal length, the organelle density was quantified by measuring the length of the hypha and quantifying the number of early endosomes or peroxisomes within that hyphal length. The length of the hyphae within the field of view was measured by manually drawing a line along the hyphal length using FIJI/ImageJ (Fig. B.1) and taking a measurement. Early endosomes or peroxisomes were identified within the same regions using the Crocker-Grier 3D particle tracking algorithm [188], implemented via publicly available code[189]. The number of organelles per unit length was then calculated to determine organelle density.

B.4.2 Estimating microtubule number

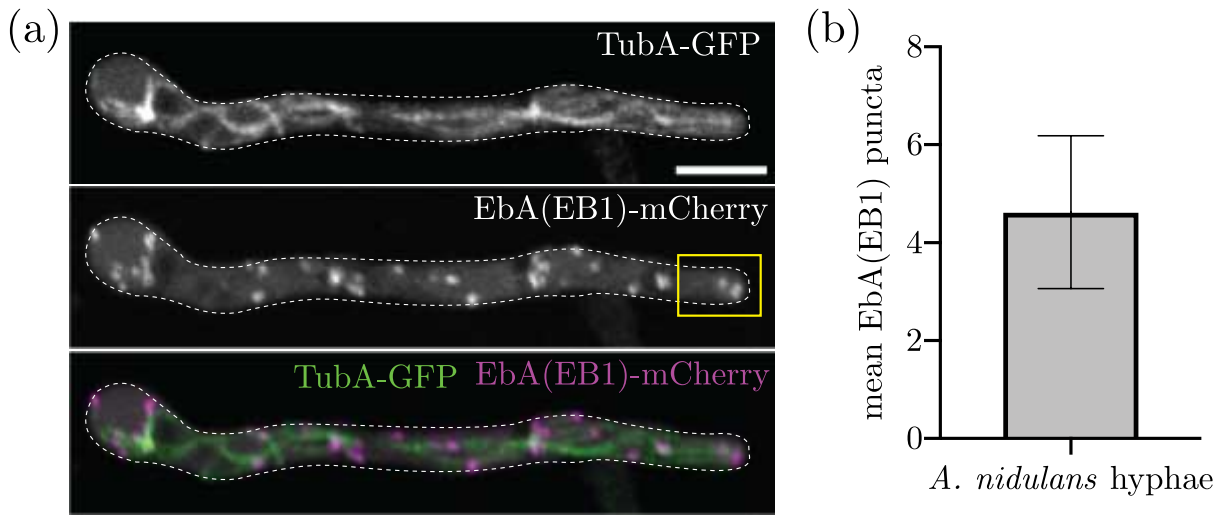

Figure B.2: (a) Maximum intensity z-projection of an *A. nidulans* germling expressing TubA-GFP (microtubules) (top) and EbA(EB1)-mCherry (microtubule plus-end marker) (middle) and a merged image (bottom). White dotted line denotes outline of *A. nidulans* germling. Yellow box denotes region in which EbA(EB1) puncta were counted (the region between the hyphal tip and the nuclei nearest the hyphal tip). Scale bar, 5μm. (b) Bar graph of number of EbA(EB1) puncta in the region between the hyphal tip and the nucleus nearest the hyphal tip. Mean number of EbA(EB1) puncta was 4.62 ± 0.14 (SEM). Error bars=SD. $n = 133$ hyphae.

To quantify microtubule number, maximum intensity projections of spinning disk images from *A. nidulans* hyphae expressing EbA-mCherry (microtubule plus-end marker) and TubA-GFP (microtubules) were created using FIJI/ImageJ[186]. Microtubule number was quantified by manually counting EbA tips within the region between the nucleus nearest the hyphal tip and the hyphal tip. The nucleus was identified as a dark circular region in the EbA background fluorescence. If the first visible nucleus closest to the hyphal tip was further than 10μm from the hyphal tip, then the EbA spots within 10μm of the hyphal tip were counted.

B.4.3 Estimating the diameter of *Aspergillus nidulans* hyphae

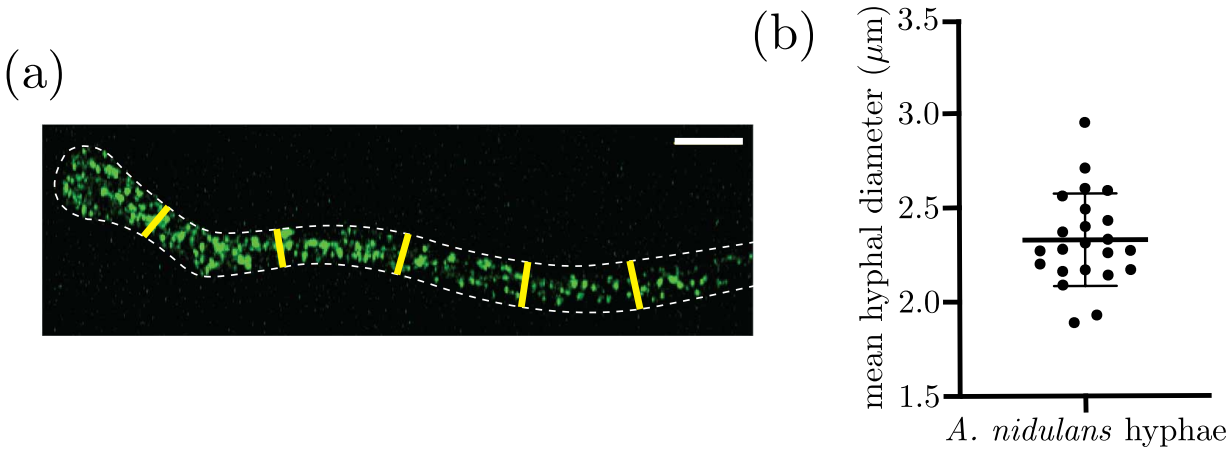

Figure B.3: (a) Schematic of hyphal diameter measurements. Maximum intensity z-projection of an *A. nidulans* germling expressing TagGFP-RabA (early endosomes). White dotted line shows outline of the hypha. Five diameter measurements were taken along each hypha, represented by yellow lines. Scale bar, 5μm. (b) Scatter plot of *A. nidulans* hyphal diameter measurements. Each circle represents the average of five measurements for one hypha. Mean hyphal diameter was 2.33 ± 0.25 (SEM) μm. Error bars=SD. $n = 23$ hyphae.

To quantify the diameter of *A. nidulans* hyphae, lattice light sheet images of an *A. nidulans* strain expressing TagGFP-RabA (endosomes) and mCherry-Pts1 (peroxisomes) were deconvolved and z-aligned as described in Section B.3.1. Five measurements of hyphal diameter were taken along each hypha by manually drawing a line across the hypha width and measuring using FIJI/ImageJ.

B.4.4 Estimating number of peroxisome movements

To quantify peroxisome movements, time lapse images of *A. nidulans* strains expressing mCherry-Pts1 with or without overexpressed PxdA(Δ1–500)-TagGFP were collected at 500ms intervals for 1 minute total. Overexpression of PxdA(Δ1–500)-TagGFP was verified by motile puncta in the GFP channel. A line was drawn perpendicular to the hyphae 10μm from the hyphal tip. The number of peroxisomes that crossed the line over a 60 second movie was counted [8]. A Mann-Whitney test was performed to determine statistical significance.

B.5 Extraction and classification of peroxisome trajectories

B.5.1 Extracting peroxisome trajectories from live-cell imaging data

Lattice light sheet images of an *A. nidulans* strain expressing mCherry-Pts1 (peroxisome signal) were deconvolved and z-aligned as described in Section B.3.1. Image stacks of voxel size $0.104\mu\text{m} \times 0.104\mu\text{m} \times 0.5\mu\text{m}$ were generated at a rate of $0.36 - 0.42$ seconds per frame. Images were thresholded to remove pixels of brightness below the 10^{th} percentile.

Peroxisome punctae in these images were located by adapting a publicly available implementation[189] of the Crocker-Grier 3D particle tracking algorithm[188]. The image is first denoised with a bandpass filter, followed by identification of brightness peak centroids. Peaks are filtered according to a minimal separation between objects. Peaks with average brightness below a certain percentile of overall image intensity (mass cutoff) were excluded. Punctae identified in frames of time-lapse images were linked together to obtain trajectories of individual peroxisomes. We allow linking of trajectories that may skip up to 1 frame, and only keep trajectories that are longer than a minimum duration. Parameters used for identifying and linking peroxisome punctae are shown in Table B.2.

Table B.2: Parameters for extracting trajectories of peroxisomes in *A. nidulans* hyphae

Parameters for particle identification

Parameter	Description	Value
bandpass filter size	size of band-pass filter	$8 \times 8 \times 3$ pixels
object separation	minimum separation between objects	$7 \times 7 \times 2$ pixels
mass cutoff	minimal percentile for average feature brightness	96

Parameters for linking tracks

Parameter	Description	Value
memory	number of frames that can be skipped while linking	1
displacement	max displacement of an object from one frame to another	0.75μm
minimum length	minimum number of frames in a trajectory	20

B.5.2 Identification of peroxisome hitchhiking events from extracted trajectories

3D trajectories of peroxisomes extracted from Lattice light sheet images were analyzed using a wavelet-based adaptive thresholding algorithm[61] to identify peroxisome hitchhiking. This approach uses the Haar wavelet transform over varying time-scales to identify segments of processive motion in trajectories. A sliding wavelet transform over a scale of 2 frames was used to extract a global estimate of noise for all the trajectories. A universal threshold was calculated based on the estimated fluctuations, to determine the typical displacement driven by diffusion over a given time-scale. We used a sliding window of 6 frames to identify time points when the wavelet coefficient was greater than 0.5 times the universal threshold. These points were marked

as corresponding to processive motion, since they corresponded to average particle displacements bigger than what would be expected for diffusion over that time scale.

Trajectory sections with at least 3 consecutive frames of processive motion were marked as “active" and assumed to correspond to hitchhiking events. The remaining sections were classified as “passive". Sample trajectories with marked active and passive sections are shown in Fig. B.4.

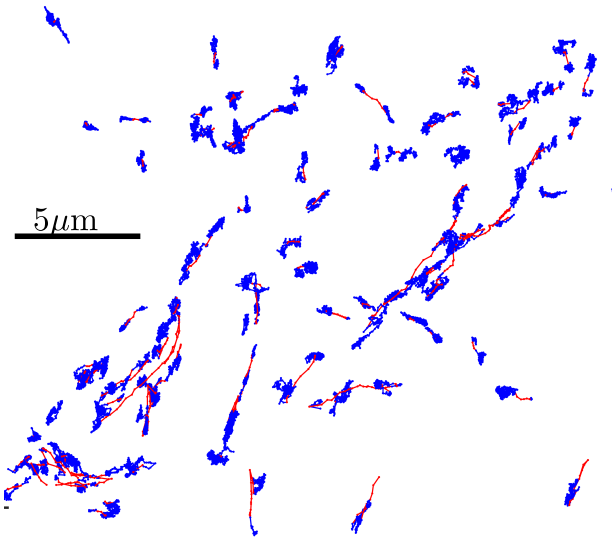

Figure B.4: Sample trajectories of peroxisomes extracted from time-lapse Lattice light sheet images. Active (red) and passive (blue) sections of trajectories are shown. Trajectories shown are extracted from multiple hyphae and from different time-lapse series (biological replicates). Only trajectories with at least one active section are shown here.

To obtain statistics for the rate of hitchhiking initiation, we included only those trajectories of length at least 100 frames. All longer trajectories were cut off beyond 100 frames ($t_{\max} \approx 40$sec). Only those trajectories which started in the passive state and had at least one active section prior to $t_{\max}$ were included in the analysis ($n = 115$ trajectories). An empirical cumulative distribution function was calculated for the waiting time until the first active section (Fig. 6b). This distribution was fit to the conditional cumulative distribution function for waiting times of a Poisson process

with rate constant k_{init}:

$$P_{\text{cum}}(t) = \frac{1 - e^{-k_{\text{init}}t}}{1 - e^{-k_{\text{init}}t_{\text{max}}}}. \tag{B.1}$$

The denominator in this expression accounts for the fact that only trajectories eventually exhibiting an active section are included in the analysis. We use bootstrapping to repeat the analysis for 100 samples of trajectories drawn with replacement from the measured trajectory population, allowing calculation of a standard error for our fitted value of k_{init}.

B.6 Derivation of timescale to encounter a carrier organelle

In this section we provide a brief derivation for the average time a cargo must wait to encounter a carrier organelle. The inverse of this timescale gives the rate of carrier encounter k_{carrier} given by Eq. 3.2. A fundamental assumption in this derivation is that the cargo organelle is initially formed with a uniform distribution within the cross-sectional area of the domain, so that its probability of starting in the microtubule-proximal region is f_N.

We label the three states in Fig. 3.2a as A (far from microtubule), B (close to microtubule), and C (hit by carrier), and treat transitions between the states as memory-less Poisson processes. The propagator functions $P_{ij}(t)$ are defined as the probability distribution that a particle arriving at state i at time 0 will first transition to state j at time t, without previously leaving state i. First passage times in a system of discrete Markovian states can be derived from a convolution of these propagator functions[175, 190], an approach which has been termed “discrete path sampling"[177] or “Markov state models"[191] in different contexts.

Namely, for a system starting in state A (outside the microtubule-proximal region), the

distribution of first-passage times to reach state C (encounter with a carrier) is given by

$$F_{AC}(t) = P_{AB} * P_{BC} + P_{AB} * (P_{BA} * P_{AB}) P_{BC} + P_{AB} * (P_{BA} * P_{AB})(P_{BA} * P_{AB}) P_{BC} \ldots \tag{B.2}$$

where $*$ denotes convolution, the first term corresponds to the particle reaching state B and then transitioning to state C, and the second term corresponds to the particle executing one excursion from B back to A before finally reaching state C, the third term has two such excursions, and so forth.

A Laplace transform in time ($\hat{P}_{ij}(s) = \mathscr{L}_{t\to s}[P_{ij}(t)]$) converts the convolutions into multiplications, allowing this expression to be simplified to:

$$\hat{F}_{AC} = \hat{P}_{AB}\hat{P}_{BC} \sum_{n=0}^{\infty} (\hat{P}_{BA}\hat{P}_{AB})^n = \frac{\hat{P}_{AB}\hat{P}_{BC}}{1 - \hat{P}_{BA}\hat{P}_{AB}} \tag{B.3}$$

The Laplace transforms for the individual propagators are:

$$\hat{P}_{AB} = \frac{k_{\mathrm{MT}}}{s + k_{\mathrm{MT}}}, \quad \hat{P}_{BA} = \frac{k_{\mathrm{leave}}}{s + k_{\mathrm{leave}} + k_{\mathrm{pass}}}, \quad \hat{P}_{BC} = \frac{k_{\mathrm{pass}}}{s + k_{\mathrm{leave}} + k_{\mathrm{pass}}} \tag{B.4}$$

Plugging these into the distribution of first passage times (Eq. B.3), and taking the limit $s \to 0$ allows the calculation of average time to encounter a carrier (for a particle starting far from a microtubule):

$$\tau_A = -\frac{d\hat{F}_{AC}}{ds}|_{s=0} = \frac{k_{\mathrm{leave}} + k_{\mathrm{MT}} + k_{\mathrm{pass}}}{k_{\mathrm{MT}} k_{\mathrm{pass}}}.$$

We note that the inverse of this first passage time is the standard rate constant for a Michaelis-Menten process which involves a substrate binding on and off an enzyme prior to a final irreversible reaction. The current model is analogous to this process, with a starting state far from the microtubules corresponding to the unbound substrate.

However, in our model system we expect the cargo to sometimes originate within the microtubule proximal region, especially if there are many microtubules in the domain. A similar analysis for particles starting with state B gives a first passage time to carrier encounter:

$$\begin{aligned} \hat{F}_{BC} &= \frac{\hat{P}_{BC}}{1-\hat{P}_{BA}\hat{P}_{AB}} \\ \tau_B &= -\frac{d\hat{F}_{BC}}{ds}|_{s=0} = \frac{k_{\text{leave}}+k_{\text{MT}}}{k_{\text{MT}}k_{\text{pass}}} \end{aligned} \tag{B.5}$$

Overall, we assume the particle starts in state A with probability $p_A = k_{\text{leave}}/(k_{\text{MT}}+k_{\text{leave}})$ and in state B with probability $p_B = 1-p_A$. This allows us to calculate the overall mean first passage time to carrier encounter

$$\tau = p_A\tau_A + p_B\tau_B = \frac{(k_{\text{leave}}+k_{\text{MT}})^2 + k_{\text{leave}}k_{\text{pass}}}{k_{\text{MT}}k_{\text{pass}}(k_{\text{leave}}+k_{\text{MT}})}. \tag{B.6}$$

The inverse of this expression gives the effective rate for carrier encounter $k_{\text{carrier}} = 1/\tau$ (Eq. 3.2).

B.7 Extracting the rate of contact between carrier and hitchhiker

The rate of contact between the carrier and the hitchhiker is extracted from the cumulative probability of contact vs time obtained from simulations. As described in the Methods section, 2500 trials of carrier passage in a tubular geometry are simulated with Brownian dynamics. For each trial, we record the probability of contact occurring within a given time-step. This probability density is integrated to obtain the cumulative probability distribution as a function of time, which is then fit to a double exponential function $F(f_1,\tau_1,f_2,\tau_2,t) = 1 - f_1 e^{-t/\tau_1} - f_2 e^{-t/\tau_2}$. The two weights f_1, f_2 need not sum to 1, because some trajectories start with the cargo already in contact

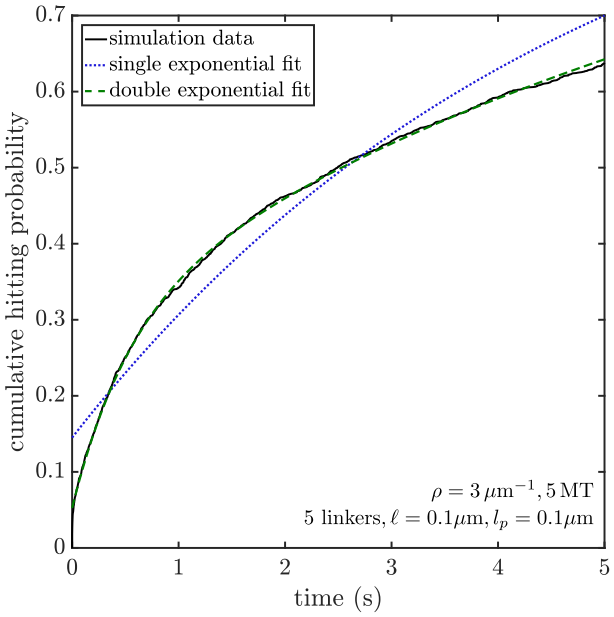

Figure B.5: Cumulative contact probability (solid black line) vs time showing single (blue, dotted line) and double (green, dashed line) exponential fits.

with a carrier organelle or linker tip. The average time to contact is obtained as $\tau = f_1\tau_1 + f_2\tau_2$, and the overall rate of contact is defined by $k_{\text{hit}} = \tau^{-1}$. This approach effectively extrapolates the cumulative contact time distribution to longer times using a double-exponential fit. It allows the calculation of an effective rate even when that rate is quite small, without the need for the very long simulations that would be required for all trials to achieve contact. We note that the double-exponential form is chosen ad-hoc as a smooth functional form that reproduces the data reasonably well. No explicit physical meaning is assigned to the two time-scales. The more commonly used single exponential fitting function [$F(f,\tau,t) = 1 - fe^{-t/\tau}$] provides a poor fit compared to the double exponential (Fig. B.5). We note that the qualitative behavior of the rate of contact between a hitchhiker and carrier remains the same regardless of the choice of fitting function.

The same fitting procedure is used to extract the rate of contact with a linker protein (Fig. 3-5, 7) and the average time for a cargo to reach a microtubule proximal region (Fig. 2b). A double-exponential functional form was used for all of these quantifications, as a single

exponential did not accurately reproduce the observed cumulative distribution.

B.8 Simulating linker protein encounters

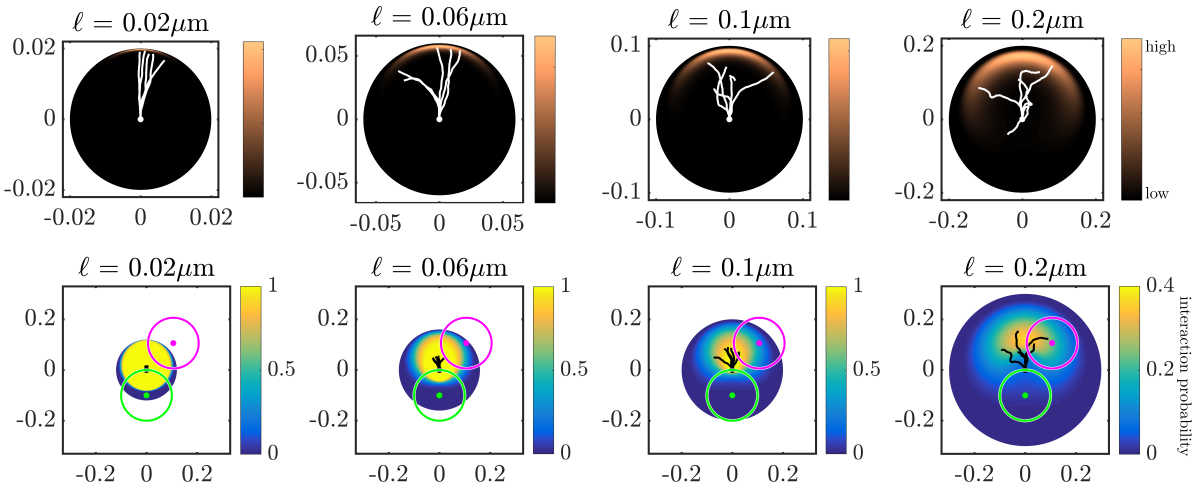

Figure B.6: (Top) Spatial distribution for the free end of a wormlike chain with persistence length $\ell_p = 0.1\mu$m, where one end has its position fixed at the white dot and orientation fixed upwards. Color indicates the probability density of finding the linker tip at a given location. Sample configurations of linkers are shown with white lines. (Bottom) Probability of contact $[p(d,\beta)]$ between a cargo organelle and a linker protein, shown as a function of cargo position relative to the linker attachment point (black dot). The carrier organelle location (green), example cargo location (magenta), and sample linker configurations (black lines) are shown. Both cargo and carrier have a radius of 0.1μm.

In *A. nidulans* hyphae, the protein PxdA is a putative linker that connects hitchhiking peroxisomes to motor-driven early endosomes. Analysis of the makeup of PxdA reveals a coiled-coil region that is predicted to be about $\approx$ 90nm in length[17]. We also note that the persistence length of coiled-coil proteins is reported to be in the range $30-170$nm [101–104]. The expected mechanical properties of these linker proteins thus fall in the category of semiflexible polymer chains, and we therefore model a typical linker protein as a “worm-like" chain[96] (WLC) whose base is fixed on the surface of the carrier organelle.

Using analytically derived Greens’ functions, we first obtain the spatial probability distribution $G(r,\theta,\phi;\hat{z})$ of the linker end point, assuming the initial orientation ($\hat{z}$) points radially

outward from the carrier [97]. Since the distribution is azimuthally symmetric, we can represent the distribution in terms of r and θ as $G'(r,\theta;\hat{z}) = 2\pi G(r,\theta,\phi;\hat{z})$. Note that this representation preserves the normalization $\int_0^{2\pi}\int_{-1}^{1}\int_0^{\ell} r^2 G(r,\theta,\phi;\hat{z})\, dr d(\cos\theta) d\phi = 1$. Fig. B.6 (top) shows the end distribution $G'(r,\theta;\hat{z})$ for a WLC with persistence length $l_p = 0.1\mu$m, and varying chain lengths (ℓ).

To determine the probability of contact between the linker and a hitchhiker located at any given position, we calculate the overlap between the equilibrium spatial distribution of the WLC tip and the volume occupied by the hitchhiking cargo. In the reference frame of the fixed linker end, we assume a sphere of radius r_p is placed at polar coordinates $(d,\beta,0)$, where d is the distance from the linker attachment point and β is the angle of the hitchhiker position relative to the initial linker orientation. The integral of the linker end distribution over the volume occupied by the sphere then gives the probability of contact for that particular position of the hitchhiking cargo.

Assuming the tip of the WLC is located at (r,θ,ϕ), its distance from the center of a hitchhiker located at $(d,\beta,0)$ is given by

$$R = \sqrt{r^2 + d^2 - 2rd(\sin\theta\cos\phi\sin\beta + \cos\theta\cos\beta)}$$

For the point (r,θ,ϕ) to be in the interior of the hitchhiker, the distance R should be less than the hitchhiker radius, or $R < r_p$. Comparing these expressions gives us a range of possible values of ϕ for which the point (r,θ,ϕ) lies inside the hitchhiker. The range of ϕ values satisfies

$$\cos\phi \geq \frac{r^2 + d^2 - r_p^2}{2rd\sin\theta\sin\beta} - \cot\theta\cot\beta.$$

The total amount of azimuthal overlap can be obtained from the values of ϕ that satisfy the above

inequality. Denoting this overlap by $\Delta\Phi(r,\theta;d,\beta)$, we can write

$$\Delta\Phi(r,\theta;\phi,\beta) = 2\cos^{-1}\left(\frac{r^2+d^2-r_p^2}{2rd\sin\theta\sin\beta} - \cot\theta\cot\beta\right).$$

Note that $\Delta\Phi = 0$ if the linker tip cannot overlap with the hitchhiker, and $\Delta\Phi = 2\pi$ for complete overlap.

Using the azimuthal overlap, we can write the probability of interaction between the tip of the WLC and the hitchhiker as

$$p(d,\beta) = \int_{-1}^{1} d(\cos\theta)\int_0^{\ell} r^2 dr \frac{\Delta\Phi(r,\theta;d,\beta)}{2\pi} G'(r,\theta;\hat{z})$$

The probability $p(d,\beta)$ is tabulated with d varying from ≈ 0 to $(\ell + r_p)$, and β varying from 0 to π. Fig. B.6 (bottom) shows $p(d,\beta)$ for varying linker lengths. In our simulations, whenever the hitchhiker comes within a distance $(\ell + r_p)$ from the base of a linker, we calculate its position (d,β) relative to that linker base and obtain the associated overlap probability $p(d,\beta)$ by interpolating the tabulated values. Successful contact is determined by sampling from this probability at each time-step.

B.9 Determining the distribution of encounter durations between linker protein and hitchhiker

In the case where the cargo's encounter with a linker protein does not immediately result in a successful hitchhiking event (Fig. 7), we sought to estimate the duration of a single encounter. During an encounter, the cargo, carrier, and linker protein can diffuse briefly in and out of contact, while remaining in close proximity to each other. We therefore define many such transient contacts as a single encounter over the time period associated with the carrier passing from one

side of the cargo to the other. Specifically, an encounter begins when a given linker first contacts the cargo (determined as described in Section B.8). The encounter terminates when the axial position of the processively moving carrier has passed a certain distance ($r_e + r_p + \ell + \Delta$) beyond the position of the cargo. This distance is picked to represent the point at which a diffusing cargo can no longer catch up to a processively moving carrier to continue the same correlated encounter event. During this period, only those time points for which the linker is in contact with the cargo (defined as in Section B.8) are included in the calculation of encounter duration.

The cutoff distance Δ is selected to be the length scale beyond which processive displacements exceed the root mean squared displacement due to diffusion:

$$vt^* > \sqrt{4Dt^*}, \quad \Delta = vt^* > 4D/v \approx 30\text{nm} \tag{B.7}$$

We pick a separation above this cutoff ($\Delta = 50$nm). Once the carrier has moved this far away from the cargo surface, it is assumed that any further contact with the same linker is an unrelated, separate, encounter event.

B.10 Contact rates for larger hitchhikers

Peroxisomes are dynamic organelles that can vary in size ranging from 0.1μm-1μm depending on the cell type. Peroxisomes are also known to modify their interactions with other subcellular components resulting from morphological changes [192]. In this section, we explore how changing the size of the hitchhiking cargo affects the rate of encounter with passing carriers.

For the tubular geometry described in the main text, increasing the size of the hitchhiker enables it to access a larger cross-section of the intracellular space, making it more likely to come in contact with a carrier. Assuming the radius of the hitchhiker as 0.3μm (compared to 0.1μm used in the main text), we calculate the rate of encounter with the tip of a linker on a carrier

organelle. We note that while the overall rate of encounter increases, the qualitative dependence on carrier density, linker length and number remains the same.

Exploring the effect of tethering large hitchhikers to microtubules, we note that the enhancement of the encounter rate due to tethering is somewhat diminished compared to smaller hitchhikers. However, the overall enhancement still remains substantial and can be up to 8-fold for carrier transport parameters discussed in the main text (compared to $\approx$12-fold for hitchhikers of radius 0.1μm).

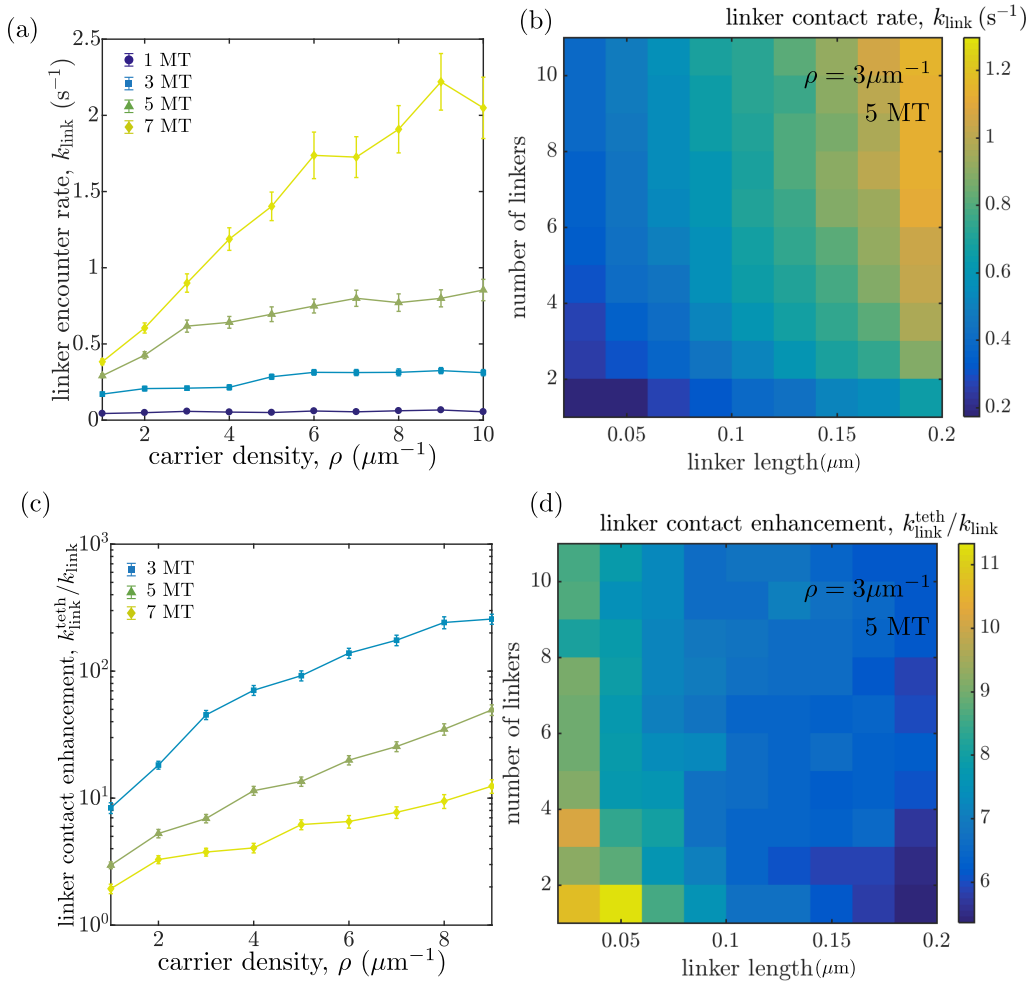

Figure B.7: Rates of linker encounters for larger hitchhiking organelles ($r_p = 0.3\mu$m). (a) Rate at which hitchhiker encounters the first linker tip as a function of carrier density and the number of microtubules. (b) Effect of linker length and linker number per carrier on the encounter rate. (c) Enhancement of overall contact rate with a linker protein tip, due to tethering of cargo. (d) Ratio of encounter rates with linker protein tips, for a tethered versus diffusive cargo.

Appendix C

Derivations, supplemental results, imaging methods and *Aspergillus nidulans* strain information for the role of microtubule arrangements in cargo capture

C.1 1D model for calculating the MFPT to capture diffusive cargo

The 1D representation of capture regions for a particular distribution of microtubule lengths can be obtained as described in the Methods section of the main text. The cellular region is denoted by a linear domain of length L, with partially absorbing intervals positioned at the axial location of microtubule plus-ends. Assume that the 1D representation divides the domain into N intervals. Each interval has a fixed, discrete number of overlapping plus-end capture regions. Boundaries of each interval are denoted by the points x_i, $0 \leq i \leq N$, such that the i^{th} interval is bounded by x_{i-1} and x_i. The first interval begins at the reflecting boundary $x_0 = L$ (cell tip), and

the last interval ends at the perfectly absorbing boundary at $x_N = 0$ (cell body). The length of an interval is denoted as ℓ_{ik}, which is the length between the node x_i and x_k, where $k = i \pm 1$. The absorption rate in the intervals bounding the node x_i is similarly denoted as γ_{ik}, $k = i \pm 1$. The absorption rates γ_{ik} are linearly proportional to the number of microtubule plus-end capture regions that overlap on that interval. The rates are treated as integer multiples of the single-end absorption rate k_a.

For a particle that starts at node x_i, the splitting probability of diffusing to the neighboring nodes $x_{i\pm1}$ without being captured is given by

$$P_{ik} = \lim_{s\to 0} \alpha_{ik} \left(\sinh \alpha_{ik}\ell_{ik} \sum_{j=i\pm1} \alpha_{ij} \coth \alpha_{ij}\ell_{ij} \right)^{-1}, \tag{C.1}$$

where $\alpha_{ij} = \sqrt{(s+\gamma_{ij})/D}$, and $k = i \pm 1$. The duration for which the particle has remained within the intervals adjacent to x_i, and has not been absorbed or reached another node ($x_{i\pm1}$) is given by the waiting time

$$Q_i = \lim_{s\to 0} \frac{1}{D} \frac{\sum_{j=i\pm1} \frac{1}{\alpha_{ij}} \tanh(\frac{\alpha_{ij}\ell_{ij}}{2})}{\sum_{j=i\pm1} \alpha_{ij} \coth(\alpha_{ij}\ell_{ij})}. \tag{C.2}$$

The mean first passage time to capture for particles starting at the distal end can then be calculated as

$$\tau = \vec{V} \cdot (\mathbf{I} - \mathbf{P})^{-1} \cdot \vec{Q}, \tag{C.3}$$

where $\mathbf{P}$ is an $N \times N$ matrix whose elements P_{ik} represent the splitting probabilities between nodes, with the rows and columns corresponding to the absorbing boundary at node x_{N+1} ($x = 0$) are set equal to zero. $\vec{Q}$ is an $N \times 1$ vector with elements representing the waiting time at each node except x_{N+1}. $\vec{V}$ is an $1 \times N$ vector denoting the initial particle distribution at each node (for

distally produced particles: $V_0 = 1$ and all other elements are zero).

For cargo that starts uniformly distributed along an interval m, the splitting probability and the waiting time to leave the interval at its bounding node x_j ($m-1 \leq j \leq m$) are given by

$$\begin{aligned} P_{mj}^{(E)} &= \lim_{s\to 0} \frac{1}{\alpha_m \ell_m} \tanh\left(\frac{\alpha_m \ell_m}{2}\right) \\ Q_m^{(E)} &= \lim_{s\to 0} \frac{1}{\alpha_m^2 D}\left[1 - \frac{2}{\alpha_m \ell_m}\tanh\left(\frac{\alpha_m \ell_m}{2}\right)\right]. \end{aligned} \tag{C.4}$$

Eq. C.3 can be modified to obtain the MFPT for cargo initially distributed uniformly throughout the cell as

$$\tau^{(E)} = \vec{W}^{(E)} \cdot \left[\vec{Q}^{(E)} + \mathbf{P}^{(E)} \cdot (\mathbf{I} - \mathbf{P})^{-1} \cdot \vec{Q}\right]. \tag{C.5}$$

Here, $\vec{W}^{(E)}$ represents the initial distribution along each interval, and elements of $\vec{Q}^{(E)}$ and $\mathbf{P}^{(E)}$ are obtained using Eq. C.4. Further details of the propagator based approach are available in Ref. [139].

C.2 Steady state distribution of dynamic microtubule plus-ends

Microtubule dynamics are incorporated using a basic model of growth and catastrophe as described in the methods section of the main text. Here, we obtain the steady-state probability density of microtubule plus-end positions $P(x)$ within the interval $0 \leq x \leq L$ representing the axis of the tubular cell. Microtubules are assumed to grow with velocity v_g within the linear interval, and enter a paused state upon reaching the cell tip at $x = L$. Both growing and paused microtubules can switch to a shrinking state with a catastrophe rate k_{cat}. Shrinking microtubules are assumed to instantaneously disappear, and are replaced by zero-length growing microtubules

to maintain a constant number of capture-capable microtubules throughout the cell. Shrinking microtubules are assumed to have lost the dynein comet due to depolymerization, and thus are incapable of capture.

The dynamics of microtubule plus-end positions under these assumptions can be represented by

$$\begin{aligned} \frac{\partial}{\partial t}P(x,t) &= -v_g\frac{\partial}{\partial x}P(x,t) - k_{\text{cat}}P(x,t), \\ \frac{\partial}{\partial t}N_{\text{end}} &= v_g P(L,t) - k_{\text{cat}}N_{\text{end}}, \end{aligned} \tag{C.6}$$

where the $P(x,t)$ is the density of growing microtubule ends and N_{end} is the number of microtubules paused at the distal tip. The boundary condition is given by setting the influx of growing microtubules at the cell body in such a way that the total number of microtubules ($n_{\text{MT}} = \int_0^L P(x) + N_{\text{end}} = 5$) stays constant. Integrating Eq. C.6 over the domain and setting the resulting time derivative to zero yields the boundary condition:

$$v_g P(0,t) = k_{\text{cat}} n_{\text{MT}}$$

The steady-state solution for this system of equations is given by:

$$\begin{aligned} P(x) &= n_{\text{MT}}\left(\frac{k_{\text{cat}}}{v_g}\right)e^{-k_{\text{cat}}x/v_g}, \\ N_{\text{end}} &= n_{\text{MT}}e^{-k_{\text{cat}}L/v_g} \end{aligned} \tag{C.7}$$

C.3 List of model parameters

List of parameters used in this study are provided in Table C.1.

Table C.1: Model parameters used in Chapter 4

Parameter	Description	Value	Source
L	Length of tubular cellular region	10μm–100μm	This study
R	Radius of tubular cellular region	1μm	[12]
D	Diffusion coefficient of cargo	$0.01\mu\text{m}^2/\text{s}$	[11]
r	Radius of dynein comet	0.2μm	[125]
n_{MT}	Number of microtubules	5	This study
v_g	Growth velocity for dynamic microtubules	0.18μm/s	[140]

C.4 Capture of cargo with a finite maturation rate

In some cases, the newly formed cargo may not be immediately available for capture, requiring additional maturation steps such as the acquisition of various adaptor proteins. We analyze optimal microtubule distributions for capture of cargo with a finite maturation time during which it moves diffusively without being able to bind to microtubule ends.

Varying the maturation rate effectively results in tuning the initial distribution of capture-ready cargo. For example, a very slow maturation rate results in a nearly uniform distribution of cargo available for capture since there is more time to diffuse before maturing. On the other hand, instantaneous maturation reverts to the previously studied case of capture-ready cargo entering at the cell tip. Maturation of cargo can be incorporated as a constant-rate Poisson process that must be completed prior to capture, convolved together with a capture process where particles start in the appropriate distribution that spreads out from the distal end. Details of the calculation are described in prior work [139].

Fig. C.1 shows the MFPT plotted against the maturation time and the separation between consecutive microtubules. As before, there is an optimum separation that minimizes the MFPT for each maturation time. The optimum separation increases as cargo maturation slows down, highlighting the need to spread microtubule plus-ends further in order to capture diffusively

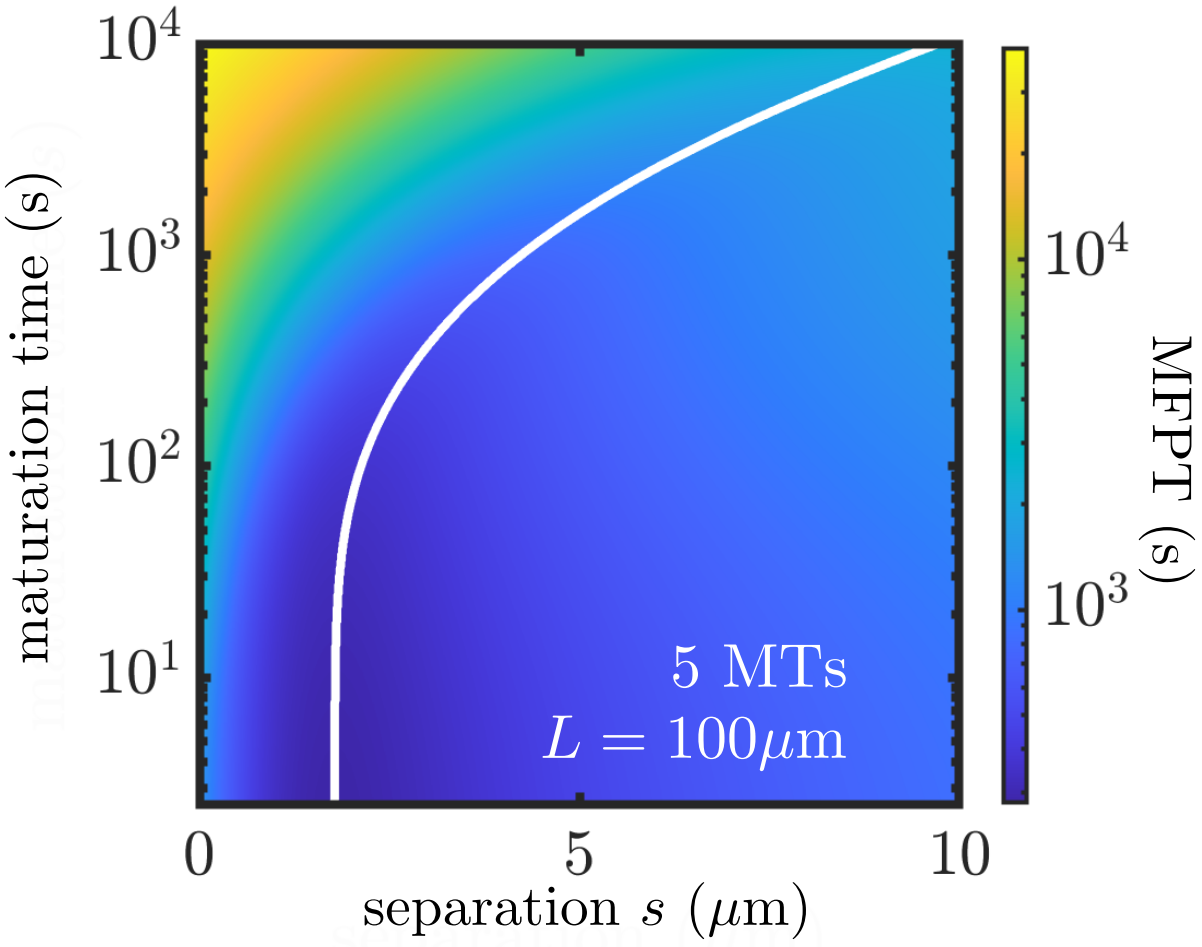

Figure C.1: **Capture times for maturing cargo.** MFPT for maturing cargos entering at the distal end of the cell and loaded at microtubule plus-ends, plotted against the maturation time and separation between consecutive microtubules. The white line denotes the separation with minimum MFPT for a given maturation time. Results are shown for a 100μm cell with 5 microtubules.

wandering cargo that matures slowly. For a 100μm cell, the optimal separation of microtubule tips begins to increase noticeably only for maturation times above 100 s.

C.5 Optimal configurations for cargo capture in long cellular regions

Fig. C.2 shows how optimal configurations for cargo capture behave in cellular regions with length 100μm.

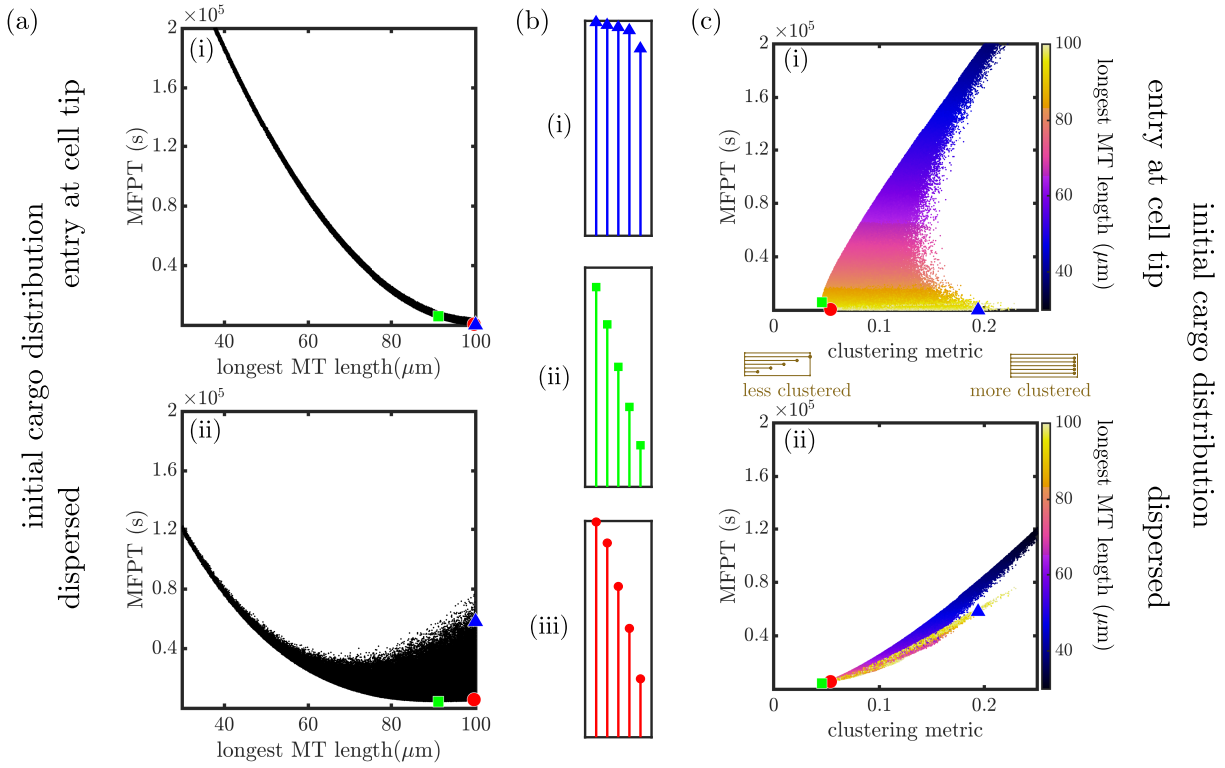

Figure C.2: **MFPT for random microtubule configurations**. (a) Scatter plots showing the MFPT to capture at microtubule plus-ends vs the length of the longest microtubule for 10^6 randomly sampled configurations with 5 microtubules each in a domain of length 100μm. (i) Cargos start at the cell tip. (ii) Cargos start uniformly. Blue triangle indicates the overall fastest configuration for (i). Green square indicates the overall fastest configuration for (ii). Red circle denotes a configuration that falls within the lowest 2.5% of MFPTs for both starting distributions. (b) Microtubule configurations corresponding to the (i) blue triangle, (ii) green square, and (iii) red circle in panel (a). (c) Scatter plots showing the MFPT plotted against a clustering metric for the randomly sampled configurations, with color indicating longest microtubule length for each configuration. (i) cargos start at cell tip. (ii) cargos start uniformly. Blue triangle, green square, and red circle denote configurations illustrated in panel (b).

C.6 Retrograde cargo delivery to the cell body

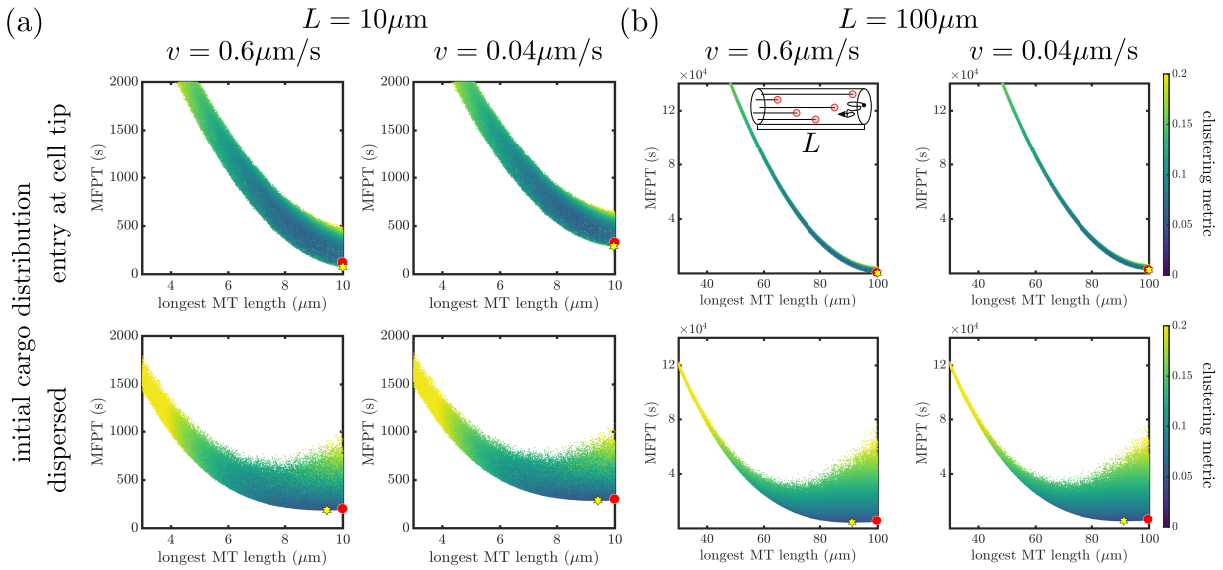

Figure C.3: **MFPT to deliver cargo to the cell body. (a)** Scatter plots showing the MFPT to reach the cell body (including the time to capture at microtubule plus-ends) vs the length of the longest microtubule for 10^6 randomly sampled configurations with 5 microtubules each in a domain of length 10μm. The cargo moves persistently towards the cell body with an effective velocity of $v = 0.6\mu$m/s (left), or $v = 0.04\mu$m/s (right) after being loaded onto the microtubule. Top: cargos start at the cell tip. Bottom: cargos start uniformly. The red circle denotes the configuration shown in Fig. 4.4b.iii of the main text. **(b)** Same plot as (a) for a cellular region of length 100μm. The red circle here denotes the configuration shown in Fig. C.2b.iii. For both (a) and (b), yellow stars denote the overall fastest configuration for a given capture condition. The color of the scatter points denotes the clustering metric described in the main text.

The results shown in the main text focus on the role of microtubule length distribution in the initial loading of cargo, neglecting the time required to deliver the captured cargo to the cell body. Here, we further explore the extent to which incorporating retrograde transport itself alters the optimal microtubule configurations. While many organelles are observed to exhibit bidirectional motion along microtubules [22, 125], others (such as neuronal autophagosomes [14] and signaling endosomes [121]) move processively towards the cell body. Our focus here is on optimizing the specific cellular objective of retrograde transport (shortest time to reach the cell body). Assuming that the cargo does not dissociate back to a diffusive state after it is loaded onto

the microtubules, the retrograde transport process can then be treated as an overall effective 'drift velocity' towards the cell body.

The retrograde transport time after capture can range widely depending on the length of the domain and the pausing or reversal behavior. We consider here two examples: particles with retrograde velocities of 0.6μm/s and 0.04μm/s, corresponding to measured values of effective average velocity towards the cell body for largely processive autophagosomes and bidirectional Rab5-marked early endosomes in hippocampal axons [173]. We also consider two domain lengths: $L = 10\mu$m and $L = 100\mu$m.

The time required to deliver cargo at a constant velocity in the retrograde direction can be incorporated in the MFPT calculations from Section C.1. The probability of cargo being captured (loaded on a microtubule) in each absorbing region is given by

$$\vec{p}_{\text{abs}} = (\mathbf{I} - \mathbf{P}) \cdot \mathbb{1}, \tag{C.8}$$

where $\mathbf{P}$ can be obtained using Eq. C.1, and $\mathbb{1}$ is an appropriately sized column vector with all elements 1. Once the cargo is captured within an absorbing region, the time required to transport it to the cell body at a constant effective velocity v is given by

$$\vec{t}_{\text{move}} = \vec{y}/v, \tag{C.9}$$

where $\vec{y}$ is a vector whose elements denote the distance of the midpoint of each absorbing region from the cell body. For the coordinates established in Sec. C.1, the corresponding distance for interval i is given by $y_i = L - (x_i + x_{i-1})/2$. Here, we have assumed that the length of the absorbing region itself is small compared to its distance from the cell body. This assumption allows us to approximate the capture location as the midpoint of an absorbing region. For cargo captured at microtubule plus-ends in fungal hyphae, the size of an absorbing region is in the order

of 0.4μm, while the distance from the cell body is in the order of 10μm, supporting the validity of the assumption for this particular system.

The overall time to deliver cargo to the cell body can be obtained by a weighted sum over all absorbing regions. The delivery time can be incorporated as an additional term in the survival time vector $\vec{Q}$. The MFPT for a cargo to reach the cell body can then be given by

$$\tau^{(CB)} = \vec{V} \cdot (\mathbf{I} - \mathbf{P})^{-1} \cdot \vec{Q}^{(CB)}, \tag{C.10}$$

where

$$\vec{Q}^{(CB)} = \vec{Q} + (\vec{p}_{\text{abs}} \cdot \mathbb{1}^T) \cdot \vec{t}_{\text{move}}. \tag{C.11}$$

Fig. C.3 reproduces Fig. 4.4a and Fig. C.2a, while incorporating the time required to travel to the cell body for two different domain lengths and effective retrograde velocities. We see that the qualitative results regarding optimal architectures for retrograde delivery still hold. For cargo originating at the cell tip, the MFPT is determined primarily by the length of the longest microtubule – an effect that is even more pronounced for longer domains. For dispersed cargo, optimal configurations have somewhat shorter maximum microtubule length and very low scores of the clustering metric. The general architecture indicated by the red dot, which has one maximally long microtubule and all other plus-ends broadly dispersed, falls within the lowest 2.5% of the calculated MSDs in each of the cases studied here. Thus, incorporation of processive retrograde movement does not substantially alter the optimal microtubule tip distribution within the range of parameters studied here.

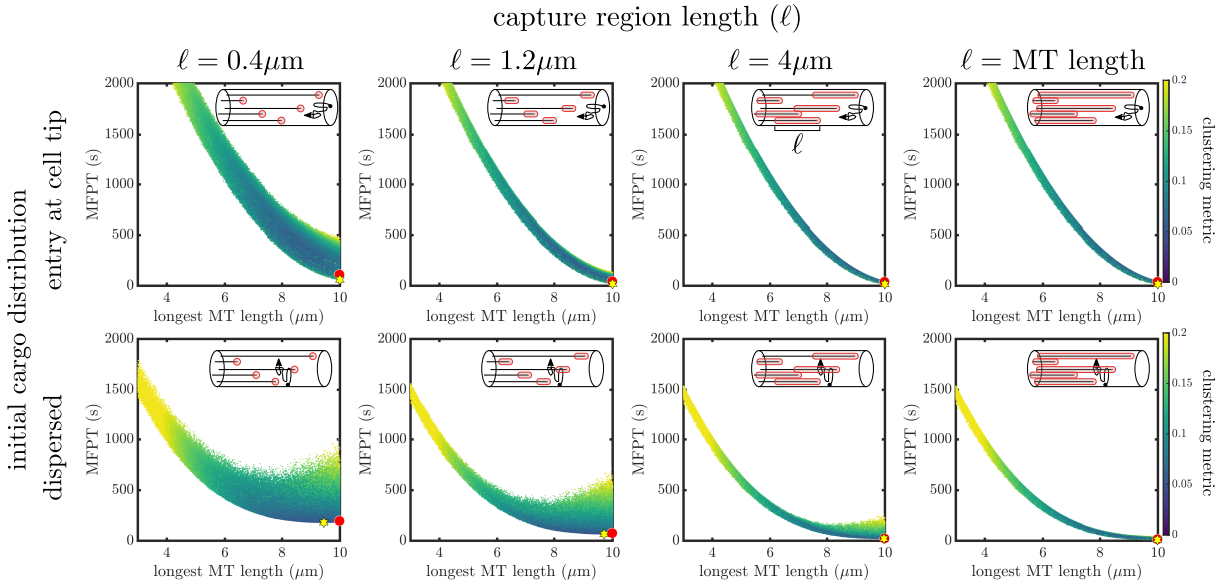

Figure C.4: **Cargo capture by regions of varying size.** Scatter plots showing the MFPT vs the length of the longest microtubule for 10^6 randomly sampled configurations with 5 microtubules each in a domain of length 10μm. The length of the capture region is indicated by ℓ. The top row denotes the MFPT for cargo formed at the cell tip. The bottom row denotes the MFPT for cargo initially dispersed uniformly. The red circle denotes a configuration that falls within the lowest 3% of MFPTs for both starting distributions for capture near plus-ends ($\ell = 0.4\mu$m, main text Fig. 4.4b.iii) and for capture along the whole microtubule (main text Fig. 4.5). Yellow stars denote the overall fastest configuration for a given capture condition. The color of the scatter points denotes the clustering metric described in the main text.

C.7 Effect of capture region size on cargo capture time

In the main text, we focused on cargo loaded onto microtubules only within a 200nm contact radius of the plus-end. However, dynein comets generally exhibit a gradual decrease in density over a micrometer length scale [125]. Furthermore, some cargos may recruit their own motor protein assembly and should be able to initiate retrograde transport elsewhere along the microtubule. For a given arrangement of microtubule lengths, the cargo capture time can vary widely depending on the size and availability of regions along the microtubule where the cargo can bind. In this section, we quantify the relation between the size of the capture region along a microtubule and the MFPT to capture cargo.

Fig. C.4 shows the MFPT for 10^6 randomly sampled configurations of 5 microtubules, for

several different values of the capture region length ℓ (equivalent to twice the capture radius). The left-most plots correspond to Fig. 4.4a. The right-most plots represent the limiting case where cargo can be captured along the entire microtubule, corresponding to Fig. 4.5. In this limiting case, we see that the longest-microtubule length is a strong predictor of the capture time, with very little variation among the MFPT for different configurations with the same longest length. Intermediate values of the capture length behave essentially as an interpolation between narrow capture at the tip and capture along the whole microtubule.

The red dots in Fig. C.4 correspond to the configuration shown in Fig. 4.4b.iii, which performs nearly optimally for plus-end capture with both cargo entering at the cell tip and cargo starting with a uniform distribution. This configuration has a single microtubule stretching all the way to the distal tip, with the other microtubule ends spaced out evenly throughout the domain. Notably, such a configuration also falls within the lowest 3% of MFPTs for the case with capture along the entire microtubule. Thus microtubule architectures with these dual features are near-optimal for rapid initiation of retrograde transport in a broad variety of scenarios, including different cargo entry points and different lengths of microtubule capture regions.

C.8 Methods for growing and imaging *Aspergillus nidulans* strains used in Chapter 4

Aspergillus nidulans strains were grown on yeast extract and glucose media agar gum plates for maintenance [180]. For spinning disk microscopy of *A. nidulans* germlings, *A. nidulans* spores were resuspended in 1 mL of 0.01% Tween-80. The spore/Tween-80 solution was then added 1:1000 to 1% glucose minimal media with no supplements in a 4-chamber 35mm dish with #1.5 coverglass bottom (Cellvis), and incubated for 16-20 hours at 30°C. Germlings were imaged using a Yokogawa W1 confocal scanhead mounted to a Nikon Ti2 microscope with an Apo TIRF 100x 1.49 NA objective. The scope was run with NIS Elements using the 488nm and 561nm lines

of a six-line (405nm, 445nm, 488nm, 515nm, 561nm, and 640nm) LUN-F-XL laser engine and a Prime95B camera (Photometrics). Image channels in 488 and 561 were acquired sequentially using bandpass filters for each channel (525/50 and 595/50). The 488nm laser was 0.740 mW measured at the objective, and the 561nm laser was 0.980 mW measured at the objective, with an exposure time of 200 milliseconds for each. Z-stacks were acquired using a piezo Z stage (Mad City Labs). As the germlings do not grow flat along the coverglass surface but frequently extend from the surface, the z-range used to image a field of germlings was set differently for different fields depending on germling extension from the coverglass surface.

For both identification of EbA/EB1 puncta in *A. nidulans* hyphal tips and for the images shown in Figure 6A, maximum intensity projections were generated from z-stacks in FIJI [186]. To count the number of microtubules in a hyphal tip, the number of microtubule plus-ends (identified by the presence of EbA/EB1) were counted in germlings in which the entire hyphal tip was included within the maximum intensity projection. Using the multi-point tool and ROI manager in FIJI, bright EbA/EB1 puncta between the hyphal tip and the first nucleus were identified and counted. All EbA/EB1 spots were overlaid with the TubA-GFP/microtubule channel to ensure that they corresponded to a microtubule end. Hyphal tip lengths were measured by manually tracing the hyphal axis from the last nucleus to the furthest point on the hyphal tip in FIJI. Microtubule lengths were measured by first drawing a line along the hyphal axis, along which all microtubule length measurements were taken. The edge of the nucleus closest to the hyphal tip was then identified and denoted as site x=0 along the hyphal axis. Any EbA/EB1 puncta located within the region between the edge of the nucleus and the hyphal tip was then identified, and its position in x along the hyphal axis determined (position in y, perpendicular to the hyphal axis, was ignored for the purposes of this measurement). The distance between the edge of the nucleus (x=0) and each EbA/EB1 puncta (x=#) was then measured.

Aspergillus nidulans strains used in this study are listed in Table C.2. Strain RPA361 expressing EbA-mCherry, TubA-GFP, and HH1-mCherry was created through genetic crossing,

as previously described [182].

Table C.2: *A. nidulans* strain used in Chapter 4

Strain	Genotype	Source
RPA361	*[ebA*-mCherry-*Afribo]*, *[tubA*-GFP-*Afpyro]*; *[HH1*-mCherry-*AfPyrG]*; *riboB2*; *pyroA4*; *pyrG89*; Δ*nkuA::bar*	This study

Bibliography

[1] Meir Aridor and Lisa A Hannan. “Traffic jam: a compendium of human diseases that affect intracellular transport processes”. In: *Traffic* 1.11 (2000), pp. 836–851.

[2] Meir Aridor and Lisa A Hannan. “Traffic jams II: an update of diseases of intracellular transport”. In: *Traffic* 3.11 (2002), pp. 781–790.

[3] Xin-An Liu, Valerio Rizzo, and Sathyanarayanan Puthanveettil. “Pathologies of axonal transport in neurodegenerative diseases”. In: *J Transl Neurosci* 3.4 (2012), pp. 355–372.

[4] Stéphanie Millecamps and Jean-Pierre Julien. “Axonal transport deficits and neurodegenerative diseases”. In: *Nat Rev Neurosci* 14.3 (2013), p. 161.

[5] Bradley N. Smith, Simon D. Topp, Claudia Fallini, Hideki Shibata, Han-Jou Chen, Claire Troakes, Andrew King, Nicola Ticozzi, Kevin P. Kenna, Athina Soragia-Gkazi, Jack W. Miller, Akane Sato, Diana Marques Dias, Maryangel Jeon, Caroline Vance, Chun Hao Wong, Martina de Majo, Wejdan Kattuah, Jacqueline C. Mitchell, Emma L. Scotter, Nicholas W. Parkin, Peter C. Sapp, Matthew Nolan, Peter J. Nestor, Michael Simpson, Michael Weale, Monkel Lek, Frank Baas, J. M. Vianney de Jong, Anneloor L. M. A. ten Asbroek, Alberto Garcia Redondo, Jesús Esteban-Pérez, Cinzia Tiloca, Federico Verde, Stefano Duga, Nigel Leigh, Hardev Pall, Karen E. Morrison, Ammar Al-Chalabi, Pamela J. Shaw, Janine Kirby, Martin R. Turner, Kevin Talbot, Orla Hardiman, Jonathan D. Glass, Jacqueline De Belleroche, Masatoshi Maki, Stephen E. Moss, Christopher Miller, Cinzia Gellera, Antonia Ratti, Safa Al-Sarraj, Robert H. Brown, Vincenzo Silani, John E. Landers, and Christopher E. Shaw. “Mutations in the vesicular trafficking protein annexin A11 are associated with amyotrophic lateral sclerosis”. In: *Science Translational Medicine* 9.388 (2017).

[6] Y. C. Liao, M. S. Fernandopulle, G. Wang, H. Choi, L. Hao, C. M. Drerup, R. Patel, S. Qamar, J. Nixon-Abell, Y. Shen, W. Meadows, M. Vendruscolo, T. P. J. Knowles, M. Nelson, M. A. Czekalska, G. Musteikyte, M. A. Gachechiladze, C. A. Stephens, H. A. Pasolli, L. R. Forrest, P. St George-Hyslop, J. Lippincott-Schwartz, and M. E. Ward. “RNA granules hitchhike on lysosomes for long-distance transport, using annexin A11 as a molecular tether”. In: *Cell* 179.1 (2019), pp. 147–164.

[7] Lawrence SB Goldstein and Zhaohuai Yang. “Microtubule-based transport systems in neurons: the roles of kinesins and dyneins”. In: *Annu Rev Neurosci* 23.1 (2000), pp. 39–71.

[8] Martin J Egan, Mark A McClintock, and Samara L Reck-Peterson. “Microtubule-based transport in filamentous fungi”. In: *Curr Opin Microbiol* 15.6 (2012), pp. 637–645.

[9] János A Perge, Jeremy E Niven, Enrico Mugnaini, Vijay Balasubramanian, and Peter Sterling. “Why do axons differ in caliber?” In: *Journal of Neuroscience* 32.2 (2012), pp. 626–638.

[10] Douglas H Smith. “Stretch growth of integrated axon tracts: extremes and exploitations”. In: *Progress in neurobiology* 89.3 (2009), pp. 231–239.

[11] Congping Lin, Martin Schuster, Sofia Cunha Guimaraes, Peter Ashwin, Michael Schrader, Jeremy Metz, Christian Hacker, Sarah Jane Gurr, and Gero Steinberg. “Active diffusion and microtubule-based transport oppose myosin forces to position organelles in cells”. In: *Nat. Commun.* 7 (2016), p. 11814.

[12] Saurabh S. Mogre, Jenna R. Christensen, Cassandra S. Niman, Samara L. Reck-Peterson, and Elena F. Koslover. “Hitching a Ride: Mechanics of Transport Initiation through Linker-Mediated Hitchhiking”. In: *Biophysical Journal* 118.6 (Mar. 2020), pp. 1357–1369.

[13] Sandra Maday and Erika LF Holzbaur. “Autophagosome assembly and cargo capture in the distal axon”. In: *Autophagy* 8.5 (2012), pp. 858–860.

[14] Sandra Maday, Karen E Wallace, and Erika LF Holzbaur. “Autophagosomes initiate distally and mature during transport toward the cell soma in primary neurons”. In: *Journal of Cell Biology* 196.4 (2012), pp. 407–417.

[15] Xiu-Tang Cheng, Bing Zhou, Mei-Yao Lin, Qian Cai, and Zu-Hang Sheng. “Axonal autophagosomes recruit dynein for retrograde transport through fusion with late endosomes”. In: *Journal of Cell Biology* 209.3 (2015), pp. 377–386.

[16] Meng-meng Fu and Erika LF Holzbaur. “Integrated regulation of motor-driven organelle transport by scaffolding proteins”. In: *Trends Cell Biol* 24.10 (2014), pp. 564–574.

[17] John Salogiannis, Martin J Egan, and Samara L Reck-Peterson. “Peroxisomes move by hitchhiking on early endosomes using the novel linker protein PxdA”. In: *J Cell Biol* 212(3).3 (2016), pp. 289–296.

[18] Comert Kural, Anna S Serpinskaya, Ying-Hao Chou, Robert D Goldman, Vladimir I Gelfand, and Paul R Selvin. “Tracking melanosomes inside a cell to study molecular motors and their interaction”. In: *P Natl Acad Sci* 104.13 (2007), pp. 5378–5382.

[19] Jennifer L Ross, M Yusuf Ali, and David M Warshaw. “Cargo transport: molecular motors navigate a complex cytoskeleton”. In: *Curr Opin Cell Biol* 20.1 (2008), pp. 41–47.

[20] Harsha V Mudrakola, Kai Zhang, and Bianxiao Cui. “Optically resolving individual microtubules in live axons”. In: *Structure* 17.11 (2009), pp. 1433–1441.

[21] Štefan Bálint, Ione Verdeny Vilanova, Ángel Sandoval Álvarez, and Melike Lakadamyali. “Correlative live-cell and superresolution microscopy reveals cargo transport dynamics at microtubule intersections”. In: *Proceedings of the National Academy of Sciences* 110.9 (2013), pp. 3375–3380.

[22] William O Hancock. “Bidirectional cargo transport: moving beyond tug of war”. In: *Nat Rev Mol Cell Bio* 15.9 (2014), pp. 615–628.

[23] Clifford P Brangwynne, Gijsje H Koenderink, Frederick C MacKintosh, and David A Weitz. “Intracellular transport by active diffusion”. In: *Trends Cell Biol* 19.9 (2009), pp. 423–427.

[24] Matan Mussel, Keren Zeevy, Haim Diamant, and Uri Nevo. “Drag of the Cytosol as a Transport Mechanism in Neurons”. In: *Biophys J* 106.12 (2014), pp. 2710–2719.

[25] Khuloud Jaqaman, Hirotaka Kuwata, Nicolas Touret, Richard Collins, William S Trimble, Gaudenz Danuser, and Sergio Grinstein. “Cytoskeletal control of CD36 diffusion promotes its receptor and signaling function”. In: *Cell* 146.4 (2011), pp. 593–606.

[26] Vaishnavi Ananthanarayanan, Martin Schattat, Sven K Vogel, Alexander Krull, Nenad Pavin, and Iva M Tolić-Nørrelykke. “Dynein motion switches from diffusive to directed upon cortical anchoring”. In: *Cell* 153.7 (2013), pp. 1526–1536.

[27] Aljaž Godec and Ralf Metzler. “Signal focusing through active transport”. In: *Physical Review E* 92.1 (2015), p. 010701.

[28] Stefan Klumpp and Reinhard Lipowsky. “Active diffusion of motor particles”. In: *Phys Rev Lett* 95.26 (2005), p. 268102.

[29] Melanie JI Müller, Stefan Klumpp, and Reinhard Lipowsky. “Bidirectional transport by molecular motors: enhanced processivity and response to external forces”. In: *Biophysical journal* 98.11 (2010), pp. 2610–2618.

[30] L Bruno, V Levi, M Brunstein, and MA Despósito. “Transition to superdiffusive behavior in intracellular actin-based transport mediated by molecular motors”. In: *Phys Rev E* 80.1 (2009), p. 011912.

[31] D Campos, E Abad, V Méndez, SB Yuste, and K Lindenberg. “Optimal search strategies of space-time coupled random walkers with finite lifetimes”. In: *Phys Rev E* 91.5 (2015), p. 052115.

[32] Aviv Kahana, Gilad Kenan, Mario Feingold, Michael Elbaum, and Rony Granek. “Active transport on disordered microtubule networks: The generalized random velocity model”. In: *Phys Rev E* 78.5 (2008), p. 051912.

[33] C Loverdo, O Bénichou, M Moreau, and R Voituriez. “Enhanced reaction kinetics in biological cells”. In: *Nat Phys* 4.2 (2008), pp. 134–137.

[34] Olivier Bénichou, C Loverdo, M Moreau, and R Voituriez. “Intermittent search strategies”. In: *Rev Mod Phys* 83.1 (2011), p. 81.

[35] Yosuke Tanaka, Yoshimitsu Kanai, Yasushi Okada, Shigenori Nonaka, Sen Takeda, Akihiro Harada, and Nobutaka Hirokawa. “Targeted disruption of mouse conventional kinesin heavy chain kif5B, results in abnormal perinuclear clustering of mitochondria”. In: *Cell* 93.7 (1998), pp. 1147–1158.

[36] Comert Kural, Hwajin Kim, Sheyum Syed, Gohta Goshima, Vladimir I Gelfand, and Paul R Selvin. “Kinesin and dynein move a peroxisome in vivo: a tug-of-war or coordinated movement?” In: *Science* 308.5727 (2005), pp. 1469–1472.

[37] Martin Schuster, Reinhard Lipowsky, Marcus-Alexander Assmann, Peter Lenz, and Gero Steinberg. “Transient binding of dynein controls bidirectional long-range motility of early endosomes”. In: *P Natl Acad Sci* 108.9 (2011), pp. 3618–3623.

[38] Paul Targett-Adams, Doreen Chambers, Sarah Gledhill, R Graham Hope, Johannes F Coy, Andreas Girod, and John McLauchlan. “Live cell analysis and targeting of the lipid droplet-binding adipocyte differentiation-related protein”. In: *J Biol Chem* 278.18 (2003), pp. 15998–16007.

[39] Diane TW Chang, Anthony S Honick, and Ian J Reynolds. “Mitochondrial trafficking to synapses in cultured primary cortical neurons”. In: *J Neurosci* 26.26 (2006), pp. 7035–7045.

[40] Alex M Valm, Sarah Cohen, Wesley R Legant, Justin Melunis, Uri Hershberg, Eric Wait, Andrew R Cohen, Michael W Davidson, Eric Betzig, and Jennifer Lippincott-Schwartz. “Applying systems-level spectral imaging and analysis to reveal the organelle interactome”. In: *Nature* 546.7656 (2017), pp. 162–167.

[41] Nobutaka Hirokawa and Reiko Takemura. “Molecular motors and mechanisms of directional transport in neurons”. In: *Nat Rev Neurosci* 6.3 (2005), pp. 201–214.

[42] Maria Antonietta De Matteis and Alberto Luini. “Exiting the Golgi complex”. In: *Nat Rev Mol Cell Bio* 9.4 (2008), pp. 273–284.

[43] Inderjit Singh. “Biochemistry of peroxisomes in health and disease”. In: *Mol Cell Biochem* 167.1-2 (1997), pp. 1–29.

[44] Nicholas A Bright, Matthew J Gratian, and J Paul Luzio. “Endocytic delivery to lysosomes mediated by concurrent fusion and kissing events in living cells”. In: *Curr Biol* 15.4 (2005), pp. 360–365.

[45] Paul C Bressloff and Jay M Newby. “Stochastic models of intracellular transport”. In: *Rev Mod Phys* 85.1 (2013), p. 135.

[46] Jia Gou, Leah Edelstein-Keshet, and Jun Allard. “Mathematical model with spatially uniform regulation explains long-range bidirectional transport of early endosomes in fungal hyphae”. In: *Mol Biol Cell* 25.16 (2014), pp. 2408–2415.

[47] David Ando, Nickolay Korabel, Kerwyn Casey Huang, and Ajay Gopinathan. “Cytoskeletal network morphology regulates intracellular transport dynamics”. In: *Biophys J* 109.8 (2015), pp. 1574–1582.

[48] Jeremy R Cooper and Linda Wordeman. “The diffusive interaction of microtubule binding proteins”. In: *Curr Opin Cell Biol* 21.1 (2009), pp. 68–73.

[49] Tara L Culver–Hanlon, Stephanie A Lex, Andrew D Stephens, Nicholas J Quintyne, and Stephen J King. “A microtubule-binding domain in dynactin increases dynein processivity by skating along microtubules”. In: *Nat Cell Biol* 8.3 (2006), pp. 264–270.

[50] Jian-Sheng Kang, Jin-Hua Tian, Ping-Yue Pan, Philip Zald, Cuiling Li, Chuxia Deng, and Zu-Hang Sheng. “Docking of axonal mitochondria by syntaphilin controls their mobility and affects short-term facilitation”. In: *Cell* 132.1 (2008), pp. 137–148.

[51] Gulcin Pekkurnaz, Jonathan C Trinidad, Xinnan Wang, Dong Kong, and Thomas L Schwarz. “Glucose regulates mitochondrial motility via Milton modification by O-GlcNAc transferase”. In: *Cell* 158.1 (2014), pp. 54–68.

[52] Rebecca L Frederick and Janet M Shaw. “Moving mitochondria: establishing distribution of an essential organelle”. In: *Traffic* 8.12 (2007), pp. 1668–1675.

[53] Melanie JI Müller, Stefan Klumpp, and Reinhard Lipowsky. “Tug-of-war as a cooperative mechanism for bidirectional cargo transport by molecular motors”. In: *P Natl Acad Sci* 105.12 (2008), pp. 4609–4614.

[54] Debjyoti Bandyopadhyay, Austin Cyphersmith, Jairo A Zapata, Y Joseph Kim, and Christine K Payne. “Lysosome transport as a function of lysosome diameter”. In: *PloS one* 9.1 (Jan. 2014), e86847.

[55] Adam G Hendricks, Eran Perlson, Jennifer L Ross, Harry W Schroeder III, Mariko Tokito, and Erika LF Holzbaur. “Motor coordination via a tug-of-war mechanism drives bidirectional vesicle transport”. In: *Current Biology* 20.8 (2010), pp. 697–702.

[56] Aaron D Pilling, Dai Horiuchi, Curtis M Lively, and William M Saxton. “Kinesin-1 and Dynein are the primary motors for fast transport of mitochondria in Drosophila motor axons”. In: *Mol Biol Cell* 17.4 (2006), pp. 2057–2068.

[57] Wylie W Ahmed and Taher A Saif. “Active transport of vesicles in neurons is modulated by mechanical tension”. In: *Sci. Rep.* 4 (2014).

[58] Elena V Romanova, Susan P Oxley, Stanislav S Rubakhin, Paul W Bohn, and Jonathan V Sweedler. “Self-assembled monolayers of alkanethiols on gold modulate electrophysiological parameters and cellular morphology of cultured neurons”. In: *Biomaterials* 27.8 (2006), pp. 1665–1669.

[59] Sandra E Encalada, Lukasz Szpankowski, Chun-hong Xia, and Lawrence SB Goldstein. “Stable kinesin and dynein assemblies drive the axonal transport of mammalian prion protein vesicles”. In: *Cell* 144.4 (2011), pp. 551–565.

[60] L Gary Leal. *Advanced transport phenomena: fluid mechanics and convective transport processes*. Cambridge University Press, 2007.

[61] Kejia Chen, Bo Wang, Juan Guan, and Steve Granick. “Diagnosing heterogeneous dynamics in single-molecule/particle trajectories with multiscale wavelets”. In: *Acs Nano* 7.10 (2013), pp. 8634–8644.

[62] William Feller. “On the integral equation of renewal theory”. In: *Selected Papers I*. Springer, 2015, pp. 567–591.

[63] Alan Talbot. “The accurate numerical inversion of Laplace transforms”. In: *Ima J Appl Math* 23.1 (1979), pp. 97–120.

[64] PV Danckwerts. “The definition and measurement of some characteristics of mixtures”. In: *Appl. Sci. Res., Section A* 3.4 (1952), pp. 279–296.

[65] ZB Stone and HA Stone. “Imaging and quantifying mixing in a model droplet micromixer”. In: *Phys Fluids* 17.6 (2005), p. 063103.

[66] Jean-Luc Thiffeault. “Using multiscale norms to quantify mixing and transport”. In: *Nonlinearity* 25.2 (2012), R1.

[67] Peter Ashwin, Matthew Nicol, and Norman Kirkby. “Acceleration of one-dimensional mixing by discontinuous mappings”. In: *Physica A* 310.3 (2002), pp. 347–363.

[68] Marco Camesasca, Miron Kaufman, and Ica Manas-Zloczower. “Quantifying fluid mixing with the Shannon entropy”. In: *Macromol Theor Simul* 15.8 (2006), pp. 595–607.

[69] Sidney Redner. *A guide to first-passage processes*. Cambridge University Press, 2001.

[70] Kohei Ogawa and Shiro Ito. “A definition of quality of mixedness”. In: *J Chem Eng Jpn* 8.2 (1975), pp. 148–151.

[71] Gregory Jedd and Nam-Hai Chua. “A new self-assembled peroxisomal vesicle required for efficient resealing of the plasma membrane”. In: *Nat Cell Biol* 2.4 (2000), pp. 226–231.

[72] Jennifer L Ross, Henry Shuman, Erika LF Holzbaur, and Yale E Goldman. “Kinesin and dynein-dynactin at intersecting microtubules: motor density affects dynein function”. In: *Biophys J* 94.8 (2008), pp. 3115–3125.

[73] Sonita R Chada and Peter J Hollenbeck. “Nerve growth factor signaling regulates motility and docking of axonal mitochondria”. In: *Curr Biol* 14.14 (2004), pp. 1272–1276.

[74] Stephen J Peter and Mohammad RK Mofrad. “Computational modeling of axonal microtubule bundles under tension”. In: *Biophys J* 102.4 (2012), pp. 749–757.

[75] Anne Straube, Gerd Hause, Gero Fink, and Gero Steinberg. “Conventional kinesin mediates microtubule-microtubule interactions in vivo”. In: *Mol Biol Cell* 17.2 (2006), pp. 907–916.

[76] Martin Schuster, Sreedhar Kilaru, Gero Fink, Jérôme Collemare, Yvonne Roger, and Gero Steinberg. “Kinesin-3 and dynein cooperate in long-range retrograde endosome motility along a nonuniform microtubule array”. In: *Mol Biol Cell* 22.19 (2011), pp. 3645–3657.

[77] Ricardo García-Pelayo. “Distribution of distance in the spheroid”. In: *J Phys A* 38.16 (2005), p. 3475.

[78] Julia R Kardon and Ronald D Vale. “Regulators of the cytoplasmic dynein motor”. In: *Nat Rev Mol Cell Bio* 10.12 (2009), p. 854.

[79] Michael A Cianfrocco, Morgan E DeSantis, Andres E Leschziner, and Samara L Reck-Peterson. “Mechanism and regulation of cytoplasmic dynein”. In: *Annu Rev Cell Dev Bi* 31 (2015), pp. 83–108.

[80] Yujiro Higuchi, Peter Ashwin, Yvonne Roger, and Gero Steinberg. “Early endosome motility spatially organizes polysome distribution”. In: *J Cell Biol* 204.3 (2014), pp. 343–357.

[81] Sebastian Baumann, Julian König, Janine Koepke, and Michael Feldbrügge. “Endosomal transport of septin mRNA and protein indicates local translation on endosomes and is required for correct septin filamentation”. In: *Embo Rep* 15.1 (2014), pp. 94–102.

[82] Sebastian Baumann, Thomas Pohlmann, Marc Jungbluth, Andreas Brachmann, and Michael Feldbrügge. “Kinesin-3 and dynein mediate microtubule-dependent co-transport of mRNPs and endosomes”. In: *J Cell Sci* 125.11 (2012), pp. 2740–2752.

[83] Thomas Pohlmann, Sebastian Baumann, Carl Haag, Mario Albrecht, and Michael Feldbrügge. “A FYVE zinc finger domain protein specifically links mRNA transport to endosome trafficking”. In: *Elife* 4 (2015), e06041.

[84] Maria Schmid, Andreas Jaedicke, Tung-Gia Du, and Ralf-Peter Jansen. “Coordination of endoplasmic reticulum and mRNA localization to the yeast bud”. In: *Curr Biol* 16.15 (2006), pp. 1538–1543.

[85] Sofia C Guimaraes, Martin Schuster, Ewa Bielska, Gulay Dagdas, Sreedhar Kilaru, Ben RA Meadows, Michael Schrader, and Gero Steinberg. “Peroxisomes, lipid droplets, and endoplasmic reticulum “hitchhike” on motile early endosomes”. In: *J Cell Biol* 211.5 (2015), pp. 945–954.

[86] John Salogiannis and Samara L Reck-Peterson. “Hitchhiking: a non-canonical mode of microtubule-based transport”. In: *Trends Cell Biol* 27.2 (2017), pp. 141–150.

[87] Saurabh S Mogre and Elena F Koslover. “Multimodal transport and dispersion of organelles in narrow tubular cells”. In: *Phys Rev E* 97.4 (2018), p. 042402.

[88] Jared P Bergman, Matthew J Bovyn, Florence F Doval, Abhimanyu Sharma, Manasa V Gudheti, Steven P Gross, Jun F Allard, and Michael D Vershinin. “Cargo navigation across 3D microtubule intersections”. In: *P Natl Acad Sci* 115.3 (2018), pp. 537–542.

[89] Pratima Bharti, Wolfgang Schliebs, Tanja Schievelbusch, Alexander Neuhaus, Christine David, Klaus Kock, Christian Herrmann, Helmut E. Meyer, Sebastian Wiese, Bettina Warscheid, Carsten Theiss, and Ralf Erdmann. “PEX14 is required for microtubule-based peroxisome motility in human cells”. In: *Journal of Cell Science* 124.10 (May 2011), pp. 1759–1768.

[90] Thomas L Schwarz. “Mitochondrial trafficking in neurons”. In: *Cold Spring Harbor perspectives in biology* 5.6 (2013), a011304.

[91] Anamika Agrawal, Gulcin Pekkurnaz, and Elena F Koslover. “Spatial control of neuronal metabolism through glucose-mediated mitochondrial transport regulation”. In: *Elife* 7 (2018), e40986.

[92] Kari Barlan and Vladimir I Gelfand. “Microtubule-based transport and the distribution, tethering, and organization of organelles”. In: *Cold Spring Harbor Perspectives in Biology* 9.5 (2017), a025817.

[93] Wiebe H Meijer, Loknath Gidijala, Susan Fekken, Jan AKW Kiel, Marco A van den Berg, Romeo Lascaris, Roel AL Bovenberg, and Ida J van der Klei. “Peroxisomes are required for efficient penicillin biosynthesis in Penicillium chrysogenum”. In: *Appl. Environ. Microbiol.* 76.17 (2010), pp. 5702–5709.

[94] Clifford P Brangwynne, FC MacKintosh, and David A Weitz. “Force fluctuations and polymerization dynamics of intracellular microtubules”. In: *P Natl Acad Sci* 104.41 (2007), pp. 16128–16133.

[95] Elena F Koslover and Andrew J Spakowitz. “Multiscale dynamics of semiflexible polymers from a universal coarse-graining procedure”. In: *Phys Rev E* 90.1 (2014), p. 013304.

[96] O Kratky and G Porod. “Röntgenuntersuchung gelöster fadenmoleküle”. In: *Recl Trav Chim Pay-b* 68.12 (1949), pp. 1106–1122.

[97] Andrew J Spakowitz and Zhen-Gang Wang. “End-to-end distance vector distribution with fixed end orientations for the wormlike chain model”. In: *Phys Rev E* 72.4 (2005), p. 041802.

[98] Robert Stine. “An introduction to bootstrap methods: Examples and ideas”. In: *Sociol Method Res* 18.2-3 (1989), pp. 243–291.

[99] Chase P Broedersz and Fred C MacKintosh. “Modeling semiflexible polymer networks”. In: *Rev Mod Phys* 86.3 (2014), p. 995.

[100] Howard C Berg and Edward M Purcell. “Physics of chemoreception”. In: *Biophys J* 20.2 (1977), pp. 193–219.

[101] Soeren Hvidt, F Henry M Nestler, Marion L Greaser, and John D Ferry. “Flexibility of myosin rod determined from dilute solution viscoelastic measurements”. In: *Biochemistry-us* 21.17 (1982), pp. 4064–4073.

[102] George N Phillips Jr and Susan Chacko. “Mechanical properties of tropomyosin and implications for muscle regulation”. In: *Biopolymers* 38.1 (1996), pp. 89–95.

[103] Charles W Wolgemuth and Sean X Sun. “Elasticity of α-helical coiled coils”. In: *Phys Rev Lett* 97.24 (2006), p. 248101.

[104] John van Noort, Thijn van der Heijden, Martijn de Jager, Claire Wyman, Roland Kanaar, and Cees Dekker. “The coiled-coil of the human Rad50 DNA repair protein contains specific segments of increased flexibility”. In: *P Natl Acad Sci* 100.13 (2003), pp. 7581–7586.

[105] Xinnan Wang and Thomas L Schwarz. “The mechanism of Ca2+-dependent regulation of kinesin-mediated mitochondrial motility”. In: *Cell* 136.1 (2009), pp. 163–174.

[106] Xufeng S Wu, Kang Rao, Hong Zhang, Fei Wang, James R Sellers, Lydia E Matesic, Neal G Copeland, Nancy A Jenkins, and John A Hammer III. “Identification of an organelle receptor for myosin-Va”. In: *Nat Cell Biol* 4.4 (2002), p. 271.

[107] Ione Verdeny-Vilanova, Fabian Wehnekamp, Nitin Mohan, Ángel Sandoval Álvarez, Joseph Steven Borbely, Jason John Otterstrom, Don C Lamb, and Melike Lakadamyali. “3D motion of vesicles along microtubules helps them to circumvent obstacles in cells”. In: *J Cell Sci* 130.11 (2017), pp. 1904–1916.

[108] Allison L Zajac, Yale E Goldman, Erika LF Holzbaur, and E Michael Ostap. “Local cytoskeletal and organelle interactions impact molecular-motor-driven early endosomal trafficking”. In: *Current Biology* 23.13 (2013), pp. 1173–1180.

[109] Melike Lakadamyali. “Navigating the cell: how motors overcome roadblocks and traffic jams to efficiently transport cargo”. In: *Physical Chemistry Chemical Physics* 16.13 (2014), pp. 5907–5916.

[110] Mithila Burute and Lukas C Kapitein. “Cellular logistics: unraveling the interplay between microtubule organization and intracellular transport”. In: *Annu Rev Cell Dev Bi* 35 (2019), pp. 29–54.

[111] Saurabh S Mogre, Aidan I Brown, and Elena F Koslover. “Getting around the cell: physical transport in the intracellular world”. In: *Physical Biology* 17.6 (2020), p. 061003.

[112] Ariana D Sanchez and Jessica L Feldman. “Microtubule-organizing centers: from the centrosome to non-centrosomal sites”. In: *Curr Opin Cell Biol* 44 (2017), pp. 93–101.

[113] Peter W Baas and Fridoon J Ahmad. “Beyond taxol: microtubule-based treatment of disease and injury of the nervous system”. In: *Brain* 136.10 (2013), pp. 2937–2951.

[114] Paul J Mlynarczyk and Steven M Abel. “First passage of molecular motors on networks of cytoskeletal filaments”. In: *Phys Rev E* 99.2 (2019), p. 022406.

[115] Monika Scholz, Stanislav Burov, Kimberly L Weirich, Björn J Scholz, SM Ali Tabei, Margaret L Gardel, and Aaron R Dinner. “Cycling state that can lead to glassy dynamics in intracellular transport”. In: *Physical Review X* 6.1 (2016), p. 011037.

[116] Monika Scholz, Kimberly L Weirich, Margaret L Gardel, and Aaron R Dinner. “Tuning molecular motor transport through cytoskeletal filament network organization”. In: *Soft matter* 16.8 (2020), pp. 2135–2140.

[117] Andrew T Lombardo, Shane R Nelson, Guy G Kennedy, Kathleen M Trybus, Sam Walcott, and David M Warshaw. “Myosin Va transport of liposomes in three-dimensional actin networks is modulated by actin filament density, position, and polarity”. In: *Proceedings of the National Academy of Sciences* 116.17 (2019), pp. 8326–8335.

[118] Anne E Hafner and Heiko Rieger. “Spatial cytoskeleton organization supports targeted intracellular transport”. In: *Biophys J* 114.6 (2018), pp. 1420–1432.

[119] Bryan Maelfeyt, SM Ali Tabei, and Ajay Gopinathan. “Anomalous intracellular transport phases depend on cytoskeletal network features”. In: *Phys Rev E* 99.6 (2019), p. 062404.

[120] Carlos F Ibáñez. “Message in a bottle: long-range retrograde signaling in the nervous system”. In: *Trends Cell Biol* 17.11 (2007), pp. 519–528.

[121] Praveen D Chowdary, Dung L Che, and Bianxiao Cui. “Neurotrophin signaling via long-distance axonal transport”. In: *Annu Rev Phys Chem* 63 (2012), pp. 571–594.

[122] Charles Barlowe and Ari Helenius. “Cargo capture and bulk flow in the early secretory pathway”. In: *Annu Rev Cell Dev Bi* 32 (2016), pp. 197–222.

[123] Lukas C Kapitein and Casper C Hoogenraad. “Which way to go? Cytoskeletal organization and polarized transport in neurons”. In: *Molecular and Cellular Neuroscience* 46.1 (2011), pp. 9–20.

[124] Gongshe Han, Bo Liu, Jun Zhang, Wenqi Zuo, N Ronald Morris, and Xin Xiang. “The Aspergillus cytoplasmic dynein heavy chain and NUDF localize to microtubule ends and affect microtubule dynamics”. In: *Current Biology* 11.9 (2001), pp. 719–724.

[125] Martin Schuster, Sreedhar Kilaru, Peter Ashwin, Congping Lin, Nicholas J Severs, and Gero Steinberg. “Controlled and stochastic retention concentrates dynein at microtubule ends to keep endosomes on track”. In: *The EMBO journal* 30.4 (2011), pp. 652–664.

[126] Armen J Moughamian, Gregory E Osborn, Jacob E Lazarus, Sandra Maday, and Erika LF Holzbaur. “Ordered recruitment of dynactin to the microtubule plus-end is required for efficient initiation of retrograde axonal transport”. In: *Journal of Neuroscience* 33.32 (2013), pp. 13190–13203.

[127] Kevin T Vaughan, Sharon H Tynan, Nicole E Faulkner, Christophe J Echeverri, and Richard B Vallee. “Colocalization of cytoplasmic dynein with dynactin and CLIP-170 at microtubule distal ends”. In: *Journal of cell science* 112.10 (1999), pp. 1437–1447.

[128] Jan-Heiko Lenz, Isabel Schuchardt, Anne Straube, and Gero Steinberg. "A dynein loading zone for retrograde endosome motility at microtubule plus-ends". In: *The EMBO journal* 25.11 (2006), pp. 2275–2286.

[129] Georg Seisenberger, Martin U Ried, Thomas Endress, Hildegard Büning, Michael Hallek, and Christoph Bräuchle. "Real-time single-molecule imaging of the infection pathway of an adeno-associated virus". In: *Science* 294.5548 (2001), pp. 1929–1932.

[130] Kyoungtae Kim, Brian J Galletta, Kevin O Schmidt, Fanny S Chang, Kendall J Blumer, and John A Cooper. "Actin-based motility during endocytosis in budding yeast". In: *Molecular biology of the cell* 17.3 (2006), pp. 1354–1363.

[131] Iva Marija Tolić-Nørrelykke, Emilia-Laura Munteanu, Genevieve Thon, Lene Oddershede, and Kirstine Berg-Sørensen. "Anomalous diffusion in living yeast cells". In: *Phys Rev Lett* 93.7 (2004), p. 078102.

[132] Felix Höfling and Thomas Franosch. "Anomalous transport in the crowded world of biological cells". In: *Reports on Progress in Physics* 76.4 (2013), p. 046602.

[133] Ming Guo, Allen J Ehrlicher, Mikkel H Jensen, Malte Renz, Jeffrey R Moore, Robert D Goldman, Jennifer Lippincott-Schwartz, Frederick C Mackintosh, and David A Weitz. "Probing the stochastic, motor-driven properties of the cytoplasm using force spectrum microscopy". In: *Cell* 158.4 (2014), pp. 822–832.

[134] R Wollman, EN Cytrynbaum, JT Jones, T Meyer, JM Scholey, and A Mogilner. "Efficient chromosome capture requires a bias in the 'search-and-capture'process during mitotic-spindle assembly". In: *Current Biology* 15.9 (2005), pp. 828–832.

[135] Xufeng Wu, Xin Xiang, and John A Hammer III. "Motor proteins at the microtubule plus-end". In: *Trends in cell biology* 16.3 (2006), pp. 135–143.

[136] Manoj Gopalakrishnan and Bindu S Govindan. "A first-passage-time theory for search and capture of chromosomes by microtubules in mitosis". In: *Bulletin of mathematical biology* 73.10 (2011), pp. 2483–2506.

[137] Ying Zhang, Xiaolei Gao, Raphael Manck, Marjorie Schmid, Aysha H Osmani, Stephen A Osmani, Norio Takeshita, and Reinhard Fischer. "Microtubule-organizing centers of Aspergillus nidulans are anchored at septa by a disordered protein". In: *Molecular microbiology* 106.2 (2017), pp. 285–303.

[138] Shaul Yogev, Roshni Cooper, Richard Fetter, Mark Horowitz, and Kang Shen. "Microtubule organization determines axonal transport dynamics". In: *Neuron* 92.2 (2016), pp. 449–460.

[139] Zubenelgenubi C Scott, Aidan I Brown, Saurabh S Mogre, Laura M Westrate, and Elena F Koslover. “Diffusive search and trajectories on spatial networks: a propagator approach”. In: *arXiv preprint arXiv:2103.05065* 44.6 (2021), pp. 1–20.

[140] Gero Steinberg, R Wedlich-Soldner, Marianne Brill, and Irene Schulz. “Microtubules in the fungal pathogen Ustilago maydis are highly dynamic and determine cell polarity”. In: *Journal of cell science* 114.3 (2001), pp. 609–622.

[141] Ruth Pordes, Don Petravick, Bill Kramer, Doug Olson, Miron Livny, Alain Roy, Paul Avery, Kent Blackburn, Torre Wenaus, Frank Würthwein, Ian Foster, Rob Gardner, Mike Wilde, Alan Blatecky, John McGee, and Rob Quick. “The open science grid”. In: *J. Phys. Conf. Ser.* Vol. 78. 78. 2007, p. 012057.

[142] Igor Sfiligoi, Daniel C Bradley, Burt Holzman, Parag Mhashilkar, Sanjay Padhi, and Frank Wurthwein. “The pilot way to grid resources using glideinWMS”. In: *2009 WRI World Congress on Computer Science and Information Engineering*. Vol. 2. 2. 2009, pp. 428–432.

[143] Zhiping Xie and Daniel J Klionsky. “Autophagosome formation: core machinery and adaptations”. In: *Nature cell biology* 9.10 (2007), pp. 1102–1109.

[144] Zachary S Schultzhaus and Brian D Shaw. “Endocytosis and exocytosis in hyphal growth”. In: *Fungal Biology Reviews* 29.2 (2015), pp. 43–53.

[145] Lukas C Kapitein and Casper C Hoogenraad. “Building the neuronal microtubule cytoskeleton”. In: *Neuron* 87.3 (2015), pp. 492–506.

[146] Cecilia Conde and Alfredo Cáceres. “Microtubule assembly, organization and dynamics in axons and dendrites”. In: *Nature Reviews Neuroscience* 10.5 (2009), pp. 319–332.

[147] Marc Kirschner and Tim Mitchison. “Beyond self-assembly: from microtubules to morphogenesis”. In: *Cell* 45.3 (1986), pp. 329–342.

[148] Yuko Mimori-Kiyosue and Shoichiro Tsukita. ““Search-and-capture” of microtubules through plus-end-binding proteins (+ TIPs)”. In: *Journal of biochemistry* 134.3 (2003), pp. 321–326.

[149] Jennifer R Levy and Erika LF Holzbaur. “Special delivery: dynamic targeting via cortical capture of microtubules”. In: *Developmental cell* 12.3 (2007), pp. 320–322.

[150] Nenad Pavin and Iva M Tolić-Nørrelykke. “Swinging a sword: how microtubules search for their targets”. In: *Systems and synthetic biology* 8.3 (2014), pp. 179–186.

[151] Kaeling Tan, Anthony J Roberts, Mark Chonofsky, Martin J Egan, and Samara L Reck-Peterson. “A microscopy-based screen employing multiplex genome sequencing identifies

cargo-specific requirements for dynein velocity". In: *Molecular biology of the cell* 25.5 (2014), pp. 669–678.

[152] Juan F Abenza, Antonio Galindo, Mario Pinar, Areti Pantazopoulou, Vivian de los Ríos, and Miguel A Peñalva. "Endosomal maturation by Rab conversion in Aspergillus nidulans is coupled to dynein-mediated basipetal movement". In: *Molecular biology of the cell* 23.10 (2012), pp. 1889–1901.

[153] Gero Steinberg. "Endocytosis and early endosome motility in filamentous fungi". In: *Current opinion in microbiology* 20 (2014), pp. 10–18.

[154] Magdalena Bartoszewska, Łukasz Opaliński, Marten Veenhuis, and Ida J van der Klei. "The significance of peroxisomes in secondary metabolite biosynthesis in filamentous fungi". In: *Biotechnology letters* 33.10 (2011), pp. 1921–1931.

[155] Philipp Khuc Trong, Jochen Guck, and Raymond E Goldstein. "Coupling of active motion and advection shapes intracellular cargo transport". In: *Phys Rev Lett* 109.2 (2012), p. 028104.

[156] Lukas C Kapitein, Max A Schlager, Marijn Kuijpers, Phebe S Wulf, Myrrhe van Spronsen, Frederick C MacKintosh, and Casper C Hoogenraad. "Mixed microtubules steer dynein-driven cargo transport into dendrites". In: *Curr Biol* 20.4 (2010), pp. 290–299.

[157] Zhangyuan Yin, Clarence Pascual, and Daniel J Klionsky. "Autophagy: machinery and regulation". In: *Microbial cell* 3.12 (2016), p. 588.

[158] Yvette C Wong and Erika LF Holzbaur. "Autophagosome dynamics in neurodegeneration at a glance". In: *Journal of cell science* 128.7 (2015), pp. 1259–1267.

[159] Taichi Hara, Kenji Nakamura, Makoto Matsui, Akitsugu Yamamoto, Yohko Nakahara, Rika Suzuki-Migishima, Minesuke Yokoyama, Kenji Mishima, Ichiro Saito, Hideyuki Okano, and Noboru Mizushima. "Suppression of basal autophagy in neural cells causes neurodegenerative disease in mice". In: *Nature* 441.7095 (2006), pp. 885–889.

[160] Masaaki Komatsu, Satoshi Waguri, Tomoki Chiba, Shigeo Murata, Jun-ichi Iwata, Isei Tanida, Takashi Ueno, Masato Koike, Yasuo Uchiyama, Eiki Kominami, and Keiji Tanaka. "Loss of autophagy in the central nervous system causes neurodegeneration in mice". In: *Nature* 441.7095 (2006), pp. 880–884.

[161] Thomas Misgeld and Thomas L Schwarz. "Mitostasis in neurons: maintaining mitochondria in an extended cellular architecture". In: *Neuron* 96.3 (2017), pp. 651–666.

[162] Tamar Farfel-Becker, Joseph C Roney, Xiu-Tang Cheng, Sunan Li, Sean R Cuddy, and Zu-Hang Sheng. "Neuronal soma-derived degradative lysosomes are continuously delivered

to distal axons to maintain local degradation capacity". In: *Cell reports* 28.1 (2019), pp. 51–64.

[163] Bella Koltun, Sivan Ironi, Noga Gershoni-Emek, Iliana Barrera, Mohammad Hleihil, Siddharth Nanguneri, Ranjan Sasmal, Sarit S Agasti, Deepak Nair, and Kobi Rosenblum. "Measuring mRNA translation in neuronal processes and somata by tRNA-FRET". In: *Nucleic Acids Research* 48.6 (2020), e32–e32.

[164] Sandra Maday and Erika LF Holzbaur. "Autophagosome biogenesis in primary neurons follows an ordered and spatially regulated pathway". In: *Developmental cell* 30.1 (2014), pp. 71–85.

[165] Andrea KH Stavoe and Erika LF Holzbaur. "Autophagy in neurons". In: *Annual review of cell and developmental biology* 35 (2019), pp. 477–500.

[166] Meng-meng Fu, Jeffrey J Nirschl, and Erika LF Holzbaur. "LC3 binding to the scaffolding protein JIP1 regulates processive dynein-driven transport of autophagosomes". In: *Developmental cell* 29.5 (2014), pp. 577–590.

[167] Sydney E Cason, Peter J Carman, Claire Van Duyne, Juliet Goldsmith, Roberto Dominguez, and Erika LF Holzbaur. "Sequential dynein effectors regulate axonal autophagosome motility in a maturation-dependent pathway". In: *Journal of Cell Biology* 220.7 (2021), e202010179.

[168] Andrea KH Stavoe, Sarah E Hill, David H Hall, and Daniel A Colón-Ramos. "KIF1A/UNC-104 transports ATG-9 to regulate neurodevelopment and autophagy at synapses". In: *Developmental cell* 38.2 (2016), pp. 171–185.

[169] Tessa N Campbell and Francis YM Choy. "The effect of pH on green fluorescent protein: a brief review". In: *Mol Biol Today* 2.1 (2001), pp. 1–4.

[170] Serhiy Pankiv, Terje Høyvarde Clausen, Trond Lamark, Andreas Brech, Jack-Ansgar Bruun, Heidi Outzen, Aud Øvervatn, Geir Bjørkøy, and Terje Johansen. "p62/SQSTM1 binds directly to Atg8/LC3 to facilitate degradation of ubiquitinated protein aggregates by autophagy". In: *Journal of biological chemistry* 282.33 (2007), pp. 24131–24145.

[171] C Alexander Boecker, Juliet Goldsmith, Dan Dou, Gregory G Cajka, and Erika LF Holzbaur. "Increased LRRK2 kinase activity alters neuronal autophagy by disrupting the axonal transport of autophagosomes". In: *Current Biology* (2021).

[172] Kotaro Tsuboyama, Ikuko Koyama-Honda, Yuriko Sakamaki, Masato Koike, Hideaki Morishita, and Noboru Mizushima. "The ATG conjugation systems are important for degradation of the inner autophagosomal membrane". In: *Science* 354.6315 (2016), pp. 1036–1041.

[173] Clemens Alexander Boecker, Mara A Olenick, Elizabeth R Gallagher, Michael E Ward, and Erika LF Holzbaur. "ToolBox: Live Imaging of intracellular organelle transport in induced pluripotent stem cell-derived neurons". In: *Traffic* 21.1 (2020), pp. 138–155.

[174] Rebecca S Saleeb, Deirdre M Kavanagh, Alison R Dun, Paul A Dalgarno, and Rory R Duncan. "A VPS33A-binding motif on syntaxin 17 controls autophagy completion in mammalian cells". In: *Journal of Biological Chemistry* 294.11 (2019), pp. 4188–4201.

[175] Elena F Koslover, Mario A Díaz de la Rosa, and Andrew J Spakowitz. "Theoretical and computational modeling of target-site search kinetics in vitro and in vivo". In: *Biophys J* 101.4 (2011), pp. 856–865.

[176] M Necati Ozisik. *Heat transfer: a basic approach*. McGraw-Hill New York, 1985.

[177] David J Wales. "Discrete path sampling". In: *Mol Phys* 100.20 (2002), pp. 3285–3305.

[178] Daniel St Johnston. "Moving messages: the intracellular localization of mRNAs". In: *Nat Rev Mol Cell Bio* 6.5 (2005), p. 363.

[179] C Loverdo, O Bénichou, M Moreau, and R Voituriez. "Reaction kinetics in active media". In: *J Stat Mech* 2009.02 (2009), P02045.

[180] Edyta Szewczyk, Tania Nayak, C Elizabeth Oakley, Heather Edgerton, Yi Xiong, Naimeh Taheri-Talesh, Stephen A Osmani, and Berl R Oakley. "Fusion PCR and gene targeting in Aspergillus nidulans". In: *Nat Protoc* 1.6 (2006), p. 3111.

[181] Tania Nayak, Edyta Szewczyk, C Elizabeth Oakley, Aysha Osmani, Leena Ukil, Sandra L Murray, Michael J Hynes, Stephen A Osmani, and Berl R Oakley. "A versatile and efficient gene-targeting system for Aspergillus nidulans". In: *Genetics* 172.3 (2006), pp. 1557–1566.

[182] Richard B Todd, Meryl A Davis, and Michael J Hynes. "Genetic manipulation of Aspergillus nidulans: meiotic progeny for genetic analysis and strain construction". In: *Nat Protoc* 2.4 (2007), p. 811.

[183] Richard B Waring, Gregory S May, and N Ronald Morris. "Characterization of an inducible expression system in Aspergillus nidulans using alcA and tubulincoding genes". In: *Gene* 79.1 (1989), pp. 119–130.

[184] Daniel G Gibson, Lei Young, Ray-Yuan Chuang, J Craig Venter, Clyde A Hutchison III, and Hamilton O Smith. "Enzymatic assembly of DNA molecules up to several hundred kilobases". In: *Nat Methods* 6.5 (2009), p. 343.

[185] Bi-Chang Chen, Wesley R. Legant, Kai Wang, Lin Shao, Daniel E. Milkie, Michael W. Davidson, Chris Janetopoulos, Xufeng S. Wu, John A. Hammer, Zhe Liu, Brian P. English,

Yuko Mimori-Kiyosue, Daniel P. Romero, Alex T. Ritter, Jennifer Lippincott-Schwartz, Lillian Fritz-Laylin, R. Dyche Mullins, Diana M. Mitchell, Joshua N. Bembenek, Anne-Cecile Reymann, Ralph Böhme, Stephan W. Grill, Jennifer T. Wang, Geraldine Seydoux, U. Serdar Tulu, Daniel P. Kiehart, and Eric Betzig. "Lattice light-sheet microscopy: Imaging molecules to embryos at high spatiotemporal resolution". In: *Science* 346.6208 (2014).

[186] Johannes Schindelin, Ignacio Arganda-Carreras, Erwin Frise, Verena Kaynig, Mark Longair, Tobias Pietzsch, Stephan Preibisch, Curtis Rueden, Stephan Saalfeld, Benjamin Schmid, Jean-Yves Tinevez, Daniel James White, Volker Hartenstein, Kevin Eliceiri, Pavel Tomancak, and Albert Cardona. "Fiji: an open-source platform for biological-image analysis". In: *Nat Methods* 9.7 (2012), p. 676.

[187] Caroline A Schneider, Wayne S Rasband, and Kevin W Eliceiri. "NIH Image to ImageJ: 25 years of image analysis". In: *Nat Methods* 9.7 (2012), p. 671.

[188] John C Crocker and David G Grier. "Methods of digital video microscopy for colloidal studies". In: *J Colloid Interf Sci* 179.1 (1996), pp. 298–310.

[189] *MATLAB 3D feature-finding algorithms*. downloaded from `http://people.umass.edu/kilfoil/downloads.html`.

[190] Elena F Koslover and Andrew J Spakowitz. "Force fluctuations impact kinetics of biomolecular systems". In: *Physical Review E* 86.1 (2012), p. 011906.

[191] John D Chodera and Frank Noé. "Markov state models of biomolecular conformational dynamics". In: *Current opinion in structural biology* 25 (2014), pp. 135–144.

[192] Jennifer J Smith and John D Aitchison. "Peroxisomes take shape". In: *Nat Rev Mol Cell Bio* 14.12 (2013), p. 803.